AIX-MARSEILLE UNIVERSITE

ECOLE DOCTORALE Physique et Sciences de la Matière-ED 352

CINaM - Centre Interdisciplinaire de Nanoscience de Marseille / UMR 7325

Thèse présentée pour obtenir le grade universitaire de docteur

Discipline : Physique et sciences de la matière
Spécialité : Matière Condensée et Nanosciences

Michel Daher Mansour

Nanolignes de métaux de transition sur un gabarit d'argent nanostructuré: croissance auto-organisée et propriétés magnétiques

Transition metal nanolines on a nanopatterned silver substrate: self-organized growth and magnetic properties

Soutenue le 24/09/2019 devant le jury:

Sylvie ROUSSET	CNRS, Laboratoire Matériaux et Phénomènes Quantiques (MPQ)	Rapporteure
David MARTROU	CNRS, Centre d'Élaboration de Matériaux et d'Etudes Structurales (CEMES)	Rapporteur
Isabelle BERBEZIER	CNRS, Institut Matériaux Microélectronique Nanosciences de Provence (IM2NP)	Examinatrice
Olivier FRUCHART	CNRS, Spintec, CEA Grenoble	Examinateur
Geoffroy PREVOT	CNRS, Institut des Nanosciences de Paris (INSP)	Examinateur
Romain PARRET	Université Aix-Marseille - CINaM	Examinateur
Laurence MASSON	Université Aix-Marseille - CINaM	Directrice de thèse

Numéro national de thèse/suffixe local : 2019AIXM0287/035ED352

Acknowledgements

First of all, I would like to thank Aix-Marseille University and the doctoral school of physics and material sciences ED352 for offering me this opportunity by financing my thesis and to let me work in their laboratories so I could get this experience which it is a strong foundation for the future.

I would like to thank Pr. Frédéric Fages and Pr. Pierre Müller, directors of the 'Centre Interdisciplinaire de Nanoscience de Marseille', CINaM, for giving me the opportunity to work on the thesis in the laboratory. Of course, I would like to express my sincere gratitude to my thesis supervisor Pr. Laurence Masson. Her optimistic insights, scientific discussions and leadership/group work skills have strengthened and advanced this study significantly. I will always be thankful for giving me this opportunity to really understand the fundamental science. I would like to thank Dr. Romain Parret for his collaboration, discussions, advices and indeed the great impact he added to this work. I am also grateful of the contribution of Dr. Lisa Michez, especially for the advices related to the magnetic data interpretation.

Overall, I feel so privileged to work in the 2D-ASAP team, headed by Pr. Conrad Becker, which is a wonderful research team that works with high ambition to bring up new ideas in a great ambiance. I would like to thank Alain Ranguis, head of the scanning probe microscopy platform, for his help when needed. I would like also to thank Cyril Coudreau, Philippe Bindzi and Gilles Arthaud for their technical assistance. Without forgetting my friends in the laboratory Maxime and Fiona for the great time we shared.

I desire to thank Dr. Sylvie Rousset and Dr. David Martrou for accepting to report my thesis work and Dr. Isabelle Berbezier, Dr. Olivier Fruchart, Dr. Geoffroy Prévot to join the jury of my thesis defense.

Finally, I want to thank my family for supporting me all the time. Especially, my mom, she was the all-time support system, my sister and her family, also I would like to dedicate my work to the soul of my father, who was always encouraging and motivating me to continue my studies till the Phd.

Résumé

L'intérêt pour les propriétés magnétiques des nanostructures de métaux de transition et de lanthanides de faible dimensionnalité n'a cessé de croitre au cours des deux dernières décennies, tant pour leur intérêt en recherche fondamentale que pour la perspective d'applications technologiques. De manière remarquable, les propriétés magnétiques des nanostructures peuvent être ajustées en contrôlant leur géométrie, leur structure atomique et leur environnement chimique. Les nanostructures magnétiques unidimensionnelles sont connues pour présenter une aimantation exaltée et une forte anisotropie magnétique comparées aux matériaux massifs et aux films bidimensionnels. Cependant, la fabrication de ce type de nano-aimants à grande échelle reste un challenge. La croissance auto-organisée est prometteuse pour synthétiser, sur de grandes surfaces, de fortes densités de nanostructures homogènes et de forme contrôlée à l'échelle atomique. Dans cette thèse, un gabarit unidimensionnel composé de nanorubans de Si auto-organisés est utilisé pour guider la croissance de nanolignes de métaux de transition (Fe, Co, Ni) dans le but d'étudier leurs propriétés magnétiques. La géométrie et la structure atomique des nanorubans de Si et des nanolignes de métaux ont été étudiées *in situ* par microscopie par effet tunnel (STM). Nous nous sommes également intéressés aux mécanismes de croissance en explorant l'effet de différents paramètres physiques (température et taux de couverture). En ce qui concerne le silicium, notre étude montre qu'une température de 490 K est nécessaire pour obtenir un gabarit unidimensionnel hautement ordonné. Les résultats obtenus sur les métaux de transition ont permis de déterminer la géométrie et la structure des nanolignes. Pour accéder aux propriétés magnétiques des nanolignes de Co sur Si, des mesures par dichroïsme circulaire magnétique des rayons x (XMCD) ont été effectuées en température (4 K-100 K), en utilisant différentes orientations du champ magnétique. Les résultats montrent que les deux premières couches de Co directement adsorbées sur les nanorubans présentent une réponse magnétique faible, tandis que les couches supérieures présentent une aimantation exaltée. De manière remarquable, deux axes d'anisotropie ont été mis en évidence. Les moments magnétiques (spin et orbital) et l'énergie d'anisotropie magnétique ont été déterminés quantitativement. Les études en température suggèrent un comportement superparamagnétique, avec une température de blocage très basse comprise entre 20 K et 40 K. Enfin, nous présentons des résultats préliminaires concernant la croissance de molécules à base de porphyrines et de composés organométalliques auto-assemblés, dans la perspective de former des réseaux moléculaires supportés avec des propriétés magnétiques ajustées.

Mots clés : surfaces, croissance, auto-assemblage, nanogabarit, nanostructures unidimensionnelles, propriétés magnétiques, microscopie à effet tunnel (STM), dichroïsme circulaire magnétique des rayons x (XMCD).

Résumé substantiel

Les nanostructures magnétiques comprenant des métaux de transition et des lanthanides ont fait l'objet d'une attention soutenue au cours des vingt dernières années en raison de leur intérêt fondamental et des perspectives d'applications technologiques. Une caractéristique qui les rend intéressants est la possibilité d'ajuster les propriétés magnétiques en contrôlant la structure atomique et la géométrie des nanostructures ou l'environnement chimique des atomes magnétiques. Deux caractéristiques importantes d'un matériau magnétique sont les moments magnétiques à l'état fondamental et l'énergie d'anisotropie magnétique (MAE). La première définit l'aimantation à saturation tandis que la seconde détermine l'orientation de l'aimantation et sa stabilité thermique. D'un point de vue fondamental, l'origine du magnétisme réside dans les courants associés au mouvement électronique définissant les moments orbitaux et dans le spin intrinsèque de l'électron définissant les moments de spin. L'anisotropie magnétique est décrite comme la différence d'énergie entre l'aimantation selon les axes facile et difficile du matériau et l'ordre magnétique en dépend. Le contrôle et la compréhension de ces propriétés sont cruciaux pour le développement d'applications utilisant des nanostructures magnétiques telles que les dispositifs à base de spintronique, les dispositifs d'enregistrement magnétique ou les dispositifs à mémoire magnétique.

Les progrès réalisés dans la fabrication de nano-objets ont permis de développer des nanostructures sur des surfaces ayant une dimensionnalité inférieure à trois dimensions, ce qui entraîne l'apparition de nouvelles propriétés physiques. Par exemple, en ce qui concerne les propriétés magnétiques, le confinement des électrons dans ces nanostructures entraîne une modification des moments magnétiques orbitaux (m_L) et de spin (m_S), ainsi que de la MAE. Une augmentation de ces trois caractéristiques magnétiques (m_L, m_S, MAE) a été montrée lors du passage de systèmes tridimensionnels (3D) à bidimensionnels (2D). Un autre effet réside dans le changement de l'anisotropie magnétique, observée dans le plan dans le cas de films minces et hors plan pour des films ultra-minces. À partir de ces observations, il semblait raisonnable d'obtenir de nouvelles propriétés magnétiques pour une réduction supplémentaire de la dimensionnalité, en passant des nanostructures 2D à unidimensionnelles (1D). Des études fondamentales sur les nanostructures 1D ont été initiées par H. Elmers *et al.* en 1994, avec la fabrication de bandes 1D de Fe sur une surface vicinale de W(110). Des propriétés magnétiques spécifiques liées à l'effet 1D ont été mises en évidence par P. Gambardella *et al.* en 2002 : il a été montré que les chaînes monoatomiques de Co décorant les marches d'une surface vicinale de Pt (997) présentaient un ordre ferromagnétique à courte portée à basse température avec des moments orbitaux et une MAE très élevés. Les valeurs de ces paramètres décroissent rapidement lorsque la largeur des chaînes augmente, comme le montrent P. Gambardella *et al.* en 2004. En outre, une réduction de la dimensionnalité pour atteindre des nanostructures de dimension zéro (0D) conduit à des moments magnétiques orbitaux et à une MAE extraordinairement élevés. Les études rapportées par P. Gambardella *et al.* en 2003, associent ces valeurs à la réduction de la coordination atomique des atomes associée à un rétrécissement de la bande *3d* lors du passage du matériaux massif aux nanostructures.

L'ingénierie à l'échelle atomique est réalisée grâce aux techniques de nanofabrication dites descendante et ascendante. Alors que l'approche descendante, appelée 'top down', dominait dans les années soixante-dix, elle était confrontée à des difficultés pour la croissance de nanostructures composées de quelques atomes. La technique ascendante, appelée 'bottom up', est une approche alternative pour fabriquer des nanostructures à très petite échelle, comme l'a montré O. Fruchart en 2005 pour les matériaux magnétiques. S'appuyant sur cette approche, la

croissance sur surfaces a beaucoup progressé depuis les années quatre-vingt grâce au développement des techniques de croissance ainsi que des techniques de caractérisation. Par exemple, les techniques de dépôt ont connu une amélioration de leur fonctionnement, de leur efficacité et de la maîtrise du taux de dépôt. Dans l'objectif de développer des nanostructures identiques et bien définies couvrant toute la surface, la croissance auto-organisée s'est révélée être un moyen efficace de produire, en une seule étape, des densités élevées de nanostructures homogènes de forme contrôlée à l'échelle atomique. En effet, l'utilisation de sites de nucléation préférentiels sur des surfaces, de surfaces anisotropes ou vicinales et de gabarits spécifiques permet de guider la croissance et donne ainsi accès à un contrôle précis de la géométrie. Parmi ces méthodes, l'approche basée sur l'utilisation des gabarits s'est révélée être une voie prometteuse pour contrôler les propriétés structurales des nanostructures et a donc été utilisée dans mon travail de thèse. En outre, l'avènement de la microscopie à effet tunnel (STM) a permis le développement de ces études car les nanostructures peuvent être visualisées dans l'espace réel aux échelles les plus réduites grâce à cette technique. Dans le même contexte, l'augmentation de la sensibilité des techniques de mesure telles que la spectroscopie d'absorption des rayons x à polarisation de spin, appelée dichroïsme circulaire magnétique des rayons x (XMCD), a permis de découvrir les propriétés magnétiques spécifiques de nanostructures composées de quelques atomes jusqu'à un atome unique. Ainsi, en combinant ces deux techniques (STM-XMCD), de nouvelles investigations dans le vaste domaine du magnétisme en dessous de la monocouche sont accessibles. Il convient de souligner que puisque la croissance auto-organisée permet la fabrication d'une densité élevée de nanostructures avec une distribution de taille étroite, l'utilisation de sondes locales ou macroscopiques, moyennant l'information sur toute la surface, comme celles présentées ci-dessus, est bien adaptée pour corréler la structure atomique des nano-objets à leurs propriétés magnétiques.

Mon travail de thèse vise à développer des nanostructures 1D composées de matériaux magnétiques et à en étudier les propriétés structurales et magnétiques. Une des motivations réside dans la possibilité d'utiliser des nanogabarits pour la croissance de hautes densités de nanostructures identiques, ordonnées et possédant une géométrie contrôlée. La seconde motivation est de contribuer à la compréhension d'un point de vue fondamental du magnétisme lié aux nanostructures 1D. Par conséquent, dans mes travaux, des nanogabarits 1D ont été utilisés pour guider la croissance des nanostructures et l'auto-assemblage a été utilisé pour former des densités élevées de nanostructures 1D homogènes. Des éléments de métaux de transition (TMs) et lanthanide, connus pour être magnétiques, ont été utilisés pour faire croître les nanostructures. Les études de la morphologie des gabarits de surface, de la taille, de la forme et de la configuration atomique des nanostructures ont été réalisées par STM et les propriétés magnétiques des nanolignes de Co formées ont été étudiées par XMCD. La stratégie développée au cours de ma thèse pour réaliser ces études est présentée sur la Figure I ci-dessous.

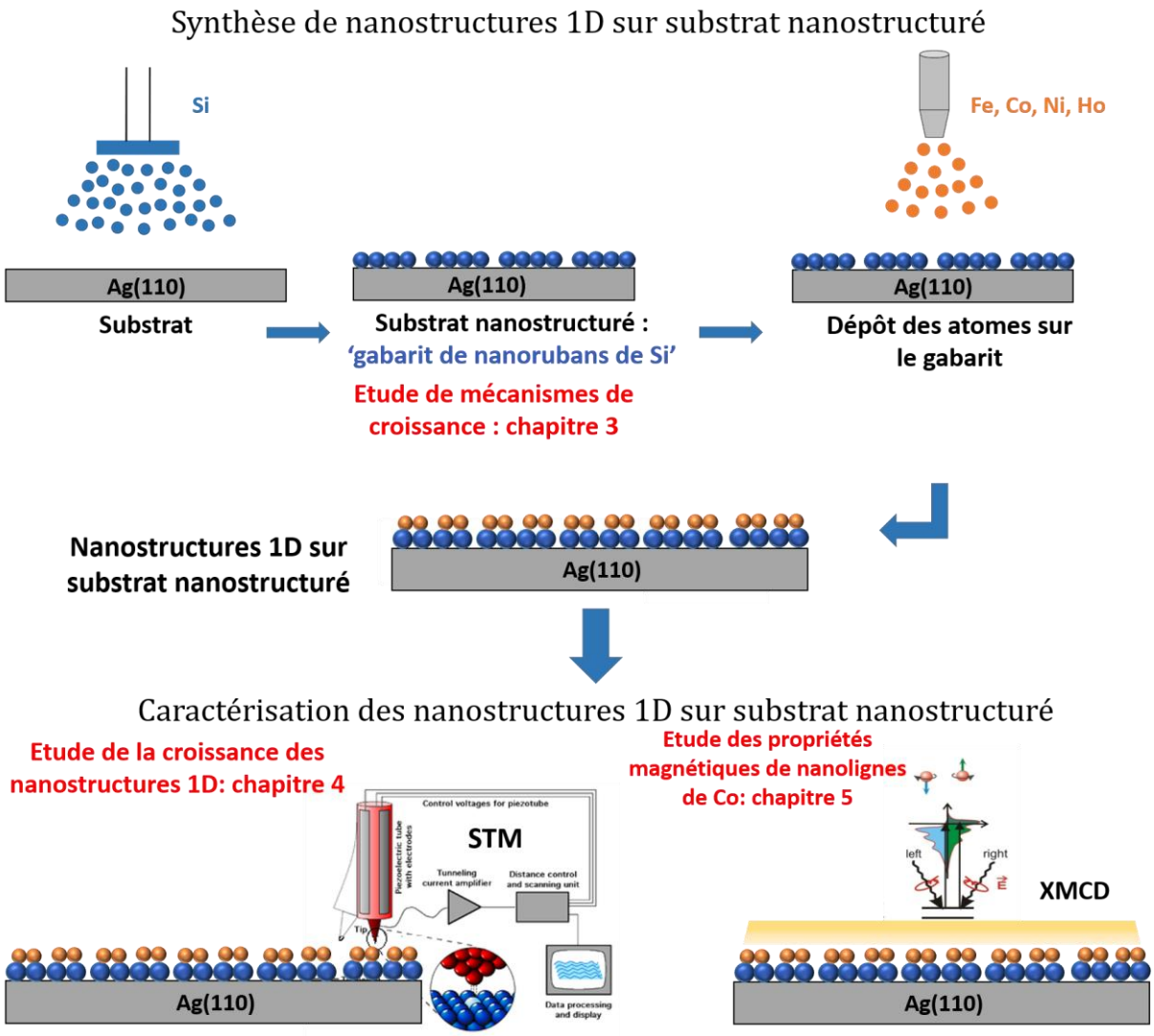

Figure I : illustration de la stratégie adoptée pour les travaux de la thèse. Dans une première étape, l'étude par STM des mécanismes de croissances du gabarit de silicium sur Ag(110) est présentée. Dans une deuxième étape, l'étude par STM de la croissance des nanostructures 1D sur le gabarit est présentée. Enfin, dans une troisième étape, les propriétés magnétiques des nanolignes de cobalt sont caractérisées par XMCD.

Cette thèse est composée de cinq chapitres. Après une introduction générale à mon travail de doctorat, les concepts généraux de la croissance, les méthodes de fabrication de nanostructures 1D ainsi que la réponse magnétique de différents nanomatériaux sont présentés dans le **chapitre 1**. Les techniques expérimentales utilisées pour ce travail sont présentées au **chapitre 2**. Les expériences réalisées pour comprendre les mécanismes de croissance des nanogabarits sont présentées et discutées au **chapitre 3**. L'étude de la croissance de nanostructures de TMs (Fe, Co, Ni) et lanthanide (Ho) sur les gabarits est présentée au **chapitre 4**, ainsi que la caractérisation magnétique des nanolignes de Co au **chapitre 5**. Enfin, une **conclusion** générale est présentée, suivie de **perspectives**.

Dans le **chapitre 1**, je présente dans une première partie **(partie A)** les techniques de croissance adoptées pour la croissance de structures à l'échelle nanométrique. La première technique qui a été développée est l'approche descendante ou 'top down', basée sur des techniques de lithographies. Cette technique repose sur un procédé en plusieurs étapes incluant l'application d'une résine, l'exposition puis l'élaboration des nanostructures et enfin le nettoyage

de la surface. La lithographie peut être réalisée soit par faisceau d'électrons soit par rayons x. Cette technique permet un contrôle accru de la taille, de la forme et de la localisation sur la surface des nanostructures mais la résolution est limitée à 20 nm. Les avantages présentés par cette technique ont entraîné un développement important de cette approche dans la recherche fondamentale et les activités industrielles. Lorsque la croissance de nanostructures composées de quelques atomes a commencé à susciter un intérêt considérable, l'approche 'top down' s'est révélée inefficace. Les chercheurs ont alors développé de nouvelles techniques, comme par exemple le déplacement d'atomes à l'aide d'une pointe de microscope à effet tunnel ou à force atomique, mais la procédure d'écriture par ces techniques est lente. Une autre technique correspondant à un dépôt physique en phase vapeur a également été développée. Elle correspond à une approche descendante ou 'bottom up' et permet de créer des agrégats composés de quelques atomes. Bien que cette approche présente des inconvénients concernant le contrôle de l'homogénéité ou de la forme des nanostructures, les études et les recherches menées en physique des surfaces ont permis de fabriquer en une seule étape des objets et des systèmes bien structurés et auto-organisés selon un réseau bien défini. L'intérêt pour l'auto-assemblage sur surfaces n'a cessé de croître depuis une vingtaine d'années.

Dans cette **partie A**, les trois modes de croissance basés sur une description utilisant des quantités thermodynamiques telles que les termes d'énergie libres de surface sont discutés : la croissance Volmer-Weber ou par îlots, la croissance Frank-van der Merwe ou couche par couche et un mode mixte, la croissance Stranski-Krastanov. Cette description des modes de croissance repose sur des considérations thermodynamiques. Elle n'est valable que lorsque la croissance a lieu proche de l'équilibre thermodynamique où la morphologie est gouvernée par l'énergie totale, quel que soit le chemin emprunté par les atomes du film, afin d'atteindre la morphologie d'énergie minimale. Dans une approche dite cinétique où la croissance est un processus cinétique hors-équilibre, l'état final du système dépend des mécanismes activés lors du dépôt des atomes sur une surface et ne correspond pas nécessairement à l'état le plus stable. Ces deux approches de la croissance, thermodynamique et cinétique, sont discutées dans le manuscrit. Puis les processus de nucléation et de croissance dans le régime de croissance cinétique sont décrits en détail. La croissance des structures se résume en quatre étapes : nucléation, nucléation et croissance des objets, croissance des objets et finalement coalescence. Il est à noter que la croissance par dépôt physique en phase vapeur sur une surface isotrope est parfaitement aléatoire. Pour obtenir des nanostructures de forme bien spécifique ou pour localiser les zones de croissance, le dépôt doit être réalisé sur des substrats nanotexturés. Ainsi, plusieurs méthodes pour guider la croissance, la forme et la taille des structures sont présentées. Par exemple, des surfaces anisotropes ont été utilisées pour réaliser la croissance de structures 1D comme des îlots de Cu sur Pd (110). Des surfaces vicinales ont également été utilisées pour développer des nanostructures 1D. L'exemple de nanolignes de Co sur Pt (997) est décrit ainsi que d'autres travaux publiés. Enfin, l'utilisation de nanogabarits préalablement formés est introduite : des nanostructures 1D ont été élaborées sur une phase de bandes alternées Cu-CuO ainsi que sur un réseau de nanorubans (NRs) de Si. Dans ce travail de thèse, le dernier gabarit, synthétisé au CINaM en 2007, a été utilisé. Par conséquent, les étapes les plus importantes de l'étude de ce système sont exposées. Suite à la découverte en 2005 de la synthèse de NRs de Si sur Ag (110) lors du dépôt de Si à température ambiante, un long débat sur la structure atomique et électronique de ces NRs a commencé après la publication d'une signature électronique similaire à celle du graphène mesurée par spectroscopie photoélectronique résolue angulairement (ARPES) et attribuée à la formation du silicène, équivalent du graphène pour le Si. Les NRs de Si d'une largeur de 0,8 nm sont répartis de manière aléatoire sur les terrasses d'Ag ou s'auto-assemblent selon une surstructure 5×2 pour former un réseau 2D de Si composé de NRs espacés de manière régulière (pas de ~ 2 nm) avec une largeur double de 1,6 nm, pour un dépôt de Si à température ambiante et à 460 K, respectivement. Une étude combinée STM-GIXD (diffraction des rayons x à incidence rasante) a permis de mettre en évidence une reconstruction inattendue de la surface Ag (110) associée à la libération d'atomes d'Ag induite par la croissance des NRs de Si. Récemment, une étude combinant théorie (DFT) et expérience (STM, GIXD) a permis d'élucider la structure atomique des NRs de Si. Les NRs correspondent à une phase originale composée de chaînes de pentamères situées dans les rangées

manquantes de la surface Ag(110) reconstruite. Enfin, les résultats sur la croissance de nanolignes de Co sur ce gabarit publiés dans la littérature sont présentés.

Dans une deuxième partie **(partie B)**, le comportement magnétique des éléments et des matériaux est introduit. Plusieurs réponses à l'application d'un champ extérieur sont décrites, dia-, para- et ferromagnétique. Une description plus détaillée est présentée pour le comportement superparamagnétique car il correspond au comportement des nanostructures étudiées dans ce travail. Un système superparamagnétique est obtenu en créant sur une surface des nanostructures suffisamment séparées les unes des autres pour ne pas interagir entre elles, formant un ensemble de macrospins découplés comparable à un système paramagnétique. Pour une température inférieure à une température critique, appelée température de blocage, les macrospins sont dans un état bloqué et pour une température supérieure, la fluctuation des spins est activée thermiquement et une aimantation apparente nulle est mesurée. De plus, le concept de MAE pour les nanostructures est présenté et discuté. Il existe plusieurs sources d'anisotropie magnétique comme par exemple la forme des nanostructures, l'anisotropie magnétocristalline, la brisure de symétrie en surface et l'interface avec le substrat qui engendrent une anisotropie dite de surface. D'autres sources sont aussi mentionnées dans cette partie comme l'anisotropie magnétoélastique. L'anisotropie totale est la somme de toutes les anisotropies existantes dans un système. Enfin, des nanostructures magnétiques 1D pouvant présenter des propriétés magnétiques intéressantes, telles qu'une forte MAE, un comportement ferromagnétique à basse température et une aimantation à orientation spécifique, sont présentées.

Dans le **chapitre 2**, les montages expérimentaux utilisés lors de ma thèse pour la croissance et la caractérisation des nanostructures sont décrits. La croissance a été réalisée par évaporation thermique du matériau et condensation sur la surface, ce qui nécessite d'être effectué dans des chambres ultravide (UHV). Les bâtis UHV sont décrits brièvement dans une première partie. Ensuite, dans ce chapitre, la procédure ainsi que les systèmes de pompage et d'étuvage pour obtenir un environnement ultravide sont présentés. Le dégazage des évaporateurs et des échantillons ainsi que la préparation de la surface Ag(110) sous UHV sont décrits. La préparation de la surface à étudier consiste à nettoyer le substrat d'argent (bombardement ionique suivi d'un recuit doux à 770 K) puis à faire croître les nanostructures sur celui-ci. Puis, les deux techniques expérimentales majeures de ce travail de thèse, STM et XMCD, sont décrits en détail. Le fonctionnement, les montages expérimentaux et l'analyse des données sont présentés pour les deux techniques. Le STM est une technique basée sur l'effet tunnel quantique. Cet effet est expliqué d'une manière générale puis de manière plus spécifique dans le cas du STM. Le principe de fonctionnement d'un STM est décrit en détail. Enfin, la pointe STM et sa procédure de fabrication sont présentées. Le STM permet d'obtenir des images des surfaces à l'échelle nanométrique, ce qui facilite l'étude de la morphologie du dépôt. De plus, il est possible d'obtenir des images STM en haute résolution qui aident à élucider les structures atomiques des nano-objets. Cette technique a contribué à rendre l'ingénierie atomique possible. D'autre part, le développement de techniques de caractérisation telles que les techniques spectroscopiques a permis d'étudier la composition chimique des nanostructures en utilisant la spectroscopie d'adsorption des rayons x et les propriétés magnétiques en analysant les spectres XMCD. Le montage expérimental de cet outil puissant d'analyse des surfaces est décrit ainsi que les phénomènes physiques le régissant. La fabrication au cours de mon travail de thèse d'assemblées de nanostructures homogènes et identiques a permis de combiner ces deux méthodes de caractérisation, le STM étant une technique de caractérisation locale et l'XMCD une technique de caractérisation moyennant l'information sur toute la surface. La combinaison de ces deux méthodes a ainsi permis d'étudier les propriétés magnétiques des nanostructures en lien avec leur forme, leur structure atomique, leur taille et leur environnement chimique.

La croissance des nanogabarits 1D sur Ag(110) est présentée au **chapitre 3**. Les gabarits utilisés pendant ma thèse correspondent à un réseau 2D avec un motif 1D de NRs de Si simples

(0,8 nm de largeur) ou doubles (1,6 nm de largeur) afin de faire croître des nanostructures 1D. Nous nous attendons à ce que la croissance des nanostructures de TMs, présentée dans le chapitre suivant, soit influencée par la largeur des NRs couvrant la surface Ag (110). Bien que la structure atomique des NRs de Si ait été largement étudiée et élucidée, peu d'études sur les mécanismes de croissance ont été conduites pour comprendre l'interaction entre la formation des NRs simples et doubles (SNRs et DNRs) de Si et les régions d'Ag reconstruites en rangées manquantes, interaction qui s'est révélée cruciale pour ajuster la géométrie du nanogabarit. Dans ce chapitre, nous présentons une étude à l'échelle nanométrique par STM des mécanismes de croissance du Si sur Ag(110) dans le régime de la sous monocouche à différentes températures. En fonction de la température du substrat, variant de la température ambiante à 500 K, différents arrangements de NRs de Si sont formés (voir Figure II). Ils se différencient par le remplacement progressif des SNRs par des DNRs et par l'organisation latérale des NRs, dans la direction perpendiculaire aux rubans. Notre étude met en évidence des transitions de croissance 1D vers 2D (i) à 380 K, correspondant à la transition de SNRs isolés en SNRs localement assemblés dans une superstructure 3×2 et (ii) à 440 K, correspondant à la transition de DNRs isolés en DNRs auto-assemblés dans une superstructure 5×2 à longue portée. Les énergies d'activation pour la formation des NRs isolés et des DNRs auto-assemblés sont déterminées à partir de l'analyse statistique des densités de NRs mesurées sur les images STM (300 nm^2). D'autre part, nos résultats confirment que la transition des nanostructures précurseurs de la formation des NRs en chaînes de pentamères est le facteur limitant pour la croissance des NRs simples. Cette transition est activée thermiquement. De plus, nos résultats suggèrent fortement que la reconstruction en rangées manquantes de la surface Ag (110) joue un rôle clé dans la formation des NRs de Si et soulignent ainsi le rôle du substrat d'argent dans les mécanismes de croissance du Si. Dans ce contexte, nous expliquons également pourquoi une superstructure 3×2 ordonnée à longue portée ne peut pas être formée, contrairement au réseau 5×2 couvrant toute la surface. Ce dernier nanogabarit sera utilisé de manière préférentielle pour la croissance et la caractérisation de nanolignes, comme décrit au chapitre 4.

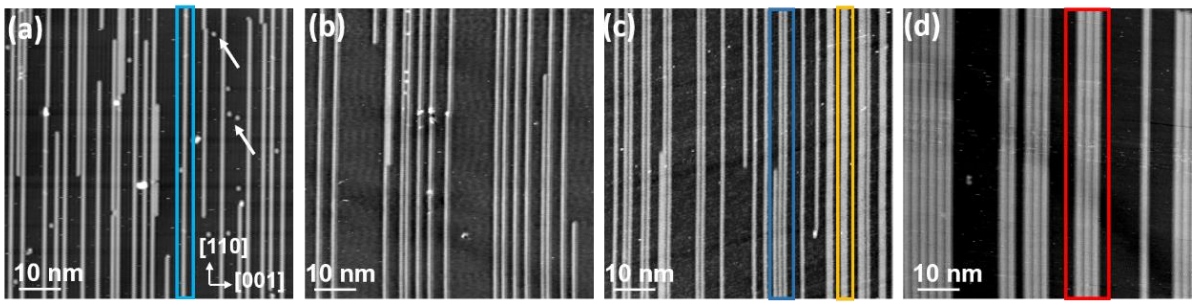

Figure II : Images STM ((70 × 70) nm^2) après dépôt de Si sur Ag (110) à quatre températures de substrat différentes et au même taux de couverture de Si ($\vartheta_{Si} \sim 0{,}22\ ML_{Si}$), montrant la formation de nanorubans simples (SNRs) et doubles (DNRs) : (a) RT, (b) 350 K, (c) 390 K et (d) 480 K. Les quatre types de nanorubans (NRs) sont indiqués par des rectangles colorés : 1D-SNRs (bleu clair en (a)), 1D-DNRs (orange en (c), à droite), SNRs 2D (bleu en (c), partie centrale droite) et 2D-DNRs (rouge en (d)). En (a), les flèches indiquent la formation de nanostructures précurseurs de Si.

Dans le **chapitre 4**, je présente la croissance de nanolignes de TMs (Fe, Co, Ni) et de nanostructures de lanthanide (Ho) sur les NRs de Si. Concernant le dépôt de TMs, nos études basées sur l'analyse d'images STM portent à la fois sur la longueur et la structure atomique des nanolignes en fonction de l'espèce métallique. Les dépôts vont de la sous monocouche (ML) à quatre monocouches. En accord avec des résultats précédents sur Co, nous avons mis en évidence l'adsorption préférentielle des atomes de TMs au-dessus des NRs de Si. De plus, nous avons réussi à faire croître des densités élevées de nanolignes identiques, régulièrement espacées et ayant la même orientation sur une surface d'argent fonctionnalisée par des NRs de Si. Nous avons montré que les nanolignes de Co et de Ni avaient la même structure en dimères et nous avons établi un lien entre la formation de ces nanolignes et les chaînes de pentamères simples et doubles de Si. Ces résultats prouvent que le réseau de NRs de Si peut parfaitement jouer le rôle de gabarit pour contrôler la croissance de différents éléments. Une observation détaillée des images STM a révélé la formation de trous associée au processus de diffusion des atomes de TMs dans les NRs de Si, facteur cinétique limitant la croissance de nanolignes de TMs longues et sans défauts. Nous avons montré que ce processus atomique de diffusion est thermiquement activé et peut être partiellement bloqué par le dépôt des atomes de TMs à basse température (220 K pour le Co). De plus, nous avons montré que la longueur des nanolignes dépend de la nature chimique des éléments. Les longueurs moyennes sont de 3,5 nm, 4,5 nm et 5,5 nm pour les nanolignes Fe, Co et Ni, respectivement, pour le dépôt de TMs à température ambiante sur la superstructure 5×2 (voir Figure III). Par conséquent, pour faire croître des nanolignes longues et sans défauts, il faut optimiser les paramètres de croissance avec un choix optimisé de l'élément chimique. Pour les couvertures de TMs supérieures à 1 ML, nous avons montré que le dépôt reproduit le motif 1D du gabarit de Si avec une structure en dimère similaire à celle des nanolignes de première couche. La longueur des nanolignes des couches supérieures est supposée être régie par celle des nanolignes de la première couche. Enfin, le dépôt de Ho sur le nanogabarit de Si a également montré une adsorption préférentielle sur les NRs de Si. Cependant, des nanostructures 1D de Ho faiblement organisées ont été formées à la périphérie des îlots de NRs à température ambiante. Cet effet est lié à la faible longueur de diffusion des atomes de Ho sur les NRs à cette température. Un léger recuit de l'échantillon s'est avéré activer la destruction du gabarit de Si sans formation de nanostructures 1D ordonnées sur les NRs.

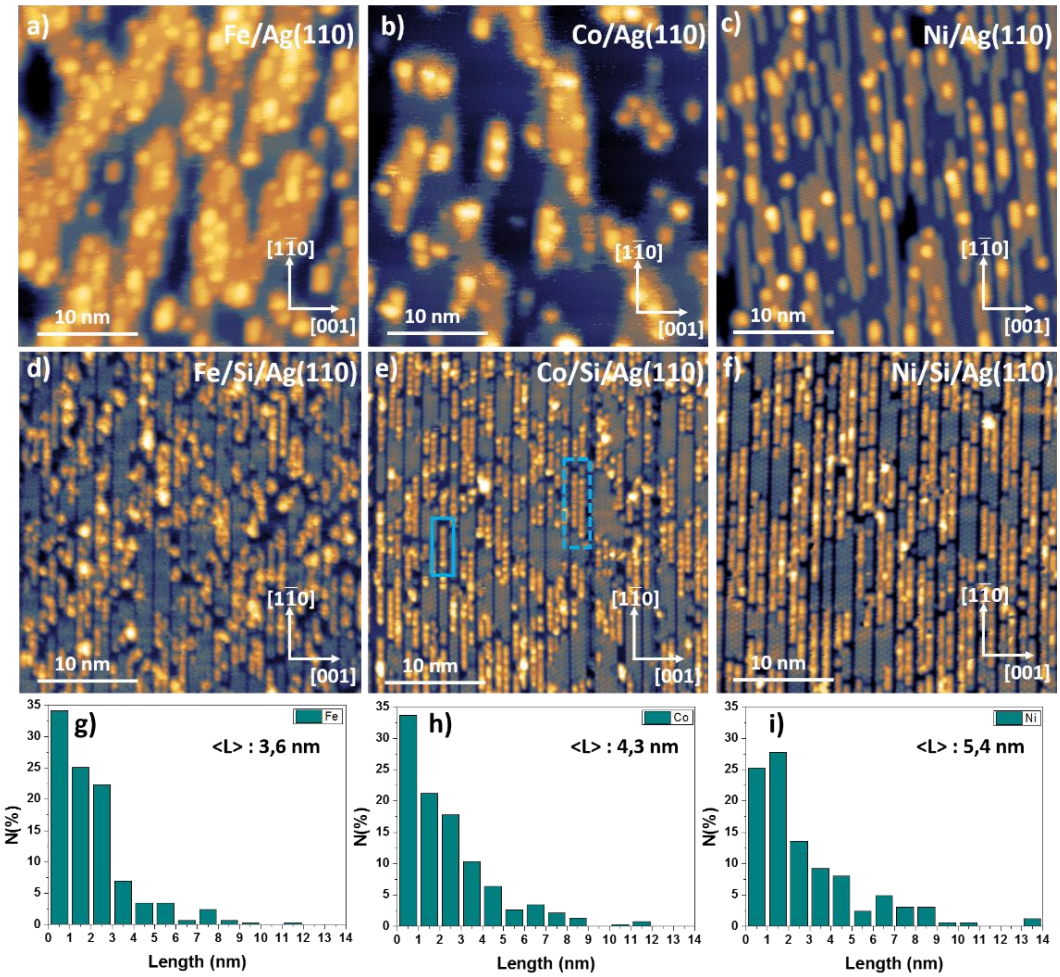

Figure III i: (a), (b) et (c) images STM montrant le dépôt de Fe, Co et Ni sur Ag (110) à température ambiante, respectivement. Dépôt de Fe (d), Co (e) et Ni (f) sur le réseau 5 ×2 de Si, à température ambiante ($\theta_{TM} \sim 0.6\ ML_{TM}$). Histogrammes montrant la distribution en taille L des nanolignes de Fe (g), Co (h) et Ni (i) et <L> la longueur moyenne des nanolignes. Les rectangles en trait plein et en pointillé en (e) identifient les nanolignes simples et couplées, respectivement.

Dans le **chapitre 5**, je présente les propriétés intrinsèques magnétiques d'un film ultra-mince composé de nanolignes de Co formées à 220 K sur le gabarit 5×2 de Si. Des études en température (allant de 4 K à 100 K) et avec différentes orientations du champ magnétique appliqué (de l'incidence normale à rasante) ont été effectuées par XMCD. Les moments magnétiques orbital et de spin ont été déterminés, en fonction de l'angle du champ magnétique, grâce aux règles de somme fournies par cette technique. Notre étude montre que les deux premières couches de Co présentent une réponse magnétique faible, tandis que les couches de Co supérieures présentent une magnétisation exaltée. L'énergie d'anisotropie magnétique est également mesurée à partir des courbes d'aimantation dépendantes du champ magnétique. De manière remarquable, deux axes faciles d'aimantation ont été mis en évidence avec une anisotropie légèrement plus favorable dans la direction parallèle à l'axe des nanolignes par rapport à l'axe perpendiculaire (voir Figure IV). Une étude en fonction de la température a révélé un comportement superparamagnétique du système de nanolignes de Co avec une température de blocage comprise entre 20 et 40 K. Les macrospins 1D, d'une épaisseur de deux couches, sont composés d'environ 74 atomes, avec une longueur estimée à 4 nm, proche de la longueur des nanolignes de Co. Notre étude illustre la richesse de l'anisotropie magnétique des systèmes de basse dimension.

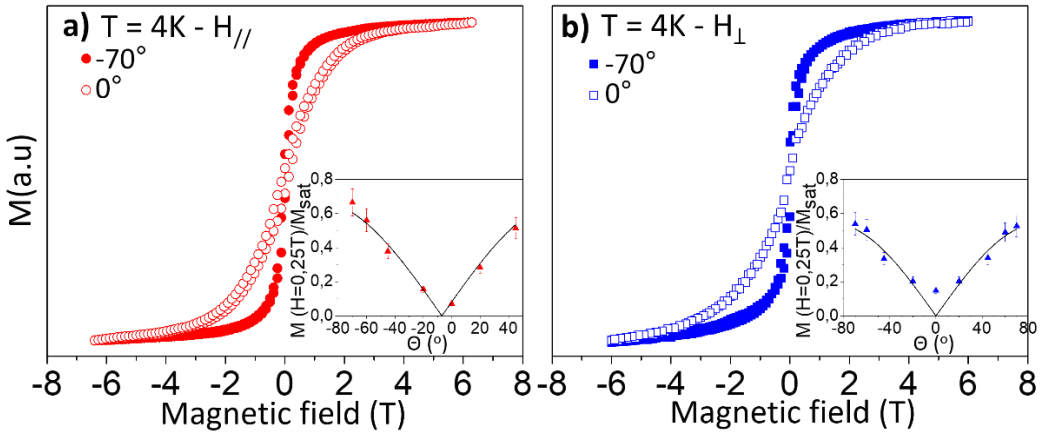

Figure IV : Magnétisation (M) pour 4 ML_{Co} mesurée à 4K au seuil L_3 du Co. M en fonction du champ appliqué (a) dans la configuration $H_{//}$ et (b) la configuration $H_{\perp}$. Les courbes d'aimantation sont mesurées en incidence rasante (θ = 70 °, points rouges pleins et carrés bleus pleins) et en incidence normale (θ = 0 °, points rouges vides et carrés bleus vides). Encadrés : dépendance angulaire de l'aimantation. Variation dans les deux configurations $H_{//}$ et $H_{\perp}$ de l'aimantation à 0,25 T, normalisée à l'aimantation à saturation (M_{sat}) en fonction de l'angle d'incidence. Les lignes continues correspondent à la fonction $a|\sin(\theta-\theta_0)|$.

Enfin, je présente une conclusion générale à l'ensemble des résultats issus des travaux réalisés pendant ma thèse. Elle est suivie de perspectives dans le cadre de mon travail de doctorat. Au cours de la dernière décennie, une autre voie prometteuse est apparue pour manipuler les propriétés magnétiques des atomes de TMs supportés. L'approche consiste à les lier de manière sélective à des ligands fonctionnels pour former des assemblages métal-ligand supportés afin de contrôler le champ de ligand agissant sur ces atomes magnétiques, comme l'ont montré Gambardella *et al.* en 2009. Dans ce contexte, de nouvelles stratégies basées sur la synthèse chimique sur surface se sont développées. Dans cette dernière section dédiée aux perspectives, je présente les résultats préliminaires que j'ai obtenus sur l'adsorption de molécules à base de porphyrines (tetrabromoanthracenylporphyrine) et de complexes dinickel-quinone sur Ag (110). De manière remarquable, nous montrons que les deux molécules, synthétisées *ex-situ*, s'adsorbent sur la surface d'argent pour former des réseaux supramoléculaires 2D. Ces résultats préliminaires ouvrent de nouvelles perspectives pour synthétiser des réseaux organométalliques innovants potentiellement dotés de propriétés magnétiques remarquables.

Abstract

Interest in the magnetic properties of low dimensional transition metal and lanthanide nanostructures has seen an unprecedented rise in the last two decades due to both their fundamental interest and perspectives of technological applications. Remarkably, the magnetic properties of nanostructures can be tuned by controlling their geometry, atomic structure and chemical environments. One-dimensional magnetic nanostructures are known to exhibit exalted magnetization and strong anisotropic behavior compared to bulk material and two-dimensional films. However, the fabrication of such nanomagnet using scalable process remains challenging. A promising way to produce high densities of homogeneous surface-supported nanostructures with controlled shape at the atomic scale relies on the self-organized growth. In this thesis, a one-dimensional template composed of self-organized Si nanoribbons is used to grow transition metal (Fe, Co, Ni) nanolines, prior to the characterization of their magnetic properties. The geometries and the atomic structure of both the Si nanoribbons and the metal nanolines were investigated *in situ* by scanning tunneling microscopy (STM). The growth mechanisms were investigated by exploring a large set of growth conditions (temperature and coverage). Regarding the Si growth, our study shows that a temperature of 490 K is necessary to obtain a long-range ordered one-dimensional template. Concerning the transition metal study, the results resolved the nanoline geometries and atomic structures. To access the magnetic properties of the Co nanolines on Si, x-ray magnetic circular dichroism (XMCD) measurements were performed in the temperature range 4 K – 100 K, using different magnetic field orientations. The results show that the first two Co layers directly adsorbed onto the Si nanoribbons present a weak magnetic response while the upper Co layers exhibit an enhanced magnetization. Remarkably, two easy axes of magnetization were evidenced. The magnetic moments (spin and orbital) and the magnetic anisotropic energy are determined quantitatively. Temperature-dependent investigations strongly suggest a superparamagnetic behavior, with a very low blocking temperature, between 20 and 40 K. Finally, we show preliminary results concerning the growth of self-assembled porphyrin-based molecules and organometallic compounds, in the purpose to form surface-supported molecular networks with tuned magnetic properties

Keywords: surfaces, growth, self-assembly, nanotemplate, one-dimensional nanostructures, magnetic properties, scanning tunneling microscopy (STM), x-ray magnetic circular dichroism (XMCD)

Acronyms

CINaM:	Centre Interdisciplinaire de Nanoscience de Marseille
STM:	scanning tunneling microscopy
XAS:	x-ray absorption spectroscopy
XMCD:	x-ray magnetic circular dichroism
XPS:	x-ray photoelectron spectroscopy
PES:	photoemission spectroscopy
ARPES:	angle resolved photoemission spectroscopy
SDRS:	surface differential reflectance spectroscopy
LEED:	low energy electron diffraction
GIXD:	grazing incidence x-ray diffraction
DFT:	density functional theory
UHV:	ultra-high vacuum
RT:	room temperature
LT:	low temperature
T_c:	Curie-temperature
T_B:	blocking temperature
1D:	one-dimensional
2D:	two-dimensional
3D:	three-dimensional
ML:	monolayer
MR:	missing-row
NRs:	nanoribbons
SNRs:	single nanoribbons
DNRs:	double nanoribbons
TM:	transition metal
TLD:	transverse linear density
MAE:	magnetic anisotropy energy
MOFs:	metal-organic frameworks
TBrAPorph:	tetra-bromoanthracenyl porphyrin

Thesis contents

Acknowledgements 1
Résumé 3
Résumé substantiel 5
Abstract 15
Acronyms 17
Introduction 23
Chapter 1 27
Material growth and magnetic behaviors 27
A- Growth 28
Introduction 28
I- Growth modes and nucleation theory 28
i- Growth modes 28
ii- Thermodynamic vs kinetic growth 30
iii- Nucleation and growth processes 31
II- Self-organized growth 37
i- Anisotropic surfaces 37
ii- Vicinal surfaces 39
iii- Nanopatterned surfaces 40
B- Magnetism 52
I- Types of materials 52
II- Introduction to superparamagnetism 54
III- Magnetic anisotropy 55
IV- Magnetism in nanostructures 57
Chapter 2 61
Experimental techniques 61
I- UHV Chambers and protocol 62
II- Scanning tunneling microscopy (STM) 64
i- STM set-up 65
ii- Principle of STM 65
iii- STM functioning 68
iv- STM-tip preparation 68
III- X-ray absorption spectroscopy (XAS) and x-ray magnetic circular dichroism (XMCD) ... 70
i- Principle of XAS 70

ii- Polarization of x-ray 72
iii- Principle of XMCD 72
iv- XAS-XMCD set-up 75
Chapter 3 79
Nanoscale investigation of Si nanoribbon growth on Ag(110) 79
I- Introduction 80
II- Ag(110) surface 81
III- Growth of Si nanoribbons (NRs) 81
1) Experimental methods 81
2) Statistical analysis of STM images 82
3) Growth description of the four types of Si NRs 82
4) Transverse linear density (TLD) of Si SNRs and Si DNRs 83
5) Temperature-dependent percentage of the four types of Si NRs 84
6) Transverse linear density (TLD) of the Si SNR and Si DNR islands 86
7) Thermal stability of the 5×2 superstructure 87
IV- Discussion 88
V- Conclusion 90
Chapter 4 91
Self-organized growth of transition metal and lanthanide 1D nanostructures 91
I- Introduction 92
II- Growth of transition metal (TM) nanolines 92
1) Experimental methods 92
2) Statistical analysis of STM images 93
3) TM on Ag(110) surface 93
4) Si template effect 93
5) Structure of TM nanolines 95
6) Formation of holes 97
7) Temperature effects 98
8) Growth at higher TM coverage 99
9) Discussion 100
III- Growth of Ho 1D nanostructures 101
1) Experimental methods 102
2) Ho growth 102
IV- Conclusion 103
Chapter 5 105
Magnetic properties of Co nanolines 105

I- Introduction 106
II- Magnetic properties 108
1) Experimental methods 108
2) Orbital and spin moment determination 109
3) Magnetic anisotropy energy (MAE) 111
4) Temperature-dependent magnetization 112
III- Conclusion 114
Conclusion 115
Perspectives 119
Figure list 124
References 129

Introduction

Nanostructures made of magnetic materials involving transition metals and lanthanide elements have received, in the last twenty years, a lot of attention due to both their fundamental interest and the perspectives of technological applications. A feature that makes them interesting is the possibility to tune the magnetic properties by controlling either the atomic structure and the geometry of the nanostructures or the chemical environment of the magnetic atoms. Two important characteristics of a magnetic material are the ground-state magnetic moments and the magnetic anisotropy energy (MAE). The first one defines the saturation magnetization whereas the second one determines the orientation of the magnetization and its thermal stability. Basically, the sources of magnetism are the currents associated to the electronic motion defining the orbital moments and the electron's intrinsic spin defining the spin moments. The magnetic anisotropy is described as the energy difference between the magnetization in the easy and hard axes and the magnetic ordering relies on it. The control and understanding of these properties are crucial for the development of applications using magnetic nanostructures like spintronic based devices, magnetic recording or memory devices.

The improvement in experimental realizations provides routes to grow nanostructures on surfaces in less than three dimensions, which results in the appearance of new physical properties. For instance, regarding the magnetic properties, the confinement of electrons in less than three dimensions leads to a change of orbital (m_L) and spin (m_S) magnetic moments as well as the MAE. An enhancement of these three magnetic characteristics (m_L, m_S, MAE) is shown upon going from three-dimensional (3D) to two-dimensional (2D) systems. Other effect lies in the change of the magnetic anisotropy: in-plane MAEs appeared in the case of thin films while out-of-plane MAEs are observed in ultra-thin films. At this point, expectations of obtaining new magnetic properties for a further reduction in dimensionality from 2D to one-dimensional (1D) nanostructures seemed reasonable. Fundamental studies of 1D structures was pioneered by Elmers *et al.* in the nineties, who fabricated 1D Fe stripes on vicinal W(110) surface. Specific magnetic properties linked to the 1D effect was shown by P. Gambardella *et al.* in 2002, where Co monoatomic chains grown at step edges of a vicinal Pt(997) surface were shown to present a short-range ferromagnetic order at low temperature with a very high orbital moments and MAE. The values of these parameters decrease rapidly when the width of the chains increases as shown by P. Gambardella *et al.* in 2004. Furthermore, a reduction in dimensionality to reach zero-dimensional (0D) nanostructures leads to extraordinary high orbital magnetic moments and MAE. Studies reported by P. Gambardella *et al.* in 2003 associated these large values to the reduced atomic coordination of atoms associated with a 3d band narrowing, when passing from the bulk to nanostructures.

The atomic engineering is now possible due to experimental achievements involving top-down and bottom-up approaches. While the top-down technique was dominating in the seventies, it was confronted with difficulties for the growth of nanostructures composed of few atoms. The bottom-up technique is an alternative approach to fabricate nanostructures at a very low scale as reported by O. Fruchart in 2005 for magnetic materials. In this context, the growth at surfaces have seen a lot of progresses since the eighties due to the development of the techniques of growth as well as the techniques of characterization. For instance, the deposition techniques have seen improvement in their functioning and efficiency and in the fine control of the deposition rate. In the objective to grow similar well-defined structures covering the entire surface, the self-organized growth has proven to be an efficient way to produce in a one-step process high densities

of homogeneous nanostructures with controlled shape at the atomic scale. In this approach, the use of preferential nucleation sites on surfaces, anisotropic or vicinal surfaces and specific templates helps to guide the growth, and thus, allows a fine control of the geometry. Among these methods, the template approach showed to be a promising route to tune the structural properties of nanostructures and thus it has been used in my thesis work. In addition, the extension of the scanning tunneling microscopy (STM) technique has allowed the development of these studies as the nanostructures can be imaged in real space to the lowest scales by this technique. In the same context, the increase of the sensitivity in measurement techniques such as spin polarized x-ray absorption spectroscopy called x-ray magnetic circular dichroism (XMCD) has allowed to discover the peculiar magnetic properties of nanostructures made of few atoms down to single adatoms. Thus, by combining these two techniques (STM-XMCD), novel investigations in the vast field of submonolayer magnetism are accessible. It has to be underlined that since self-organized growth allows the fabrication of a high-density of nanostructures with a narrow size distribution, the use of the local or macroscopic integration probes presented above are well-suited to correlate the atomic structure of the nanoobjects to their magnetic properties.

My thesis work aims at growing 1D nanostructures made of magnetic materials and to study their structural and magnetic properties. One motivation lies in the possibility to use nanotemplates for the growth of high densities of identical high-ordered nanostructures with a control geometry. The second motivation is to contribute to the fundamental understanding of nanomagnetism related to 1D nanostructures. Therefore, in my work, 1D nanotemplates were used to guide the growth of the nanostructures and self-assembly was used to grow high densities of homogenous 1D nanostructures. Transition metal (TM) elements as well as lanthanide, known as magnetic elements, were used to grow the nanostructures. The investigations of the surface template morphology, the size, shape and atomic configuration of the nanostructures were accomplished by means of STM and the magnetic properties of Co nanolines were investigated by XMCD.

This thesis is composed of five chapters. After a general **introduction to** my PhD work**,** the general concepts of growth along with methods to create 1D nanostructures and the magnetic response of different nanomaterials are presented in the **chapter 1**. Measurement techniques used for this work are presented in **chapter 2**. Experiments made to understand the growth mechanisms of the nanotemplates are presented and discussed in **chapter 3**. The investigation of the growth of nanolines on the templates is presented in **chapter 4**, along with the magnetic characterization of the Co nanostructures in **chapter 5**. Finally, a general **conclusion** is presented, followed by **perspectives**.

In **chapter 1**, I present in a first part **(part A)** the growth techniques adopted for the growth of structures at the nanoscale. The first technique developed was the top-down approach. The advantages presented by this technique in fundamental research and industrial activities lead to a big development of this approach. When the growth of nanostructures made of few atoms started to arouse considerable interest, the top-down approach was not efficient, limited in scale. The bottom-up approach, with for instance self-assembly on surfaces, started to take place and the interest in this method is continuously rising since then. In addition, in this part, growth modes based on a description using thermodynamic quantities such as surface energy terms are discussed. The difference between the description of the growth using thermodynamic or kinetic expressions is explained. The nucleation and growth processes in the kinetic growth regime are presented in this part. Then, multiple ways to guide the growth, shape and size of structures, are presented. For instance, anisotropic surfaces were used for the growth of 1D structures and the example of Cu islands on Pd(110) is presented. Vicinal surfaces were also used to grow 1D nanostructures. The example of Co nanolines on Pt(997) is mentioned along with other reported

works. Finally, the use of other templates is introduced: 1D nanostructures were grown on Cu-CuO stripe phases as well as on a Si nanoribbon (NR) template. In this work, the latter template, synthesized firstly at CINaM in 2007, is heavily use. Therefore, a detailed review is presented and the most important evolution steps of this system are wildly explained. In addition, the growth of 1D nanostructures on this template were reported in the literature and the results are presented. In a second part **(part B)**, the magnetic behavior of elements and materials is introduced. Several behaviors are explained such as the dia-, para- and ferro-magnetic behaviors. A more detailed study is presented for the superparamagnetic behavior since it corresponds to the behavior of the nanostructures studied in this work. Moreover, the MAE concept for nanostructures is introduced and explained. Finally, 1D magnetic nanostructures that can present interesting magnetic properties such as ferromagnetic behavior at low temperature and specific orientation magnetization are presented.

In the **chapter 2**, the experimental set-ups employed during my PhD thesis for the growth and characterization of the nanostructures are described. The growth was realized by thermal evaporation of the material and condensation on the surface, which requires to be done in ultra-high vacuum (UHV) chambers. In this chapter, the preparation of the surface in UHV-chambers is presented. The preparation of the surface consists to clean the surface (ionic bombardment followed by soft annealing) and then to grow the nanostructures on it. In addition, in this chapter, STM and XMCD are described in details. The functioning, experimental set-ups and data analysis are presented for both techniques. By STM, images of surfaces at the nanoscale can be achieved which helps to study the surface morphology. Moreover, high-resolution STM images can be obtained which help to elucidate the atomic structures of nano-objects. This technique has helped to make the atomic engineering possible. In addition, the development of other characterization technique such as spectroscopic techniques have helped to study the chemical components by using x-ray adsorption spectroscopy signals and the magnetic properties by analyzing the XMCD spectra.

The growth of the 1D nanotemplates was investigated in **chapter 3**. My PhD work was focused on the use of Si NRs templates to grow the 1D nanostructures. These templates present a 2D array with a 1D pattern of single (0.8 nm in width) or double (1.6 nm in width) Si NRs. We expect that the growth of the nanostructures, presented in the next chapter, will be influenced differently in function of the NRs covering the Ag(110) surface. These Si templates were known since 2007 but not perfectly figured out. While the atomic structure of the Si NRs was largely studied, few studies on the growth mechanisms have been led to understand the interplay between the formation of the Si single and double NRs (SNRs and DNRs) and the missing-row (MR) reconstructed Ag surface which turned to be crucial to tune the geometry of the nanotemplate. In this chapter, we present a nanoscale investigation of the Si growth mechanisms in the submonolayer regime at different temperatures, using STM. Depending on the substrate temperature, from room temperature (RT) to 500 K, different arrangements of the Si NRs are formed. They differ by the progressive replacement of SNRs by DNRs and by the lateral organization of the NRs, perpendicularly to the ribbons. Our study evidences transitions from 1D to 2D growth (i) at 380 K, corresponding to the transition of isolated SNRs to SNRs locally assembled in a 3×2 superstructure and (ii) at 440 K, corresponding to the transition of isolated DNRs to DNRs self-assembled in a long-range 5×2 superstructure. The activation energies for the formation of different Si species are determined from the statistical analysis of NR densities measured in STM images (300 nm^2). Our results strongly suggest that the transition between SNR and DNR superstructures is driven by the MR reconstruction of the Ag(110) surface induced by the Si NR growth. We also explain why a long-range ordered 3×2 superstructure cannot be formed, on the contrary to a 5×2 grating covering the whole surface. The latter highly-perfect

nanotemplate, having long-range ordered Si DNRs with a low density of defects, will be preferentially used for the growth and characterization of nanolines, as described in chapter 4.

In **chapter 4,** I present the growth of TM (Fe, Co, Ni) nanolines and lanthanide (Ho) nanostructures on the Si templates. Our studies based on STM image analysis are focused on both the length and the atomic structure of the nanolines as a function of the metal species. The depositions range from submonolayer to four monolayers (ML) of TM nanolines. For the submonolayer range, our results show that we have similar atomic configuration for the TM nanolines. Emphasizing the template effect, dimers of Fe, Co and Ni arranged in nanolines were obtained indicating the role of Si NRs in guiding the growth of these nanostructures. The average lengthes were found to be 3.5 nm, 4.5 nm and 5.5 nm for Fe, Co and Ni nanolines, respectively, for TM deposition at RT on the 5×2 template. We show that the length of these nanolines is limited by the in-diffusion process of TM atoms into the Si NRs. To partially hinder the thermally activated process of TM atom diffusion into the Si array and thus increase the length of TM nanolines, Co and Ni were deposited at 220 K. For higher coverages, the TM growth reproduces the 1D pattern of the Si template. The submonolayer growth of lanthanide (Ho) is also presented in this part.

In **chapter 5**, I present the magnetic intrinsic properties of an ultrathin film composed of Co nanolines grown at 220 K on the 5×2 Si template. Temperature (ranging from 4 K to 100 K) and angle (from normal to grazing incidence) investigations have been made using XMCD. Orbital and spin magnetic moments are determined, as a function of the angle of the applied magnetic field, through the sum rules provided by this technique. The first two Co layers present a weak magnetic response while upper Co layers exhibit an enhanced magnetization. The magnetic anisotropic energy is also measured from field-dependent magnetization curves. Temperature-dependent investigations evidence a superparamagnetic behavior of thermally fluctuating segments containing each ~ 74 coupled Co atoms, with a very low blocking temperature between 20 K and 40 K. Moreover, angle-dependent study shows two easy axes of magnetization, parallel and perpendicular to the Co nanoline axis.

Finally, after the **conclusion**, I will give some **perspectives** in the framework of my PhD work. In the last decade, a promising alternative route has emerged to manipulate the magnetic properties of supported TM atoms. The approach consists in selectively bonding them to functional ligands in surface-supported metal-organic frameworks (MOFs) to tune the ligand field acting on the atoms, as shown by P. Gambardella *et al.* in 2009. In this context, new aims are being settled and plans are being drawn. In this final section, preliminary results on the adsorption of tetra-bromoanthracenyl porphyrins and dinickel-quinone complexes on Ag (110) surfaces are presented. Remarkably, we show that both molecules, synthesized *ex-situ* by coordination chemistry, wet the Ag(110) surface to form 2D supramolecular networks. These preliminary results encourage to continue in a next future the investigation of metal-ligand networks grown on nanopatterned substrates and the characterization of their magnetic properties.

Chapter 1

Material growth and magnetic behaviors

Contents

Chapter 1 27
Material growth and magnetic behaviors 27
A- Growth 28
Introduction 28
I- Growth modes and nucleation theory 28
i- Growth modes 28
ii- Thermodynamic vs kinetic growth 30
iii- Nucleation and growth processes 31
II- Self-organized growth 37
i- Anisotropic surfaces 37
ii- Vicinal surfaces 39
iii- Nanopatterned surfaces 40
B- Magnetism 52
I- Types of materials 52
II- Introduction to superparamagnetism 54
III- Magnetic anisotropy 55
IV- Magnetism in nanostructures 57

In this thesis work, our aim was to grow 1D nanostructures with magnetic properties. To do that, we used the bottom-up technique of self-assembly on surfaces. Moreover, we have influenced the growth by the use of 1D templates. Therefore, this chapter will be divided into two sections: the first section handles the growth processes while the second one introduces concepts of magnetism.

In the first section (A- Growth) a brief summary of different ways to grow 1D nanostructures is presented. In a first step, a summary of the top-down and bottom-up techniques used to grow nanostructures, a description of the three growth modes and an explanation of the role of nucleation in the growth are presented. In a second step, different ways to grow 1D nanostructures are described.

In the second section (B- Magnetism), the classification of materials (diamagnetism, paramagnetism, ferromagnetism) depending on their behavior in the presence of a magnetic field, the superparamagnetism, the magnetic anisotropy as well as the magnetic nanostructures, with a focus on the 1D nanostructures, are introduced.

A-Growth

Introduction

Thirty years ago, studies on fabrication of structures at the nanoscale have been launched. While the research advances, these nanostructures have gained more interest for several reasons. They have different properties from the bulk materials, high potential for technological applications and miniaturization of devices. Therefore, methods and techniques were developed to produce such structures. One of the first and most used techniques to fabricate these nanostructures is the lithography. The lithography technique can basically be found in two forms: optical lithography (light to x-ray wavelengths) and electron-beam lithography. Each of these methods follows a procedure of several steps (masking, exposure and etching) to elaborate these nanostructures. Lithography is a 'top-down' technique and has the advantage to perfectly control the size, form and the location of the nanostructures. Unfortunately, this technique need high technical means which make it hard to utilize for fundamental research in the laboratories. Moreover, the maximal resolution of the 'top-down' technique is ranged from 20 to 100 nm[1,2], depending on the procedure and the surface used. This resolution is not enough to fabricate nanostructures with limited number of atoms. In order to overcome this limitation, research groups used the tip of the scanning tunneling microscopy (STM) or atomic force microscopy (AFM) to manipulate atoms. For instance, move the atoms one by one, and put them in specific locations[3,4]. However, the fabrication of these artificial drawn nanostructures are time consuming and generally down at low temperature. A more recent way to create nanostructures is based on the bottom-up approach. This technique allows to fabricate in a one-step process a high-density of nanostructures with uniform size, composition and geometry by using the natural self-assembling properties of matter. By manipulating the physical-chemical properties of the substrate and the deposit material together with growth conditions (temperature and flux of incoming species), high densities of ordered nanostructures can be formed spontaneously on templates. This technique, not straightforward, requires to work in UHV chambers and to master the growth of the system. In this chapter, I present some studies to introduce the concepts of the bottom-up fabrication of nanostructures on surfaces.

I- Growth modes and nucleation theory

i- Growth modes

The fabrication of nanostructure using the bottom-up approach usually proceeds through nucleation and growth stages. Those stages involve adsorption, surface diffusion, chemical binding and other atomic processes at surfaces. The first use of surface energies to describe the growth modes was made by Bauer in 1958 [5]. It is accepted that there are three possible modes for crystal growth: island, layer and layer plus island growth modes.

First, the island, or Volmer-Weber mode, consists in the nucleation of small clusters directly on the substrate surface which grow into islands of the condensed phase. This occurs when the atoms of the deposit are more strongly bounded to each other than to the substrate.

Secondly, the layer, or Frank-van der Merwe mode, displays the opposite characteristics. Because the atoms of the deposit are more strongly bounded to the substrate than to each other, the first atoms to condense form a complete monolayer on the surface, which form a less tightly bound intermediate layer. A characteristic for this mode is the monotonic decrease in binding energy, toward the value for a bulk crystal of the deposit.

Thirdly, the layer plus island, or Stranski-Krastanov mode, is an interesting intermediate case. After the formation of the first monolayer, or few monolayers, subsequent layer growth is unfavorable and islands are formed on top of these intermediate layers. Many reasons that make this mode to occur, any factor that disturbs the monotonic decrease of the binding energy, characteristic of the layer growth mode, will result in a high surface free energy of the deposited intermediate-layer which will favors the formation of islands. For example, the lattice parameter of, or molecular orientation in, the intermediate layer may cause the transition from 2D to 3D growth.

These distinctions can be understood qualitatively in terms of relative surface energies.[5] 2D growth is preferred if the sum of the surface free energy of the adsorbate and its interface free energy is larger than the substrate free energy. The 3D growth is preferred if the sum of the surface free energy of the adsorbate and its interface free energy is smaller than the substrate free energy. The Stranski-Krastanov mode is the intermediate case, where this energetic difference changes sign at a critical layer thickness provoking a transition from 2D, layer growth, to 3D, island growth. [6]

To resume:

For γ_s = surface free energy;

γ_a = adsorbate free energy;

$\gamma_{interface}$ = interface free energy between adsorbate and substrate.

- The Volmer–Weber (VW) growth mode (3D morphology, island growth):
  $$\gamma_s < \gamma_a + \gamma_{interface}$$
- The Frank–van der Merwe (FM) growth mode (2D morphology, layer-by-layer, or step-flow growth): $\gamma_s \geq \gamma_a + \gamma_{interface}$
- The Stranski–Krastanov (SK) growth mode (initially 2D, after critical thickness, 3D morphology, layer-plus-island growth)
  initially : $\gamma_s \geq \gamma_a + \gamma_{interface}$ finally : $\gamma_s < \gamma_a + \gamma_{interface}$

  Note: If this last criterion is commonly accepted, Müller *et al.* showed in 1996 that the elastic striction energy induced in the substrate by appearing islands has to be considered. Over a number of layers greater than a critical one, striction opposes to wetting and a 2D to 3D transition occurs.[7]

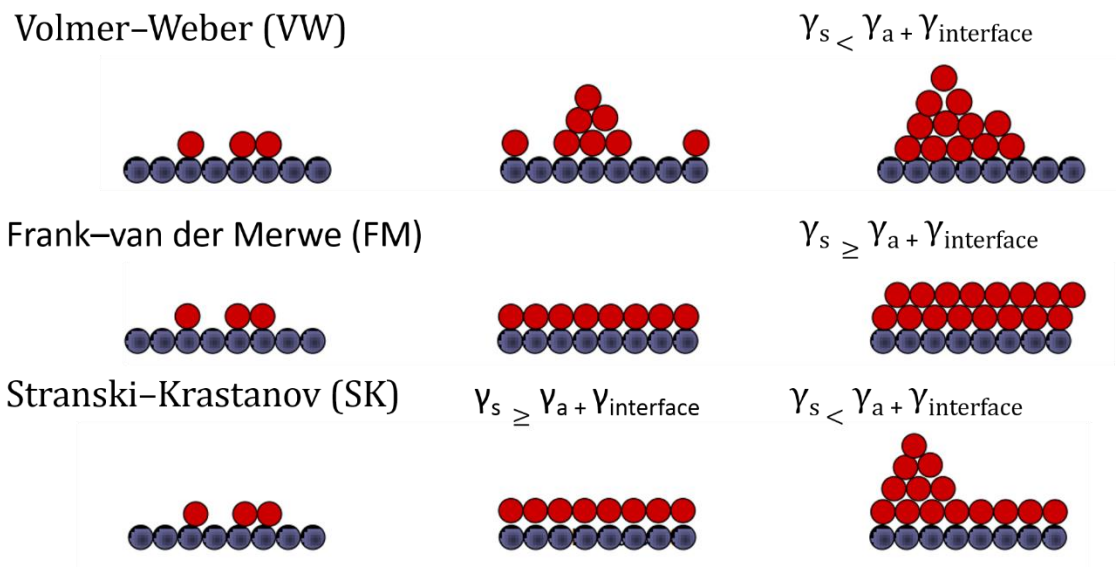

Figure 1: Illustration of the three growth modes

ii- Thermodynamic vs kinetic growth

This concept of growth modes is based on thermodynamic considerations. It is valid only when growth takes place close to equilibrium such that the morphology is given by the total energy, irrespective of the path taken by the film atoms in order to reach the minimum energy morphology. In thermodynamic equilibrium, all processes proceed in opposite directions at equal rates, as required by consideration of 'detailed-balance'. Thus, in equilibrium adsorption, surfaces processes such as condensation and re-evaporation, decay and binding of 2D clusters must be in detailed balance (equal rates). Therefore, no net growth occurs and the system can be described unchanging macroscopic variables as the temperature, coverage and pressure, while microscopically the system is continually changing via these various surface processes. Equilibrium statistical mechanics can be used to describe models of such situations.[8,9]

By contrast, crystal growth is a non-equilibrium kinetic process and the final state of the system depends on the route taken through the various reaction paths indicated in Figure 2. The state which is obtained is not necessarily the most stable, but is kinetically determined. In general, certain parts of the overall process may be kinetically forbidden (e.g. dissolution into the substrate), others may be in 'local' thermodynamic equilibrium, and some will be kinetically rate-limiting. In the second case, equilibrium arguments may be applied locally, e.g. to the adsorption/desorption cycle. In addition, other cases can be treated in the equilibrium thermodynamic form such as: the growth of small clusters that decay rapidly (Walton relation) or the description of the shape of islands formed in terms of surface and interfacial energies (Wulff theorem).

However, in other many cases, the equilibrium is not maintained. In particular, growing crystals are often more facetted than the equilibrium form, due to slower growth of the atomically flat facets than of the atomically rough rounded parts of the equilibrium form. A few processes, at most, will be kinetically rate-limiting, corresponding to the most difficult steps through the reaction paths indicated in Figure 2. For nucleation processes on perfect terraces, the rate-limiting step is usually the formation of small clusters that can grow: due to their small size, they have a

large surface to volume ratio and hence positive free energy. Another parameter is the critical cluster size i, under which the cluster is unstable: clusters of size > i tend to grow rather than decay, and so local equilibrium tends to hold.

In many cases, the growth of epitaxial films is performed far away from equilibrium. The energy barriers encountered by the deposited atoms along their migration path on the surface matter define the kinetics of growth. The ensemble of barriers separates the manifold of all possible film morphologies. They will never be exactly the same but exhibit common features. Kinetics has advantages and drawbacks. It helps to realize thermodynamically unstable morphologies, but the grown films have generally a limited stability upon thermal treatment or exposure to another species. This can hinder their use as a template for instance. Understanding and controlling growth morphologies in the kinetic regime therefore requires detailed knowledge of the processes involved at the atomic scale. Measurements of the activation barriers and prefactors are required to determine the hierarchy of rates and thus to identify the rate limiting steps. Knowledge on these energetic barriers in turn allows one to predict and influence island and film morphologies. The nucleation of islands in the middle of atomically flat terraces is the most central kinetic process. Therefore, atomic processes, nucleation on surfaces, theoretical studies and equations stressing kinetic behavior are discussed in the following section.

iii- Nucleation and growth processes

The atomic processes responsible of nucleation and growth on thin films on a substrate are illustrated in Figure 2. Over the recent past, considerable progress has been achieved in the understanding of how atomic processes contribute to ultrathin film growth, as well as in quantifying their rates. On the experimental side, this is largely due to the extension of scanning tunneling microscopy (STM) [10,11] This technique, discussed in details in the next chapter, provides an unprecedented microscopic view of activated processes taking place on surfaces, such as chemical reactions or atomic diffusion.

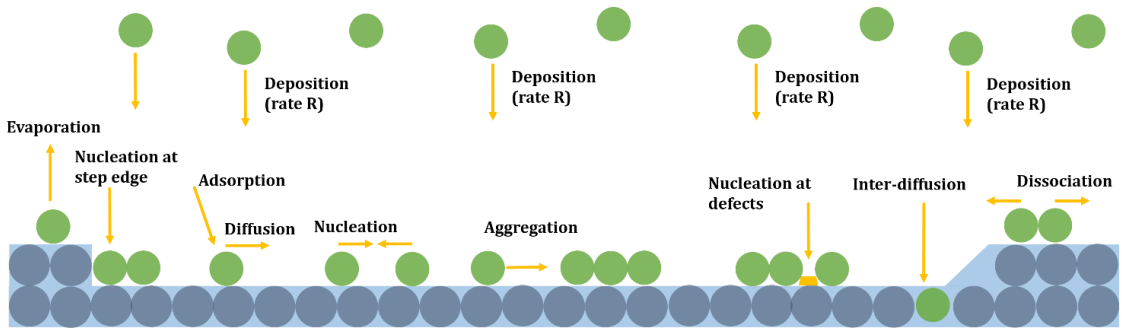

Figure 2: Illustration of the atomic processes during the deposition of material on a surface.

For the growth by physical vapor deposition, atoms are evaporated on the surface with a rate R. Once the atom adsorbs on the surface, several processes are possible. The atom can stick to its place, diffuse along different directions on the surface, inter-diffuse into the surface, adsorbs at specific surface sites such as defects or join another atom to form dimers as shown in Figure 2. The processes that occur on the surface depend on the chemical nature of both adsorbate atoms and surface substrate atoms, the temperature of the substrate T and the rate R of the deposit. In fact, all these atomistic processes can be characterized by an activation energy and a frequency

so-called 'attempt frequency'. For example, atoms arrive on the surface from vapor at rate R, or at an equivalent gas pressure p, such that R= p/(2πmkT)$^{1/2}$, where m is the atom mass, k is Boltzmann's constant and T the absolute temperature of the vapor source. This leads to an areal single atom density of $n_1(t)$= Rt. Or, at the highest temperature, these adatoms will only stay on the surface for a limited time, before re-evaporation, called the adsorption residence time τ_a, during which they migrate over the surface with a diffusion coefficient D. This time is determined by the adsorption energy, E_a, and expressed with a vibrational frequency ν_a, of order 1-10 THz.

$$\tau_a^{-1} = \nu_a \exp(\frac{-E_a}{kT}) \quad (1\text{-}1)$$

where k is Boltzmann's constant and T the substrate temperature.

During the time where the adatom is on the surface, it can diffuse on the surface and its random movement can be estimated by the mean square displacement, $\langle \Delta x^2 \rangle$, for a time t. The diffuson process obeys Einstein relation:

$$\langle \Delta x^2 \rangle = 2da^2Dt \quad (1\text{-}2)$$

where a is the distance between two consecutive sites, estimated from 0.2 to 0.5 nm, d is the dimensionality of the displacement and D is the coefficient of diffusion, given by:

$$D = \frac{n\,\nu_d a^2}{2d} \exp\left(-\frac{E_d}{kT}\right) \quad (1\text{-}3)$$

where n is the number of directions available to take from the occupied site, E_d the diffusion energy and ν_d is a frequency (typically somewhat less than ν_a).

For example, if we ignore the exchange mechanism, we can define for: fcc(001): d=2 and n=4, fcc (111): d=2 and n=3 and for fcc (110): d=1 and n=2.[12,13] This coefficient, D, is important for the diffusion of single atoms in early growth stages and also in the advanced growth stages because it can lead to the density of grown islands.

Once the adatom arrives to the surface, it makes random walk on terrace and two processes can occur: the adatom meets another adatom and form a stable nucleus (nucleation) and so a new island is formed, or the adatom meets an existing island and stick to it and so participate to the growth. Therefore, the evolution of the growth of thin films can be described by four stages: (1) pure nucleation, (2) nucleation and growth of islands, (3) growth of islands and finally (4) coalescence. In addition, this evolution depends on the atom diffusion coefficient and the deposition rate. For example, a high diffusion coefficient means high probability for an adatom to find an existing island before another adatom is deposited in its vicinity to provide chance for nucleation, leading to an overall lower island density. A high deposition rate leads to a high probability for an adatom to nucleate with another adatom and thus to a high island density.

During the evaporation, we consider that, in the first stage, the atoms arrive to the surface with a rate R (ML/s) and diffuse with a coefficient D to meet another single atom and form one dimer. To simplify, we will consider that the dimer is stable and forms a nucleus. As the deposition proceeds, the number of dimers will increase and will reach a concentration n_2 near to the concentration of a single (diffusing) atoms n_1. In this case, the probability of an arriving single atom to form a new dimer is comparable to the probability that this single atom encounters a dimer and assists to the growth of stable clusters, leading to the second stage mentioned earlier, nucleation and growth of islands. Thus, the competition between the growth of stable clusters and the growth of new ones starts to appear. With an enough large concentration of stable islands n_x ($n_x = \sum_{s>1} n_s$, n_s is the density of stable islands with a size s), every atom arriving on the surface

has a higher probability to join a stable island than to meet another adatom. As a consequence, arriving atoms will contribute to the growth of existing islands. At this point, we achieved the saturated density, n_x^{sat}. In this stage (stage (3) mentioned earlier), the mean-free path of the adatoms is equal to the mean distance between two islands and the single atoms have more probability to join and stick to an island than to meet another single atom and form a dimer. For high coverage ~ 0.5 ML, coalescences of islands start to occur which lead to the decrease of the density of islands. This behavior is presented in Figure 3[14] for different ration of D/R; (in the graph F=R representing the rate deposition).

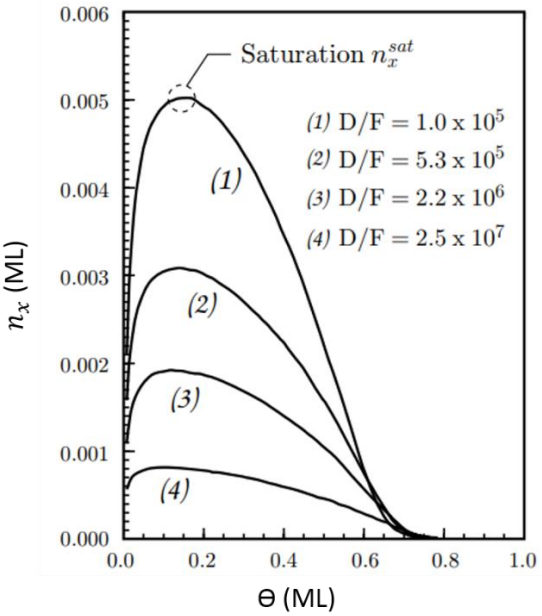

Figure 3: Stable compact island density, n_x, curve as a function of the coverage for different ratio of D/F.[H.Brune et al. ref :14]

The mean-field nucleation theory relates n_x to the ratio of diffusion D to deposition rate R and to the cluster binding energy E_i by the following expression for complete condensation and 2D clusters[9,15–18]

$$n_x = \eta(\theta, i)\left(\frac{D}{R}\right)^{-\chi} \exp\left(\frac{E_i}{(i+2)k\,T}\right); \text{ with } \chi = \frac{i}{i+2} \qquad (1\text{-}4)$$

where $\eta(\theta, i)$ represents the cluster density for a coverage θ and critical cluster size i.

We can see clearly the link between D, R and n_x. Since we took the example of the irreversible growth regime, where the critical cluster is a monomer, the stable cluster is a dimer, so i = 1. The critical size is defined as the cluster becomes stable after adding one atom to it. Then the cluster binding energy is E_i =0 and the equation (4) becomes:

$$n_x = \eta(\theta, 1)\left(\frac{D}{R}\right)^{-\frac{1}{3}} \qquad (1\text{-}5)$$

An experimental work combined with a theoretical study (Monte-Carlo simulations) has been made on the growth of islands of Ag on Pt(111). The application of this equation to $n_x(T)$ data inferred from STM has proved to yield accurate values for the barrier and attempt frequency of terrace diffusion. We show in Figure 4 the Arrhenius plot of n_x: $\ln(n_x^{sat})$ is shown as a function of $1/T^{dep}$. The results show a linear regime in the range $10^5 \leq D/R \leq 10^9$, (F=R) in agreement with Equation (1-5).

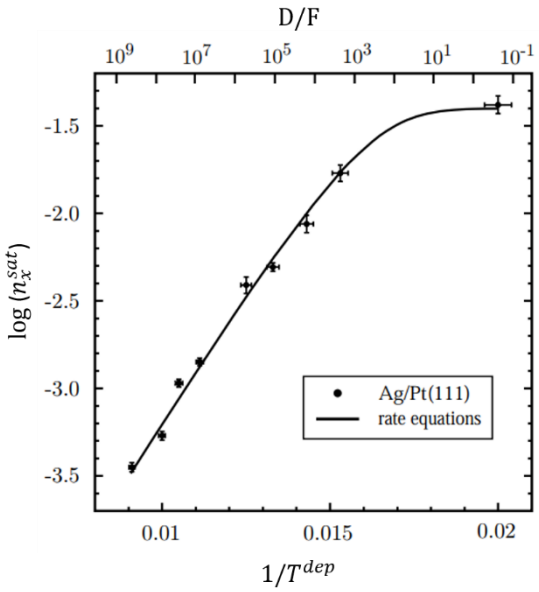

Figure 4: Arrhenius plot: island density at saturation, as a function of the deposition temperature (F=10^{-3} ML/s), for stable dimers regime (i=1). [H.Brune et al. ref: 14]

It is important to mention that the critical cluster size i define the shape of the curves of the cluster size distribution obtained by nucleation on homogeneous substrates. The scaling law is obtained when the size distributions are plotted as $n_S \times \frac{\langle S \rangle^2}{\theta}$ versus S/⟨S⟩, where S and $\langle S \rangle$ are the size and its mean value, respectively, and n_N is the density of N-sized clusters. All the curves fall onto a Gaussian shape curves with a half width at half maximum(HWHM) of $\sigma \sim 0.55$ in the case of i = 1.[19] Annealing treatment discussed hereafter contributes in narrowing down the size distribution.

These equations were also confirmed by other experimental works such as the diffusion of Pt adatoms on Pt(111)[20], Al/Al(111) and Al/Au(111)-($\sqrt{3} \times 22$)[20,21].

Interestingly, epitaxial growth can be followed by coarsening. The term epitaxy refers to the growth of a crystalline layer (epi) on the surface of a crystalline substrate, where the crystallographic orientation of the substrate surface imposes a crystalline order (taxis) onto the thin film. This implies that film elements can be grown, up to a certain thickness, in crystal structures differing from their bulk. Coarsening mechanisms occurs mainly from annealing treatment following the deposition of atoms. Two coarsening processes are described in the following paragraphs.

The first mechanism describing this phenomenon is as follows: if the substrate is heated after island growth, the evaporation of atoms from the islands surface might be thermally activated. These evaporated atoms diffuse into the surrounding medium and condense either back to the same or to another cluster. This phenomena is known as Ostwald ripening[21] , where an ensemble of different-sized 3D clusters embedded into a host. This process is driven by the minimization of the overall cluster interface with the surrounding phase that has the surface or interface free energy (γ). As small clusters have a significantly higher fraction of surface atoms, statistical fluctuations of their size will have larger amplitude and the probability that they dissolve is higher than that for larger clusters. This effect can be described thermodynamically by the Gibbs-Thomson equations. While the Ostwald ripening is linked to the local curvature(κ) of

the interface (island-surface), the Gibbs-Thomson equation relates this curvature to a change in the atoms' chemical potential($\Delta\mu = \gamma\kappa$) and indicates that the vapor pressure (here the diffused atoms) in equilibrium with their condensed phase (islands) decreases with the radius of the curvature of the interface (radius of the curvature of the islands). Thus, the periphery atoms of small clusters tend to dissolve faster than the one of larger clusters. Several experimental examples has been reported such as Ag/Ag(111)[22], Cu/Cu(100)[23]. In Figure 5, we show the example of Ostwald ripening for Cu islands on Cu(100). The substrate was maintained at 343K, after a 5h33 min of annealing, the small islands disappeared and the growth of large islands were observed[23]. As consequence, we show in Figure 6 the size distribution of islands of Ag/Pt(111) after annealing: a narrower distribution is obtained, compared to the distribution of pure nucleation (without heating)[24], the size distribution is reduced from $\sigma \sim 0.55$ in the case of nucleation with critical cluster size i = 1 to $\sigma = 0.3$ after annealing.

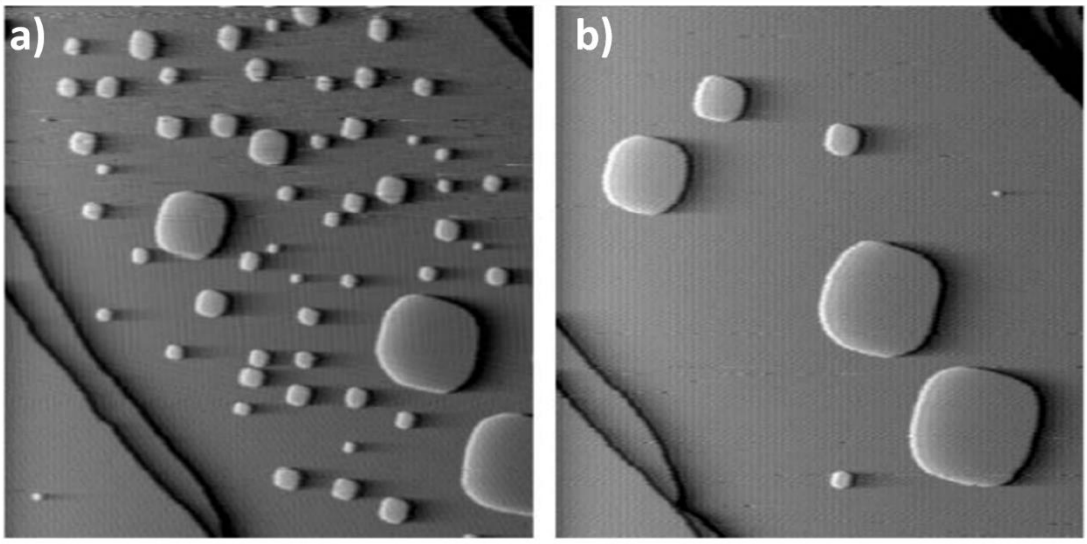

Figure 5: (a) and (b) Two STM images (300x300) nm^2. An annealing of 5h33 min has passed between (a) and (b) images, with the substrate held at 343 K. STM images show ripening of an assembly of about 60 Cu adatom islands on Cu(100). [J. B.Hannon et al. Ref: 23]

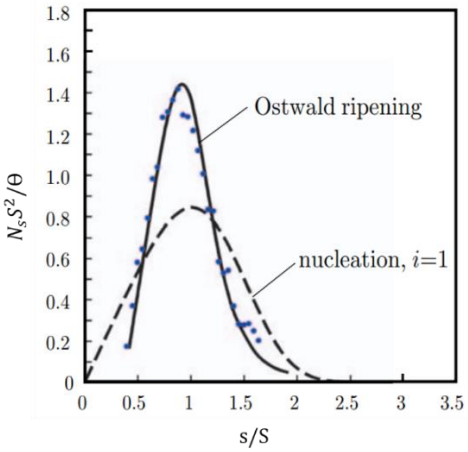

Figure 6: Experimental normalized distribution of islands' size before and after the annealing (blue dots). Ostwold ripening (solid line) and nucleation (dashes line, theoretical i=1 scaling curve). [H. Roder et al. ref: 24, Amar et al. ref: 19]

The second mechanism, known as Smoluchowski ripening, is the diffusion of entire islands and their coalescence. This mechanism can dominate the Ostwald ripening, especially for systems with high cohesive energy, or for very low surface adhesion and therefore also low diffusion barriers, such as in the case of metal islands on graphene or h-BN. For this mechanism, every cluster size has its characteristic onset temperature of diffusion, giving rise to a stepwise increase in the mean island size distribution as a function of annealing temperature. For experimental studies, we refer to Co/Pt(111) and Fe and Pt on Pt(111)[8]. The respective onset temperatures are system specific, they give access to the cluster diffusion energy of each size. An example where this ripening process has been observed on a Pt(111) surface is shown in Figure 7. All monomers start to diffuse simultaneously at their onset temperature and form dimers and trimers. The trimers result when a monomer is close to two monomers that have already met. Once the dimers start to diffuse, they might meet another dimer or join an immobile trimer giving rise to a mixture of tetramers, pentamers, and remaining trimers. At the next higher temperature, these trimers start to move and join the other islands (larger clusters are immobile at this temperature).

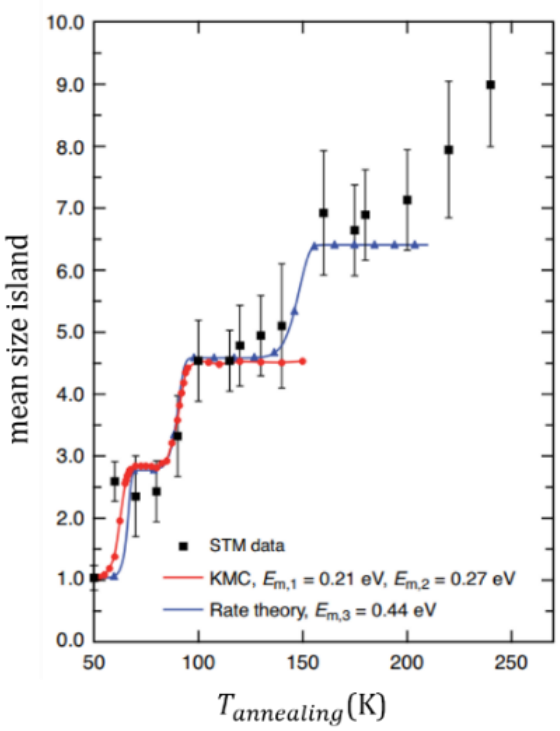

Figure 7: Mean island size in atoms as a function of annealing temperature derived from STM for Co/Pt(111) (Θ = 0.01ML, t_{ann} = 1h). Red curve shows kinetic Monte Carlo simulations with monomer and dimer diffusion; blue curve represents integration of mean-field rate equations considering in addition trimer diffusion. [H. Brune ref: 8]

II- Self-organized growth

As mentioned earlier, the kinetically control growth allows to produce metastable nanostructures with a morphology tailored by the growth parameters such as the deposition temperature and the deposition rate. Nevertheless, generally speaking, this approach provides a large size distribution and unlocalization of the grown nanostructures. As previously mentioned, post-deposition annealing treatments were made in order to narrow the size distribution but results are not sufficiently satisfying. Whereas, our goal in my thesis was to grow high densities of 1D homogeneous nanostructures periodically arranged on the surface. Therefore, self-organized growth was employed. Basically, this process consists in the growth of nanostructures on a nanopatterned surface. The self-organized growth provides a low dispersion of size and shape and a spatial localization of the nanostructures. These features affect the physical properties of the nanostructures. Thus, we can measure the signal of nanostructure assemblies at the macroscale and consider it as the amplified measurement of a single nanostructure signal. Moreover, it can be outlined that in the perspective of applications, the control of the localization of nanostructures on the surface is required.

Numerous examples of nanopatterned surfaces were proposed in the literature: using an inhomogeneous stress field, specific morphology at the surface or functionalizing the surface of the substrate. Any localized structural features such as atomic steps[25], incorporated or contaminant particles[26,27], dislocations and surface reconstructions[28], can induce the self-organized growth of nanostructures. In the early stage of its development, several ordering effects induced by stress have been demonstrated. For example, the spontaneous ordering of metallic islands by a strain-relief pattern[29] and the localized growth on thin films with an underlying network of dislocations[30]. Regarding the growth of 1D nanostructures, specific nanopatterned surfaces were proposed. Among these surfaces, some are "naturally" patterned such as anisotropic and vicinal surfaces. Others correspond to fabricated nanopatterned surfaces which induce a 1D periodicity on the surface by growing, for instance, an ultrathin film which plays the role of a template. It is important to mention that the morphology of the nanopatterned surface contribute to define the shape and size of the grown nanostructures.

Numerous studies showed that specific electronic, optical and magnetic properties are strongly dependent on the dimensionality, size and shape of the nanostructures. Therefore, the choice of the nanopatterned surface is crucial in order to define these criteria. In the following, I describe anisotropic and vicinal surfaces along with a description of 1D templates used to grow 1D nanostructures.

i- Anisotropic surfaces

The anisotropic substrates have orientation dependent diffusion barriers. An example of anisotropic surfaces is the fcc (110) surface. Any unreconstructed fcc (110) surface consists of closed-packed atomic rows along the $[1\,\bar{1}\,0]$ direction separated by deep channels in which preferential diffusion of incoming adatoms takes place. At low temperature, adatoms diffusion occurs along the $[1\bar{1}0]$ channels leading to the growth of 1D islands. This growth is limited by the substrate temperature. Above a critical temperature, the cross-channel activation energy is achieved and 2D islands start to grow kinetically.

The first growth of 1D islands was reported by Röder *et al.* for the nucleation of Cu on Pd(110).[24] It was followed by a combined experimental and theoretical study which demonstrated that the transition from 1D to 2D island growth is associated to the thermally activated barrier energy of diffusion in the transverse [001] direction.[31] In this case, when Cu is deposited below 300 K, the adatoms diffuse along the easy $[1\bar{1}0]$ direction forming 1D Cu chains with a migration barrier along the $[1\bar{1}0]$ direction of $E_{[1\bar{1}0]} = (0.51 \pm 0.05)$ eV. At higher temperatures, above 300K, transverse diffusion of adatoms is activated and 2D islands start to grow. The migration barrier across the $[1\bar{1}0]$ direction is found to be $E_{[001]} = (0.75 \pm 0.07)$ eV. The results are presented in Figure 8.

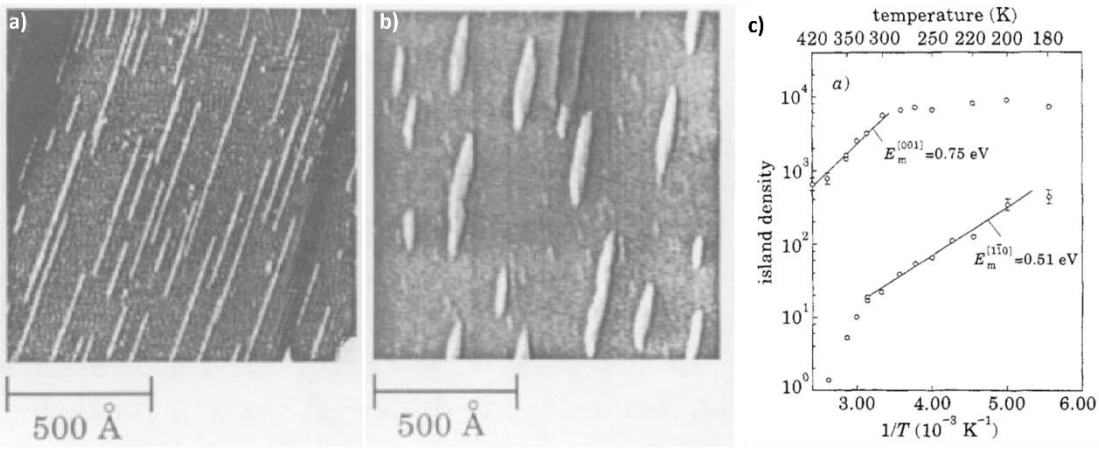

Figure 8: (a) and (b) STM images of the Cu islands on Pd(110) taken at 300 K and 350 K respectively.(c) Arrhenius plot of island density as a function of 1/T revealing energy barriers along and across the $[1\bar{1}0]$ *direction . [J.P; Bucher et al. ref: 31]*

Many diffusion mechanisms have been proposed for cross-channeling diffusion. For instance embedded atom method (EAM) calculations proposed an exchange mechanism[31]: Cu-Pd exchange was proposed, leaving a mobile Pd atom on the surface while the adsorbed Cu atom is incorporated in the substrate. The transverse diffusion of Cu atoms, along the [001] direction, is achieved via a further Pd-Cu exchange, and thus the chemical order is recovered.

More recently, on the same substrate, Pd(110), 1D Co nanowires were grown along the $[1\bar{1}0]$ direction, taking privilege of the anisotropic properties of this substrate.[32]

Other experiments where done in order to grow 1D structures, although one would expect the alloying to occur in heteroepitaxy due to the exchange mechanism as seen for Au/Ni(110), Ni/Au(110) and Au/Ag(110).[33–35]

More recent examples have been reported: NaCl nanostripe pattern on Cu(110) evidences anisotropic surface effects[36], uniaxial transitions of Xe on Cu(110) emphasizes also the anisotropic diffusion of the adatoms on such substrates[37], deposition of Si on Au(110) leads to the growth of 1D nanowires at RT[38], similarly to the deposition of Si on Ag(110) leading at RT to the growth of quantum NRs as reported by Leandri *et al.*[39] and at 490 K to the growth of Si NR arrays as described by Sahaf *et al.*[40] We will discuss in more details the system Si/Ag(110) later in this section.

ii- Vicinal surfaces

Among self-organization techniques, step decoration on periodically stepped substrates can be used to grow arrays of 1D nanostructures. Experimental work on nucleation at step edges was originally used as a method to obtain electron microscopy images of monatomic steps on rocksalt surfaces. The studies by Bassett and Bethge[41,42], showed that step edges act as preferential nucleation sites for metal adatoms due to the reduced coordination with respect to the terrace sites. However, only with the rapid development of thin film deposition techniques in the last three decades, the role of steps in homo- and heteroepitaxial growth has been extensively characterized.

Initially, molecular-beam epitaxy on vicinal surfaces has been investigated to improve layer-by-layer growth on AlAs-GaAs interfaces but it was soon recognized that ordered stepped substrates can be employed as nanoscale templates for the growth of superlattices of quantum wires. The advantage of this parallel process is to organize regular nanostructures over macroscopic areas with a high spatial density. Normally, growth is performed on a surface that is cut parallel to one of the primary crystallographic planes, but, in order to obtain the vicinal surface, if the orientation of the cut is instead slightly away from such a plane, the surface will intersect the primary atomic planes at regular intervals, resulting in a periodically stepped surface. The period, or terrace width, of the steps depends on the angle the surface is misoriented away from the primary plane.

Several experimental studies on these types of surfaces have been made, I mention here two examples. Firstly, the growth of Ag, Cu and Co metal chains on Pt(997)[43] this surface is obtained by cutting it with 6.5° off normal with respect to the (111) crystal plane which results in a surface with a periodic lattice of monatomic steps with a periodicity of 20.1 Å. Results of this growth are presented in Figure 9.

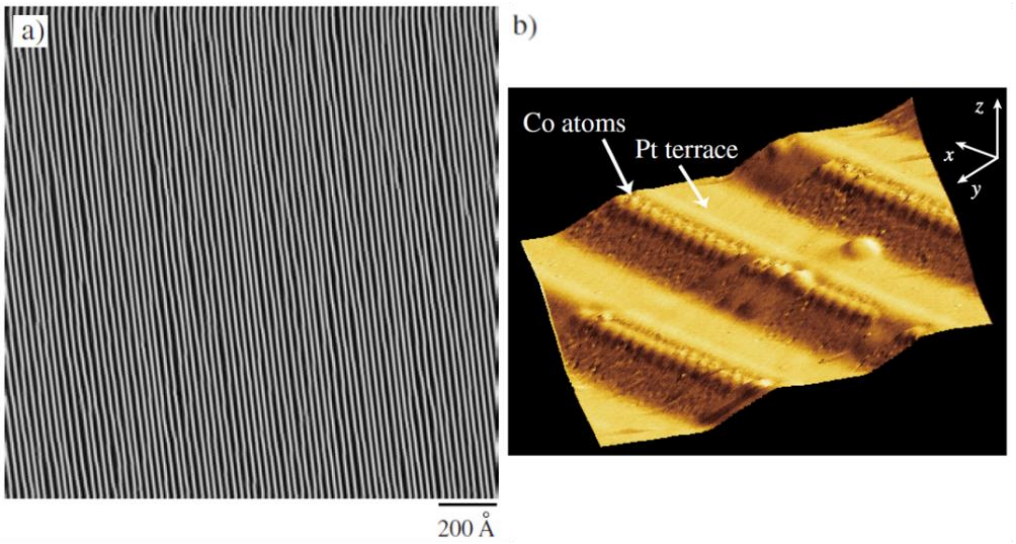

Figure 9: a) STM $\frac{dz}{dx}$ image of the clean vicinal Pt(997) surface. The average terrace width is 20.1±2.9 Å, step down direction is from right to left. (b) Co monatomic chains decorating the Pt step edges. The monatomic chains are obtained by evaporating 0.13 ML of Co onto the substrate held at T= 260 K. The chains are linearly aligned with a periodicity equal to the step width. [P. Gambardella et al. ref: 43]

A second well-known example is the 2D self-organized growth of Co nanostructures on Au(788). This surface is misoriented by 3.5° with respect to the (111) orientation towards the $[\bar{2}11]$ azimuthal direction. In this latter example, it has been used a strain-relief vicinal patterned substrate to achieve 2D long-range ordered growth of uniform Co dots.[28,44–47] This patterned surface consists of a strain relief patterns (herringbone reconstruction) crossing the steps of the vicinal surface which result in a macroscopically phase-coherent lattices. The 2D patterned substrate presents a periodicity in two directions: (i) the step periodicity (3.9 nm associated to the terrace width along the $[\bar{2}11]$ direction) and (ii) the surface herringbone reconstruction periodicity (7.2 nm along the $[00\bar{1}]$ direction). We mention also the possibility to grow molecules on this type of substrate.[48,49] Results on the growth of Co on the Au(788) are shown in Figure 10.

The remarkable magnetic properties of these self-organized chains and dots made of Co will be described at the end of this chapter.

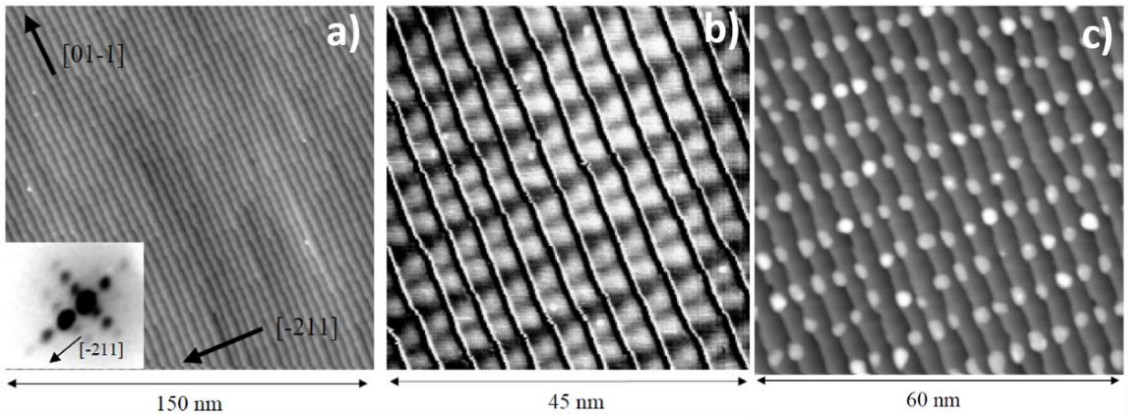

Figure 10: (a) STM image displaying regular and straight step array of a single-crystal Au(788) sample. The inset displays a LEED pattern of the specular spot taken at E= 23 eV. (b) STM image showing a close view of Au(788) where the corrugation due to the terrace levels has been subtracted in order to enhance the reconstruction lines (c) STM image of 0.2 ML coverage of Co deposited on Au(788) at 130 K. [V. Repain et al ref:.44-47]

iii- Nanopatterned surfaces

I present a third way to grow self-organized 1D nanostructures, which corresponds to the growth on functionalized surfaces. An intermediate ultrathin layer is grown on the substrate prior to the deposition of the species (adatoms, molecules) of interest. The role of this intermediate layer is to guide the growth of species and to create specific adsorption phases and thus to form long-range ordered networks of nanostructures by replicating the nanopattern of the template. In this section, I present a widely used template - the CuO-Cu stripe phase – and the Si NR array grown on Ag(110) corresponding to the template used during my thesis work.

a- Cu-CuO template

A famous and well-understood self-organized system is the periodic organization of CuO stripes on Cu(110).[50,51] The 'stripe-phase' consists of elongated Cu(110)-(2x1)O stripes separated by clean Cu(110) areas. The Cu-O stripes are formed during oxygen adsorption through the nucleation and aggregation of Cu-O added rows. Studies showed that the surface stress difference between oxygen covered and bare Cu(110) regions is the origin of the self-ordering of the stripe pattern.[52,53] The stability of the stripe pattern and the variation of its periodicity D and the Cu–O stripe width l can be understood on the basis of continuum elasticity theory.[51,54] The width l and periodicity D are calculated by these equations:

$$l = \frac{l_0\, 2\pi\theta_0}{\sin(2\pi\theta_0)}, \qquad D = \frac{\pi l_0}{\sin(2\pi\theta_0)} \tag{1-6}$$

The resulting analytic expressions fits perfectly the experimental data for l_0= 2.2 nm. The above equations imply that the width l of the Cu-O stripes can be tuned by simply varying the oxygen coverage θ_0 between 0 and 0.5 ML (the (2×1) saturation value) to increase the width from 2 nm up to 10 nm. Figure 11 presents the CuO-Cu stripe phase.[55]

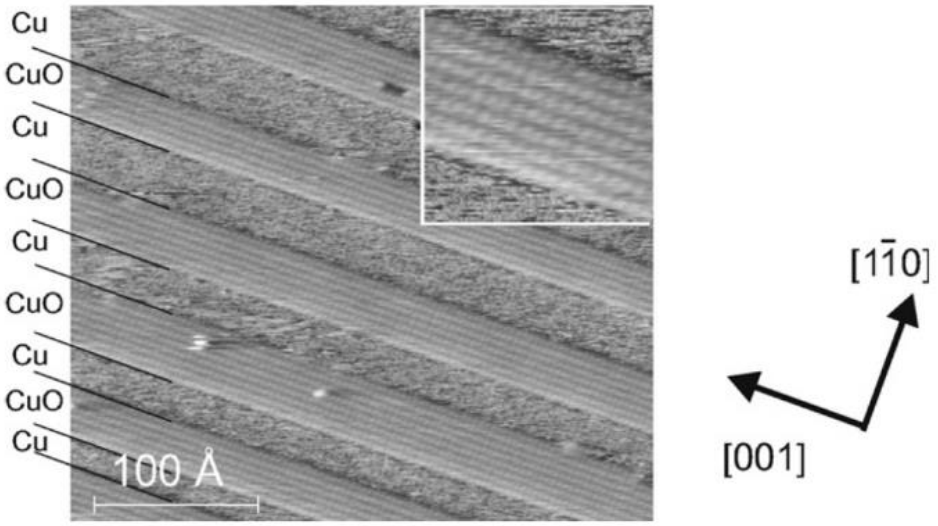

Figure 11: STM image of the Cu–CuO stripe phase with oxygen coverage θ_0=0.25 ML. The image was recorded at room temperature using a tip bias voltage V= -1 V and tunneling current I = 5 nA. [L.D. Sun et al. ref : 55]

The prefect control of the growth of this system gives it a great advantage of being a variable size template that can be used for the growth of different size deposited nanostructures.

Studies showed that this patterned substrate is an almost ideal template to study the adsorption properties of atoms and molecules.[56] Therefore, adsorption of N_2 , Xe and CF_4 were studied on this substrate.[56,57] Other properties, such as the electronic surface state properties, were investigated by means of reflectance difference spectroscopy.

This nanopatterned surface presents several advantages, such as variable sizes of the 1D phase stripes, preferential adsorption properties and the presence of oxygen as surfactant to improve the quality of the grown thin film. For instance, Co nanostructures were studied for growth coverage from sub-monolayer to 7 ML.[58] Ni nanostructures were also grown on this substrate and a study on their spin orientation transitions was reported by Denk *et al.* [59]. Recently, the growth of long 1D molecular nanostructures - the Violet Lander molecules - on this template was studied by Otero *et al.*[60] Moreover, on-surface synthesis of molecular chains was investigated: the authors showed that different conformations of organometallic chains and macrocycles can be achieved by modulating the width of alternating bare Cu and Cu-O stripes.[61] Growth of organometallic structures on the Cu-CuO stripe-phase is shown in Figure 12.

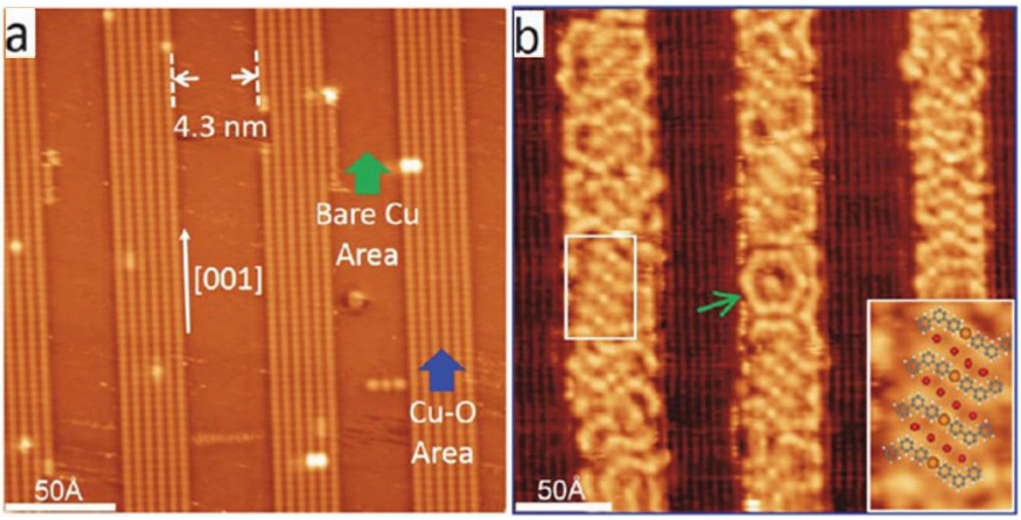

Figure 12: (a) High-resolution STM image of the Cu(110)-(2×1)O stripe-phase created by exposure of the Cu(110) surface to O_2 (Θ_o= 0.24 ML). (b) Periodically separated molecular sheets formed on CuO stripes after deposition of 0.55 ML of 4,4''-dibromo-meta-terphenyl (DMTP) onto the surface shown in (a) held at 300 K. The inset shows the zoom-in of the white-framed region overlaid with the molecular model; [Q. Fan et al. ref: 61]

b- Si/Ag (110) template

Another template is presented here, the Si NR template. This template consists of massively parallel Si NRs grown on the reconstructed surface Ag(110). At RT, parallel, randomly distributed, single Si NRs (width of 0.8 nm) are grown. At 490 K, double Si NRs (width of 1.6 nm) self-assemble to form a 1D array with a pitch of ~ 2 nm. It has been reported that the self-assembled DNR array can be efficiently used as a template to guide the growth of nano-objects. In our work, we used this template to grow 1D nanomagnets. Therefore, I present in this section a state of the art of the Si/Ag(110) system, focused on structural and electronic investigations made on this system.

b1- Si nanoribbons: structure and electronic properties

At first, this system was discovered in 2005 upon deposition of ~0.25 ML of Si on Ag(110). Perfectly aligned along the [1$\bar{1}$0] direction, Si NRs were obtained with a length reaching up to about 30 nm at RT. The NRs elongated up to 100 nm when annealed at 500 K. The width of these structures was found to be 1.6 nm and rarely 0.8 nm. The so-called 'Si quantum nanowires' were imaged by STM after the Si deposition. Further information on the structure of these isolated Si NRs was obtained by LEED. The spots of the LEED patterns confirmed the parallel assembly with a double periodicity in the [1$\bar{1}$0] direction but a lack of periodicity in the perpendicular direction, reflecting the variable separations of NRs. Photoemission (PES) experiments was carried out, at the core level of Si 2p and at the valence bands. The Si 2p spectrum proves the perfect atomic order within the nanowires and the existence of just two non-equivalent silicon environments. In addition, a careful fit of both Si 2p components in the experimental data requires parameters which are typically associated to a metallic character for both types of Si components. This metallic character has also been suggested by STS measurements on individual NRs. The PES valance band measurements revealed four new, discrete, electronic states compared to the sp valance band of the bare Ag(110) surface. These remarkable new electronic states were associated to the Si NRs.[39]

The first atomic structural model of the individual NRs devised from first-principles calculations has been proposed by He in 2006.[62] This model comprises a layer of Si atoms located in hollow sites of the Ag(110) surface and a top layer of Si dimers above.

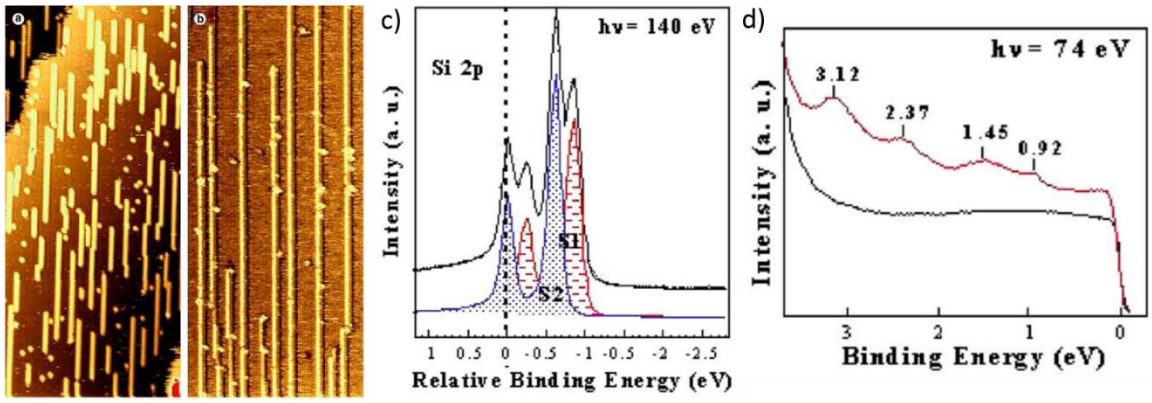

Figure 13: STM images and photoemission spectra on a Ag(110) covered with 0.25 ML of Si. Si NRs before (a), and after (b), annealing at 500 K. Longer NRs were formed by annealing accompanied with the disappearance of the nanodots observed in (a). (c) Si 2p core level spectrum (higher curve) and two asymmetric components (bottom curves) indicating the two non-equivalent Si environments. (d) Valence band spectra for the bare Ag(110) surface (bottom curve) and for the same surface as in (a) and (c) (upper curve) [C. Leandri et al. 2005 ref: 39]

In 2007, deposition of Si on the Ag substrate heated at 470 K, for a higher Si coverage than before, leads to the growth of long Si NRs self-assembled laterally. These self-assembled NRs form an array, with a periodicity of 5 $a_{Ag\perp}$ (~ 2 nm) where $a_{Ag\perp}$ is the lattice parameter of Ag(110) in the [001] direction. This was confirmed by LEED pattern at completion of this arrangement: this 1D superlattice displays a sharp 5×2 pattern, associated to a 5 $a_{Ag\perp}$ peridocity in the [001] direction and a $2a_{Ag//}$ periodicity along the [1$\bar{1}$0] direction, where $a_{Ag//}$ is the lattice parameter of Ag(110) along [1$\bar{1}$0]. The first STM image of the Si grating is shown in Figure 14.[40]

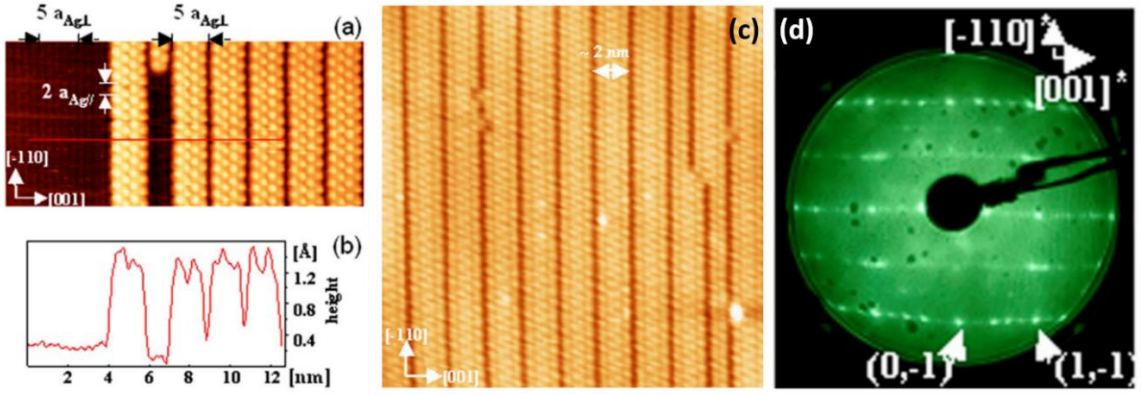

Figure 14: (a) STM image (17.4 x 8 nm^2) below full Si monolayer coverage of the Ag(110) surface. (b) Height profile along the transverse line in (a). (c) STM image (24 nm)^2 of the surface at completion of the Si layer(d) 5×2 LEED pattern [H. Sahaf et al. 2007 ref: 40]

In 2010, low temperature STM/STS study of silicon NRs grown on Ag(110) surface confirmed the results on the structure previously described by Sahaf *et al.* and are in agreement with the presence of a quantum confinement of electrons in the direction perpendicular to the NRs. High-resolution STM images of Si nanodots, isolated NRs and self-assembled NRs are shown in Figure 15. The Si nanodots, shown in Figure 15(a), were considered as seeds for the growth of the Si NRs. Moreover, STS measurements shows no variation on the structure and electronic properties upon cooling down from room to liquid helium temperature.[63]

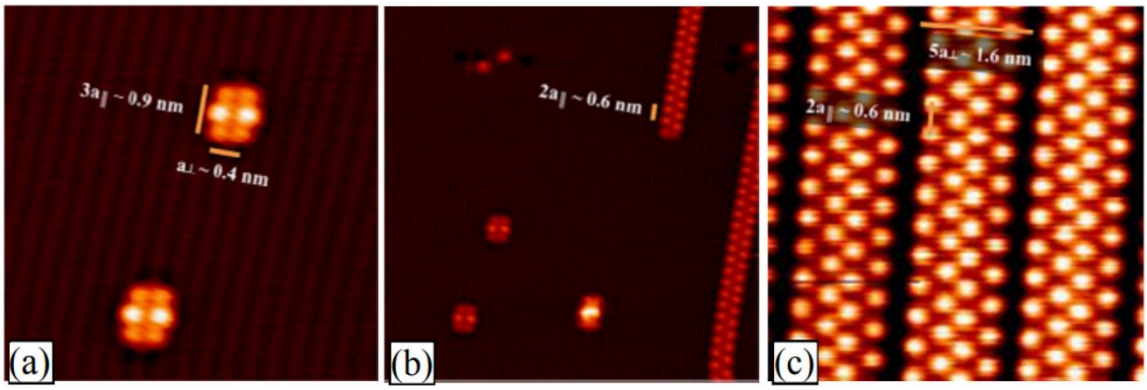

Figure 15: Constant current STM images of Si/Ag(110): (a) 6.5×6.5 nm^2 STM image, V = ±1.0 V, I = 2 nA. (b) 15×15 nm2 STM image, V = ±1.0 V, I = 2 nA; (c) 6.5×6.5 nm2 STM image, V = ±0.05 V, I = 200 nA. [F. Roncci et al. 2010 ref: 63]

After these important findings, high-resolution STM did not provide a satisfactory comparison with the atomic structure proposed by He. Therefore, theoretical studies based on DFT calculations were carried out with a different approach.[64] The study proposed a Si arch-shaped hexagonal configuration that was consistent with the experimental observations reported by Leandri *et al.* in 2005. For instance, the calculated new electronic states near the Fermi level were in good agreement with the ones observed experimentally. The hexagonal atomic structure was also in good agreement with the spectroscopic signature of the Si NR oxidation process, which is very close to the one observed on the Si(111) surface.[64,65] Nevertheless, as the proposed atomic structure was not confirmed by diffraction experiments, further investigations were done.

Further combined theoretical (DFT) and experimental (STM, ARPES) studies were published in 2010 in agreement with the latest result mentioned previously. DFT within generalized gradient approximation (DFT-GGA) calculations provided an optimized Si30 structure comprising a honeycomb silicon architecture. The Si30 structure consists in the arrangement of 30 silicon atoms arranged in a 4×6 unit cell on the Ag(110) surface which relaxes into an arch-shaped graphene-like configuration, possibly pointing to silicene synthesis.[66] This study was followed by ARPES measurements carried out on laterally compact Si NRs arranged in a 1D grating.[67] The electronic states deriving from this grating display a quasi-1D character, as reported previously. Bands crossing the Fermi level, at the zone boundary, similar to the Dirac cones observed in graphene, were identified, as shown in Figure 16. The dispersion of the bands allows to identify states corresponding to the 1D projection of π and π^* Dirac cones. Their location in the reciprocal space are in agreement with the structural parameters derived from STM images and the DFT-GGA theoretical analysis presented just above. Moreover, the angular dependence of the Si K absorption edge was reported by means of reflection electron energy loss spectroscopy (REELS) measurements. The angular dependence of the Si K-edge suggests an sp^2-like hybridization of the silicon valence orbitals similar to that of the carbon atomic bonds of graphene. Hence, based on these results, the first synthesis of silicene, the counterpart of graphene for silicon, was claimed. Since then, several publications about the silicene character of Si NRs and multilayer Si NRs have been published.[68,69]

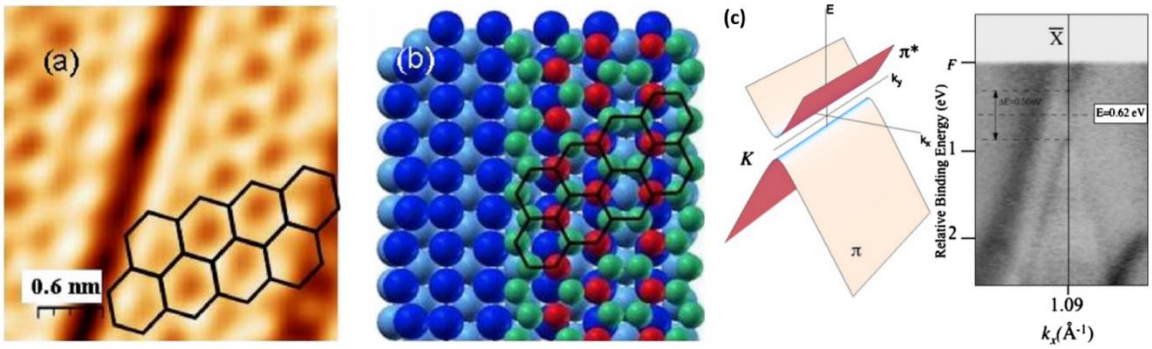

Figure 16: (a) STM image revealing honeycomb arrangements with superimposed honeycomb drawings (b) ball model of the corresponding calculated atomic structure (large dark balls (blue)) representing Ag atoms in the first layer; top most Si atoms are represented by small dark balls (red) while others represented by light small balls (green), the whole forming hexagons (highlighted on the silicon NR). (c) ARPES data are displayed for the Si NRs grating. [(a),(b) ref: 66; (c) ref: 67]

At this point, the growth of Si NRs became a subject of interest for many research groups. After the claim that such Si NRs have properties similar to those of graphene, a debate was launched to investigate the internal structure of these Si NRs. Despite the strong scientific interest and the considerable theoretical and experimental activity, the atomic structure of silicon NRs remained unsolved for ten years. Several theoretical calculations were done, by He.[62], Kara and al.[64], with conflicting results providing simulated STM images with unsatisfactory agreement with experimental ones. Moreover, these proposed geometries were not tested experimentally by surface x-ray diffraction methods. Another discrepancy concerns the periodicity of the Si NRs at full coverage, where both STM images and LEED patterns confirm the formation of a superlattice with a 5×2 periodicity[40] while a ×4 modulation of the Si NRs along the [$1\bar{1}0$] direction was also reported on the basis of LEED and STM measurements[66], with conflicting explanations. Previous work attributed such ×4 periodicity to the presence of 'multilayer silicene NRs'.[69] Finally, the

control of the Si NR width was not clear: in the literature it was mentioned the growth at RT of Si NRs with a width of 1.6 nm and rarely 0.8 nm. This width was shown to be a crucial issue affecting the electronic properties of confined states[63].

In 2013, Colonna *et al.*[70] have made a systematic investigation of the growth of Si NRs on the Ag(110) surface by means of STM and LEED. In this study, the authors answered to several intriguing questions concerning the LEED patterns previously reported in the literature and clarified the conditions of the growth of these Si NRs. The study consists in depositing silicon under different growth conditions. Si was deposited at different coverages, below and above completion of the Si monolayer as a function of the deposition temperature (from RT to 550 K). This investigation demonstrated that the deposition temperature is a key parameter to control the width of the produced Si NRs. The Si NRs observed at the surface present the two most common widths of 0.8 and 1.6 nm. The 0.8 nm width is obtained for deposition temperatures lower than 460 K, with a 3×2 LEED pattern, whereas 1.6 nm-wide NRs are formed at temperatures higher than 460 K. These NRs will be denoted hereafter as single NRs (SNRs) and double NRs (DNRs), respectively. Larger Si NRs were rarely observed at the surface. However, as a general rule, the width of all the measured NRs was always found to be an integer multiple of 0.8 nm (i.e. 0.8, 1.6, 2.4 and, very rarely, 3.2 nm). At 490 K, regardless of the Si coverage amount, the 5×2 LEED pattern was obtained. At higher temperatures, it was observed the formation of large 1D nanostructures growing parallel to the Si NRs but extending in the normal direction to the surface either outwards (nanodikes) or inwards (nanotrenches). The first kind of nanostructures was previously reported to be 'multilayer silicene nanoribbons' mentioned previously.[69] The number of nanodikes and nanotrenches increases with the deposition temperature regardless of Si amount, at the expense of Si NRs. These structures remain the only kind of nanostructures covering the surface for a deposition temperature of 550 K. Such findings cast important doubts on the hypothesis that such massive 1D nanostructures may be 'multilayer silicene nanoribbons'. For Si amount higher than one ML deposited on a substrate preheated at 490 K, *c*(8×4) patches are observed. S. Colonna and al. demonstrated that the ×4 periodicity observed in LEED patterns, previously attributed to Si NRs or to multilayer Si NRs, is actually related to the formation of this novel reconstruction. Finally, the possibility that STM tip artifacts may provide anomalous results is discussed: on the basis of the analysis of a very large set of acquired high-resolution STM images, the authors singled out an image artifact that can give rise to a fictitious honeycomb internal structure of the Si NRs. LEED patterns for different temperatures of Si deposition are shown in Figure 17.

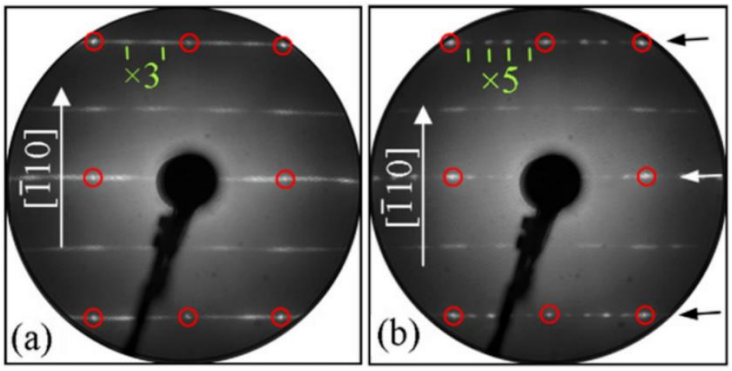

Figure 17: LEED patterns measured on 0.8 full Si monolayer coverage on Ag(110) for different deposition temperatures, the red circles evidence the 1×1 spots: (a) 430 K (E = 50 eV), the green dashes indicate the ×3 periodicity along the [001] direction; (b) 490 K (E = 50 eV), the green dashes indicate the ×5 periodicity of the Si NR grating along the [001] direction. The arrows indicate the lines on which the ×5 periodicity is clearly observed [S. Colonna et al. ref: 70]

These important findings have called for a revisitation of the proposed structural models of the Si NRs based on a hexagonal crystallographic cell. A second decisive step in the description of the Si/Ag(110) system was achieved in 2013 with the study reported by Bernard *et al.* [71] STM and GIXD measurements were carried out for Si deposition at RT and 460 K. The results evidence that the Si NR growth on Ag(110) induces a missing row reconstruction of the Ag layer beneath the NRs. At RT, STM images presented in Figure 18, show the growth of Ag islands associated to the release of Ag adatoms during the deposition of Si on the surface. For a low NR density, Ag adatoms are incorporated at step edges, inducing the motion of the steps. At higher Si coverage, Ag adatoms cannot reach step edges, leading to the formation of elongated shape island on terraces. The Si growth at 460 K was followed by GIXD. At this temperature, the 5×2 superstructure was obtained, without any significant increase of the surface roughness. In Figure 19(a), we see that the diffraction peaks associated with the Si overlayer at completion are very narrow, indicating the high structural order of the Si NR array. The most striking feature revealed by GIXD measurements was the strong decrease of the diffracted intensity associated with the silver substrate, which almost vanishes at completion of the Si overlayer, as shown in Figure 19(b), The best agreement of the diffraction peaks associated with the grown system is obtained for two missing Ag rows within the 5×2 unit cell. Thus, STM and GIXD results demonstrate the removal of part of the Ag atoms of the Ag(110) surface during Si deposition and are in agreement with a MR reconstruction of the Ag layer underneath the NRs. These results provided key elements for the determination of the exact atomic structure of the first system which has been interpreted within the framework of silicene models.

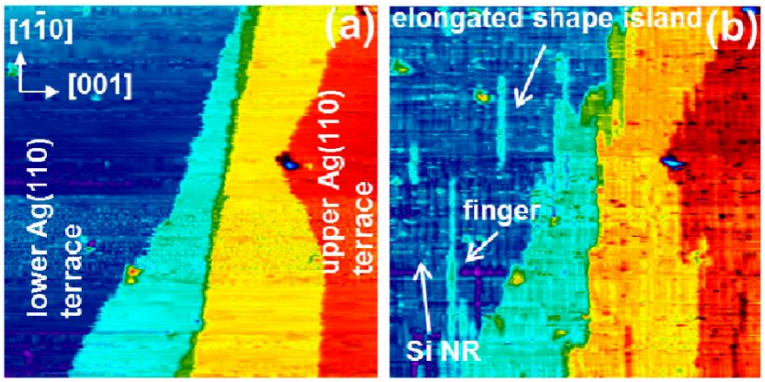

Figure 18: (a-b) STM images (234×234 nm^2) of the same area showing the evolution of the Ag(110) surface upon Si deposition at RT. (a) bare silver surface. (b) Θ_{Si} = 0.3 ML. [R. Bernard et al. ref: 71]

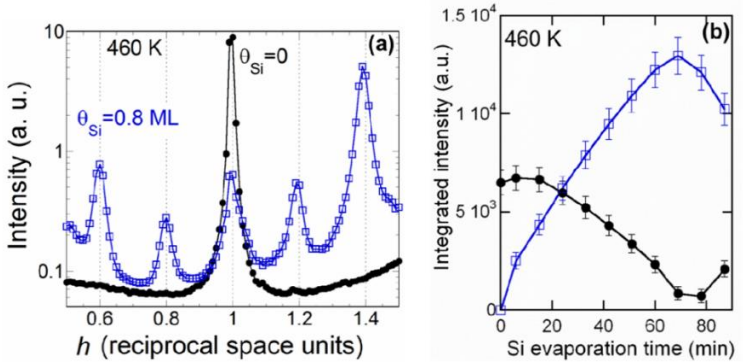

Figure 19: (a) h-scans for k = 0 and l = 0.05 recorded at T_{sub} = 460 K during Si deposition. Dots: bare Ag surface. Empty squares: Θ_{Si} =0.8 ML (completion of the 5×2 Si overlayer). (b) Evolution, during Si deposition at T_{sub} = 460 K, of the integrated intensities associated with the Ag(110) surface at (1,0,0.05) (dots) and with the 5×2 superstructure at (1.4,0,0.05) (empty squares). [R. Bernard et al. ref: 71]

Apart from to these studies on the atomic structure of the Si NRs, a theoretical explanation of the origin of the Dirac cone observed for Si NRs deposited on Ag(110) was reported by Gori *et al.* [72] in 2014: the Dirac-cone is associated to the silver substrate, as an effect of band folding induced by the Si NR periodicity.

At the same time, optical properties of Si ultrathin films on Ag(110) were studied by Borensztein *et al.* in 2014[73,74] and compared to those calculated for silicone on Ag. The optical properties of Si NRs grown on Ag(110) have been experimentally determined by use of *in-situ* surface differential reflectance spectroscopy (SDRS). Real-time measurements showed a sudden change of the optical response at the transition from ×2 to ×4 periodicity, the ×4 periodicity was described by Colonna *et al.*[70]. The spectra measured for the complete self-assembled NR layer are clearly different from the reflectance spectrum calculated for a layer of silicene on silver, which rules out the possible silicene-like character of this layer. Furthermore, the dielectric function of the NRs is calculated from the experimental data and is similar to the one of amorphous silicon, with a red shift of about 0.6 eV to 0.8 eV of the main absorption feature. This result indicates that the Si NRs display a preferential sp^3 hybridization as in amorphous Si and not a partial sp^2 hybridization as expected for silicene. Comparison of optical adsorption spectra for Si NRs with other Si structures, including the calculated silicene one, are shown in Figure 20.

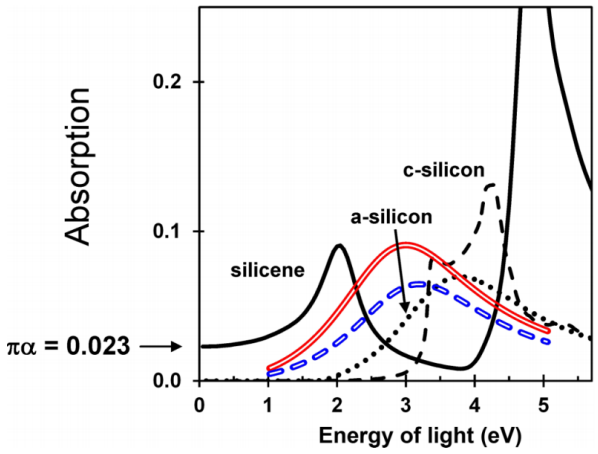

Figure 20: (a) Optical absorption of a silicene layer (black continuous line), of a crystalline Si layer (black dashed line), of an amorphous Si layer (black dotted line) for the same amount of Si atoms. Absorption of a 1 ML of Si NRs on Ag(110) determined from the SDRS measurements performed between 1 and 5 eV, parallel to the NRs (red double line) or normal to the NRs (blue dashed double line) is also shown. [Y. Borensztein et al. ref: 73]

In 2016, a review of the atomic models reported in the last ten years was published, showing that most of them were in favor of a Si honeycomb structure, eventually buckled, grown on a unreconstructed Ag(110) surface.[75]

Nevertheless, new models started to be proposed. For instance, Hogan *et al.*, using total-energy calculations within DFT, proposed in 2015 two models, called zigzag A and zigzag B, which took into consideration the reconstruction of the silver surface.[76] Their main structure motif is a zigzag chain of Si adatoms backboned to Si dimers lying within the silver MRs. Comparison of simulated STM images with experimental ones was satisfying. Their study provides clear evidence for a strongly bound Si-Ag reconstruction of Ag(110), and does not find any support for models based on silicene. Unfortunately, it was not confirmed by GIXD experiments.

Further studies have been made to unveil the internal structure of these Si NRs. In 2016, Cerdà *et al*. reported a study consisting on extended DFT calculations and STM image simulations.[77] Firstly, the authors confirm previous results concerning the presence of two environments for the Si atoms, described by Si subsurface atoms and Si surface atoms. Thus, the authors proposed a model of a silicon phase consisting in alternating pentagons residing in the MR troughs of the reconstructed surface, as shown in Figure 21 (a)-(e). They also proposed a quasi-hexagonal model for the Si nanodots previously mentioned by Ronci *et al.*[63], comprising ten Si atoms located in a silver di-vacancy. These nanodots, shown in Figure 21(f) and (g), may be the seed for the formation of the extended Si NRs. Finally, concerning the electronic structure, a sp^2 type bonding was suggested for the Si atoms located in the MR troughs (Si_s in Figures 21(b) and (e)) while a sp^3 type bonding was attributed to the Si atoms located at the edges of the NRs ((Si_{ad} in Figures 21(b) and (e)).

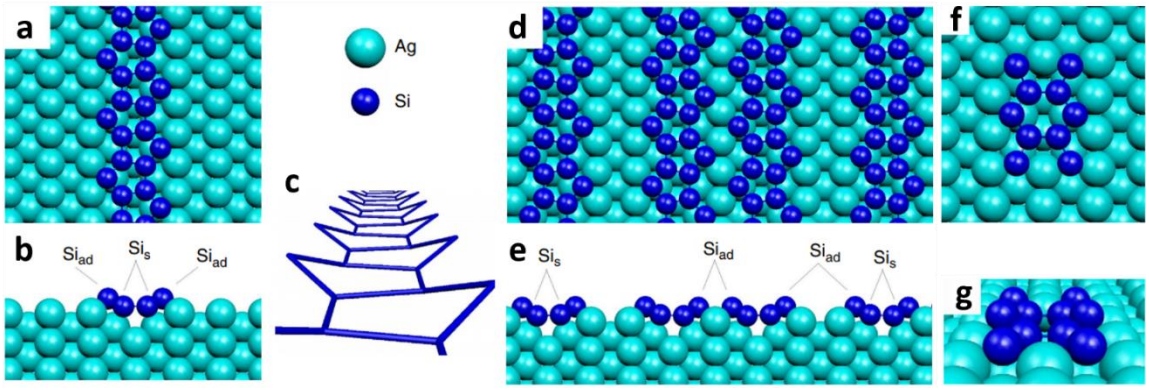

Figure 21: (a,b) top and side view of the SNRs: Si atoms are arranged in pentagonal rings running along the missing rows with alternate orientation. (c) Perspective view of a Si pentagonal strand without the silver surface. The strand is made of alternating buckled pentagons. (d,e) Top and side view of the DNRs; DNRs are generated by placing two SNRs within a c(10×2) cell to form a double-strand Si pentagonal NRs.(f,g) Top and side view of the nanodot structure. [J.I. Cerdà el al. ref: 77]

Finally, in 2016, a study presented by Prévot *et al.* elucidated the internal atomic structure of the Si NRs grown on the missing-row reconstructed Ag(110) surface.[78] A combined theoretical (DFT) calculations and experimental measurements (STM and GIXD) study allows to discriminate between the theoretical models published in the literature till 2006 and the dimer-based model of He. The pentamer atomistic model accurately matches the high-resolution STM images of the Si NRs adsorbed on Ag(110), as shown in Figure 22. We see also that the zigzag B model is in agreement with the experimental STM image. Nevertheless, this latter model was shown to be unfavorable energetically by DFT formation energies calculation. Remarkably, GIXD measurements unambiguously validate the pentamer model grown on the reconstructed Ag(110) surface, initially proposed by Cerdà *et al.*

This study closed the long-debated atomic structure of the Si NRs grown on Ag(110) and definitively excludes a honeycomb structure similar to that of freestanding silicene.

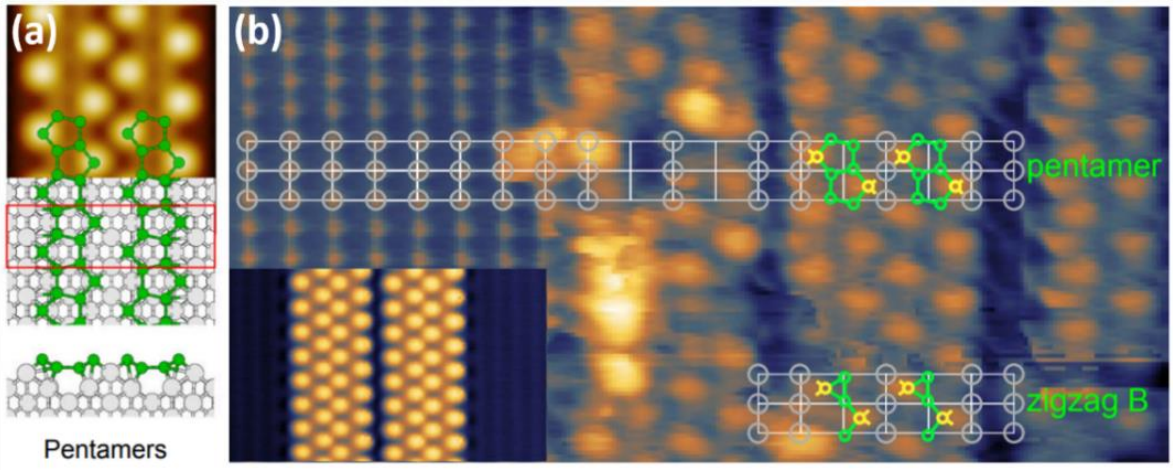

Figure 22: (a) Pentamer schematic model of 1.6-nm-wide Si NRs and corresponding simulated STM images (b) STM image (9 × 4.5 nm^2) of Si DNRs below 1 ML. The high resolution allows to visualize both the Ag atoms (left part) of the (110) substrate and the protrusions of the DNRs (right part). Both pentamer and zigzag B models match the STM image. Si adatoms (yellow circles) appear as protrusions in the STM images whereas Si atoms in the missing rows (green circles) are not imaged. The high tunneling current used to resolve the atomic structure of the Ag(110) substrate induced a partial alteration of the Si NRs. The inset in the bottom-left corner shows two unaltered Si DNRs.[G. Prévot et al. ref: 78]

In 2017, a study was published on the investigation on the structure of the Si NRs by means of x-ray photoelectron spectroscopy (XPS) and x-ray photoelectron diffraction (XPD).[79] An evaluation of almost 30 models was made, the matching model that agrees with the experimental results of XPD is the one validated by Prévot *et al.* with some modifications. For instance, a weak bonding between Si NRs and the silver substrate is indicated by XPS and confirmed by XPD analysis with a large distance between the NRs and the substrate. The two Si environments showed by XPS were attributed to Si atoms bonded to three or two neighbors. The crucial point of Si-Ag bonding has to be further investigated because the weak interaction mentioned is in contrast with previous results in favor of Si NRs strongly interacting with the substrate beneath.

Finally, a study was published in 2018, based on non-contact atomic force microscopy (nc-AFM) and tip enhanced raman spectroscopy (TERS) measurements.[80] This study confirmed the pentagonal structure of the Si NRs by visualizing pentagonal structures by nc-AFM and by measuring vibrational fingerprints of the Si NRs which fit perfectly the pentagonal model. Finally, another structure for the Si nanodots that are considered to be the seed of NRs, is reported: instead of a quasi-hexagonal structure[77], the authors proposed that these clusters consist of two pentagons siting side by side with four Si adatoms attached to the edge, located on a Ag di-vacancy. This model was in agreement with both nc-AFM images and TERS vibrational measurements. This nanodot model is similar to the pentagon chain model.

In other perspectives, a study on the etching of Si NRs by atomic hydrogen was made by Salomon *et al.* in 2009[81] and the interaction of Si NRs with hydrogen was studied by Dàvila *et al.* in 2012.[82] Other studies on the oxidation of the Si NRs was made by De Padova *et al.* in 2011.[83]

b2- Si nanoribbons: template

In parallel to the long debate about the structural, electronic and optical properties of the Si NRs, the self-assembled Si NR grating has been used as a template to grow 1D nanostructures.

In 2009, after the discovery of the lateral self-assembly of Si NRs grown at 470 K, studies have been dedicated to the formation of 1D metal array made of cobalt or manganese, with the aim of fabricating 1D magnetic nanostructures.[84] Other studies tried to guide the growth of molecules such as C_{60}[85] or tris{2,5-bis(3,5-bis-trifluoromethyl-phenyhl)-thieno}[3,4-b,h,n]-1,4,5,8,9,12-hexaazatriphenylene (THAP) and 9,10-phenanthrenequinone (PQ)[86] on this template.

The deposition of Co on the Si NRs has succeeded to grow 1D nanostructures, called Co nanolines. Sahaf *et al.* made the first deposition of Co at RT on the Si NRs grown on Ag(110).[84] This deposition leads to the growth of Co nanolines on Si SNRs and two adjacent Co nanolines on Si DNRs. A preferential adsorption on the Si NRs has been observed in STM images. High-resolution STM images showed the growth of nanolines consisting of two adjacent protrusions forming dimers on the Si NRs. Height profiles strongly suggest that Co atoms are adsorbed on top of the Si NRs. This study was followed up by another ones[85,87], where the deposition of Co was held on the self-assembled Si DNRs organized in the 5×2 superstructure. This study confirms the results obtained previously and showed that more than 80% of the nanolines are coupled to a second adjacent one of similar length on a Si DNR. In addition, the formation of black dots in the Si NRs array were reported, most of them being located at the end of a nanoline. These black dots were associated to the in-diffusion of Co atoms into the Si array. This process turned to be thermally activated and was assumed to be a limiting process for the growth of long free-defect Co nanolines. Deposition at lower temperature (220 K) was performed in order to partially block the Co in-diffusion into the array and thus, grow longer nanolines, as shown in Figure 23.[88] Finally, preliminary magnetic characterizations of the Co nanolines were carried out by XMCD. This preliminary study, important in the framework of my thesis work, will be presented in details in the chapter 5.

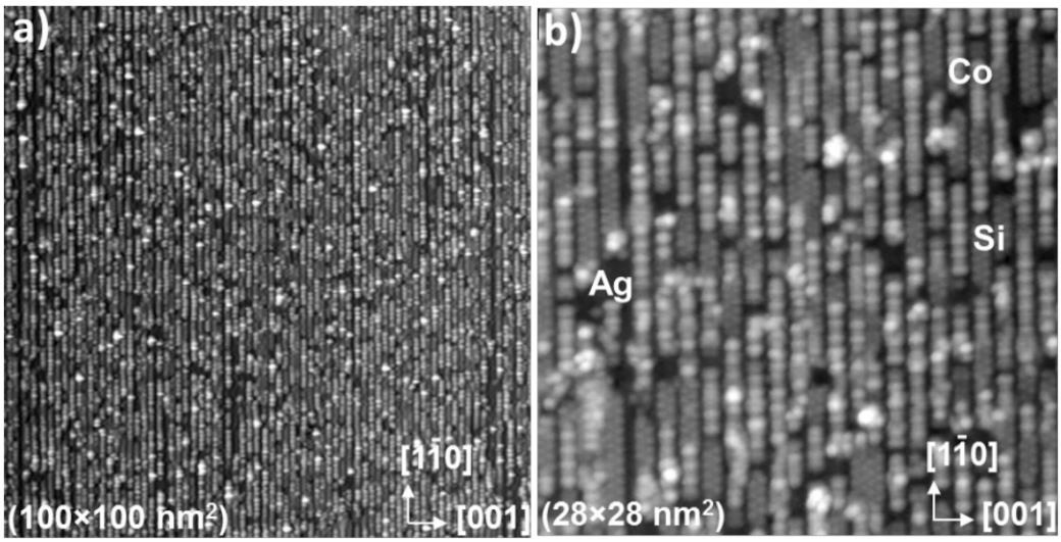

Figure 23: (a,b) STM images at different magnification scales, recorded at 77 K for a Co coverage of ~0.6 ML, showing the formation of Co dimer nanolines on the Si NR array grown on Ag(110) after Co deposition at 220 K. [L. Michez et al. ref: 88]

The deposition of Mn on the Si NR array was reported by De Padova *et al.* in 2012.[89] This experimental study showed the growth of metallic 1D Mn-silicide nanostructures. These nano-objects develop along the edges of the Si NRs.

These pioneering works have confirmed that the Si NR array is a template well-suited to guide the growth of 1D nanostructures.

B-Magnetism

In my thesis work, the aim was to control the growth of 1D nanostructures to study their magnetic properties. Therefore, I present in this part, in a general manner, the magnetic properties of nanostructures going from macro- to nano- scale with a focus on 1D nanostructures made of magnetic atoms. I present, firstly, the classification of the materials in function of their behavior in the presence of a magnetic field, followed by a discussion on the superparamagnetism, the anisotropy and the magnetism in nanostructures with a focused on 1D nanostructures.

I- Types of materials

In this section, I discuss the basic concepts related to the magnetic properties of materials. The classification of different materials in groups is in function of their magnetic response to an applied magnetic field. This classification results from a study of (i) the orbital and spin magnetic moments of electrons and (ii) the interaction between electrons, in the presence and absence of an external magnetic field. The different responses described here correspond to diamagnetism, paramagnetism and ferromagnetism.

a- Diamagnetism

This type has the most elements in the periodic table including noble metals. These elements are usually referred to as non-magnetic. They present low and negative magnetic susceptibility. All the diamagnetic atoms have all the orbital shells filled and there are no unpaired electrons, thus, no net magnetic moment. However, when exposed to a magnetic field, magnetic moments are aligned in an opposite direction of the applied field, therefore, a negative magnetization is produced and thus the susceptibility is negative.

b- Paramagnetism

In these materials, the atoms have unpaired electrons in partially filled orbitals. That means that each atom in a paramagnetic substance has a small net magnetic moment, thus a small positive susceptibility. However, there is no exchange interaction between these atomic magnets. The magnetic moments are not coupled, each one is randomly oriented. The exchange energy is negligible compared to the thermal one. The application of a magnetic field creates an alignment of these magnetic moments and hence a low magnetization in the same direction as the applied field. When the external magnetic field is removed, influenced by the thermal excitation, the magnetic moment re-orients randomly.

The susceptibility for such materials is temperature dependent and obeys the Curie law:

$$\chi = \frac{C}{T} \tag{1-7}$$

where χ is the susceptibility, T the temperature and C is a Curie constant. C depends on the material and defined as $C = \frac{N\mu_0\mu_B^2}{3k_B}$; where N is the number of magnetic moments in the material and μ_B is Bohr magneton.

For some paramagnetic elements, this law presents a particularity and they are described by the Curie-Weiss law. The susceptibility is expressed as:

$$\chi = \frac{C}{T-T_C} \tag{1-8}$$

Where C is the curie constant., and T_C is the Curie temperature. Above T_c the behavior is paramagnetic, whereas, below T_C ferromagnetic behavior occurs. For $T = T_C$, χ becomes infinite, signifying a transition phase between para- and ferro- magnetism.

c- Ferromagnetism

The first materials found as magnetic materials were the magnetite (Fe_3O_4) and nickel at room temperature. In the periodic table, there are only the Fe, Co and Ni as ferromagnetic elements. Magnetism occurs in this type of materials because the magnetic moments couple to one another and form magnetically ordered states. The coupling, which is quantum mechanical in nature, is known as the exchange interaction and is rooted in the overlap of electrons in conjunction with Pauli's exclusion principle. Whether it is a ferromagnet, antiferromagnet or ferrimagnet, the exchange interaction between the neighboring magnetic ions will force the individual moments into parallel (ferromagnetic) or antiparallel (antiferromagnetic, ferrimagnetic) alignment with their neighbors. The parallel alignment of magnetic moments in terms of exchange interaction were described by the Heisenberg model of ferromagnetism. This type of materials consists on having high and positive susceptibility and they retain their magnetic properties after the remove of the external magnetic field. The parallel alignment of the magnetic moments is only valid below a critical temperature, the Curie temperature (T_c). For temperature higher than T_c, transition from ferromagnetic behavior to paramagnetic behavior occurs.

In a ferromagnetic material, the magnetic moments are not macroscopically all aligned in the same direction. We can have a bulk of iron with no macroscopic magnetization. This can be explained by the Weiss theory: the bulk can be divided into domains (Weiss domains), each domain exists in a microscopic region where the magnetic moments are aligned. Thus, each domain has its own orientation and magnetization. Hence, the macroscopic magnetization is the vector sum of all the microscopic magnetizations. This configuration, Weiss domains, minimizes the demagnetizing field and hence the dipolar energy of the system. The exchange interactions and the dipolar coupling interplay in contrary aims. It is possible to have the two interactions at the same time, since they act at two different regions: the exchange interaction reacts on the close neighbors or the dipolar coupling reacts on spaced regions.

We introduce a typical distance, the exchange interaction distance:

$$l_{exch} = \sqrt{2\frac{A_{\text{exch}}}{\mu_0 M_S^2}} \quad (1\text{-}9)$$

where A_{exch} is the constant of exchange interaction and M_s is the saturated magnetization.

This distance is the limit distance that separates the region where the exchange interaction is dominant ($l<l_{\text{exch}}$) from the region where the dipolar coupling dominates ($l> l_{\text{exch}}$).

In addition, Weiss domains are dependent on the characteristic of each material (constant of exchange, shape, defects, crystallography…), and on the applied magnetic field. These domains are separated by walls, known as 'Bloch wall'. Crossing these walls, the magnetic moment changes its direction and magnetization in a gradient way. The creation of a wall costs energy (exchange and anisotropic energies). The final magnetic configuration is the combination of all these exchange interactions and dipolar energies.

II- Introduction to superparamagnetism

So far, I have discussed the ferromagnetic behavior at the macroscopic scale. I introduce in this section ferromagnetism at the nanoscale. The objects at this scale can be small enough that they are considered individually as one single unique magnetic domain. Let consider a ferromagnetic nanostructure with a Curie temperature T_C and dimensions all smaller than the exchange length. At $T < T_C$, if a snapshot was experimentally feasible, it would reveal essentially uniform magnetization, with a direction lying along an easy direction of magnetization of the system. However, at $T > 0$ K, thermal fluctuations allow the system to explore its entire phase space.

To define superparamagnetism, it is necessary to consider monodomains without reciprocal interactions, isolated from each other. The monodomains are single-domain magnetic states as their physical size is smaller than the exchange interaction length. The total moment of a monodomain is the so-called macrospin. The macrospin is the sum of all the magnetic moments of all the atoms in a monodomain. At thermal equilibrium, the macrospin of a monodomain is oriented along an axis called easy axis of magnetization and can adopt two equilibrium positions: parallel or antiparallel.

The evolution of macrospin from one equilibrium position to another requires energy of activation to overcome the energy barrier $E = K_{\text{at}} N$ where K_{at} is the magnetic anisotropy energy per atom and N the number of atoms of the macrospin. Considering the size of a single-domain, the energy barrier is of the order of magnitude of the thermal energy $k_B T$, where k_B represents the Boltzmann constant and T the temperature. Thus, at a given temperature for which $k_B T > K_{\text{at}} N$ and in the absence of an applied magnetic field, the macrospin carried by a monodomain is relaxed between the two positions of equilibrium. This physical phenomenon defines superparamagnetism (paramagnetism of a macrospin).

More precisely, Louis Néel and J. Brown showed that the lapse of time, τ, to overcome the barrier energy can be described by a simple Arrhenius law based on the Boltzmann probability of states occupancy and obeys to :

$$\tau = \tau_0 \exp(\beta K_{at} N) \quad (1\text{-}10)$$

where $\beta = 1/k_B T$ and $\tau_0 \sim 10^{-9}$s [90] is the so-called attempt period.

The system is observed for a duration τ_m (measuring time). For $T < T_B$, with $T_B = K_{at}N/[k_B \ln(\tau_m/\tau_0)]$ called the blocking temperature, the system has not switched over time τ_m and is said to be in a blocked state. For $T > T_B$, the system switches spontaneously in the interval of time τ_m. Thus, a magnetization measurement performed over that time scale reveals zero apparent magnetization, although the magnitude of the microscopic moment is still the same at any time. This is the so-called superparamagnetic state. A consequence is that for $T_B < T_C$, what can be measured practically in nearly all experiments is T_B, not T_C. The fact that $T_B < T_C$ was clearly illustrated in the case of in-plane magnetized Fe/W(110) dots.[91]

III- Magnetic anisotropy

One factor which may strongly affect the shape of the field-dependent magnetization curves, H (or B, H) curve, is the magnetic anisotropy. This term simply means that the magnetic properties depend on the direction in which they are measured. This results from preferential set of directions along which the magnetization will lie. This effect is associated with the MAE which describes the tendency of the magnetization to align along specific spatial directions rather than randomly fluctuate over time. This general subject is of considerable practical interest, because anisotropy is exploited in the design of most magnetic materials of commercial importance. A thorough knowledge of anisotropy is thus important for an understanding of these materials. In this section, I present different origins of magnetic anisotropy for the nanostructures made of magnetic materials.

The first remarkable source of anisotropy is the shape of the object. If it is spherical in shape, the same applied field will magnetize it to the same extent in any direction. But if it is non-spherical, it will be easier to magnetize it along a long axis than along a short axis. The reason is that the demagnetizing field along a short axis is stronger than along a long axis. The applied field along a short axis then has to be stronger to produce the same true field inside the object. Thus, shape alone can be a source of magnetic anisotropy. The magnetic anisotropy stressed as: $E_{Shape} \sim M^2 \cos^2\theta$ where M is the total moment and θ is the angle between the magnetization direction and the normal to the surface of the structure. It can be noticed that for $\theta = \pi/2$ the anisotropic energy is minimal, and thus the shape anisotropic energy tends to maintain M in the plane of the object (wire or film for instance).

The crystallographic structure of the material is a second source of anisotropy. The magnetocrystalline anisotropy arises due to the spin-orbit interaction, where the orbital path of the electrons is determined by the crystallographic environment and lies along particular crystallographic axes. Magnetocrystalline anisotropy is intrinsic to the material since it depends on the crystal structure. As a consequence, magnetic measurements along different crystallographic directions yield different magnetization curves, as shown in Figure 24. The magnetocrystalline energy can be written as : $E_m = K_m \sin^2\theta$ where θ is the angle between the magnetization direction and the anisotropic axis (easy axis) and K_m is an magnetocrystalline anisotropy constant.

Two cases present: 1) for K_m >0, E_m is minimal for θ=0 and thus M is parallel to an anisotropic axis (easy axis) and 2) for K_m <0, E_m is minimal for θ=π/2 and thus M is perpendicular to an anisotropic axis.

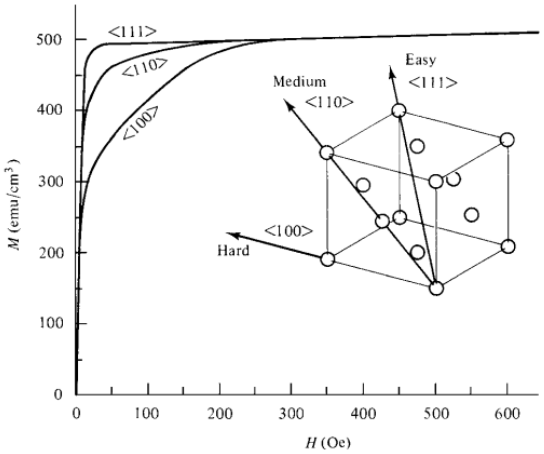

Figure 24: Magnetization curves for the principal axes of a single crystal of Ni. Graph replotted from C. Kittel 1953

The physical origin of this anisotropy is to the spin-orbit coupling and orbit-lattice coupling that together result in a preferential set of directions along which the energy of the system (material) is minimized and hence where the magnetization will lie.

A third source of anisotropy is the presence of an interface. Interfacial anisotropy arises due to symmetry breaking at the interface between two materials. The possibility of interface or surface anisotropy was originally noted by Neel[92] , and later Bruno[93] provided a theoretical model of interface anisotropy in terms of a modified spin-orbit interaction due to the symmetry splitting at the interface. In essence, interface anisotropy arises because the electronic orbitals of atoms at the surface are modified in the direction of the surface normal. Films of two different elements or alloys in direct contact which have different spin-orbit interactions can therefore generate a strong, intrinsic anisotropy. The electronic structure (wave function overlap) will be different in the plane where the environment of the atoms is similar to a 3D bulk crystal, compared with the out-of-plane direction where the electronic structure is significantly modified by the presence of different elements. Since the physical origin of interfacial anisotropy is structural, it is often convenient to consider this as equivalent to magnetocrystalline anisotropy. Good examples of interfacial anisotropy are Co/Pt or Co/Pd multilayer materials. The anisotropy as a function of Co layer thickness has been explored by a number of researchers over the years, An illustration of this behavior is given in Figure 25.[94] This example shows that interfacial anisotropy is dominant only for approximately five monolayers or less of Co.

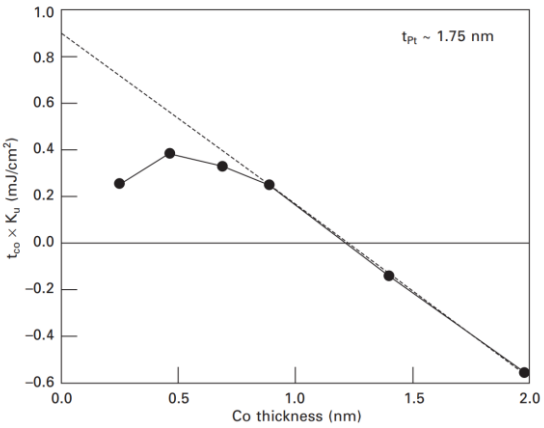

Figure 25: Anisotropy multiplied by Co layer thickness ($t_{Co}K_u = 2K_{surface}$ Co + K_{volume}) as a function of t_{Co} for a Co/Pt multilayer grown on Si. The data show a crossover to a perpendicular easy axis for t_{Co} less than 1.2 nm. [Zeper et al. ref: 94]

In addition, strain anisotropy can also be significant in some material systems. Strain anisotropy is due to an expansion or contraction of the crystal lattice. In thin films, this can arise due to a lattice mismatch between a seed layer and a magnetic layer where the magnetic film is forced to assume a non-equilibrium lattice parameter. This is also defined by the magnetoelastic effect that arises from the spin-orbit interaction. The spin moments are coupled to the lattice via the orbital electrons. If the lattice is changed by strain, the distances between the magnetic atoms is altered and hence the interaction energies are changed. This produces magnetoelastic anisotropy.

Finally, I mention the Zeeman energy which represents the interaction of the magnetization with the applied magnetic field.

To resume, the global anisotropy in the structure is the sum of all the anisotropies mentioned above. In general, it is critical to define separately each anisotropy constant. To simplify, effective anisotropy constant is used and the energy can be expressed as:

$$E_a = K_{eff} \sin^2\theta$$

where θ is the angle between the magnetization direction and the anisotropic axis (easy axis). As mentioned before, according to the sign of K_{eff} we can be out of plane for $K_{eff}>0$, or in-plane for $K_{eff}<0$. This term is of prime importance to describe the magnetic behavior of an object and has to be measured in experiments.

IV- Magnetism in nanostructures

As previously mentioned, the MAE is governed by the symmetry breaking at interfaces, the shape of the objects and the crystallinity of the materials. Néel predicted in 1954 that the interfacial anisotropy yields a 1/t dependence of the total MAE density of a film with thickness t.[92] This law was proved experimentally by Gradmann *et al.* in 1968.[95] Moreover, Bruno *et al.* predicted that the MAE follows the anisotropy of the orbital magnetic moments[93], which was checked experimentally on perpendicularly magnetized Au/Co/Au(111).[96]

The MAE and magnetic moments of 2D, 1D and 0D nanostructures are now achievable due to development in both growth and characterization techniques. Gambardella *et al.* showed in

2003[97] the variation of the orbital magnetic moment and MAE as a function of the cluster size, as shown in Figure 26. MAE and orbital magnetic moments were studied for cluster size decreasing from 40 to 1 Co atom on Pt(111) surface, i.e reducing the dimensions from 2D to 0D. As the cluster size decreases, these parameters increase markedly. Remarkably, giant MAE (MAE= 9.3 meV/atom) and enhanced orbital magnetic moment (1.1 μ_B/atom) were measured for single Co atom, compared to bulk material (orbital magnetic moment 0.153 μ_B/atom; MAE= 0.07 meV/atom). This behavior was associated to the low coordination of Co atoms which results in a 3d band narrowing. Although these Co nanoparticles present a superparamagnetic behavior down to the lowest temperatures (few K), this pioneering work opened new perspectives in the field of magnetic data storage.

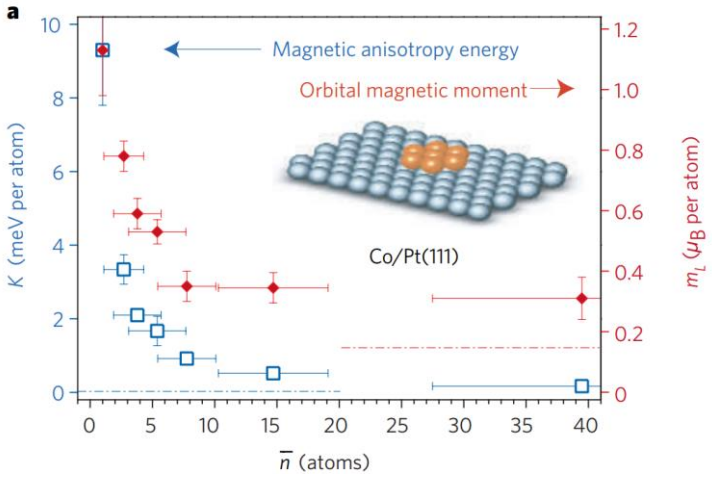

Figure 26: MAE per atom (K) and orbital magnetic moment (m_L) as a function of the number of atoms in the cluster.(blue empty squares for K, red filled dots for m_L) [Gambardella et al. 2003, ref: 97]

In 2005, N. Weiss *et al.* used the self-organized growth to produce and study the magnetic properties of an ultrahigh density lattice of Co nanodots. [98] As mentioned in a previous section of this chapter, 2D long-range ordered Co nanodots were grown on a combined herringbone reconstruction-vicinal Au surface. The magnetic behavior of these Co nanodots was studied by XMCD and magneto-optical Kerr effect (MOKE). Superparamagnetic behavior was revealed for the Co nanodots with a relative high blocking temperature of 50 K. For a Co nanodots density of 26 Tera/in^2, no interaction between the Co nanodots was detected and a uniaxial out-of-plane anisotropy was determined. A very narrow MAE distribution was found compared to assemblies of 3D nanoparticles, associated to the narrow temperature window of transition from blocked state to superparamagnetic state.

Later on, studies were extended to include other magnetic elements such as lanthanide.[99–102] The 4f lanthanide elements such as Ho are presented as a promising alternative to *3d* TM elements. Lanthanides present stronger spin-orbit coupling than the TM elements which results in larger splitting of the quantum levels (between the magnetic ground and first excited state). The splitting of quantum levels has been shown to be crucial for the magnetic anisotropy of single atoms on surfaces. In addition, they present 4f orbitals strongly localized which provide a weaker interaction with the surrounding medium. This feature lead to a weak scattering with the electrons and phonon of the substrate. Experimental studies on single-molecule magnet showed that single lanthanide atoms exhibit a large zero field splitting, together with hysteresis loops and magnetic lifetimes up to seconds at 3 K at zero magnetic field.[103–105] However, recent experimental studies reported on single atoms of Ho on Pt(111) and Cu(111) surface denied any long spin relaxation time even at 2.5 K, and showed that the ground state and magnetic anisotropy is

influenced by the interaction with the substrate orbitals.[101] Remarkably, Ho atoms adsorbed on MgO ultrathin film on Ag(100) showed magnetic remanence up to 30 K with a relaxation time of 1500 s at 10 K. The MgO film with low phonon density of states insured the decoupling of Ho atoms from the conduction electrons of the surface and longer lifetimes are achieved.[102] However, while several studies were made on single Ho atoms adsorbed on surfaces, no experiments about the growth of 1D Ho nanostructures have been reported so far.

Concerning 1D nanostructures made of magnetic materials, pioneering work on Fe nanostripes on W(110) surface presented a ferromagnetic behavior in narrow stripes (width ~ 1-10 nm) for the first time.[91] A breakthrough occured in 2002, with the discovery by Gambardella *et al.* of an unprecedented ferromagnetic order in Co monoatomic chains formed at step edges of Pt(997), associated with the enhancement of Co orbital magnetic moments and in turn of MAE.[106] Such behavior results from kinetic barriers and below a threshold temperature, called blocking temperature, the strong MAE efficiently pins the orientation of the magnetization of each spin blocks along an easy axis without external magnetic field, on the timescale of the experiments. According to Eq. (1-9) with $\tau_0 \sim 10^{-9}$s, the MAE= 31± 1 meV yields a relaxation time $\tau \geq 100\ s$ at $T_B \leq 15$ K. Consequently, hysteresis loops displayed remanence and coercivity below 15 K, as shown in Figure 27. It has to be noted that spin lattice models predict that an infinite 1D chain with short-range magnetic interactions spontaneously breaks up into segments with different orientation of the magnetization, thereby prohibiting long-range ferromagnetic order at a finite temperature. Here, the system is superparamagnetic, but due to kinetics barriers, the MAE efficiently pins the orientation of the magnetization of each spin blocks containing ~ 15 atoms along an easy axis without external magnetic field, on the timescale of the experiments and below T_B, leading to a magnetic long-range ordered state in the Co chains. This experimental pioneering work corroborates numerous theoretical calculations predicting that the reduced symmetry of 1D magnetic systems produces strong modifications of the electronic band structure and thus, significant effects on the MAE are expected[107–110]

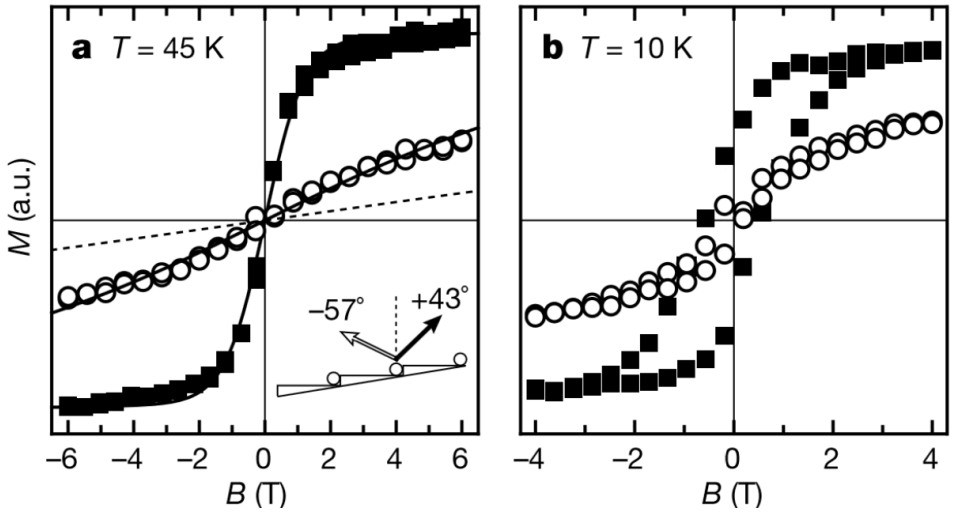

Figure 27: Magnetization of Co monoatomic chains. Filled squares and open circles correspond to measurements along the easy direction and at 80° away from it, respectively: a) M as a function of the magnetic field at T= 45 K. b) hysteresis measured at T= 10K (below the blocking temperature), showing remanence and coercivity. [Gambardella et al. ref 105]

The attractiveness of these 1D magnetic systems is reinforced with the recent theoretical prediction of an anisotropic spin-polarized electronic current along transition metal (TM) nanolines, such as Mn, Fe or Co nanolines, on graphene[111] which opens the possibility of their integration in spintronics devices.

Another important feature of 1D magnetic nanostructures is an expected strong anisotropic behavior of the magnetization axis, determined by both the 1D geometry of the nanolines and the interaction with the substrate. Experimental studies have often revealed an uniaxial easy axis of magnetization in the plane perpendicularly to the TM chain axis, canted from the surface normal with different tilt angles.[106,112,113] Moreover, it has been shown that the easy axis of magnetization oscillates in the plane perpendicular to the chains axis as a function of the transverse width of Co chains grown on Pt(977).[114] These different orientations corroborate several theoretical studies showing that the orientation of the easy axis is very sensitive to the change in environment. For instance, a rotation of the easy axis from the direction parallel to the chain to the out-of-plane one has been theoretically predicted for freestanding Co chains and after deposition on Pd(110)[107] while the magnetization of Co wires supported on Cu(100) and Pt(100) substrates was found to align with the wire axis.[115]

To conclude this chapter, the development in atomic engineering during the last two decades has made possible to design 1D nanostructures, allowing productive confrontations with theoretical works. Template directed-growth using intrinsic structural properties of surfaces has proven to be a powerful route to produce high densities of 1D nanostructures with controlled geometries, regular sizes and spacings, allowing the investigation of their intrinsic structural and magnetic properties using either local probes (STM) or surface-average probes (XMCD).

In my thesis work, STM and XMCD were used. The former has allowed to determine the morphology of the surface and the structure of the nanolines. The latter was used to investigate the magnetic properties of the grown 1D nanostructures. Thus, in the next chapter, I will describe in details these two powerful techniques.

Chapter 2

Experimental techniques

Contents

Chapter 2 61
Experimental techniques 61
I- UHV Chambers and protocol 62
II- Scanning tunneling microscopy (STM) 64
i- STM set-up 65
ii- Principle of STM 65
iii- STM functioning 68
iv- STM-tip preparation 68
III- X-ray absorption spectroscopy (XAS) and x-ray magnetic circular dichroism (XMCD) ... 70
i- Principle of XAS 70
ii- Polarization of x-ray 72
iii- Principle of XMCD 72
iv- XAS-XMCD set-up 75

In this chapter, I present the experimental set-ups used for the growth and characterization of nanostructures described in chapters 3 and 4 and in the last part 'Perspectives'. I describe the physical principles of the different experiments, the experimental protocols as well as the procedures employed for the data analysis.

I- UHV Chambers and protocol

In this work, the fabrication of nanostructures is conducted under UHV. The chambers are equipped with different growth and characterization techniques. In fact, the evaporation and characterization techniques employed in this experimental work require a UHV environment. This necessity is for two reasons. The first one is to provide the atoms with a free path in a line-of-sight process, in which they are traveling directly from a source to a substrate to be coated or etched. The second reason is minimizing the impingement of air or other gas molecules at the target surface, causing contamination.

The main UHV chamber I used at CINaM, shown in Figure 28, is divided in two stages according to their functionalities. The preparation part of the UHV chamber is equipped with evaporators of different materials used in this thesis (Si, Co, Fe, Ni, Ho, organic molecules), ion bombardment gun (Ar^+ sputtering) and leak valve (Ar^+). A transfer arm is equipped with a sample holder, a resistance (tungsten wire enrolled by ceramics) on the back of the sample holder to heat the sample for the preparation of the surface and during evaporation and a thermocouple (very close to the sample position) to measure the temperature of the substrate. An ionization gauge controls the pressure during experiments. This chamber is connected to a load lock to introduce the samples or STM tips into the UHV chamber without breaking the UHV. In addition, a system was installed during my PhD thesis for a direct current heating of tips. The characterization part of the UHV chamber is equipped with a Scienta Omicron variable-temperature STM (VT-STM) to study the morphology of the surface down to the atomic scale. The UHV chamber is made of stainless steel and are connected to a pumping system. The pumping system is constituted of primary, turbomolecular and ionic pumps to achieve UHV conditions, in addition to a titanium sublimation pump combined to a liquid nitrogen cryopanel that helps to maintain a low pressure during experiments.

Some of our experiments were made in another UHV set-up at CINaM with two separate chambers equipped with, in addition to the systems mentioned before, a cooling system of the sample which allows to cool-down the sample to 120K during the deposition, a LEED set-up and a low-temperature STM (LT-STM) as characterization techniques.

Each result obtained is due to a succession of several steps. In this section, I present the protocol of each step: achieve UHV conditions, clean the surface sample, deposit the materials and finally characterize the surface.

- How to get UHV conditions?

The preparation and characterization chambers were emptied at the beginning by the primary pump. Then the turbomolecular pump helps to achieve a pressure of ~ 10^{-8} Torr. The walls of the chamber are thus annealed at ~ 150 °C to accelerate the desorption of the contaminants. The bake-out lasts two days and it is done by heating the Ti wires of the sublimation pump below the sublimation point, lamps inside the chambers and enrolling heating wires on the external walls of the chambers. After these two days, the ionic pump takes over to achieve UHV conditions with a pressure of 10^{-10} Torr.

- Surface preparation

The Ag(110) surface is prepared by repetitive cycles of Ar^+ bombardment and subsequent UHV annealing at T= 770K. In the case of a silver sample exposed to air, four cycles of 40 min bombardment and 40 min annealing are required to remove the oxide layer from the Ag(110) surface and obtain large terraces of hundreds of nanometers. A precise control of the pressure is demanded during the annealing.

- Deposition of materials

For the evaporation of materials, the sample is held in the transfer arm in a specific position, facing the evaporator. The transfer arm with four degrees of freedom (x, y, z and rotation of the surface plane) allows to position the sample with high precision. There are several ways of thermal evaporation depending on the type of materials used: joule effect evaporation (Si) or electronic bombardment evaporation using a wire (Co, Fe, Ni) or a crucible (Ho, organic molecules). The conditions of deposition depend on each material in each experiment, therefore, I will mention in details the conditions of deposition in the next chapters according to the experiment meant to be done.

Once the evaporation is done, the surface is characterized by STM to study the surface morphology and structure. Using a wobble-stick, the sample is transferred to the characterization stage and installed in front of a STM tip.

Thus, the procedure of manipulations is:

1. Introduce the samples and the STM tips. Heating STM tip to eliminate residual elements and then install it in the STM set-up.
2. Degas the evaporators.
3. Prepare the surface: Ar^+ bombardment and annealing the sample at 770K.
4. STM observation to verify the cleanness of the surface.
5. Deposition of materials on the clean surface.
6. STM imaging to study the surface morphology.

Concerning the XMCD experiments, performed on the beamline DEIMOS (synchrotron SOLEIL) in 2015, the samples were also prepared *in-situ*, following the same procedure as described above, before the transfer in the cryo-stage for XMCD measurements. At each step of the sample preparation, the surface structure was controlled by LEED. STM images were also recorded *in-situ* on the samples probed by XMCD.

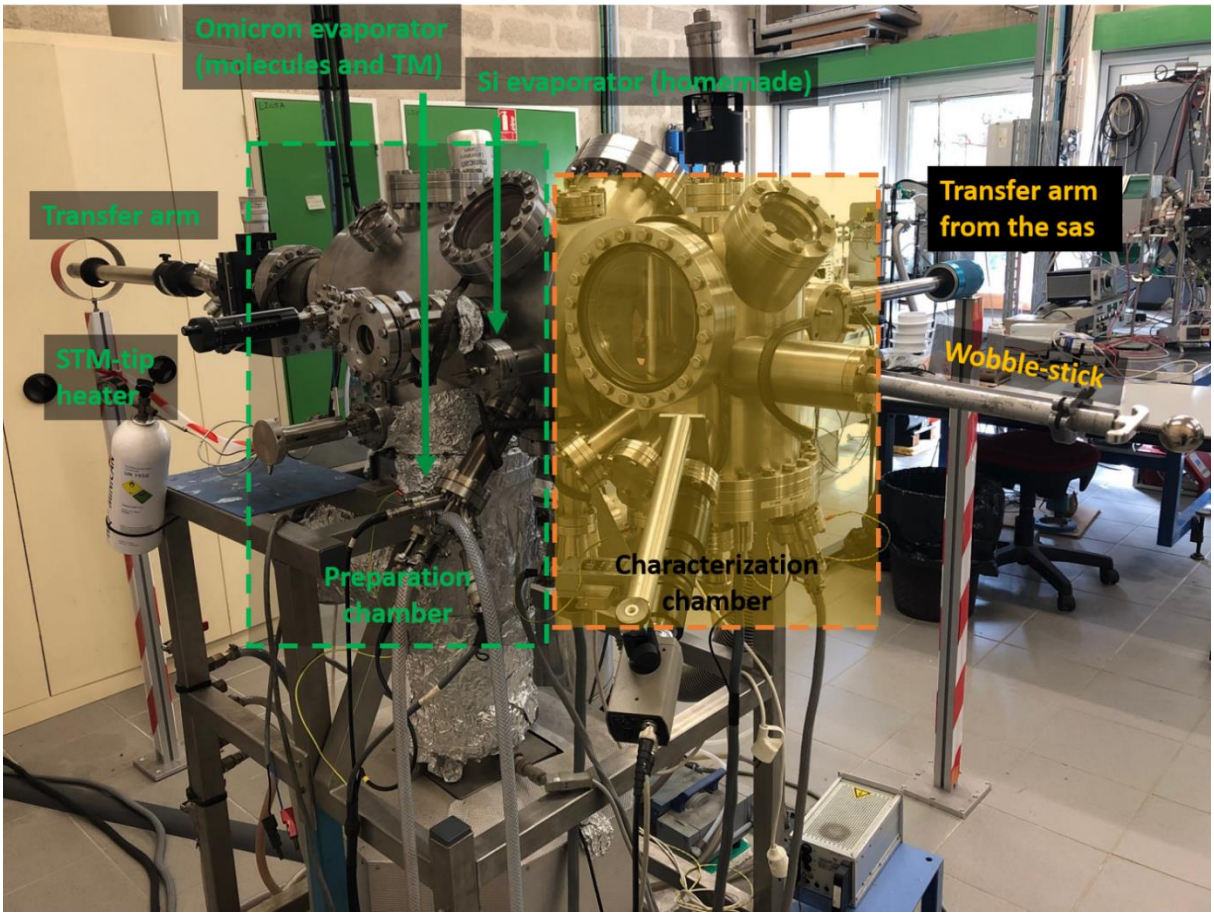

Figure 28: Photo of the experimental set-up mostly used during my thesis at CINaM.

Hereafter, I describe the principles of STM and XMCD techniques.

II- Scanning tunneling microscopy (STM)

STM is a very powerful experimental tool because of its variety in functionalities. It gives an apparent topography of a solid conducting surface with atomic resolution, it can provide spectroscopic measurements on different type of elements (metals and semiconductors) and it can manipulate atoms. Experiments can be carried out at different temperatures, ranging from 4 K to 1000 K and in different environment (air, liquid, UHV). This technique was invented and developed by Gerd Binnig and Heinrich Rohrer[116,117] at IBM laboratories in Zurich in the eighties. They were awarded the Nobel Prize in Physics in 1986. This technique is the first among the near-field microscopies (STM, atomic force microscopy (AFM), near-field scanning optical microscopy (NSOM), …) known nowadays.

i- STM set-up

As mentioned before, once the evaporation is finished, the sample is transferred to the characterization stage to study the surface morphology. The main characterization technique is a VT-STM or LT-STM, both controlled by the MATRIX software.

Our VT-STM can operate in a wide temperature range (300 K-1000 K). The sample is heated by direct current heating or through the heating of a pyrolytic boron nitride (PBN) element integrated in the sample holder. The LT-STM operates at 77 K for a N_2 flow or 4 K for a He flow. The STM technique is highly sensitive to vibrations, and isolation from internal and external vibrations is a necessity in order to achieve high-resolution images below nanometric scale. Vibrations can be electrical or mechanical and can be directly seen in STM images. Therefore, the STM is stabilized by springs and by an eddy current damping system. When a non-magnetic conductive material is put in a time-varying magnetic field, eddy currents are formed in the material. These currents generate a magnetic field in opposite direction to the applied one, inducing a force which attenuates the vibrations of the system.

The STM tip is mounted on a 3 axes piezoelectric drive called 'piezoelectric motor', which is responsible of its macroscopic displacement. The tip is scanned over the sample surface using a single piezoelectric tube scanner with a maximum scan range of (12 µm x 12 µm) and a z-displacement of about 1.5 µm. Upon applying a voltage, the piezoelectric transducers expand or contract, moving the tip on the surface with a sensitivity of ~10 pm. The displacement of the STM tip is controlled by the MATRIX software. All the STM data presented in the manuscript have been processed using the Gwyddion software.[118]

ii- Principle of STM

- Quantum tunneling and tunneling current

The tunneling effect is a consequence of quantum mechanics. If we consider two metals separated by an insulating material, the isolator acts as potential barrier that prevents the electron to pass from the first metal to the second one. When the distance between these two metals is sufficiently small which means the thickness of the insulator is sufficiently thin (few Å), there is a probability that an electron passes through it by tunneling effect.

More details about the quantum tunneling is discussed in this section. If we consider the simplest model - the 1D potential rectangular barrier - quantum mechanics calculations show that a particle of energy E has non-zero probability to pass through a barrier of energy U with U>E and with a thickness d, as shown in Figure 29.

The solution of the Schrödinger time-independent equation for a plane wave hitting the barrier can provide the transmission coefficient of the particle:

$$H\,\psi_k(x) = E\psi_k(x)$$

$$\text{with}\quad \psi_k(x) = \begin{cases} Ae^{ikx} + Be^{-ikx}, & x < 0 \\ Ce^{ik'x} + De^{-ik'x}, & 0 < x < d \\ Fe^{ikx} & x > d \end{cases} \qquad (2\text{-}1)$$

k and k' are the wave vectors, with

$$k: \frac{(2mE)^{1/2}}{\hbar} \;\; ; \;\; k': \frac{(2m(E-U_0))^{1/2}}{\hbar}$$

and the barrier $U(x) = \begin{cases} 0, & x < 0 \; and \; x > d \\ U, & 0 < x < d \end{cases}$ (2-2)

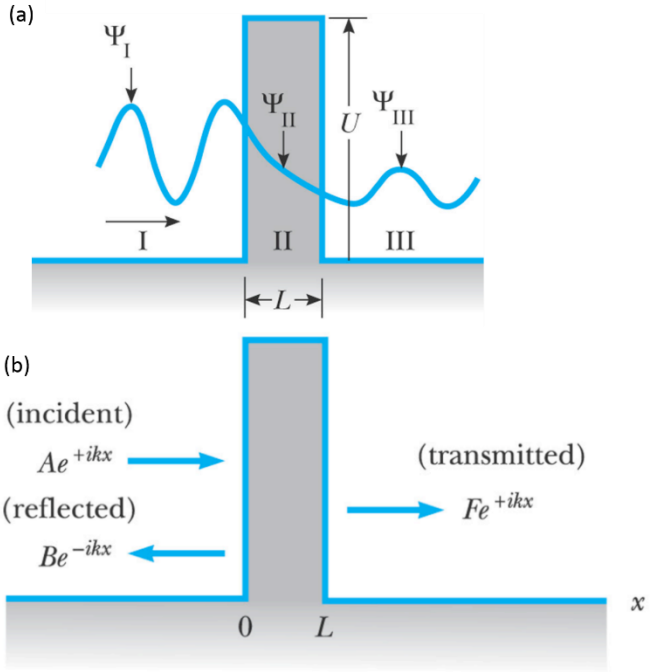

Figure 29: Representation of the wavefunction of a particle hitting a rectangular barrier of height U and width L. (L=d for our calculations). Illustration reproduced from 2005 Brooks/Cole – Thomson.

In order to determine the coefficients A, B, C, D, F, the continuity equations for the wave functions and their first derivative at the points x=0 and x=d are imposed.

The solution gives a transmission coefficient, defined as the statistical fraction of electrons transmitted through the barrier:

$$T_k(E,d) = [\,1 + (k\kappa)^2 \sinh^2(\kappa d)]^{-1} \quad (2\text{-}3)$$

where $\kappa = \frac{(2m(U_0-E))^{1/2}}{\hbar}$

The interesting case is obtained for κd >>1, which means for high attenuating barriers, the equation reduces to:

$$T_k(E,d) \xrightarrow{\kappa d >> 1} \frac{4}{(k\kappa)^2} e^{-2\kappa d} \quad (2\text{-}4)$$

This exponential relation between the transmission coefficient and the distance is extremely important for the STM.

In our case, we consider two metallic electrodes close to each other. The electrons are confined on the surface of the metals. A potential barrier of few eV between these two electrodes

is present (for metals the work function ∅ is of the order of 4 eV)[119]. The wave function of the electrons at the fermi level extends outside the metals for a distance of few Å (the inverse of the characteristic penetration length is k: $\frac{(2m\emptyset)^{1/2}}{\hbar}$). When the two electrodes are close enough, the wave functions of the fermi electrons overlaps and thus there is a non-zero probability for electrons to cross the potential barrier. It is possible to obtain a current between these two electrodes if we applied a voltage V is applied. This current is due to tunneling effect.

For low voltage applied and for T= 0K, Simmons[120] stressed the tunneling current to be:

$$I_t = \frac{e^2}{\hbar}\frac{k}{4\pi^2 d} \times V_t \times e^{-2kd} \quad (2\text{-}5)$$

where $V_t << \emptyset$ with V_t : tunneling voltage; ∅ the work function of the electrodes; d: distance between the two electrodes.

This exponential dependence of the current I_t with the distance d is fundamental for STM. For a variation of 1 Å, the current varies of a decade. The two electrodes mentioned before are replaced by the STM tip and the sample which are necessary conductive.

- **Interpretation of the atomic resolution**

To interpret the atomic resolution obtained in STM images, J. Tersoff and D.R. Hamann proposed a model where the tunneling current is directly linked to the local density of states of the surface sample at the Fermi level. [121,122] The authors proposed a spherical model for the tip with radius R_0, which center is located at $\vec{r}_0$ and described by a single s-orbital wavefunction. In this model the STM measurements carries information only about the surface sample. In the conditions of low voltages and low temperatures the current is stressed as:

$$I_t \propto V_t \rho_t(E_F)\, \rho_s(E_F, \vec{r}_0) \quad (2\text{-}6)$$

where V_t is the bias voltage, $\rho_t(E_F)$ the density of states of the tip at the Fermi level, $\rho_s(E_F, \vec{r}_0)$ the local density of states of the surface at the Fermi level and at $\vec{r}_0$.

In this model, the tunneling current is thus directly associated to the local density of states of the surface sample at the Fermi level. It has to be underlined that the Tersoff Hamann approach is widely used to calculate simulated constant-height STM images.

N.D. Lang[123] has extended the model of J. Tersoff and D.R. Hamann to higher bias voltage and proposed the following expression:

$$I_t \propto \int_{E_F}^{E_F+eV_t} \rho_t(E)\, \rho_s(E - eV_t, \vec{r}_0)\; T(E, V_t)\, \mathrm{dE} \quad (2\text{-}7)$$

where $T(E, V_t)$ is the transmittance of the tunnel barrier, strongly increasing with E.

The tunneling current can thus be simply interpreted as the sum of currents associated with energy states in the interval $[E_F, E_F + eV_t]$, weighted by the transmittance of the barrier.

Moreover, the author demonstrated that the variation of $(\frac{\partial I}{\partial V})/(\frac{I}{V})_{V_t}$ is proportional to the local density of states of the surface at eV_t, which opened a new function of the STM which is the spectroscopy of local density of states and thus defines the electronic structure of materials.

iii- STM functioning

In STM characterization, the STM tip has to be approached very close to the surface of the sample (few Å). This approach is made in two steps. The first approach of the STM tip is done manually (by the user) with the piezoelectric motor, to a distance relatively small. A second approach is done by the piezoelectric transducers controlled by a feedback loop to reach the distance for which the tunneling current is established. The current tunnel as well as the applied voltage are chosen by the user. The STM provides a real space image of a surface by applying a voltage difference between the sample and a metallic tip, which is scanned over the sample surface. For the constant current acquisition mode, used during my PhD work, the tunneling current is held at a chosen constant value (I_{set}) and the the tip-sample distance is adjusted by the feedback loop (see Figure 30). The voltage needed to adjust the tip-sample distance is recorded for each point scanned and it is then converted in an apparent height z. The 2D map obtained in this way constitutes the STM image. The feedback loop response can be adjusted by tuning its gain. The user has the access to adjust the gain accordingly to the experiment. In order to get clear STM images, an optimization of the gain value is needed; high-frequency oscillation of the scan can be created by high gain values, whereas, the crash of the tip can be caused by a low gain value. In addition, the user has access to set other parameters such as the size of the image, the number of points scanned and the scanning speed.

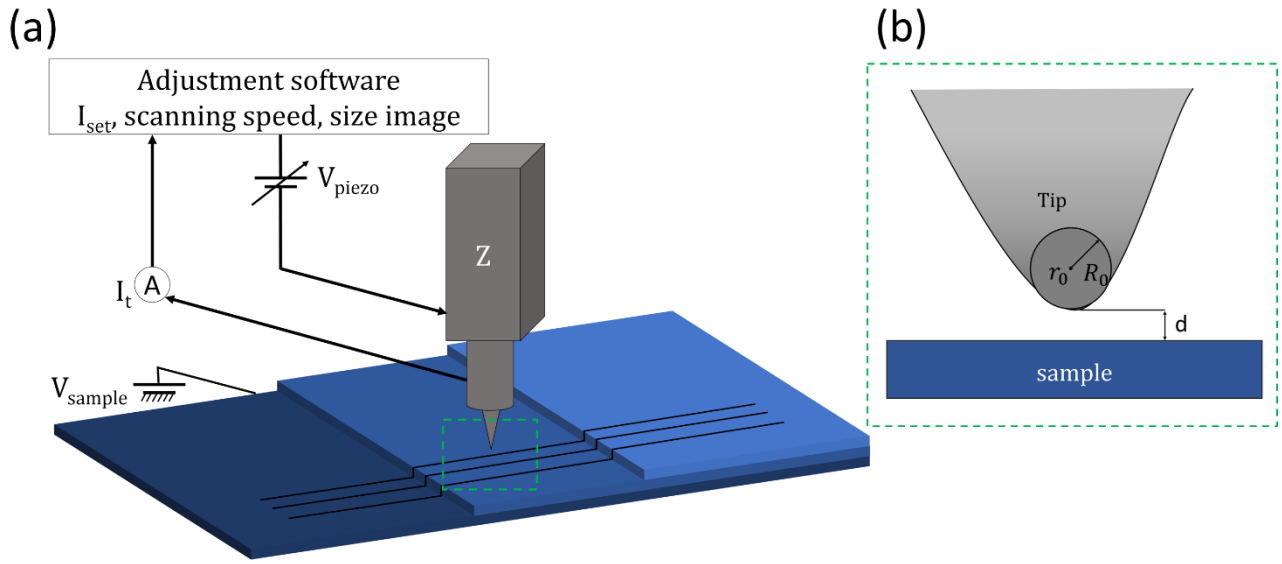

Figure 30: a) Schematic representation of the functioning of the STM. For each point the voltage needed to the z-piezodrive to maintain the tip at the distance for which $I_t = I_{set}$ is recorded; I_t and I_{set} are respectively the tunneling current and the current requested by the user. b) schematic representation of the tip in Tersoff-Hamman model. Spherical-head tip with a radius of R_0.

iv- STM-tip preparation

The lateral resolution depends drastically on the radius of the tip[122]. To obtain STM images with atomic resolution, it is thus crucial to have atomically sharp tips. During my PhD thesis, I have fabricated STM tips by chemical etching, which is an efficient way to produce highly sharp tip. A

rod of W (0.3 mm in diameter – 5 mm in length) is installed on a tip holder. This piece of rod is then half-dipped in a 2 M solution of NaOH. The set-up is shown in Figure 31(a). A bias voltage is applied between the tip and the solution via an electrode plunged in the solution. The induced current launches the electrochemical attack of the rod and causes its dissolution. The etching takes place at the air-solution interface, where a meniscus is formed around the tip. Since the rate of the reaction is slower at the top of the meniscus than at the bottom, a necking effect occurs, until the section of the rod at the interface is thin enough, which eventually results in the detachment of the dipped part of the tip. As the tip is sharpest at the moment of the drop-off, the tip and the counter-electrode are connected to a controller which monitors the current between the anode and the cathode in order to quickly switch off the voltage when a sudden drop in current is detected. Once the etching is finished, the tip is cleaned with water and ethanol to stop the reaction and eliminate the residues left by the process.

Then the tip is directly introduced in the UHV chamber via the load lock. However, it is known that a layer of oxide is formed on the tip and other contaminants which cannot be removed by rinsing still exist on the tip. Therefore, one more cleaning step have to be done in the UHV chamber. A direct current heating of the tip is used to remove the thin oxide layer and other contaminants. This system consists in a Ta rod that can be translated inside the chamber to be in direct contact with the tip. The current between the tip and Ta wire is controlled by a power supply. A current ranging from 4 to 6 A is needed to heat up the tip to a temperature of 1270 K. At this temperature, the oxide layer WO_3 is desorbed according to[124]:

$$2WO_3 + W \rightarrow 3WO_2 \qquad (2\text{-}8)$$

The heating of the tip has also other advantages: it can heal defects in the crystallographic structure of the tip. Usually, we heat the tip at 5-6 A for 30 s, while observing the pressure which should not exceed 10^{-8} Torr.

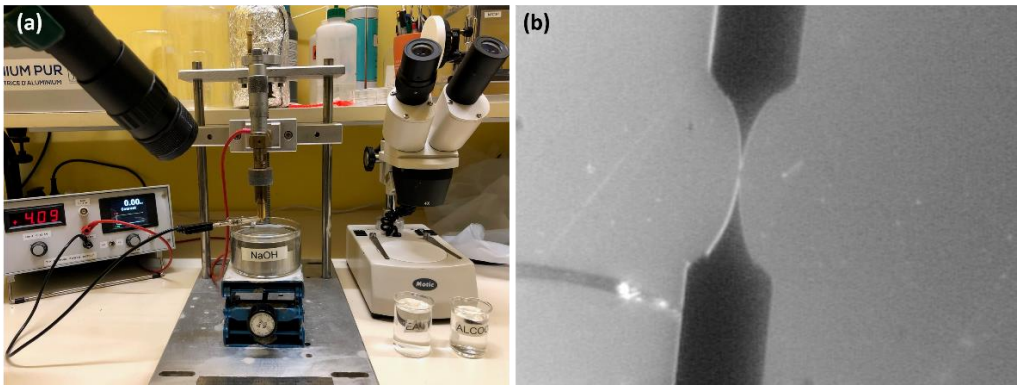

Figure 31: a) set-up of the STM tip fabrication at CINaM. b) Very sharp STM tip inserted on the STM stage and approached to a sample. The diameter of the W rod is 0.3 mm.

In the next section, I introduce the second characterization technique – XMCD – used to study the magnetic properties of the grown nanostructures.

III- X-ray absorption spectroscopy (XAS) and x-ray magnetic circular dichroism (XMCD)

In this section, I present a brief introduction to the experimental techniques that have been used to measure the magnetic properties of Co nanolines studied in the framework of my PhD thesis. The x-ray absorption spectroscopy (XAS) and x-ray magnetic circular dichroism (XMCD) are element specific techniques. Their extreme sensitivity allows to determine the details of the electronic and magnetic structures of nanoparticles made of few atoms down to single atoms. The XMCD spectra is the difference between two x-ray absorption polarized spectra, one with left and the second with right circular polarized x-rays. XMCD probes the magnetic moment of individual atoms thanks to the chemical and orbital selectivity of x-ray absorption and can separate the orbital and spin contributions to the total magnetic moment of the absorbing atom.

i- Principle of XAS.

x-rays were discovered in 1895 by Röntgen in Wurzburg. In 1913, de Broglie reported the observation of an x-ray absorption spectrum[125,126]. However, the success story of XAS had to wait until the 1980s, when intense, monochromatized x-rays became available at synchrotron facilities. Since then, XAS has been applied to answer a multitude of questions[125,127,128]. It can be applied to solid-state samples as well as small particles, molecular complexes, gases or liquid. XAS is a core level spectroscopy that is element specific and is considered as surface sensitive technique in the soft x-ray range (300 to 3000 eV) due to the detection mode that is usually the Total Electron Yield (TEY). The chemical sensitivity of XAS is obtained by tuning the incident x-ray photon energy from the core to valence transition energy of a specific element

When Röntgen discovered x-rays in 1895, he characterized this "new kind of rays" primarily by the absorption in solids. He already pointed out that the thickness as well as the density of an absorber determine the magnitude of absorption. Concerning the absorber thickness, x-ray absorption follows the Bouguer-Lambert-Beer law, as is the case for all electromagnetic waves. It states that the decrease of intensity I of a radiation that propagates along the z-direction in a medium is proportional to the incoming intensity,

$$dI(E,z) = -\mu(E)\, I(E,z)dz \tag{2-9}$$

Equivalently, the z-dependence of the intensity can be formulated as exponential law,

$$I(E,z) = I_0 e^{-\mu(E)z} \tag{2-10}$$

where μ(E) is the linear photo-absorption coefficient of the sample, I_0 is the incident intensity and I is the intensity measured after absorption. μ(E) is connected to a characteristic length scale, the x-ray penetration length l= 1/μ(E).

At low x-rays energy, the media are generally not transparent so that the absorption coefficient is not directly measured in the transmission mode and one has to detect a phenomenon that is expected to be proportional to the absorption coefficient. For energies below 20 keV, photoelectric effect is the dominant process compared to both elastic Rayleigh scattering and inelastic Compton scattering.[129] When an x-ray photon with energy E= $\hbar\omega$ is absorbed, a core-level electron with binding energy E_i in the initial state $|i\rangle$ is excited to an empty level $|f\rangle$ above the Fermi level with energy $E_f = E_i + E$. Therefore, XAS probes the empty states of the absorbing

atom. The x-ray absorption cross-section is defined as the number of photons absorbed per atom divided by the number of incident photons per unit area and hence has the dimension [length^2/atom].[130] The photoabsorption coefficient is proportional to the absorption cross section.

In the electric dipole approximation, the interaction Hamiltonian is reduced to $\hat{\varepsilon}.\vec{r}$ and the transition probability per unit time is given by the 'Fermi's golden rule':

$$\sigma(\hbar w) = 4\pi^2 \alpha\, \hbar w \sum_{i,f} \frac{1}{d_i} |\langle f|\hat{\varepsilon}.\vec{r}|i\rangle|^2 \delta(E_f - E_i - \hbar w) \qquad (2\text{-}11)$$

where α is the fine structure constant, $\hbar w$ is the photon energy, $|i\rangle$ and $|f\rangle$ are multi-electronic wavefunctions for the initial and the final state, respectively, d_i is the degeneracy of the multi-electronic ground state, $\hat{\varepsilon}$ is the photon polarization vector, $\vec{r}$ is the integration variable, E_i and E_f energies associated to wavefunctions, $\delta(E_f - E_i - \hbar w)$ is the Dirac distribution that ensures energy conversation and the sum $\sum_{i,f}$ extends over all the populated terms of the initial state and all the terms of the final state configuration.

When the x-ray energy is close to the binding energy of a core-level, a sharp variation of the absorption coefficient is observed as a function of the x-ray energy, that is known as the absorption edge. The characteristic edge jumps are the result of the consecutive excitation of core levels. Core level binding energies are specific for each atom and the absorption edges are labeled as K, L_1, $L_{2,3}$, M_1, $M_{2,3}$, or $M_{4,5}$ edges when the core level is present in the $|1s\rangle$, $|2s\rangle$, $|2p\rangle$, $|3s\rangle$, $|3p\rangle$ or $|3d\rangle$, respectively. The transition matrix elements $|\langle f|\hat{\varepsilon}.\vec{r}|i\rangle|^2$ characterize the absorption coefficient if the initial and the final state are well described. The initial states are atomic-like in character and thus easy to describe. But the final state description is in general difficult. In photoabsorption, effects such as chemical shift, splitting due to spin-orbit coupling, multiplet interactions due to Coulomb repulsions occur and leave their signatures on the XAS spectrum. Thus, valuable information about the electronic structures or the site-symmetry can be extracted from XAS.

Selection rules

For XAS, the transitions in the atom shells obeys the electric dipole selection rules. After long calculations using the Hamiltonian mentioned before, the selection rules allow transitions for orbital momentum quantum number *L* changes by unit, $\Delta L = \pm 1$ and conserve the spin $\Delta s = 0$, the spin is not affected by the dipole operator and is thus conserved during the transition. In addition to the selection rules involving *l*, other selection rules involve the magnetic quantum number *m*. Stohr and Seigmann calculations gives, for linear polarized light the selection rule $\Delta m_L = 0$, for left circularly polarized light $\Delta m_L = -1$ and for right circularly polarized light $\Delta m_L = +1$.

For the quadrupole electric transitions, the selection rules are $\Delta L = 0, \pm 2$. For *3d* transition elements, the electric quadrupole transitions are negligible at $L_{2,3}$ edges and often detectable at K edges although they are found between 10 and 100 times weaker than the electric dipole transitions.

ii- Polarization of x-ray

The transition matrix element in the dipole approximation as given by equation (2-11) depends on the polarization vector of the x-rays. Hence, the absorption signal can be significantly influenced by the details of light polarization. For instance, this is reflected by the Δm_L selection rule mentioned above which depends on the light polarization. The light helicity also influences the oscillator strengths of the different transitions in a spectrum. This leads to the observation of dichroism, which denotes a finite difference in two absorption spectra obtained for different polarization states. A prerequisite for the observability of this effect is the presence of anisotropy in the electronic states that are involved in the transition. In the central field of an atom, the spatial distribution of the charge is closely connected to angular momenta, which are related to magnetic moments. Hence, dichroism occurs for spatial anisotropy as well as for the presence of magnetic polarization.

The difference in absorption of left and right circular polarized light is closely connected to the rotation of the polarization direction of linear polarized light. For magnetic materials, such rotation has been known since the mid of the 19th century as the Faraday and Kerr effects in transmission and reflection, respectively. Hence, it comes as no surprise that a magnetized sample also shows circular dichroism.

Regarding XAS, magnetic circular dichroism becomes apparent at the resonant edges. This has been theoretically predicted in 1975 by Erskine and Stern[131], who transferred considerations on magneto-optical properties to the x-ray region, more precisely to the $M_{2,3}$ edges of Ni. The first experimental realization was achieved in 1987 by Schutz *et al.*[132], who detected a small but unambiguous dichroic signal at the K edge of Fe. The effect is nowadays referred to x-ray magnetic circular dichroism (XMCD).

One year prior to the pioneering experimental work on XMCD in the hard x-ray region, magnetic linear dichroism was experimentally discovered in XAS by van der Laan *et al.* at the $M_{4,5}$ edges of a rare earth material[133]. The same group had theoretically proposed the XMLD effect in 1985[134]. Nowadays, XMCD and XMLD are understood on the same basis. The choice between the experimental techniques depends on the material under investigation. For ferro-, ferri-and paramagnetic samples, XMCD is usually preferred. In general, the XMCD signal vanishes in antiferromagnets and XMLD is thus used.

iii- Principle of XMCD

For XMCD, the dichroism refers to the polarization dependent absorption of a material, i.e. the manifestation that the optical response of a material depends upon the relative orientation of the polarization direction of light with respect to the symmetry axes of the material. It arises due to the charge or spin anisotropy in the system. The charge anisotropy (crystal field) causes the 'natural dichroism' like x-ray natural linear dichroism (XNLD) and x-ray natural circular dichroism (XNCD) whereas, x-ray magnetic linear dichroism (XMLD) and X-ray magnetic circular dichroism (XMCD) occur due to the anisotropy spin distribution. When a sample carries a net magnetic moment, the absorption with left polarized x-rays is no more equal to the absorption with right polarized x-rays: this is the origin of XMCD. The difference between the spectra measured with left and right circular polarized light is called x-ray magnetic circular dichroism. Its analysis yields valuable and quantitative information on element- and specific magnetic moments of the material under investigation.

At $L_{2,3}$ edges, a strong XMCD effect was first reported in ferromagnetic nickel by Chen *et al.*[135] The effect was ~2 orders of magnitude larger than those at the K edges of transition metals[132]. The principle of the XMCD is explained by a two-step model, presented in Figure 32. In the first step, left (right) circularly polarized X-rays excite more spin-up (spin down) electrons from the $2p_{3/2}$. In the second step, the final states determined by the selection rules act as spin detector. The quantization axis of the detector is given by the magnetization direction. The magnetization must be aligned with the photon wave vector to maximize the dichroic effect.

The XMCD signal is the difference Δσ between the two absorption cross sections for left and right polarized x-ray beam defined as, for B parallel the propagation vector,

$$\Delta\sigma = \sigma^{+}(B) - \sigma^{-}(B) = \sigma_{right}(B) - \sigma_{left}(B) \qquad (2\text{-}12)$$

The signs '+' or '-' in σ^{+} or σ^{-} are associated to x-ray helicity with '+' for right and '-' for left polarized x-ray.

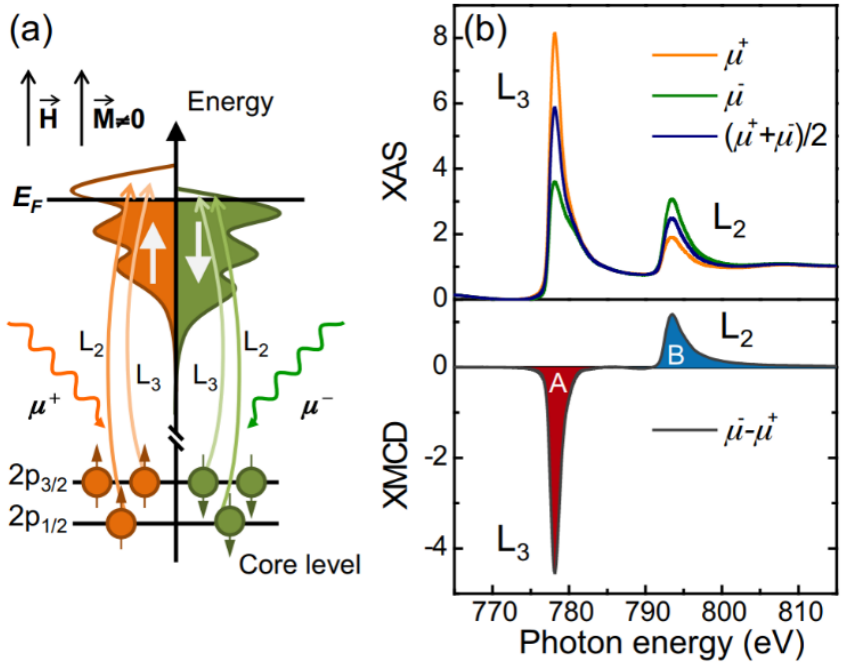

Figure 32: (a) illustration of the two-step model for XMCD, in the first step, spin-polarized photoelectrons are generated. In a second step, they are 'detected' by the spin-split final state. (b) XAS at the Co $L_{2,3}$ for right (μ^+) and left (μ^-) circular polarization together with the difference spectrum: the XMCD. [Van der Laan et al. ref: 143]

A second way to obtain XMCD spectra is by taking the difference of two XAS spectra for the same polarization state of incoming x-rays but with two magnetic field direction, parallel and antiparallel to the propagation vector. The XMCD signal in both cases remains the same.

One of the important aspect of XMCD is the ability of measuring the element-specific magnetization curves. In this method, the intensity of dichroic signal is recorded at a given x-ray energy and the external magnetic field is varied. When the XMCD signal is proportional to the magnetization of the absorbing atom, the XMCD detected magnetization curve is specific of the magnetization of the absorbing atom and can be compared to conventional magnetization curves such as those measured by SQUID or VSM magnetometers. It has to be underlined that, on the

contrary to SQUID and VSM, XMCD measured in the total electron yield mode is inherently surface sensitive, due to the limited escape depth of low-energy photoelectrons.

In addition to the qualitative understanding of the mechanisms behind the XMCD effect, the considerations made so far can be developed further to connect the integrated XMCD signal to the expectation values of the magnetic moments of the valence shell in the initial state. This is done by the so-called orbital and spin moment sum rules. While the theoretical derivation of the magnetic sum rules is, in a general way, sophisticated and will thus not be reproduced here, their application and the resulting formulae are rather simple. In Figure 33, the integrals p, q and r are shown by dashed lines and are used to determine the spin and orbital moments from the sum rules according to Thole *et al.*[136] and Carra *et al.*[137], and following the procedure of Chen *et al.*[138] , for the $L_{2,3}$ edges:

$$m_S = -\frac{6p-4q}{r}\, n_h \qquad\qquad m_L = -\frac{4q}{3r}\, n_h \tag{2-13}$$

where $n_h = 10 - n_{3d}$ is the number of holes in the 3d band.

In our case, we consider for the cobalt nanolines $n_h = 2.5$.[139,140] Moreover, the L_3 and L_2 edges have to be well separated to ensure correct integration on each edge.

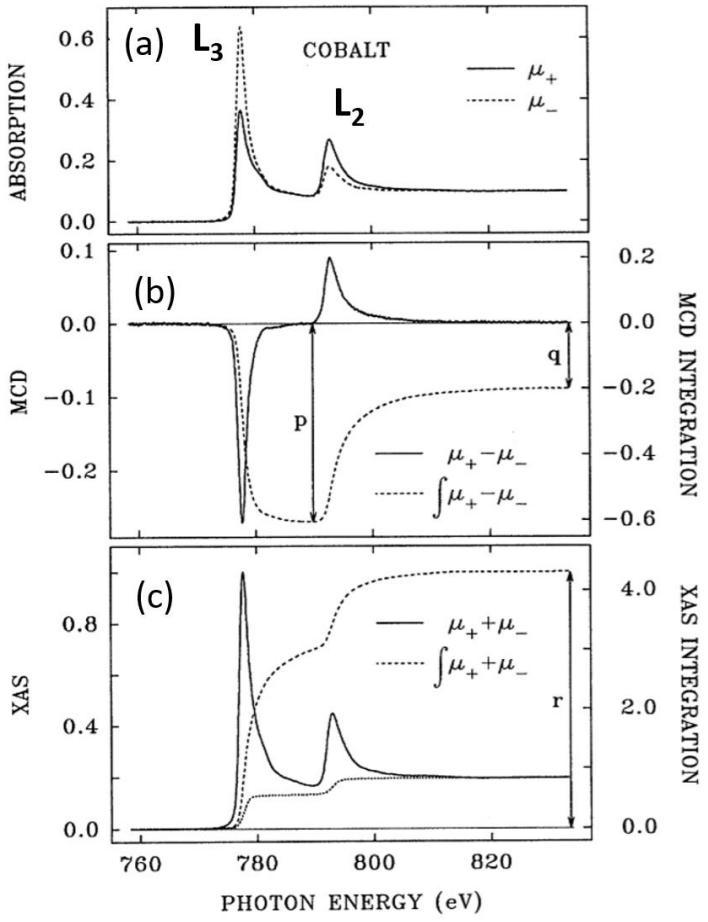

Figure 33: $L_{2,3}$ edge XAS and XMCD spectra for cobalt: (a)are the XAS absorption spectra; (b) and (c) are the XMCD and summed XAS spectra and their integrations calculated from the spectra shown in (a). p and q shown in (b) and r shown in (c) are the three integrals needed in the sum-rule analysis. [Chen et al. 1995 ref: 137]

For different absorption edges, the sum rules exhibit different numerical factors, whereas the general structure of the equations is always the same. The orbital moment is proportional to the integral of the total XMCD spectrum of a certain transition. The spin moment is obtained from the difference of the integrated signals of two separated, spin-orbit split edges. This reflects that the orbital polarization of the excited core electron has the same sign for the two edges, while the signs are different for the spin polarization.

The sum rules yield the magnetic moment per atom. Results of the application of the sum rules to experimental data in the present thesis are given in units of Bohr magnetons and per atom (μ_B/at) and will be presented in chapter 5.

iv- XAS-XMCD set-up

For XMCD measurements, the key ingredients are: (1) a source of circularly polarized X-rays, (2) a monochromator and optics (beamline), (3) a means for producing a magnetized sample, (4) an x-ray detection system. As XMCD measurements require intense and monochromatized x-rays, set-ups have been developed on beamlines of synchrotron facilities.

In the framework of this thesis work, XMCD was used to study the magnetic properties of Co nanolines. The experiments were carried out in 2015 at the DEIMOS (Dichroism Experimental Installation for Magneto-Optical Spectroscopy) beamline at of the French national synchrotron facility (SOLEIL). Therefore, the set-up description, based on the publication of Ohresser *et al.*[141], will be focused on the DEIMOS beamline implementation. Figure 34 illustrates the light trajectory from the source via grazing mirrors to the sample.

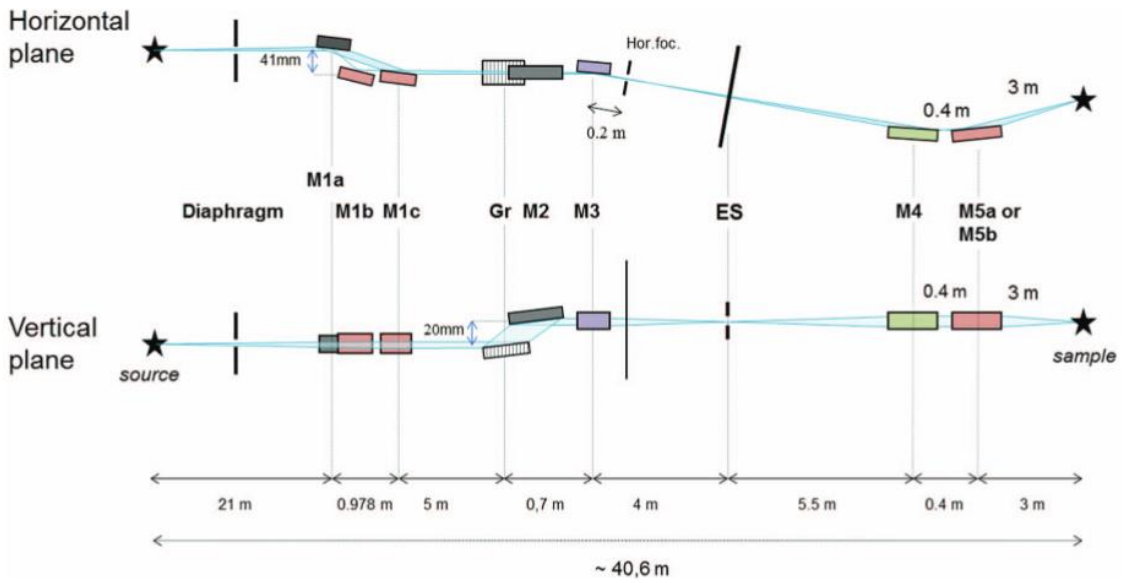

Figure 34: Schematic layout of the experimental XMCD setup at DEIMOS beamline. [Ohresser et al. 2014 ref: 141]

1) Sources

There are several sources such as bend magnets, insertion of devices, soft x-rays beamlines, hard X-rays beamlines and quarter wave plates.

The synchrotron SOLEIL uses third-generation light sources which are built around insertion devices that produce very high intensity x-rays. These consist of periodic arrays of magnets, causing the electrons to oscillate around an otherwise straight trajectory. In a helical or elliptical polarization undulator (EPU) the magnetic field vector rotates as the electron passes through the device, resulting in a spiral trajectory about the central axis. The most popular design is the 'Apple-II type' undulator. Fast polarization switching with frequencies of around 10 Hz has been achieved using two tandem Apple-II type EPUs with in between a fast kicker system to alternate the beam so that the spectator receives the beam only from one undulator at the time. DEIMOS beamlines are equipped by two undulators: an Apple-II HU-52 undulator and an EMPHU-65 (ElectroMagnet/Permanent magnet Helical Undulator). The Apple II was chosen in order to reach all polarizations and the EMPHU-65 was chosen to enhance its sensitivity. [141]

2) Optics and monochromators

The x-rays produced at the bending magnet or insertion devices pass down the beamline from the storage ring, toward the experimental station. The beam is reflected by grazing incidence mirrors, monochromatized, and focused in the optics hutch, before passing to the experimental chamber where it impinges onto the sample. There are two classes of monochromators, based on diffraction gratings or crystals. Both make use of the Bragg condition, $n.\lambda = 2d \sin(\theta)$, where d is either the line grating spacing or the crystal periodicity. From magnetic materials perspective, the Fe, Co, and Ni $L_{2,3}$ edges are of great interest, their dichroism was only first observed in 1990. This was primarily due to the poor accessibility of the soft x-ray range below 800 eV. Improvements in the performance of grating monochromators, especially the design of the double-headed Dragon, opened up the new territory of high resolution spectroscopy[142]. In a soft x-ray beamline, the mirrors and gratings are at a few degrees grazing incidence, so that the polarization is nearly completely preserved. The grating monochromator (usually a set of gratings) needs to have a sufficient energy resolution in the order of the core-hole lifetime (0.2–0.3 eV).

For instance, at DEIMOS, the beam is reflected to the sample by using several consecutive grazing incidence mirrors, as shown in Figure 34. The last optical object can modify the spot size of the beam on the sample. This light is monochromatized by a plane grating monochromator.

3) Magnet chambers

High magnetic fields can be obtained using a superconducting magnet. The split-coil design has a coil at each opposite site of the sample holder, and gives a positive or negative field along the x-ray beam direction. Magnetization switching can suffer from artefacts caused by magnetic history and hysteresis effect. Opposite magnetic fields can influence the electron yield detection differently due to space charge effects. This is usually seen in the hysteresis loops; large spikes appear while the switching of the magnetization. Nevertheless, it is often advantageous to measure the XMCD by switching the applied magnetic field at each photon energy data point. This eliminates the influence of beam drift and instabilities, as well as that it avoids errors due to backlash in the mechanics of the undulator and the monochromator.

4) System detection - end-station

To detect the response of the sample, there is three detection modes: (i) the transmission mode with a removable diode located at the back of the end-station chamber. [141,143] (ii) the total electron yield (TEY) and the fluorescence yield. In our work, we used the TEY detection mode. It consists on the strong secondary electron emission renders TEY as the preferred detection method in the soft X-ray region. The TEY can be measured either using a channeltron electron multiplier (CEM) or as the drain current flowing from ground to the sample to compensate the electron emission current. The TEY intensity is related to the x-ray absorption, μ as following:

$$I_{TEY}(w) = C\frac{\mu(w)L}{\mu(w)L+cos\theta} \quad (2\text{-}14)$$

where C is a constant and L is the electron escape depth, which is approximately constant over the region of the spectrum: L ~ 3–5 nm[144,145], θ is the angle between the x-ray wave vector and the surface of the sample. Note that at grazing incidence angle the spectra are more prone to saturation in contrary to normal incidence. Conversely, the saturation is minimized at normal incidence, in turn reduces the TEY. TEY detection shows a high surface sensitivity due to the short electron escape depth, which makes it rather sensitive to oxidation. Such oxidation effects in the XAS show up as extra features usually a few eV above the main peak, while the intensity of the XMCD is reduced when the oxidized atoms are non-magnetic. Therefore, samples prone to oxidation necessitate a special treatment, such as *in situ* preparation or alternatively the sample should be capped with a few nm thick layer of an inert material.[144] In the present study, the samples have prepared *in situ*, prior to XMCD measurements. It has to be noted that during the XAS/XMCD measurements performed in 2015, it was not possible to rotate the sample in the plane of its surface.

Finally, the end-station is connected to a set of UHV chambers, which allow the preparation of the sample and characterization via STM.

To conclude, experiments presented in my manuscript were conducted by means of STM and XMCD. Thus, in this chapter, I have presented in a first part the STM. The functioning and set-up were discussed, together with the contribution of the STM in the development of the experiments. In a second part, basic principles of XAS and XMCD were presented. The XAS-XMCD set-up was focused on the instruments of the DEIMOS beamline, as it was used for our measurements. The surface-sensitivity of the XMCD was highlighted.

In the next chapter, I will discuss the growth mechanisms of the Si NRs, which were used as a template to grow 1D nanostructures made of TMs (Fe, Co, Ni) and lanthanides (Ho).

Chapter 3

Nanoscale investigation of Si nanoribbon growth on Ag(110)

Contents

Chapter 3 79
Nanoscale investigation of Si nanoribbon growth on Ag(110) 79
I- Introduction 80
II- Ag(110) surface 81
III- Growth of Si nanoribbons (NRs) 81
1) Experimental methods 81
2) Statistical analysis of STM images 82
3) Growth description of the four types of Si NRs 82
4) Transverse linear density (TLD) of Si SNRs and Si DNRs 83
5) Temperature-dependent percentage of the four types of Si NRs 84
6) Transverse linear density (TLD) of the Si SNR and Si DNR islands 86
7) Thermal stability of the 5×2 superstructure 87
IV- Discussion 88
V- Conclusion 90

In this chapter, I present a detailed study of the growth mechanisms of the Si NRs. More specifically, a study as a function of temperature revealed kinetic limiting factors and activation energies for the growth of Si NRs. Finally, I present long-range ordered Si NRs which provide high potential to play the role of a template to grow 1D nanostructures.

I- Introduction

As presented in chapter 1, interest in the nanopatterning and functionalization of surfaces has risen in the last two decades due to their potential in guiding the growth of nanostructures and thus playing the role of templates. Kinetically controlled growth has proven to be an efficient way to achieve such templates by producing high densities of homogeneous nanostructures with controlled shape at the atomic scale. Moreover, investigation of their properties can be led by using either local (STM) or macroscopic integration, for instance GIXD probes. As already shown for Co and Mn nanolines[87,89], self-assembled silicon NRs grown on Ag(110) has guided the growth of 1D nanostructures at large scale. In addition, two species can be grown: Si single and double NRs (indicated hereafter as SNRs and DNRs) which can potentially provide two different templates.

Since the discovery in 2005 of the synthesis of Si NRs on Ag(110) upon Si deposition at RT, this system has proven to have intriguing properties. I summarize here the main results presented in chapter 1. Si SNRs, with a width of 0.8 nm, are randomly distributed on silver terraces and regularly spaced Si DNRs with a width of 1.6 nm are self-assembled in a (5×2) unit cell to form a 2D single-atom-thick Si layer, for Si deposition at RT and 460 K, respectively. A long debate concerning the atomic structure of these NRs began after the reported graphene-like electronic signature in 2010 measured by ARPES[67] and attributed to the silicene character of the Si NRs. In 2013, Bernard *et al.*[71] provided compelling evidence, by a combined STM-GIXD study, of an unexpected Ag(110) MR surface reconstruction associated with the release of Ag atoms induced by the Si NR growth. Recently, Prévot *et al.*[78] published a combined theoretical (DFT calculations) and experimental (STM, GIXD) study which definitively elucidates the atomic structure of the Si NRs, among the numerous models proposed in the literature[77]. The Si NRs correspond to an original Si phase composed of pentamer chains lying in the MR troughs of the reconstructed Ag surface.

While the structural studies of the Si NRs have solved their atomic configuration, few studies on the growth mechanisms have been lead to understand the interplay between the formation of the Si SNRs and DNRs and the MR reconstructed Ag surface. However, an investigation of the atomic scale processes involved is needed for several reasons: (i) to understand the growth mechanisms of the Si NRs at early stages and the role of the Si nanodots seen by STM[63,77,80], considered as the precursors for the formation of Si SNRs and (ii) to control the growth of the 3×2 and 5×2 Si superstructures mentioned in chapter 1. The control of such types of superstructures will help us to define new templates with different geometries (Si NR width and pitch of the 1D grating) to tune the configuration of the nanostructures grown on them.

Therefore, in this chapter, I present a nanoscale study of the Si NR growth in the submonolayer regime, based on statistical analysis of STM images.[146] I describe the behavior of four types of Si nanostructures and their assembly, as a function of the substrate temperature: isolated SNRs and isolated DNRs (indicated hereafter as 1D-SNRs and 1D-DNRs, respectively) and their respective 2D counterparts in the self-assembly regime (indicated hereafter as 2D-SNRs associated with the 3×2 superstructure and the 2D-DNRs associated with the 5×2 superstructure, respectively). I will show that our results strongly suggest that the transition from Si nanodot structure to NR structure is the limiting process for the growth of SNRs while the transition between SNR and DNR superstructures is driven by the MR reconstruction of the Ag(110) surface.

II- Ag(110) surface - 3x2 and 5x2 Si superstructures

The lattice parameters of the anisotropic Ag(110), showed in Figure 35, is $a_{Ag\perp}$=0.408 nm in the [001] direction, perpendicular to the Si NR axis and $a_{Ag//}$=0.289 nm in the [1$\bar{1}$0] direction, parallel to the Si NR axis.

The surface of the Ag(110) was prepared by repeated cycles of Ar^+ sputtering and annealing at 770 K, as described in chapter 2.

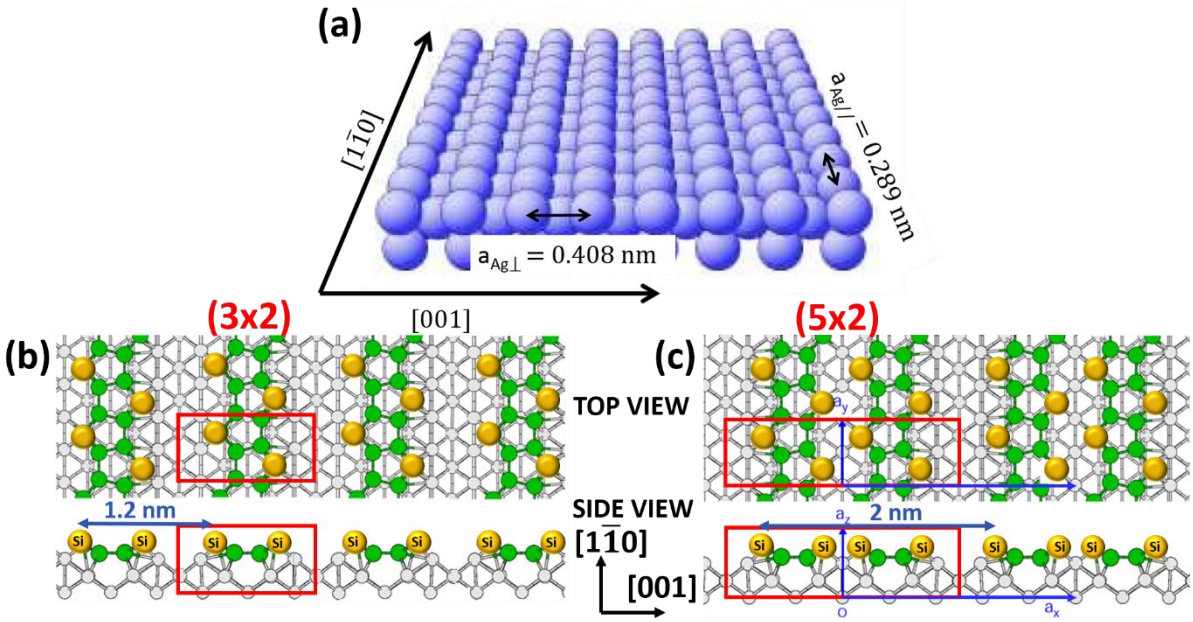

Figure 35: a) Representation of the Ag(110) surface. Deep channels along the [1$\bar{1}$0] direction can be seen. Ag(110) lattice parameters are indicated. b) Representation of the (3x2) superstructure composed of self-assembled Si SNRs. c) Representation of the (5x2) superstructure composed of self-assembled Si DNRs.

III- Growth of Si nanoribbons (NRs)

In this work, we have studied the growth of Si on Ag(110) as a function of the substrate temperature, from RT to 500 K, in the submonolayer regime.

1) Experimental methods

Si was evaporated from a direct current heated piece of silicon wafer kept at 1520 K onto the clean Ag(110) surface after preoutgassing at 1070 K. The clean Ag(110) sample was exposed to a Si flux at a constant deposition rate of 5.10^{-4} ML_{Si} per second. 1 ML_{Si} corresponds to the

Ag(110) surface atom density, which also equals the density of the perfect 3×2 superstructure completely covering the Ag(110) surface.

The experiments were focused on two low Si coverages (θ_{Si} ~ 0.22 and 0.54 ML_{Si}) to avoid coalescence of the Si NR islands. The reproducibility of the deposition of the home-made Si evaporator used is ~ ± 10 %. The substrate was heated at the rear side by radiation emitted by a commercial Scienta Omicron heater made of a W filament. The sample temperature during Si deposition was measured using a chromel-alumel thermocouple, spot welded very close to the Ag sample and calibrated prior to the set of experiments, using a heating power-substrate temperature relationship established with the thermocouple spot welded instead of the Ag sample. The accuracy of the temperature measurement is ± 10 K.

After Si deposition at substrate temperatures ranging from 300 K to 500 K, the surface was frozen down to RT, where no motion or modification of the Si NRs is observed. All STM images were obtained at RT in the constant current mode with sample voltages from -1.2 V to 0.7 V and tunneling current of ~300 pA.

2) Statistical analysis of STM images

The Si NR counting was performed from STM images with typical size (300×300) nm^2, insuring that SNRs and DNRs can be distinguished and the spacing between Si NRs can be measured. For each temperature, the statistical analysis has been performed on at least two STM images. The typical number of Si NRs in one STM image, counted along the direction perpendicular to the Si NRs, is ~70 SNRs at low temperature and ~35 DNRs at high temperature, for θ_{Si} ~ 0.22 ML_{Si}. For each STM image, several measurements of (i) the percentage of the different types of Si NRs formed and (ii) the transverse linear density (TLD) of Si NRs along the direction perpendicular to the NRs have been performed using line profiles, except for the higher growth temperatures (T > 420 K), where the length of the Si NRs was longer than the size of STM images (300 nm) and thus only one measurement was possible. The error bar of the Si NR density is ±10%, corresponding to the mean statistical variation observed, for a given temperature, between the different measurements made.

3) Growth description of the four types of Si NRs

As described in the literature[39,70], different configurations of Si flat NRs have been seen for a substrate temperature ranging from 300 K to 500 K . These configurations differ by the length, width and lateral arrangement of the Si NRs, depending on the growth temperature. The temperature dependence of the growth of Si on Ag(110) for a coverage of θ_{si} ~ 0.22 ML_{Si} has been studied by STM and is presented in Figure 36. At RT, as shown in Figure 36(a), 1D-SNRs are dominating the growth with a mean length of ~ 40 nm in the longitudinal [$1\bar{1}0$] direction and they are randomly distributed on the Ag(110) surface, in agreement with previous studies[71]. Si nanodots, precursor of Si NRs, are also visible at this temperature[63,77,80]. Upon Si deposition at 350 K, as illustrated in Figure 36(b), we notice the formation of longer SNRs with a length up to 300 nm along the [$1\bar{1}0$] direction. These SNRs start to agglomerate in the [001] direction. For higher temperature growth, at 390 K, we observe in Figure 36(c) small packs of 2D-SNRs locally

organized in a 3×2 superstructure distributed on the surface and the appearance of a new type of Si NRs, the 1D-DNRs. This 3×2 superstructure was rarely studied before. Finally, at 480 K, 2D-DNRs are formed and self-assembled in a 5×2 superstructure as shown in Figure 36(d), largely described in previous publications.[40,70,71]. High-resolution STM images have revealed that, at this growth temperature, the Si NRs present a very low density of atomic defects.

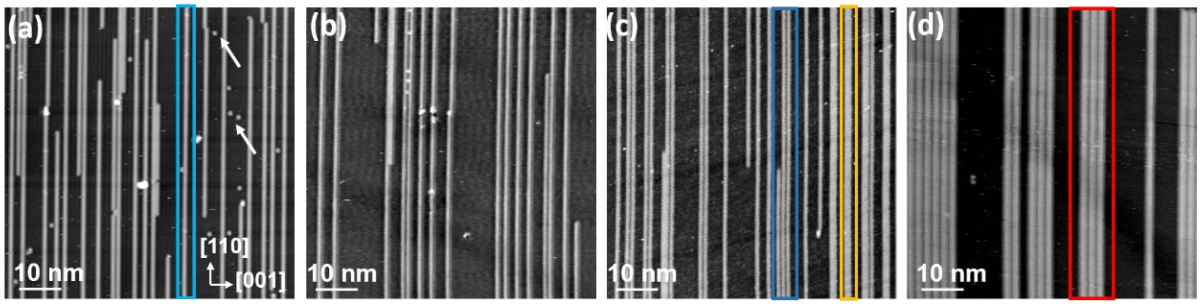

Figure 36: STM images ((70×70) nm2) of Si deposited on Ag(110) at four different substrate temperatures and nearly the same Si coverage ϑ_{Si} ~ 0.22 ML_{Si}, showing the formation of SNRs and DNRs : (a) RT, (b) 350 K, (c) 390 K and (d) 480 K. The four kinds of Si NRs are indicated by colored rectangles: 1D-SNRs (light blue in (a)),1D-DNRs (orange in (c), right side), 2D-SNRs (blue in (c), right middle part) and 2D-DNRs (red in (d)). In (a), the arrows indicate the formation of Si nanodots.

4) Transverse linear density (TLD) of Si SNRs and Si DNRs

Since the configurations of the Si NRs seen by STM differ essentially by their lateral ([001] direction) organization, we have focused our statistical analysis on the linear density of the Si NRs in the [001] direction (TLD). It is important to note that, here, the Si SNRs and DNRs are counted individually, without taking into account their eventual self-assembly. In Figures 37(a) and (b), we show the TLD of SNRs and DNRs for θ_{Si} ~ 0.22 ML_{Si} and θ_{Si} ~ 0.54 ML_{Si}, respectively. In these graphs, we can clearly see the transition from SNR to DNR regimes in the [370 K-440 K] temperature range. The non-immediate transition from SNRs to DNRs may indicate the competition between the formation of different types of Si NRs. The ratio between the TLD of SNRs and DNRs is ~2, within the error bars. This ratio is in agreement with the pentamer model showing that DNRs correspond to twin Si pentamer chains, by a lateral repetition of the motif of SNRs. This indicates that no other Si nanostructures are formed in this temperature range [300 K-500K].

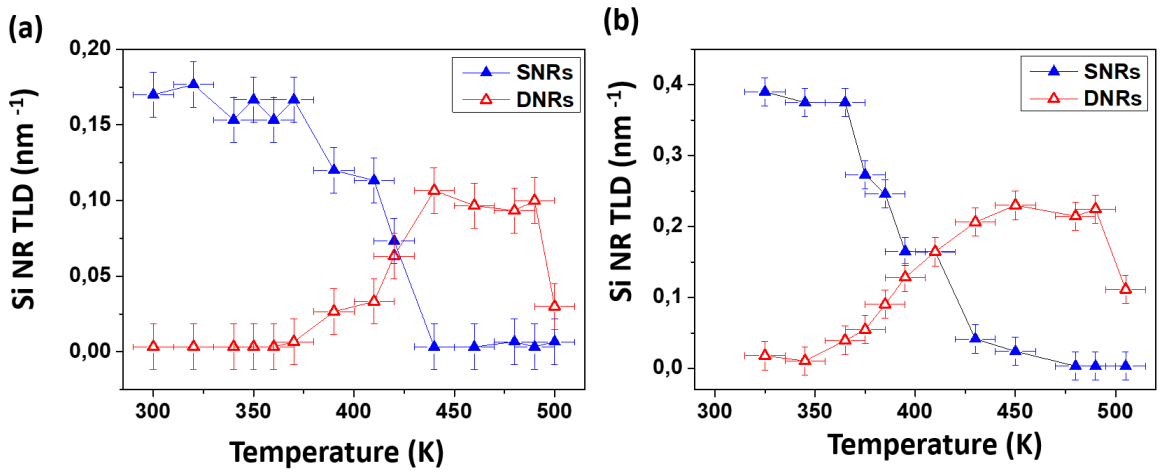

Figure 37: Transverse linear density (TLD) of Si NRs, perpendicular to the NRs (filled blue and open red triangles) as a function of the substrate temperature for $\theta_{Si} \sim 0.22$ ML_{Si} in (a) and $\theta_{Si} \sim 0.54$ ML_{Si} in (b).

5) Temperature-dependent percentage of the four types of Si NRs

To go further in the description of the growth mechanisms of the four types of Si NRs formed, I have plotted in Figure 38, for each substrate temperature, the percentage of each type of NRs: 1D-SNRs, 1D-DNRs and their 2D counterparts 2D-SNRs and 2D-DNRs self-assembled in 3×2 and 5×2 superstructures, respectively (even locally, when only two SNRs or DNRs are assembled). In the temperature range [300 K-370 K], the formation of 1D-SNRs is dominating while the percentage of 2D-SNRs is rising with the substrate temperature, which indicates the beginning of the agglomeration of the SNRs. At higher temperatures, [390 K-440 K], 2D-SNRs species are dominating with a slight increase in percentage of 1D-DNRs. Similar results concerning the formation of the 3×2 structure in this range of temperature were presented by S. Colonna *et al.*[70]. Their study by means of LEED showed that for silicon deposition at 430 K, broad diffraction spots associated with the ×3 periodicity in the [001] direction are observed, indicating the formation of a short-range 3×2 superstructure, in agreement with our STM observations. Above 440 K, we observed high abundance of 2D-DNRs with percentage higher than 70% to reach almost 95% at 490K, when the 2D-SNRs are no longer formed and the DNRs are assembled to form large domains of the 5×2 structure. The well-defined bright spots observed in LEED patterns[70] and the narrow diffraction peaks of GIXD spectra[71] indicate a large scale highly-ordered 5×2 superstructure.

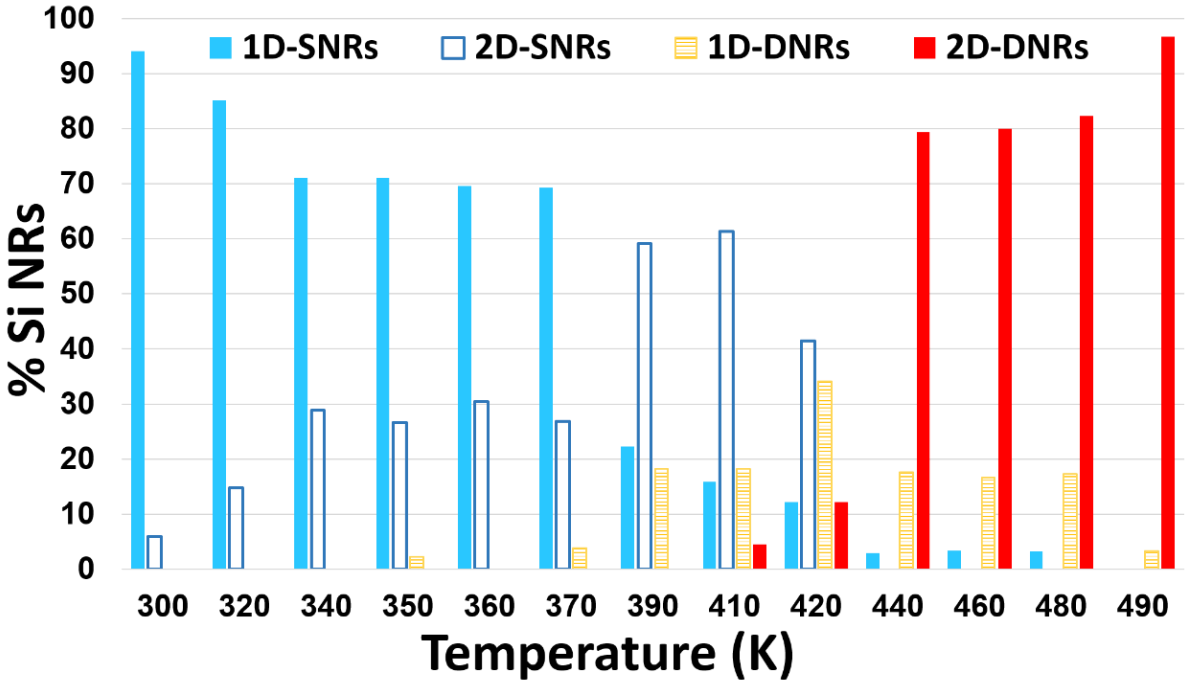

Figure 38: Percentages of 1D-NRs, 1D-DNRs, 2D-NRs and 2D-DNRs for θ_{Si} ~ 0.22 ML_{Si} and for each substrate temperature.

The morphology of the surface composed of the four types of Si NRs can correspond to a surface at thermodynamic equilibrium or can result from a growth controlled by kinetics and thus out-of-equilibrium. Chaumeton *et al.*[147] have recently shown that the concentration of the three types of reconstructions observed on AlN(0001) can be derived from a thermodynamical description and obeys to:

$$c_i = \frac{\exp(-\frac{\Delta G_i^f}{k_B T})}{\sum_{\text{all reconstructions}} \exp(-\frac{\Delta G_i^f}{k_B T})} \quad (3\text{-}1)$$

where c_i is the concentration of the reconstruction i, ΔG_i^f its Gibbs free energy of formation and T the substrate temperature. The Gibbs free energy, calculated by DFT, and the evolution of c_i for the three reconstructions are shown in Figures 39(a) and (b), respectively, for specific experimental growth conditions.

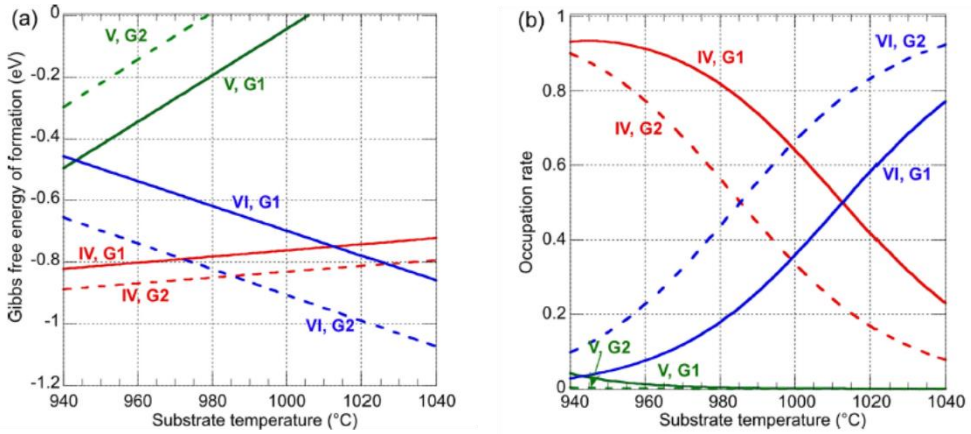

Figure 39: (a) Calculated Gibbs free energy of formation of the three reconstructions (IV,V,VI) observed on AlN(0001) for two growth rates (G1 and G2) (b) Corresponding occupation rates calculated using the Boltzmann distributions according to Equation (3-1). [F. Chaumeton et al. ref: 147]

The temperature-dependent percentage of the four types of Si NRs present similarities with the Boltzmann distributions shown in Figure 39(b), especially regarding the 1D-SNRs and 2D-DNRs. A modeling similar to the one developed by Chaumeton *et al.*[147], could be lead for our Si system and compared to the experimental distributions of the four types of Si NRs to evaluate the degree to which the growth occurs far from equilibrium conditions.

In the study reported by Chaumeton *et al.*, the thermodynamic equilibrium is assumed to be achieved since the growth is performed by molecular beam epitaxy (MBE) with a growth rate of 10 nm/h and 100 nm/h. In our experiments, the growth rate is much slower (~ 1 ML_{Si}/h) and thus kinetic effects are expected to be not favored. In the next paragraph, I will show that the Si growth can be interpreted through the introduction of energy barriers for the formation of the Si NRs.

6) Transverse linear density (TLD) of the Si SNR and Si DNR islands

The interpretation of our STM images has been done by analyzing the TLD of the Si NR islands as a function of the growth temperature. In Figure 40, I show semi-log plots of the TLD of SNR islands and DNR islands as a function of 1/T for (a) $\theta_{Si} \sim 0.22$ ML_{Si} and (b) $\theta_{Si} \sim 0.54$ ML_{Si}. SNR islands refer either to 1D-SNRs or 2D-SNRs and DNR islands to either 1D-DNRs or 2D-DNRs. In addition, in Figure 40(a) I have plotted the overall surface density of NRs in the lower temperature range [300 K-340 K], where the 2D counting of Si NRs was possible using STM images (300 x 300 nm^2), i.e the Si NRs had shorter length that the size of the scan. For $T \leq 340$ K, this overall surface density shows Arrhenius behavior with an activation energy of (125 $\pm$ 15) meV, showing that the longitudinal Si adatom diffusion, along the easy $[1\bar{1}0]$ direction, is already active for the lowest temperatures of our experiments. The plateau observed above 340 K illustrates that most of the Si NRs have reached more than 300 nm in length. In Figures 40(a) and (b), the TLD of SNR islands remains almost constant below 370 K. The break in the TLD, for both coverages, between 320 K and 340 K, can be attributed to Si adatom transverse migration, perpendicularly to the Si NRs, leading to a local packing of the 1D-SNRs. Above 370 K, we observe an abrupt decrease of the SNR island TLD due to either the formation of 2D-SNRs composed of ~ 3 SNRs or the formation 1D-DNRs. Between 370 K and 430 K, there is a clear competition between the formation of both Si arrangements, in correlation with the percentages shown in Figure 39. At higher temperature

(above 440 K), the break of the DNR island TLD for both coverages clearly reflects the transition from 1D-DNR to 2D-DNR growth with an activation energy of (210 ± 20) meV.

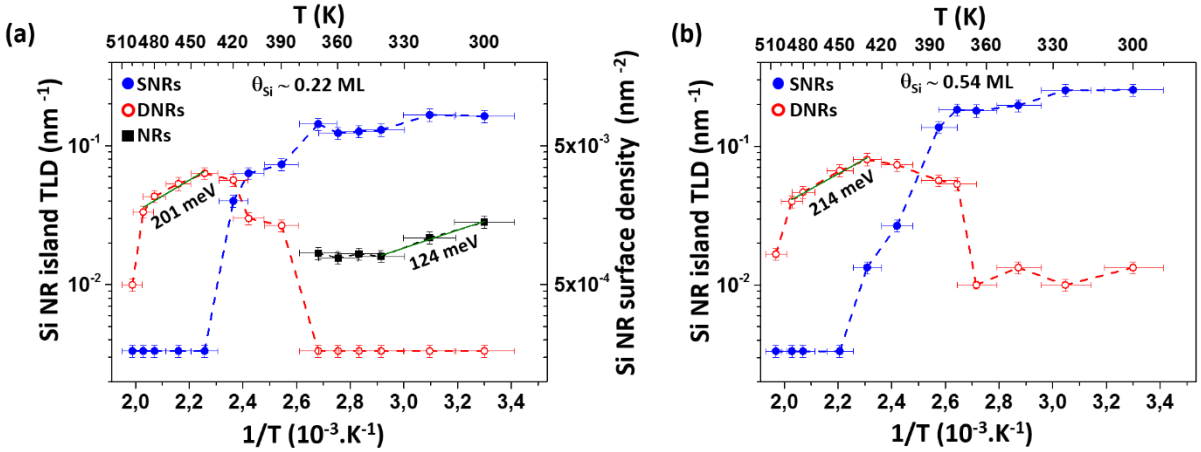

Figure 40: (a) Arrhenius plot of the transverse linear density (TLD) of Si SNR islands (blue filled dots) and Si DNR islands (red empty dots), in nm^{-1}, and the surface density of Si NRs (black filled square), in nm^{-2}, for θ_{Si} ~0.22 ML_{Si} as a function of 1/T. (b) Arrhenius plot of the transverse linear density (TLD) of Si SNR islands (blue filled dots) and Si DNR islands (red open dots), in nm^{-1}, for θ_{Si} ~0.54 ML_{Si} as a function of 1/T.

7) Thermal stability of the 5×2 superstructure

As reported in previous publications[70] and presented in chapter 1, at temperatures above 490 K, a drastic change of the morphology of the surface is seen and described by the growth of nanodikes at the expense of the Si NRs. This explains the strong decrease of the Si NR TLD measured in our STM images. In Figure 41(a), the Si NR TLD is plotted for θ_{Si} ~ 0.22 ML_{Si} and θ_{Si} ~ 0.54 ML_{Si} as a function of the substrate temperature. The TLD is expressed in SNRs/nm (i.e. each DNR is counted twice). This behavior has also been evidenced by GIXD experiments, performed in 2010 at the ID3 beamline of the European Synchrotron Radiation Facility (ESRF). In Figure 41(b), the evolution of the intensity of three intense GIXD diffraction peaks associated with ×5 periodicity of the 5×2 superstructure at completion is shown as a function of the substrate temperature (see [71] for more information on GIXD experiments). The abrupt break observed in both figures at 490 K is caused by a drastic change of the morphology described as a faceting of the silver surface induced by Si adatoms. The 2D-DNRs associated with the 5×2 structure thus disappear while new objects start to grow.

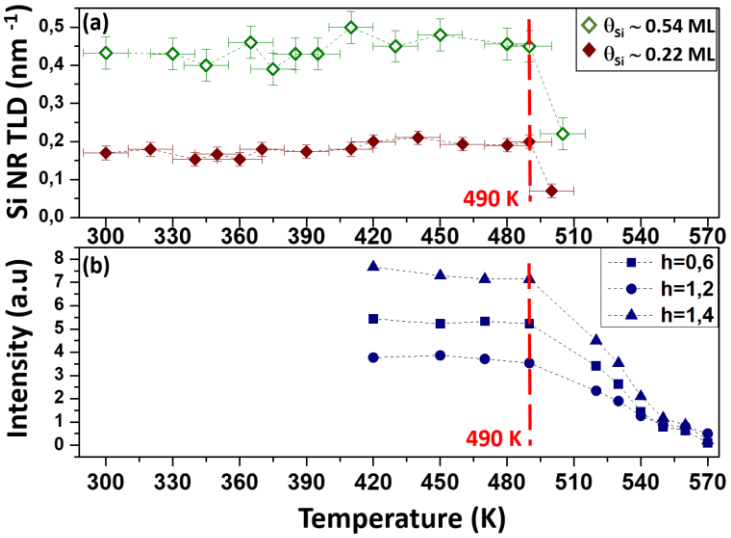

Figure 41: (a) : transverse linear density (TLD) of Si NRs, expressed in SNRs/nm, as a function of the substrate temperature during Si deposition for θ_{Si} ~0.22 ML_{Si} and 0.54 ML_{Si}. (b) : evolution, as a function of the annealing substrate temperature, of the GIXD diffracted intensities associated with the 5×2 DNR superstructure for h=0,6 (blue squares), h=1.2 (blue dots), h=1.4 (blue triangles), k=0 and l=0.05. The intensity of the (1.4,0,0.05) reflection is divided by a factor of 5. (h,k,l) indices are used for indexing a reflection in reciprocal space.

IV- Discussion

Two transitions from 1D to 2D growth of anisotropic islands are clearly observed in our experiments: (i) in the middle temperature range, with the formation of 1D-SNRs and 2D-SNRs self-assembled in a 3×2 superstructure above 370 K and (ii) in the higher temperature range, with the formation of 1D-DNRs and 2D-DNRs self-assembled in a 5×2 superstructure above 440 K. Similar behavior has been reported by Bucher *et al.* in the growth of anisotropic islands of Cu on a Pd(110) anisotropic substrate.[31] This transition was associated with the anisotropy of the diffusion along and across the easy [1$\bar{1}$0] direction of the substrate terraces, corroborated by several theoretical models.[148] In our system, the transverse migration is activated above 320 K but it does not lead to the formation of 3×2 islands, which is observed above 370 K. The same behavior occurs at higher temperature with the formation of 1D-DNRs above 370 K and 5×2 islands above 440 K. This clearly demonstrates that the formation of the Si species on Ag(110) is driven by the activation barriers for their formation rather than by the diffusion of Si adatoms. From our results, we can easily rank from the lowest to the highest the activation energy for the formation of 1D-SNRs, 2D-SNRs, 1D-DNRs and 2D-DNRs.

In 2013, an experimental study proved the MR reconstruction of the Ag(110) surface associated with the release of Ag atoms induced by the growth of Si NRs[71]. Here, in agreement with previous publications, we consider the Si nanodots observed in Figure 36(a) as the precursor of SNRs. Two models have been proposed for the structure of these Si nanodots, shown in Figures 42(a) and (b): one has a quasi-hexagonal geometry[77] and the other corresponds to two Si pentagons sitting side by side[80], both structures are located in a Ag di-vacancy. These two models

are different from the Si pentamer NR model and are considered unstable. In both articles, a transition from unstable cluster precursors to SNRs is mentioned, when more Ag atoms are removed to form a trough in the [1$\bar{1}$0] direction. In our study, these precursors are observed at RT and are no longer observed at higher temperature. We can assess that the transition from Si nanodots to NR structures is the limiting process for the growth of 1D-SNRs. I remind that a DNR corresponds to not-linked twin Si SNRs running along a silver MR. Thus, the formation of a 1D-DNR requires that a second Si nanodot nucleates in the close vicinity of a Si SNR and leads to the growth of a twin SNR. This process, with the formation of two close-packed MRs, requires a higher activation barrier as discussed in the next paragraph and the formation of DNRs occurs thus at higher temperature. Finally, while never observed, we cannot exclude that double Si nanodots are the precursor structure for the formation of DNR.

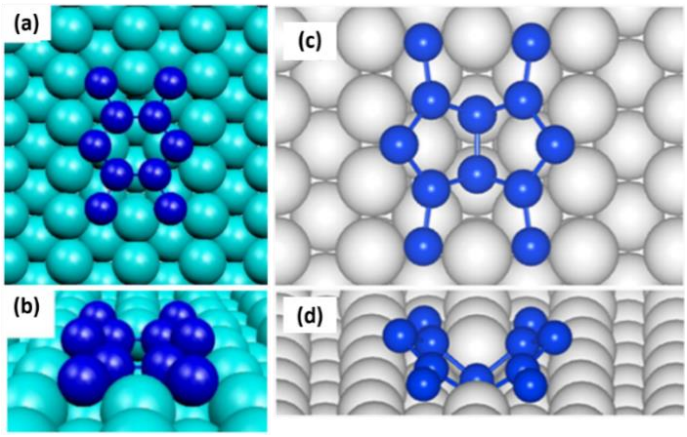

Figure 42: (a), (b) Top and Side-view of Si nanodot model presented by Cerdà et al. [J.I. Cerdà et al.ref: 77]. (c), (d) Top- and side- view of the Si nanodot model presented by Sheng et al. [S. Sheng et al. ref: 80]

I now discuss why a transition from 1D to 2D NR growth does not occur once the transverse diffusion of Si adatoms is activated. One argument can be given if we consider the 3×2 and 5×2 superstructures, which have a silver MR TLD of 1/3 and 2/5, respectively and remark that the denser 2×2 superstructure made of pentamer chains with a silver MR TLD of 1/2 is not formed. For a better understanding, the mentioned superstructures are represented in Figure 43. This indicates that the formation of close-packed silver MR is a limited process for the formation of self-assembled Si pentamer chains. Between 370 K and 440 K, we observe a competition between the formation of local 3×2 arrangements composed of ~ 3 SNRs and 1D-DNRs. This occurs when the number of close-packed silver MRs of the local 3×2 arrangement induces an activation barrier higher than the one for the formation of 1D-DNRs. We can note that this transition occurs when the number of Ag MRs of the 3×2 structure is higher than the one of 1D-DNRs, with similar spacing. This could explain why no extended 3×2 superstructures are formed on Ag(110) in our experiments.

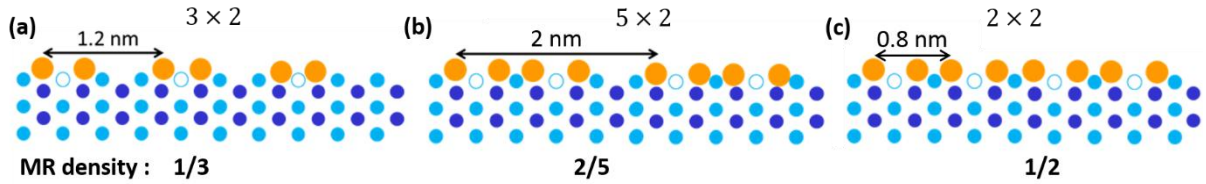

Figure 43: Side view illustration of the Si structures on the Ag(110) surface: (a) 3×2 structure (b) 5×2 structure and (c) non-observed 2x2 structure expected to be formed; Ag layers (filled dark and light bleu circles), missing Ag atoms (blue open circles), Si atoms of the pentamer chains (filled orange cirles). The missing-row (MR) density is given for each structure.

V- Conclusion

In this chapter, I have presented a nanoscale investigation of the Si NR growth which allows for a better description and understanding of the different growth mechanisms in the submonolayer regime. Our results strongly suggest that the transition from Si nanodot structure to NR structure is the limiting process for the growth of SNRs. Moreover, our results highlighted the important role of the silver substrate in the growth mechanisms of Si NRs and emphasized the role of the MR reconstruction of this substrate. I have explained why no extended self-assembled SNR array (3×2 superstructure) can be formed, in contrary to the case of self-assembled DNRs (5×2 superstructure). Thus, the 5×2 DNR array has a high potential to be a template for the growth of high densities of homogeneous 1D nanostructures while the 3×2 SNR array has a limited reliability for its use as a 1D template.

In the next chapter, I will present the results concerning the growth of 1D nanostructures made of TM (Fe, Co, Ni) and lanthanide (Ho) atoms using the 5×2 and 3×2 templates.

Chapter 4

Self-organized growth of transition metal and lanthanide 1D nanostructures

Contents

Chapter 4 91
Self-organized growth of transition metal and lanthanide 1D nanostructures 91
I- Introduction 92
II- Growth of transition metal (TM) nanolines 92
1) Experimental methods 92
2) Statistical analysis of STM images 93
3) TM on Ag(110) surface 93
4) Si template effect 93
5) Structure of TM nanolines 95
6) Formation of holes 97
7) Temperature effects 98
8) Growth at higher TM coverage 99
9) Discussion 100
III- Growth of Ho 1D nanostructures 101
1) Experimental methods 102
2) Ho growth 102
IV- Conclusion 103

In this chapter, I discuss the self-organized growth of TM and lanthanide atoms on the Si NR templates presented in chapter 3. More specifically, I show the results of the experiments carried out by means of STM and I discuss the growth of nanolines of *3d* transition metals (Fe, Co, Ni) and 4f lanthanide element (Ho) on the 5×2 and 3×2 Si superstructures.

I- Introduction

In order to allow the study of the magnetic properties of nanostructures of interest by using an average probe (XMCD), scalable processes are required to produce a homogeneous array of 1D nanostructures over the entire surface. An efficient way to achieve this aim is the use of the self-organized growth. To steer the growth, nanopatterned surfaces such as vicinal or anisotropic surfaces or templates have been proposed (See Chapter 1 section II).

At CINaM, in our team, 1D templates composed of Si NRs were used for the growth of 1D nanostructures made of Co and C_{60}.[84,85,87] Regarding the case of Co, these first studies allowed to figure out the dimer structure of the Co nanolines adsorbed on top of the Si NRs. In my thesis work, I was interested to grow other magnetic atoms and to understand the growth mechanisms to control the geometry of the nanolines (length and width) by a fine tuning of the growth temperature or the geometry of the Si template.

Thus, I have compared the growth of Co with Fe, Ni and Ho to investigate if the chemical nature of the atom plays an important role in the atomic structure and morphology of the nanolines or in the growth mechanisms. The substrate temperature during the deposition was varied, this parameter is a crucial factor since the growth is controlled by kinetics. Moreover, the magnetic atoms were deposited on the 5×2 and 3×2 Si NR superstructures, in the purpose to study the template effect on the growth of the nanostructures.

II- Growth of transition metal (TM) nanolines

The growth of TM atoms on the Si NR templates is presented in this section.

1) Experimental methods

The Si NR templates were obtained upon Si deposition on Ag(110) surfaces held at a temperature leading to the formation of the 5×2 and 3×2 superstructures (for experimental details see chapter 3). For this work, the Ag(110) surface was covered at nearly completion of the Si NR overlayer.

The Ag surface nanopatterned with Si was cooled down to RT and checked by STM and LEED (if available) before the deposition of TM or lanthanide elements.

TM elements were evaporated using a rod (purity 99.99%), each element was inserted in a commercial Scienta Omicron e-beam evaporator. Fe, Co and Ni were deposited on the Si NR templates at different temperatures (RT and below RT). Moreover, some depositions were followed by an annealing at 320 K or 370 K for several minutes. The pressure in the chamber never raises more than 2.10^{-9} Torr during the deposition. 1 ML_{TM} of Fe, Co, Ni corresponds to the 5×2 Si NR array completely covered with Co nanolines and equals 0.6 ML in silver (110) surface atom density. In our experiments, the TM coverages range from 0.6 to 4 ML_{TM}.

All STM images were acquired at RT and 77K in the constant current mode with sample voltages from -0.7 V to 1.2 V and tunneling current in the range of ~ 100 pA-300 pA. It is important to note that after the deposition of TM at LT, the substrate was immediately transferred to the STM stage held at 77 K to avoid any effects due to an increase of the substrate temperature.

2) Statistical analysis of STM images

The TM nanolines were characterized from STM images with typical sizes of (40 × 40), (70 × 70) and (100 × 100) nm^2. For each element and growth parameter, the statistical analysis has been performed on at least two STM images at different scale and it was carried out with Matlab. For each STM image, the coverage of TM elements and the average length of the nanolines were measured. In our calculation, the nano-objects with length smaller than 1 nm were not taken into account as a close inspection of STM images revealed that they don't correspond to nanolines.

3) TM on Ag(110) surface

Iron, cobalt and nickel were deposited on the bare Ag(110) surface at RT. Figures 44(a), (b) and (c), respectively after Fe, Co and Ni deposition, show the formation of elongated islands, in the $[1\bar{1}0]$ direction. These elongated islands are decorated by small round islands. We can assimilate the elongated islands to silver islands since they have height very close to one silver layer (0.145 nm) and similar shape to the ones observed by Bernard *et al.* during the growth of Si on Ag(110) at RT.[71] The silver islands were associated to the Ag atoms released during the deposition of Si on the surface. The round islands can be associated to the formation of TM islands. Our results are in agreement with previous reported STM studies[149], which have shown that, in the submonolayer regime, the growth of Co on Ag(100) is governed by the surface free energy. As the Co has a higher surface free energy than silver[150], Co atoms are incorporated in the first silver layers at 425 K. Since the Ag(110) is less stable than the Ag(100), one can expect that the incorporation can be activated at lower temperature. The incorporation process can be achieved by exchange of Co adatoms with silver atoms or by incorporation of Co at step edges.[149] Similar processes of incorporation have been reported for Ni and Fe deposition on Ag(111)[151] and Ag(100)[152], respectively.

This growth results in a rough surface and a random distribution of TM islands. Therefore, the bare Ag surface has been functionalized with a Si NR array to control the growth of TM nanostructures.

4) Si template effect

a) Growth on the 5×2 Si template

The growth of Fe, Co and Ni nanolines at RT on the 5×2 Si NR template, composed of DNRs, is presented in Figures 44(d), (e) and (f), respectively. The histograms of Figures 44(g), (h), and (i) present the length distribution of the nanolines for each TM element. Average length of the TM nanolines were calculated for a coverage of ~ 0.6 ML_{TM}: 3.6 nm for Fe, 4.3 nm for Co and 5.4 nm

for Ni. A detailed observation of these STM images showed that most of the TM nanolines are side by side with a second one on the same Si DNR and that two coupled nanolines have similar length. This result was previously reported for the growth of Co on Si DNRs, showing that after deposition of 0.16 ML_{TM} of Co at RT, more than 80 % of the nanolines are coupled to a second one[87]. Interestingly, the presence of black protrusions, mostly located at the terminations of the TM nanolines, can be observed. These features did not exist on the Si NR surface. The depletion process, already described by Dettoni et al.[87] for the Co atoms deposited on the Si NRs, is also seen in STM images after Ni and Fe deposition. These features are attributed to the local destruction of the Si NRs induced by the deposited atom diffusion into the Si layer, leaving uncovered parts of the silver substrate.

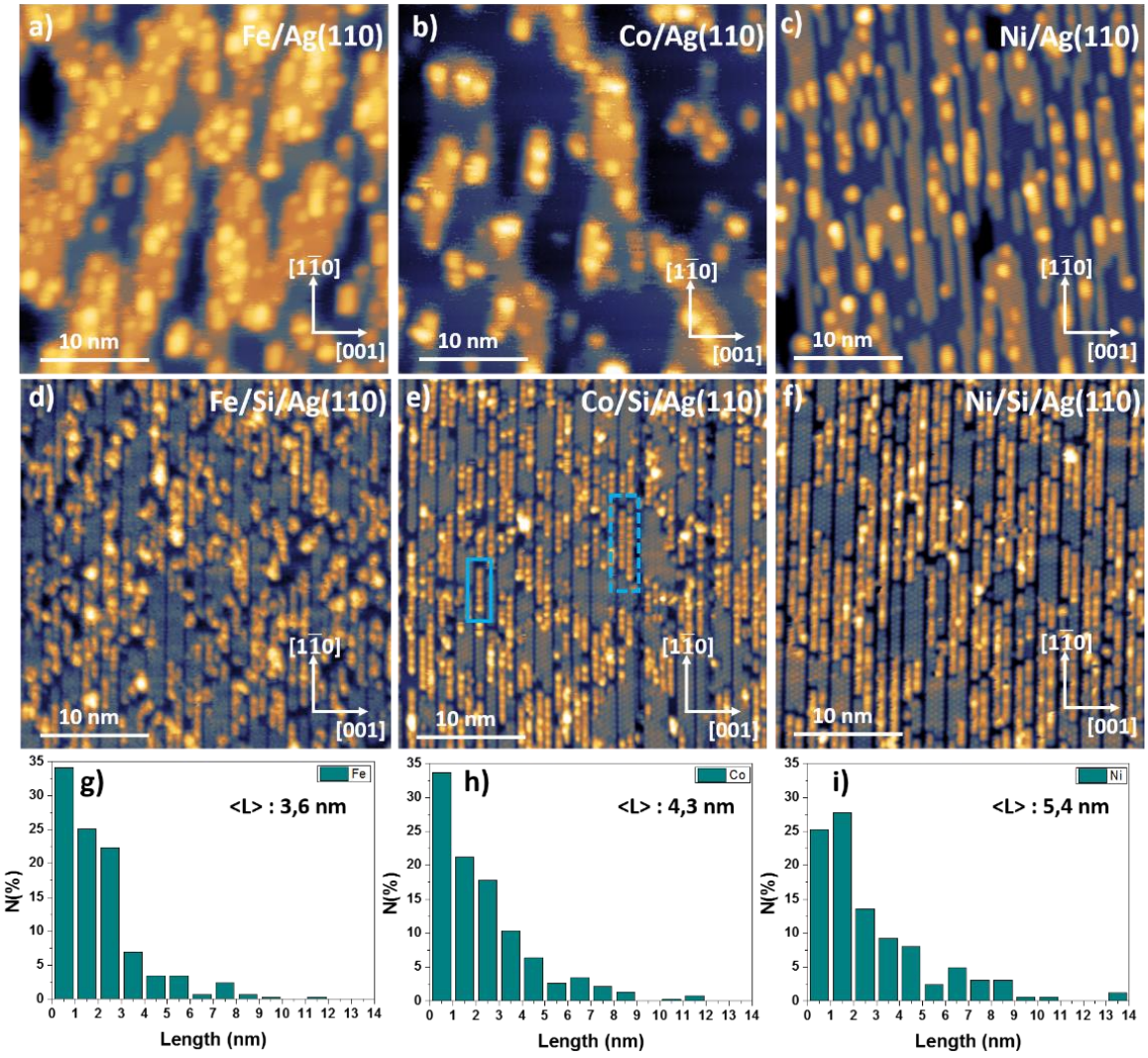

Figure 44: (a), (b) and (c) STM images showing the deposition of Fe, Co, Ni on Ag(110) at RT, respectively. Deposition of Fe (d), Co (e), Ni (f) on the 5×2 Si grating grown at 480 K, at RT (θ_{TM} ~ 0.6 ML_{TM}). Histograms showing the distribution of Fe (g), Co (h), Ni (i) nanoline lengths L and <L> the mean length of the nanolines. The rectangle and dashed-rectangle in (e) identify the single and coupled nanolines, respectively.

b) Growth on the 3×2 Si template

Deposition of Ni and Co atoms on the 3×2 Si NR template has led to the growth of longer nanolines, compared to the ones formed on the 5×2 Si NR template. The results are presented in

Figure 45. I remind that the 3×2 Si NR template consists in single NRs locally arranged in a 3×2 superstructure. I show in Figure 45(a) the deposition of Ni on the 3×2 template, at RT. Longer Ni nanolines were obtained on the SNRs with an average length of 7 nm, compared to Ni nanolines on the 5×2 template presented in Figure 45(b) with an average length of 5.4 nm. It can be seen in the left part of Figure 45(a) that nanolines are not coupled to a second one on neighboring Si SNRs, on the contrary to the 5×2 Si DNR template.

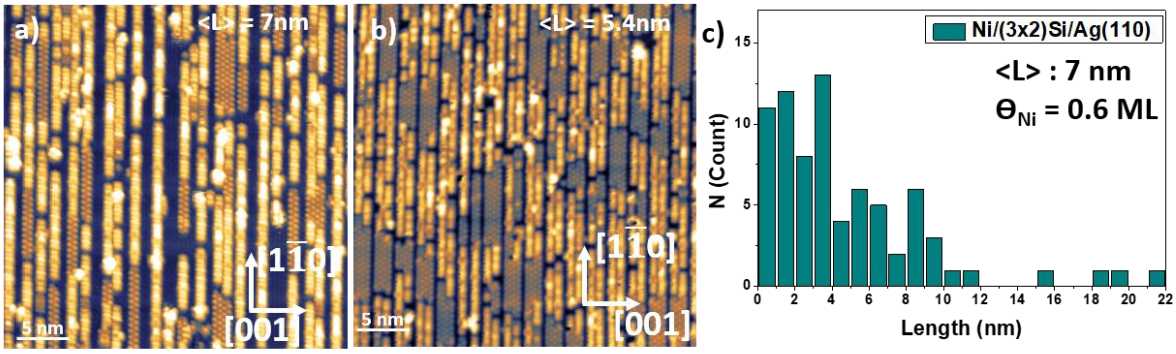

Figure 45: STM images presenting the growth at RT of Ni nanolines on single Si NRs grown at 360 K in a) and double Si NRs grown at 480 K in b) for the same coverage of 0.6 ML_{TM} of Ni. c) Histogram presenting the distribution of Ni nanoline lengths L and <L> the mean length of the nanolines, for the Ni nanolines showed in a).

Results not presented here revealed that Fe deposition on the Si 3×2 structure led to an important destruction of the Si NRs. This behavior is in agreement with the deposition of Fe on the 5×2 Si NR template, where the shortest nanolines and the highest black protrusion density have been observed. This can be explained by stability arguments: knowing that the 5×2 structure is more stable than the 3×2 structure, one could expect higher black protrusion density for the latter one.

5) Structure of TM nanolines

High-resolution STM images has been recorded in the purpose to study the atomic structure of the Ni nanolines. I remind that the atomic structure of the Si NRs was elucidated in 2016. The crystallographic atomic positions determined by GIXD (see [78] and the supplemental material) together with the resolution of the atomic rows along the $[1\bar{1}0]$ direction in STM images allow an accurate calibration of the piezoelectric scanner.

Figures 46(a) and (b) present the dimer structure of the Ni nanolines. In contrast with other Ni depositions on Si surfaces[154–156], Ni dimer nanolines are described here for the first time. The measurements have been made in STM images: the distance Ni-Ni in a dimer is $d_{Ni\text{-}Ni\perp}$ = (3.0 ± 0.5) Å and the distance between two dimers along the Si NRs is $d_{Ni\text{-}Ni//}$ = (4.4 ± 0.5) Å (i.e. ~ 1.5. $a_{Ag//}$).

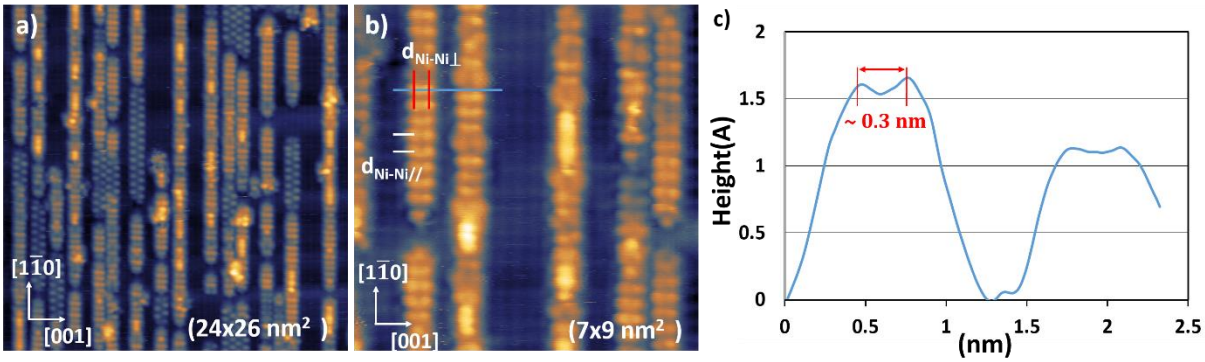

Figure 46: a) and b) STM images taken after the deposition of Ni at RT on Si SNRs grown at 360. In b) dimers of Ni nanolines on the Si SNRs and atomic rows of Ag(110) are clearly seen. In c) profile of the blue line traced in b). The distance between two Ni atoms in a dimer is measured.

Our results obtained on the dimer Ni nanoline structure corroborate previous studies led in our group and reported by Sahaf *et al.* on Co nanolines in 2009. [84] The measurement of the distance between two adjacent Co atoms in a dimer gave $d_{Co\text{-}Co\perp}$~ 0.4 nm and the distance between two dimers along the Si NRs $d_{Co\text{-}Co//}$~ 0.43 nm (i.e. ~ 1.5. $a_{Ag||}$). Based on the crystallographic atomic positions determined by grazing incidence x-ray diffraction (GIXD) (see ref. 78) which allow for an accurate calibration of the STM image, the distance between two Co atoms of a dimer turned to be $d_{Co\text{-}Co\perp}$ = (3.0 ± 0.5) Å and the distance between two adjacent Co atoms along the nanolines is slightly higher, $d_{Co\text{-}Co//}$ = (4.5 ± 0.5) Å i.e ~ 1.5 $a_{Ag||}$. This latter periodicity, in the direction parallel to the nanolines, leads to a modulation of the corrugation observed by STM: one out of every two dimers appears slightly brighter, as observed in Figure 47. It can also be noted a preferential adsorption on top of the Si NRs with respect to the surrounding Ag(110) surface.

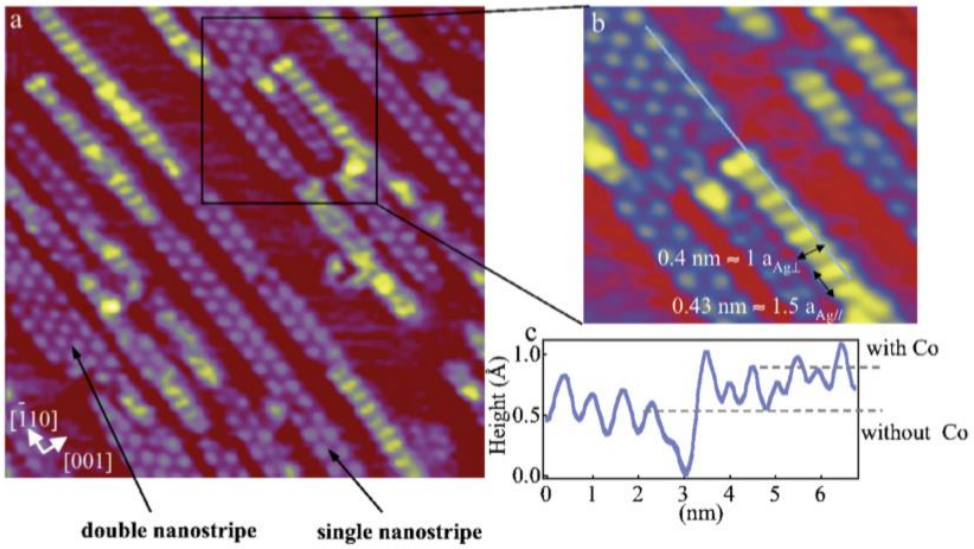

Figure 47: High resolution STM images revealing the dimer structures of the Co nanolines grown on Si NRs at RT. [Sahaf et al. 2009 ref: 84]

We can thus conclude that the Co and Ni nanolines adsorbed on the Si NRs have the same dimer structure. Although no atomic resolution was achieved in the case of Fe nanolines, we can assume that these nanolines have the same dimer structure.

The STM image in Figure 48(a) illustrates the growth of the first and second layers of Co nanolines on the 5×2 Si array, after deposition at 220K. The brighter protrusions correspond to Co dimers of the second layer while the other protrusions correspond to those of the first layer. For both Co layers, the distance between the protrusions along the nanoline axis is 2 $d_{Co\text{-}Co//}$, indicating that only the protrusions with the higher corrugation of each layer are visible. Our STM observations suggest that the Co atomic arrangement in nanolines directly adsorbed on Si NRs and in the upper layers is similar. From STM images, we have analyzed the height of the Co nanolines measured from local bare parts of the silver substrate. As exemplified by the height profile displayed in Figure 48(b), the corrugation of the first and second Co nanolines is found to be ~ 50 pm.

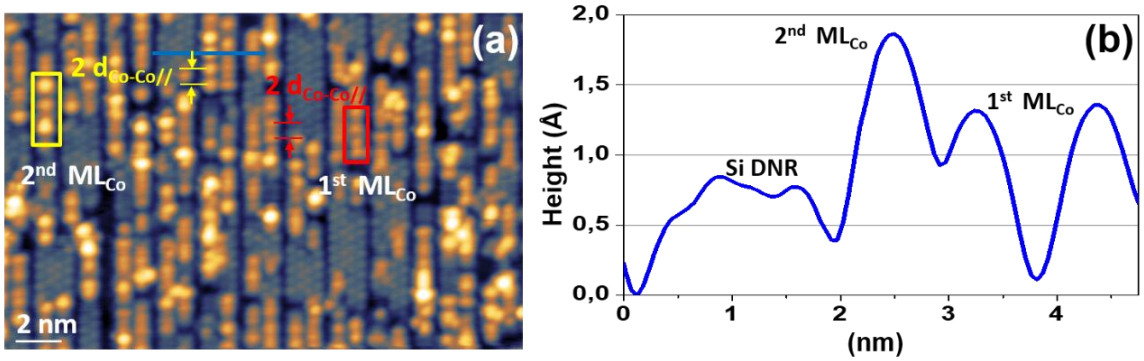

Figure 48: (a) STM image of Co nanolines grown at 220 K on the 5×2 Si NR array. Co nanolines of the 1st and 2nd layers are indicated by colored rectangles (b) Height profile along the blue line in (a), showing typical corrugations associated with the different grown nanostructures on Ag(110).

6) Formation of holes

To illustrate the formation of the black protrusions, we have directly recorded successive STM images after deposition of Fe on the Si DNRs, at RT. The choice of Fe is justified by the high density of black protrusions formed under Fe deposition. Thus, their emergence is expected to occur during the scanning of the surface. STM images shown in Figure 49 are recorded successively with the same tunneling conditions, immediately after the deposition of Fe. We can observe in Figure 49(a) that holes have already been formed. The successive STM images allow to observe the evolution of the surface and reveal the formation of other black protrusions, at the termination of the nanolines. For instance, Figures 49(c) and (f) reveal the formation of new holes (in the selected area) with respect to the Figures 49(a) and (d) respectively, leading to a reduction of the nanoline length.

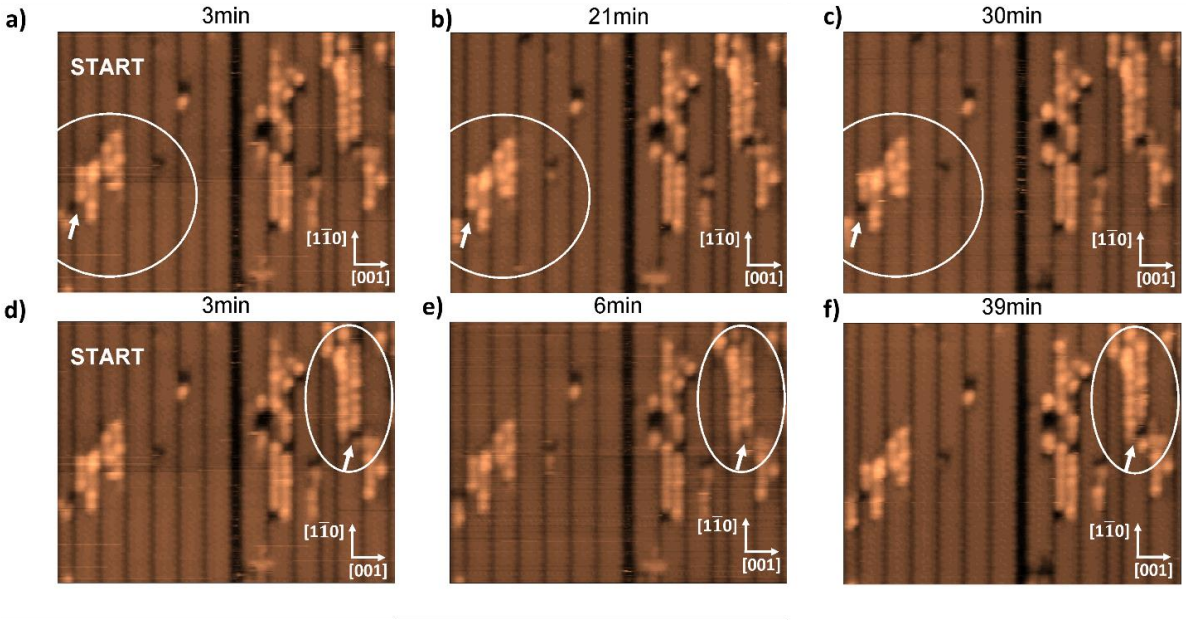

Figure 49: STM images recorded directly after depostion of Fe on the 5x2 structure, at RT. a) and d) are the same first image recorded, highlighting different parts of of the same area, Consecutive images a), b) and c) focus on the circled area where the formation of a hole with time is observed. Same for the images d), e) and f) but focusing on a second circled area.

7) Temperature effects

After deposition of Ni, the density of black protrusions increased while increasing the temperature, showing that the TM in-diffusion process is thermally activated. Annealing at 320 K for 10 minutes after the growth of Ni nanolines led to the partial destruction of the Si NR template. Similar behavior was observed for Co nanolines, in agreement with previous studies which reported a massive destruction of the Si NRs after an annealing at 370 K for 20 minutes after Co deposition[84,87].

To partially hinder the thermally activated process of TM atom diffusion into the Si array and thus increase the length of TM nanolines, Co and Ni were deposited at 220 K. A close inspection of the STM image displayed in Figure 50(a) reveals that several Co nanoline terminations remained intact, without black protrusions. As shown by the histogram displayed in Figure 50 (b), the nanoline length reaches an average value of 5.7 nm, almost at completion of the first Co layer (θ_{Co} ~ 0.84 ML_{TM}). In the case of Ni, preliminary experiments on the influence of a lower growth temperature did not lead to the growth of longer Ni nanolines.

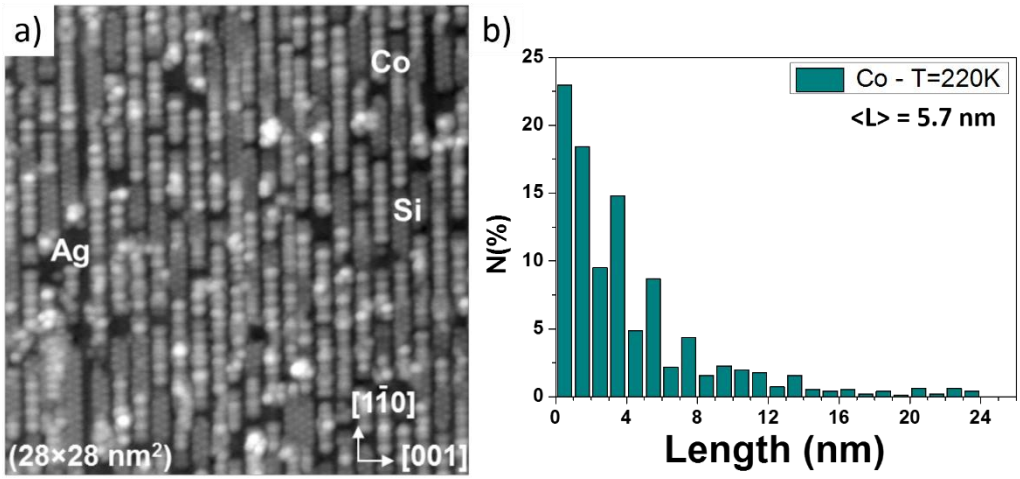

Figure 50: (a) STM image recorded at 77 K, showing the formation of Co nanolines on the Si array template, *for Co deposited at 220K and $\theta_{Co} \sim 0.84$ ML$_{TM}$. (b) Histogram showing the distribution of Co nanoline lengths L and <L> the mean length of the nanolines.*

8) Growth at higher TM coverage

For higher coverages, the Co and Ni growth reproduces the 1D pattern of the Si template as shown in Figures 51(a) for Ni and 51(b) for Co. One should mention that the growth of the nanolines is not a layer-by-layer growth. As shown in Figure 48(a), we can see the growth of a second layer before completion of the first layer of Co nanolines. Similar behavior is observed for higher coverage, as shown in Figure 52. By measuring the height of the different species observed in STM images, Co nanolines of different layers can be identified.

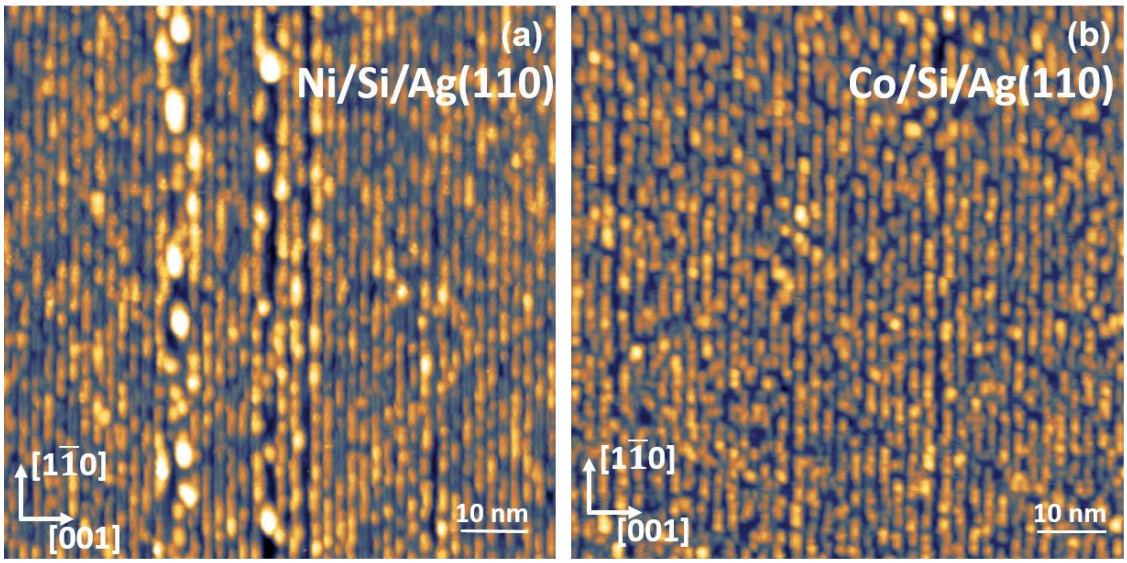

Figure 51: STM images of an ultrathin film of Ni in (a) and Co in (b) composed of nanolines (coverage $\leq$ 4 ML$_{TM}$) after deposition at RT on the 5×2 Si grating. (a) (80 nm x 80 nm). (b) (100 nm x 100 nm).

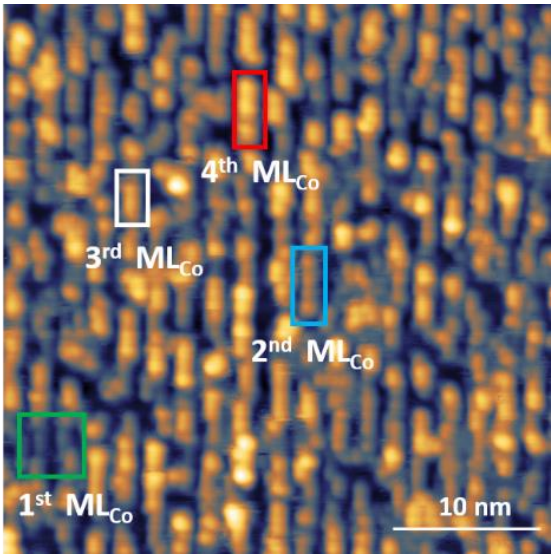

Figure 52: Close view (50 nm)^2 of Co deposition on the (5x2) superstructure at RT (coverage $\leq$ 4 ML_{TM}). Co nanolines of the different layers are indicated by colored rectangles.

9) Discussion

Remarkably, one can notice the preferential adsorption of TM atoms on top of the Si NRs. Similar effect was already reported for Co growth by Sahaf *et al.*[84]. This can be explained in two ways: (i) the kinetic control of the in-diffusion process prevents the formation of Co-Si bounds in more stable subsurface sites [157] and (ii) Si dangling bonds are preferably saturated by adsorbed adatoms to reduce the surface free energy.[158] At low Si coverage, this occurs when the deposited TM atoms on the silver surface have a sufficient diffusion length to reach Si NRs.

The adsorption on the Si NRs results in the formation of nanolines instead of islands as observed on the Ag(110) surface, which evidences the influence of the Si NRs on the TM growth. Moreover, as shown in Figure 45, longer Ni nanolines are formed on SNRs than on DNRs. This result can be explained by the fact that the TM elements arrange differently on the SNRs than on the DNRs. On the 5×2 structure, the TM atoms are arranged to sit side by side and thus the formation of coupled nanolines on the Si DNRs occurred. On the 3×2 structure, the geometry of SNRs forces the TM atoms to arrange in dimers siting one behind each other along the Si SNRs. These two different arrangements impose that the latter one provide longer nanolines. At this point, it is important to mention that the 3×2 structure (SNRs) is less stable than the 5×2 structure (DNRs), which could explain why we did not obtain a factor 2 between the length of nanolines formed on the SNRs and on the DNRs.

As shown in section 6), the formation of black protrusions at the extremities of nanolines influences their length. Moreover, we can notice from Figures 44(d), (e) and (f), that deposition at RT of the three different elements, Fe, Co and Ni, leads to different nanoline length and different hole density. Comparing the growth of Fe and Ni, the shortest nanolines are associated with the highest hole density and the longest nanolines are associated with the lowest hole density. Based on STM investigations of the early stages of Co growth, statistical analysis of the Co nanoline length were performed at different Co deposition rates and Dettoni *et al.*[87] conclude that the Co nanoline length is kinetically controlled by the in-diffusion of Co atoms into the Si NRs. This mechanism mainly concerns the Co atoms located at the termination of nanolines, less bound to Co nanostructures. Our STM observations suggest that the length of Fe and Ni nanolines is dictated

by the same atomic process. Therefore, we can consider that the in-diffusion process is a kinetic limiting factor for the growth of long defect-free TM nanolines. This in-diffusion process is highly activated in the case of Fe on the contrary to Ni. Co is an intermediate case.

In a kinetic growth mode, it is known that growth parameters such as the substrate temperature or the deposition rate allow to tune the shape and density of the nanostructures. It has been previously reported that the deposition rate did not influence the Co nanoline length. Thus, temperature-dependent experiments have been conducted. The growth of TM nanolines results from a kinetic balance between the diffusion of atoms on the surface and the diffusion of atoms into the Si NRs. As the activation energy for TM surface diffusion is expected to be lower than that of Co in-diffusion, Co deposition at lower temperature has been performed to partially hinder the process of Co in-diffusion while preserving a high degree of structural order. In the case of Co, deposition at 220 K appeared to be the best compromise. For Ni, we did not succeed to grow longer nanolines, as it would be expected from RT results. Further investigations have to be conducted. Thus, to grow long defect-free nanolines, thermal and element conditions have to be optimized. We can note here that the length of the nanoline is affected by the chemical nature of the atoms, in contrary to the nanoline dimer structure.

Original dimer structure was defined for Ni and Co nanolines. It may thus be assumed that the formation of dimers is related to the Si NR atomic structure. I remind that SNRs correspond to single Si pentamer chains and DNRs to twin Si pentamer chains in a lateral repetition of the SNR motif. We can assume that dimer nanolines are grown on single pentamer chains and side by side dimer nanolines are formed on twin Si pentamer chains. Our STM images did not allow to elucidate the adsorption sites of TM atoms on the Si NRs. Experiments carried out with x-ray diffraction techniques such as GIXD would be required.

At higher coverage, the length of the nanolines cannot be accurately estimated due to the non-perfect layer-by-layer growth. Based on statistical analysis of STM images, the average length at completion of the first Co layer grown at RT is found to be ~ 4.5 nm. Since this length is governed by this atomic process of Co diffusion into the Si array, it can be reasonably assumed that the nanoline length of this first Co layer determines those of the following layers. Thus, the maximum length of the Co nanolines of the uppest layers is estimated to be ~ 4.5 nm, which is in agreement with the STM image of Figure 52.

III- Growth of Ho 1D nanostructures

In this part, I present results on the growth of holmium on the bare Ag(110) surface and on the Si NR template. The Ho element is one of the lanthanide elements, whose spin and orbital moments originate from the strongly localized 4f orbitals. The 4f lanthanide elements are promising alternative candidates to *3d* TM elements. Therefore, it has appeared interesting in the framework of my PhD thesis to grow Ho 1D nanostructures with in the perspective to study their magnetic properties.

1) Experimental methods

For the deposition of Ho, a piece was cut from a rock of Ho and putted in a specific crucible, which was inserted in the Scienta Omicron evaporator. At first, the crucible must be heated at high temperatures to break the oxide film grown on the Ho piece. An attentive observation of the pressure must be done during this first heating as a huge increase of Ho evaporation rate suddenly occurs due to the breaking of the oxide layer. The sample was held at RT during the deposition of Ho.

STM images were obtained at RT in the constant current mode with sample voltages from -0.7 V to 1.2 V and tunneling current of ~100-300 pA.

2) Ho growth

Deposition of holmium on silver surfaces has not been reported before. Figure 53(a), shows the deposition of Ho on the Ag(110) surface at RT. Contrary to the case of TM, no etching of the silver surface with the formation of silver islands is observed. Randomly distributed islands of Ho, elongated in the $[1\bar{1}0]$ direction, are grown.

To control the growth of Ho nanostructures, Ho was deposited on the Si 5×2 superstructure. Results are displayed in Figures 53(b) and (c). Firstly, a preferential adsorption on the Si NRs with respect to the bare silver surface is observed, similarly to TM experiments. More specifically, Ho was found to adsorb at the edges of Si NR islands (see Figure 53(c)), forming poorly ordered 1D nanostructures. In the center of Si islands, small Ho clusters, randomly distributed, were formed. Interestingly, no holes in the Si NRs are observed. These observations suggest that Ho atoms that arrived on the Ag(110) surface diffused to find traps, i.e, preferential nucleation sites, and thus reached Si NRs. Nevertheless, a low diffusion length on Si seemed to prevent the formation of homogenous nanostructures on the Si array. To activate Ho diffusion, a mild annealing at 310 K for 15 minutes was performed. Figure 53(d) reveals that large holes in the Si NRs have been created. Moreover, 1D nanostructures are no longer observed which can be correlated with the etching of Si NRs at the border of Si islands (see the circle area in Figure 53(d)). Thus, upon annealing, Ho has induced the destruction of the Si NRs. Some inhomogeneous Ho clusters remained, showing that Ho did not wet the Si template.

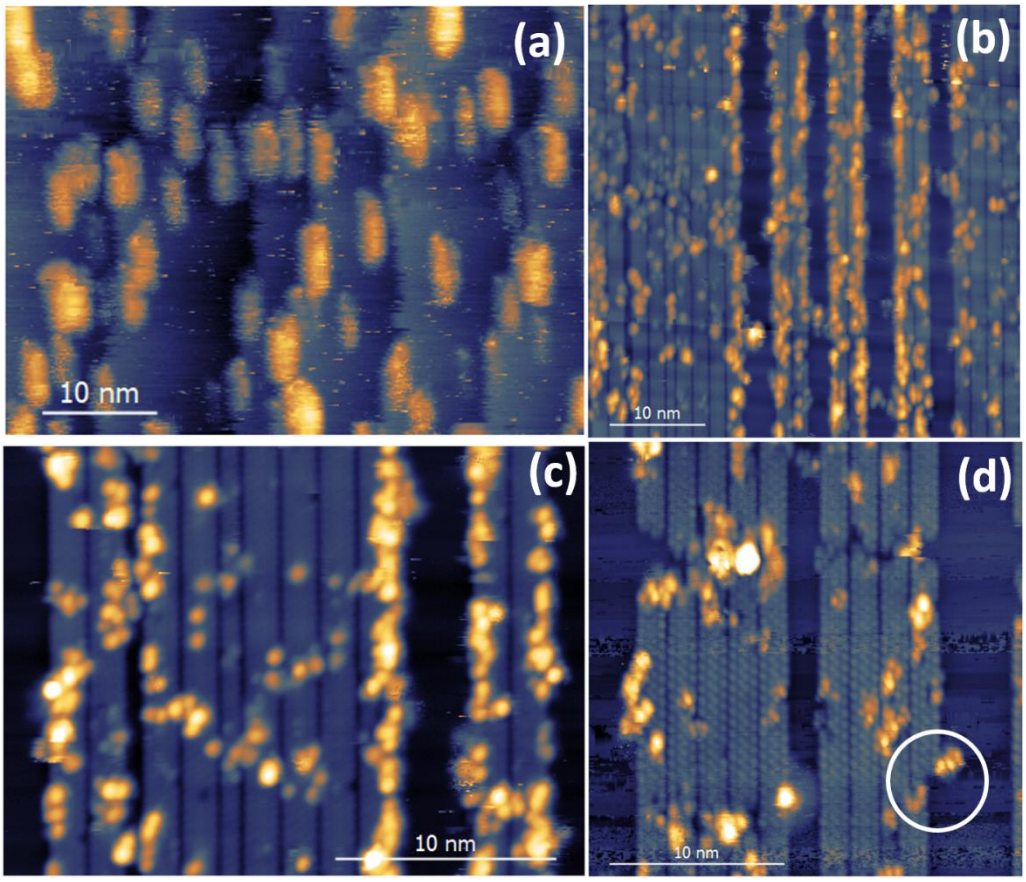

Figure 53: STM images: (a) (50x40 nm^2) Ho deposited at RT on the bare Ag(110) surface. (b) (45x45 nm^2) Ho deposited at RT on Ag(110) partially covered with Si NRs (c) close view of the surface (26x26 nm^2). (d) (24x24 nm^2) After mild annealing of the surface at 310 K for 15 minutes. The circled area shows an etched Si NR.

To conclude, our STM study did not show the formation of any specific Ho nanostructures. Opposite behavior to the TM elements is observed, the Si NRs does not steer the Ho growth at RT to form nanolines. A mild heating process performed to activate the diffusion of Ho atoms on the 5×2 superstructure turned out to activate the destruction of the Si template and no ordered nanostructures are observed.

IV- Conclusion

In this chapter, I have presented the STM investigation of the growth of TM and lanthanide elements on the Si NR templates.

Concerning the TM deposition, in agreement with previous results on Co, we have evidenced the preferential adsorption of TM elements on top of the Si NRs. In addition, we have succeeded in growing high densities of identical nanolines, regularly spaced and having the same orientation on a silver surface functionalized with Si NRs. We have shown that Co and Ni nanolines have the same dimer structure and we have related the formation of these nanolines to the Si SNR and DNR pentamer chains. These features assembled together prove that the Si NRs array can perfectly play the role of a template for different elements. Moreover, a detailed observation of

STM images has revealed the formation of black protrusions associated to the in-diffusion process of TM atoms into the Si array, which is a kinetic limiting factor for the growth of long defect-free TM nanolines. We have shown that this in-diffusion atomic process can be partially hindered by depositing TM elements at low temperature. Moreover, we have showed that the length of the nanolines depends also on the chemical nature of elements. Therefore, to grow long defect-free nanolines, one should optimize the growth parameters together with an optimized choice of the chemical element. For TM coverages higher than 1 ML_{TM}, we showed the reproduction of the 1D pattern of the Si template with similar dimer structure of the nanolines. The length of the first nanoline layer is assumed to govern the nanoline length of the upper layers.

Deposition of Ho on the Si nanotemplate has also showed a preferential adsorption on the Si NRs. However, poorly organized 1D Ho nanostructures were grown at the edges of Si NR islands at RT. This effect was related to the low diffusion length of Ho atoms on the Si NRs at RT. A mild annealing of the sample turned out to activate the destruction of the Si template without formation of 1D nanostructures lying on the Si NRs.

In our team, a study was launched on the magnetic properties of Co nanolines. Previous XMCD results reported by Michez *et al.*[88] in 2015 required further investigations for a better understanding of the Co system. In my PhD work, we pursued these investigations. In the next chapter, I will present the magnetic properties of Co nanolines grown of the 5×2 Si nanotemplate.

Chapter 5
Magnetic properties of Co nanolines

Contents

Chapter 5 105
Magnetic properties of Co nanolines 105
I- Introduction 106
II- Magnetic properties 108
1) Experimental methods 108
2) Orbital and spin moment determination 109
3) Magnetic anisotropy energy (MAE) 111
4) Temperature-dependent magnetization 112
III- Conclusion 114

In this chapter, I present the analysis of the magnetic measurements carried out by means of XAS-XMCD at the beamline DEIMOS (synchrotron SOLEIL) in 2015 to investigate the magnetic properties of Co nanolines grown on the 5×2 Si nanotemplate.

I- Introduction

As presented in chapter 1, investigations of the magnetic features of 1D nanostructures revealed the sensitivity of the MAE, spin and orbital moments to their atomic structure or geometry and chemical environment of the magnetic atoms.

In this present state of knowledge, it is still difficult to decouple intrinsic properties of nanostructures from effects related to the environment. Thus, other innovative magnetic systems need to be investigated.

In our group, preliminary investigations focused on Co nanolines grown at 220K on the 5×2 Si nanotemplate, have been carried out in 2013 by means of XAS-XMCD and published in 2015[88]. The XAS spectra displayed in the upper panel of Figures 54(a) and (b) are characteristic of metallic Co. As shown in the lower panel of Figure 54(a), a weak XMCD signal for the first two layers of Co was measured. This magnetic dead layer insures the decoupling of upper Co layers from the substrate and thus allow to investigate their intrinsic properties. Indeed, enhanced magnetization was found for higher coverage of Co nanolines, as shown in the lower panel of Figure 54(b). The shoulder peak, indicated in the XAS spectra of Figure 54 by a dotted line is attributed to the presence of interface states for Co atoms located at the Co/Si interface as suggested by Pong *et al.*[159]. The authors have excluded the formation of Co silicide or Co oxide, since in these cases, a more structured absorption spectrum is expected.[88]

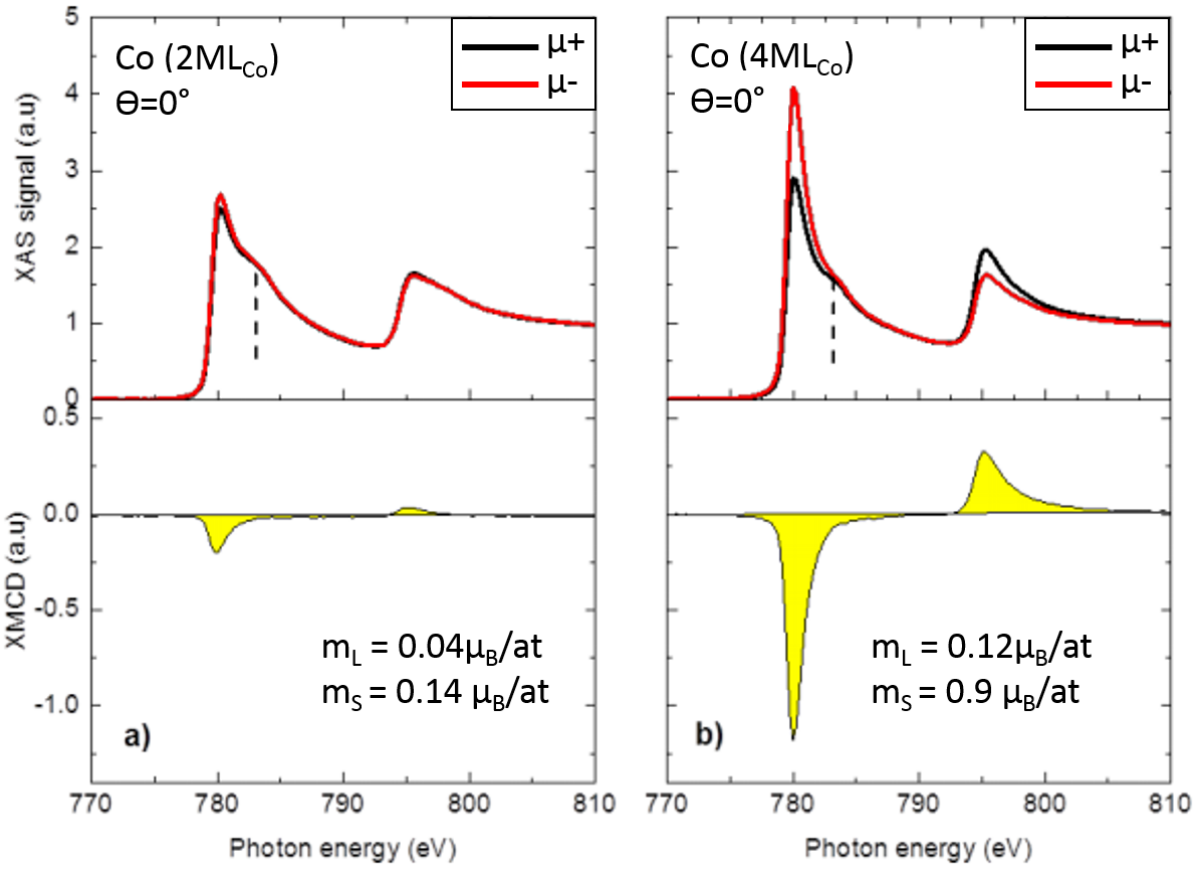

Figure 54: (a) and (b) represent XAS and XMCD spectra for 2ML$_{Co}$ and 4ML$_{Co}$, respectively. The two XMCD spectra reveal the weak vs enhanced magnetic response for the two Co coverages [L. Michez et al. 2015 ref:88]

The spin (m_S) and orbital (m_L) moments of the 2 ML_{Co} and 4 ML_{Co} Co ultrathin film have quantitatively been determined from XMCD spectra using the magnetic sum rules described in chapter 2. The values are reported in Figures 54(a) and (b). I mention that the Co coverages reported in this study[88] have been adjusted with XAS measurements performed in 2015 and STM images obtained during my PhD work, as presented in the next section.

A study as a function of the magnetic field orientation evidenced an in-plane easy axis of magnetization perpendicular to the Co nanolines axis, as presented in Figure 55(c). An in-plane MAE of 0.07 meV per Co atom is derived from the field-dependent magnetization curve displayed in Figure 55(a). A very weak remanent field can be distinguished in the magnetization curve.

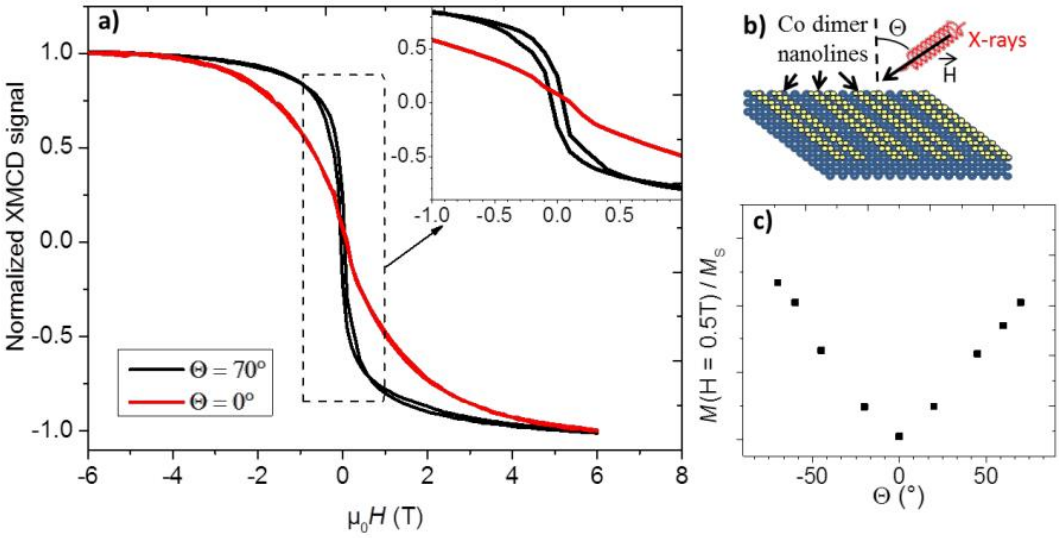

Figure 55: a) Magnetization as a function of the applied field of 4 ML_{Co} on Si/Ag(110) measured at 4 K at normal (Θ = 0°) and grazing (Θ = 70°) incidences. (b) Schematic representation of the measurement configuration. (c) Variation of the magnetization at 0.5 T normalized to the saturation magnetization (M_S) as a function of the incidence angle, Θ. The angular dependence of the magnetization evidences the existence of an in-plane easy-axis perpendicular to the nanoline axis. [L. Michez et al. ref:88]

Further investigations were required to investigate the anisotropy, in the direction parallel to the nanolines and to determine the temperature-dependent magnetic behavior of the Co nanolines, in order to have a comprehensive description of the magnetic properties of the Co nanolines grown on Si/Ag(110).

In the work reported in the next section, I present advanced magnetic investigations of the Co system by means of XAS-XMCD. This study is combined with STM results of chapter 4.

II- Magnetic properties

In 2015, a second run was performed at the DEIMOS beamline. In this section, I present the analysis I made during my PhD work of the full set of magnetic measurements performed during this run.[160]

1) Experimental methods

For this investigation, Co nanolines were grown on the 5×2 Si template at 220K. The study was focused on this nanotemplate for multiple reasons: (i) the template presents a very low defect density, (ii) it efficiently guides the growth of Co to produce a high density of nanolines regularly spaced (iii) it is more stable than the 3×2 superstructure (see chapter 3).

STM images recorded *in-situ* at the beamline DEIMOS are very similar to the one presented in Figure 51(b) of chapter 4 for Co growth at RT, with similar height profiles. A typical STM image of the surface of the Co ultrathin film investigated by XMCD is shown in Figure 56.

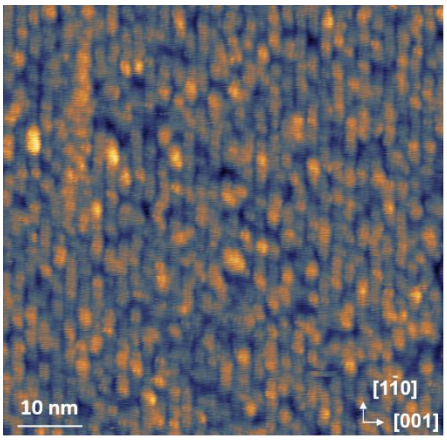

Figure 56: STM image of an ultrathin film of Co nanolines (average coverage ~4 ML_{Co}) grown at 220 K on the 5×2 Si template in the DEIMOS preparation chamber, prior to XMCD measurements.

The length of the nanolines cannot be accurately estimated from STM images due to the non-perfect layer-by-layer growth. As reported in chapter 4, the average length of the first layer of Co nanolines at 220 K is ~ 5.7 nm. Assuming that the nanoline length of this first Co layer determines those of the following layers, I will consider in the following that the maximum length reached by the Co nanolines of the different layers is 5.7 nm.

XMCD experiments were performed at the DEIMOS beamline at the french national synchrotron facility (SOLEIL), which operates in the soft x-ray range[141]. XMCD measurements were performed by detecting x-ray absorption spectra (XAS) at the Co $L_{2,3}$ edges (2p to 3d transitions) using left and right circularly polarized light in the total electron yield mode. The spectra were recorded at various substrate temperatures, ranging from 4 K to 100 K, under a variable magnetic field of up to 6 T, collinear with the incident x-ray direction.

XAS spectra were recorded with a magnetic field of 6 T applied in the different geometries illustrated in Figure 57, for right- and left-handed circularly polarized light denoted as μ_+ and μ_-, respectively. $H_{//}$ and $H_\perp$ denote a magnetic field parallel or perpendicular to the axis of the Co nanolines, respectively. To probe both the out-of-plane and the in-plane magnetic moments, the sample was rotated with respect to the direction of $H_{//}$ or $H_\perp$ collinear to the x-ray beam, by an angle θ comprised between 0° (normal incidence) and 70° (close to grazing incidence). I point out that the set-up did not allow to perform measurements at an angle θ higher that 70°. The strong non-magnetic background signal coming from the Ag substrate has been removed from the Co-$L_{2,3}$ XAS spectra. The spectra are normalized to the incident beam intensity that is set to zero at the L_3 pre-edge and to one far above the L_2 edge.

All the XAS spectra presented here have been recorded at the same Co coverage of (4.0 ± 0.5) ML_{Co} i.e. an average of four layers of Co nanolines. This coverage has been estimated from XAS measurements at the $L_{2,3}$ Co absorption edges, in agreement with STM height profile measurements. According to chapter 4, 1 ML_{Co} of Co corresponds to the 5×2 Si NR array completely covered with Co nanolines and equals 0.6 ML in silver (110) surface atom density.

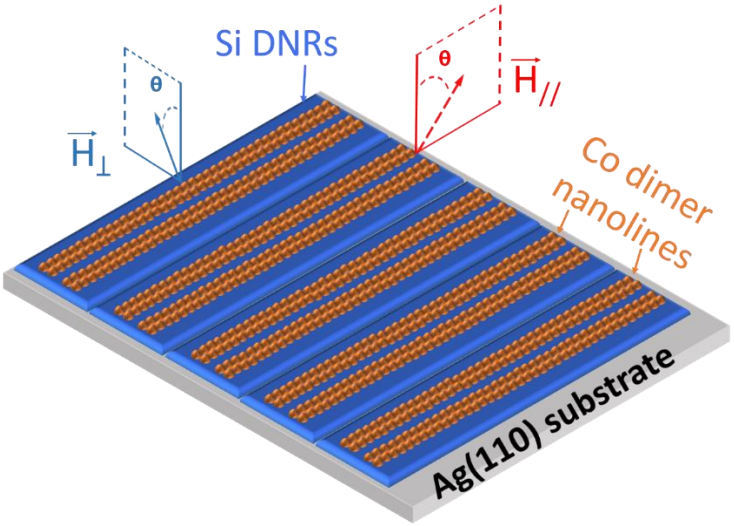

Figure 57: Schematic representation of the $H_{//}$ and $H_\perp$ configurations for the XAS and XMCD measurements. For the angle-dependent measurements, the sample was rotated by an angle θ relative to the surface normal, from normal (θ = 0°) to grazing incidence (θ =± 70°).

2) Orbital and spin moment determination

The XAS spectra at 4 K for both x-ray polarizations and respectively $H_{//}$ (upper panel) and $H_\perp$ (middle panel) are shown in Figure 58. Two broad absorption resonances are clearly visible at the L_3 and L_2 edges of Co. Although the XAS spectra are similar for both orientations of the magnetic field, we note that the corresponding XMCD spectra reported in the lowest panel of Figure 58 display differences. The XMCD signal that represents the difference between the XAS spectra for left- and right-handed light polarization gives access to the magnetization magnitude of a specific element. The magnetization of the Co film is expected to be saturated by the applied magnetic field of 6 T. The spin (m_S) and orbital (m_L) moments can be quantitatively determined using the magnetic sum rules described in[161,162]. Here, we have applied the formalism described by Chen *et al.*[163], in order to evaluate the spin and orbital contributions to the magnetization of the

Co nanolines. The number of holes in the Co 3d band has been considered to be 2.5, which corresponds to an average theoretical value for bulk Co[164,165], in agreement with the value of 2.4 used in the case of Co adatoms on Pt(111) [97]. The spin and orbital moments of the 4 ML_{Co} ultrathin film derived from our measurements taken at grazing incidence are $m_{S//}$ = (1.15 ± 0.05) μ_B per atom (μ_B/at) and $m_{L//}$ = (0.16 ± 0.01) μ_B/at for $H_{//}$ and $m_{S\perp}$ = (1.07 ± 0.05) μ_B/at and $m_{L\perp}$ = (0.17 ± 0.01) μ_B/at for $H_\perp$. At normal incidence, where $H_{//}$ and $H_\perp$ configurations are equivalent, we obtain m_S = (1.00 ± 0.05) μ_B per atom and m_L = (0.14 ± 0.01) μ_B/at. The decrease of $m_{L//}$ and $m_{L\perp}$ when passing from the in-plane to the out-of-plane configuration (13 % and 18 %, respectively) reveals the presence of in-plane easy axis and out-of-plane hard axis of magnetization, associated with a magnetic anisotropy with a similar magnitude in both directions. The values of the spin and orbital moments are closed to the ones measured in an out-of-plane geometry, i.e. θ=0° (m_S = 0.90 μ_B/at ; m_L = 0.14 μ_B/at) (see Ref. [88]). In Michez *et al.*[88], it was reported a weak XMCD signal for the 2 ML_{Co} with a spin and orbital moments of m_S = 0.14 μ_B/at and m_L = 0.04 μ_B/at measured at θ = 0°. To evaluate the real orbital and spin moments per atom, the weak contribution of the first two Co layers have to be retrieved to the measurements reported above for 4 ML_{Co}. The moments of the Co atoms in the upper two layers of the 4 ML_{Co} film can thus be estimated to $m_{S//}$ = (2.16 ± 0.20) μ_B/at and $m_{L//}$ = (0.28 ± 0.03) μ_B/at for the $H_{//}$ configuration. Similar estimations for the $H_\perp$ configuration lead to $m_{S\perp}$ = (2.00 ± 0.20) μ_B/at and $m_{L\perp}$ = (0.30 ± 0.03) μ_B/at. The large uncertainties take into account the fact that we consider an average Co coverage of 4 ML_{Co}. It can be noticed that these values are higher than the bulk ones (m_S = 1.55 μ_B and m_L = 0.153 μ_B)[163]. The explanation lies in the reduced atomic coordination of Co when passing from the bulk to nanostructures[97].

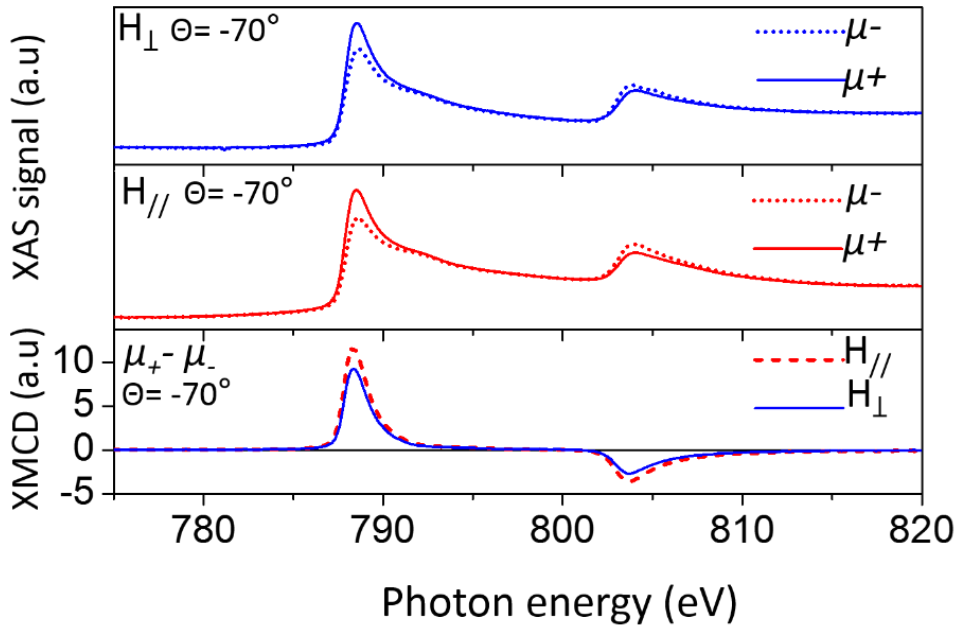

Figure 58: XAS spectra for a Co coverage of 4 ML_{Co}, taken at grazing incidence (ϑ =70°) at 4 K with a magnetic field of 6 T for both light helicities (μ_+ and μ_-) and for $H_{//}$ (upper panel) and $H_\perp$ (middle panel). The corresponding XMCD spectra are displayed in the lowest panel for both $H_{//}$ and $H_\perp$ configurations.

3) Magnetic anisotropy energy (MAE)

Field-dependent magnetization curves, obtained from the XMCD signal have been recorded at 4 K for different angles θ varying from normal incidence (θ = 0°) to grazing incidence (θ = 70°) in the $H_{//}$ and $H_{\perp}$ configurations (see Figure 59). No significant remanent magnetization at zero magnetic field was observed for both configurations, indicating the absence of long-range ferromagnetic order. However, the square shape of the magnetization curves suggests a short-range magnetic order and therefore an interatomic magnetic coupling. The angular dependence of the magnetization measured for an applied magnetic field of 0.25 T and normalized to the saturation value is plotted in the inset of Figures 59(a) and (b) for the $H_{//}$ and $H_{\perp}$ configuration, respectively. The results clearly evidence the presence of two easy axes of magnetization: one in-plane axis, perpendicular to the nanoline axis and one axis parallel to the nanoline direction, slightly canted away from the surface by an angle of 7°. These results are in agreement with the angle dependence of the orbital moments described above. The MAE can be derived from the magnetization curves displayed in Figures 59(a) and (b) using Eq. (2) in Ref.[166]. We obtain a MAE in the direction parallel to the Co nanolines : $K_{//}$ = (0.11 ± 0.03) meV/at and a MAE in the direction perpendicular to the Co nanolines : $K_{\perp}$ = (0.10 ± 0.03) meV/at. These values are higher than bulk h.c.p. Co (0.07 meV/at), in agreement with the higher value of the orbital moment measured. As the MAE is directly related to the anisotropy of the orbital moment measured in the easy and hard axes, the weak difference between $MAE_{//}$ and $MAE_{\perp}$ is in agreement with the similar angular dependence of $m_{L//}$ and $m_{L\perp}$ reported above. The presence of two easy axes of magnetization is original as uniaxial anisotropies are usually assumed to model single-domain particles. Nevertheless, it can be outlined that two in-plane favorable magnetization directions have been theoretically predicted for Co chains deposited on Pd(110) along the [1$\bar{1}$0] direction.[167]

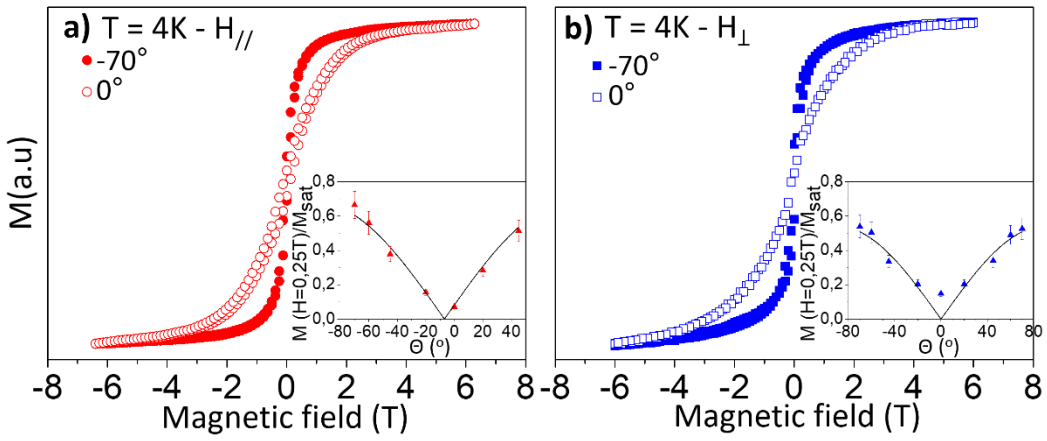

Figure 59: Magnetization (M) of 4 ML_{Co} recorded at 4K at the L_3 Co edge. M as a function of the applied field in the (a) $H_{//}$ configuration and (b) $H_{\perp}$ configuration. Magnetization curves are measured at the grazing incidence (θ = 70°, filled red dots and filled blue squares) and at the normal incidence (θ = 0°, open red dots and open blue squares). Inset: angular dependence of the magnetization: variation in both configurations of the magnetization at 0.25 T normalized to the saturation magnetization (M_{sat}) as a function of the incidence angle θ. The solid line are fits according to the function $a|\sin(\theta-\theta_0)|$.

4) Temperature-dependent magnetization

To provide a comprehensive description of the magnetic behavior of our Co system, temperature-dependent magnetization has been carried out. In Figure 60, we have plotted the magnetization measured for an applied magnetic field $H_{//}$ and $H_{\perp}$ of 0.25 T as a function of the temperature, after having saturated the sample. A plateau is observed below 20 K for both $H_{//}$ and $H_{\perp}$ configurations, suggesting that a transition from a blocked state to a superparamagnetic one occurs above 20 K. We can thus estimate that the blocking temperature T_B is between 20 K and 40 K. It can be noted that the magnetization along the Co nanoline axis is less sensitive to thermal fluctuations than the magnetization in the perpendicular direction.

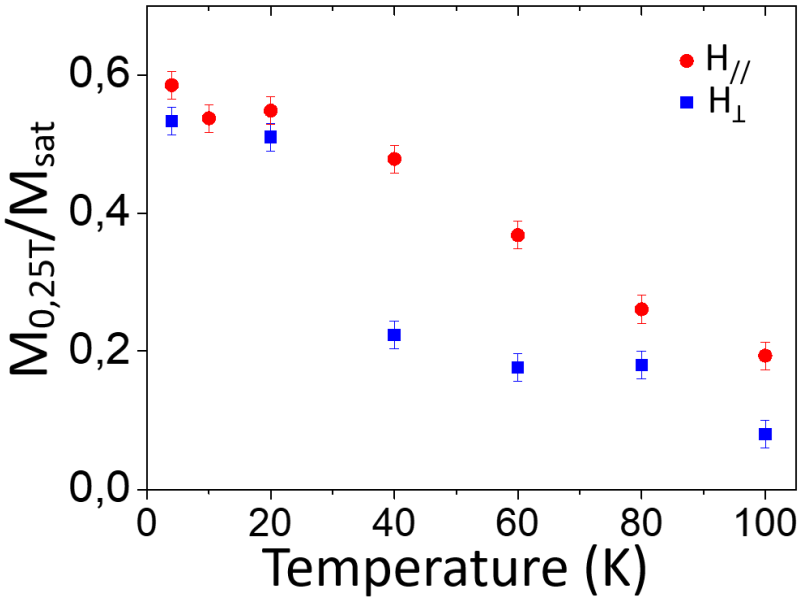

Figure 60: Variation of the magnetization for an applied magnetic field 0.25 T normalized to the saturation magnetization (M_S) as a function of the temperature, for an applied magnetic field $H_{//}$ (filled red dots) and $H_{\perp}$ (filled blue squares).

To get a deeper insight in the magnetic coupling of Co atoms, we have studied the field dependence of the magnetization as a function of the temperature in the $H_{//}$ and $H_{\perp}$ configurations. In Figures 61(a) and (b), we report magnetization of the 4 ML_{Co} film recorded at 60K, measured along the two easy axes of magnetization, parallel and perpendicularly to the Co nanolines. The magnetization curve has a more pronounced square shape in the $H_{//}$ configuration. In the framework of classical Boltzmann statistics, the field-dependence of the magnetization of an assembly of particles composed of N coupled atoms with magnetic moment Nm_{tot} and magnetic anisotropy NK obeys to:

$$M = M_{\mathrm{Sat}} \frac{\int \hat{\boldsymbol{m}}_{\mathbf{tot}}.\hat{\boldsymbol{H}} e^{(N\vec{\boldsymbol{m}}_{\mathbf{tot}}.\vec{\boldsymbol{H}}+NK(\hat{\boldsymbol{m}}_{\mathbf{tot}}.\hat{\boldsymbol{e}})^2)/k_B T} d\Omega}{\int e^{(N\vec{\boldsymbol{m}}_{\mathbf{tot}}.\vec{\boldsymbol{H}}+NK(\hat{\boldsymbol{m}}_{\mathbf{tot}}.\hat{\boldsymbol{e}})^2)/k_B T} d\Omega} \tag{5-1}$$

where M_{Sat} is the saturation value of the magnetization, $\hat{\boldsymbol{e}}$, $\hat{\boldsymbol{m}}_{\mathbf{tot}}$, and $\hat{\boldsymbol{H}}$ represent the unit vectors of the easy axis, the magnetic moment per atom and the field direction, respectively. The integration is carried out over the solid angle Ω of the magnetic moment in spherical coordinates.

Considering that the upper Co layers are decoupled from the metallic silver substrate by the weakly magnetic Co–Si layer, $m_{tot//} = m_{L//} + m_{S//}$ and $m_{tot\perp} = m_{L\perp} + m_{S\perp}$. The dashed lines in Figure 61(a) and (b) represent the magnetization given by Equation (5-1) with N=1. We clearly see that the magnetic response of our Co system is different from the one of an assembly of non-interacting paramagnetic moments. Thus, the Co nanolines behave more likely as a superparamagnetic system composed of segments (spin blocks) containing *N* exchange-coupled Co atoms. We define $N_{//}$ and $N_\perp$ the number of coupled Co atoms derived from Equation (5-1) with a magnetic field applied along and perpendicularly to the axis of the nanolines, respectively. By fitting the experimental magnetization curves shown in Figures 61(a) and (b) with the set of parameters ($m_{tot//}$= 2.44 μ_B/at ; $K_{//}$ = 0.11 meV/at) and ($m_{tot\perp}$= 2.30 μ_B/at, $K_\perp$ = 0.10 meV/at), we obtain $N_{//}$ = 74 and $N_\perp$ = 54. We note that $N_{//}$ and $N_\perp$ are different, even taking into account the uncertainties, as shown in Table I. The upper (respectively lower) value of $N_{//}$ and $N_\perp$ are obtained by fitting the magnetization with the lower (respectively upper) values of the total magnetic moment and the MAE. We underline that the values of $N_{//}$ and $N_\perp$ allow to fit according to Equation (5-1) the experimental magnetization curves recorded with angle θ ranging from easy to hard axis of magnetization.

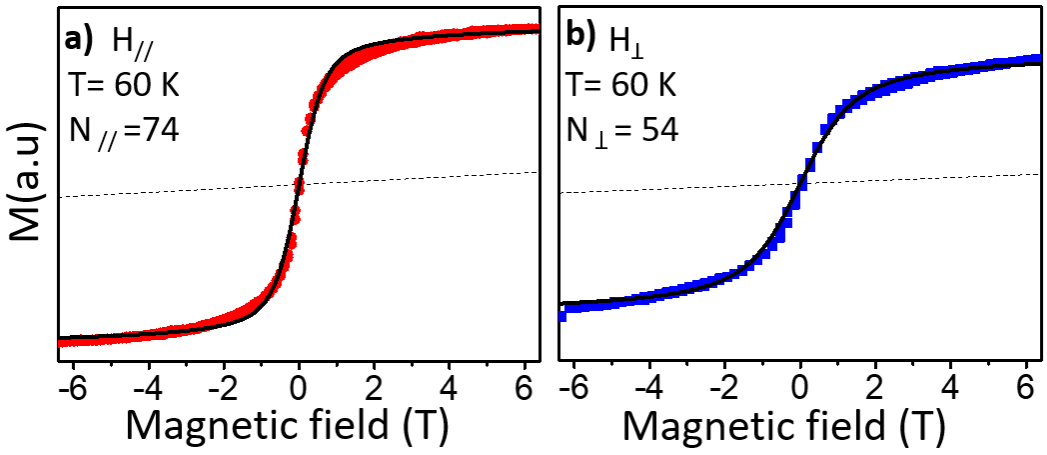

Figure 61: Magnetization (M) of 4 ML_{Co} recorded at 60 K at the L_3 Co edge. (a) M as a function of the applied field measured in the $H_{//}$ configuration with θ = 70° *(filled red dots). The solid line is the fit to the data according to Equation (5-1) with $m_{tot//}$= 2.44 μ_B/at and $K_{//}$ = 0.11 meV/at giving $N_{//}$ = 74. The dashed line corresponds to the magnetization of an isolated Co atom, given by Equation (5-1) with N =1. (b) the same as (a) in the $H_\perp$ configuration with $m_{tot//}$= 2.30 μ_B/at and $K_{//}$ = 0.10 meV/at, giving $N_\perp$ = 54. Experimental magnetization M is represented with filled blue squares.*

The fits made at T= 40 K, 60 K, 80 K and 100 K are summarized in Table 1. Firstly, we note that $N_{//}$ and $N_\perp$ are different from each other for all temperatures, even considering the uncertainties. Secondly, we can assume that within the uncertainties, $N_{//}$ and $N_\perp$ remain constant while varying the temperature, leading to an average value of ~ 74 Co atoms and ~ 52 Co atoms, respectively. Taking into account that a Co nanoline is composed of a double row of dimers and considering the two upper Co magnetic layers, the length of a spin block corresponds to $N_{//}/8 \sim 9$ dimers i.e. ~ 4 nm which is close the maximum length of the Co nanolines (~ 5.5 nm) estimated from STM measurements. We can thus assume that the Co system behaves as a superparamagnetic system composed of thermally fluctuating 1D segments. In the $H_\perp$ configuration, the length of the spin block is found to be $N_\perp/8 \sim 7$ dimers i.e. ~ 3 nm. The lower value of $N_\perp$ along the perpendicular axis could result from a higher demagnetization field along

the short axis of the nanolines. A higher magnetic field is thus needed to saturate the magnetization inside the spin block.

	T=40 K	T=60 K	T=80 K	T=100 K
$N_{//}$	59<**67**<78	65<**74**<85	67<**76**<87	71<**79**<90
$N_{\perp}$	43<**50**<60	47<**54**<64	51<**58**<68	41<**46**<53

Table 1: Values of $N_{//}$ and $N_{\perp}$ as a function of the temperature derived from fits of the experimental magnetization of 4 ML_{Co} according to Equation (5-1).

III- Conclusion

In this chapter, I have reported a description of the magnetic behavior of Co nanolines grown on a 1D Si grating, based on the analysis of XMCD measurements. Remarkably, two easy axes of magnetization were found with a slightly most favored anisotropy in the direction parallel to the nanoline axis compared to the perpendicular one. Temperature-dependent study revealed a superparamagnetic behavior of the Co nanoline system with a blocking temperature lying between 20 and 40 K. The thermally fluctuating 1D spin blocks, of ~ two layers thick are composed of ~ 74 atoms, with an esteemed length of ~4 nm which matches the length of the grown Co nanolines. Our study illustrates the richness of the magnetic anisotropy of low dimensional systems.

After a general conclusion, I will present in the last section “Perspectives”, preliminary results on new research activities launched in our group on magnetic atoms arranged in molecular networks.

Conclusion

In this manuscript, I have presented the studies conducted during my PhD thesis. I have focused my investigations on the growth of transition metal (TM) 1D nanostructures on Si nanoribbon (NR) templates and on the magnetic properties of Co nanolines. In chapters 3, 4 and 5, I have presented original results, concerning these systems, obtained by means of scanning tunneling microscopy (STM) and x-ray magnetic circular dichroism (XMCD).

Here, I summarize the main results I have obtained, pointing out the strategy and the aims of this work.

In chapter 1, I have presented, in a general manner, the growth mechanisms and the magnetic behavior of materials. Concerning the growth of nanostructures, I have showed that the self-organized growth is a powerful method to fabricate nano-objects with well-defined structure and homogeneously distributed on the surface. More specifically, I have showed that the use of templates is a very promising route to get high densities of identical nanostructures. In this context, several examples are given and a detailed review on the Si NRs grown on the Ag(110) surface is presented. Concerning the magnetic properties, different types of materials are presented. Ferromagnetic behavior is discussed for dimensionality going from bulk to single atoms. The surperparamagnetism - magnetic behavior frequently observed in nanostructures - is introduced, and the threshold temperature, called blocking temperature, associated with the transition from a blocked state to a superparamagnetic one is defined. The anisotropy of materials is presented in details since it plays a key role in defining the magnetization axis. Finally, a review on the magnetism in 1D nanostructures revealed the exalted MAE, spin and orbital moments of these nanostructures, compared to 2D films. In addition, the ferromagnetic behavior at low temperature observed in 1D TM chains was discussed.

In chapter 2, I have presented STM and XMCD characterization techniques. STM is a very powerful technique to study the structure of the nano-objects with atomic resolution in real space. XMCD is a surface-sensitive technique which can define chemically the elements by x-ray absorption spectra and allows to determine magnetic properties of nano-objects down to single atoms by a spin-polarized x-ray study. By realizing scalable ordered systems, combined studies using these two techniques is allowed, and thus, one could reveal the magnetic properties as a function of the size, shape and structure of the nano-objects.

In chapter 3, I have studied the growth mechanisms of Si NRs on Ag(110), in purpose to define a template for the growth of highly-ordered 1D TM nanostructures. While the pentamer structure of the Si NRs was elucidated in previous studies, our investigation has figured out the growth conditions which allow the formation of the different types of Si NRs and their self-assembly. Our results confirm that the transition from the Si nanodot structure to the pentamer structure is the limiting factor for the growth of single NRs. This transition is thermally activated. Moreover, our results strongly suggest that the missing row reconstruction of the Ag(110) surface plays a key role in the formation of Si NRs and thus underline the role of the silver substrate in the growth mechanisms. Statistical analysis made from STM images allowed us to calculate two activation barrier energies for the formation of isolated single NRs and for the formation of self-assembled double NRs. Our study has revealed an extended self-assembly of double NRs (5×2 superstructure), in contrary to the local self-assembled single NR array (3×2 superstructure). The 5×2 double NR array has thus the potential to be a template for the growth of high densities of homogeneous 1D nanostructures.

In chapter 4, 1D Fe, Co and Ni nanolines were grown on the 5×2 and 3×2 superstructures. In both cases, the Si NRs turned to be preferential adsorption sites. Homogeneous TM nanolines were obtained for both the single and double Si NRs. Thus, Si NRs were proven to be a well-suited template for the growth of 1D nanostructures. Longer TM nanolines were obtained on the 3×2 than the ones on the 5×2 superstructure, but are less spatially organized. Therefore, studies were focused on 1D nanolines grown on the 5×2 Si nanotemplate. STM images showed that the length of TM nanolines grown on the Si array were limited by the presence of black protrusions. We associate these black protrusions to holes resulting from the in-diffusion process of TM atoms into the Si NRs, leading to a local destruction of the template. In agreement with previous studies, this process was defined as a kinetic limiting factor for the growth of long defect-free TM nanolines. In our study on the 5×2 Si nanotemplate, TM nanolines with different lengths were obtained, depending on the deposited element. Nanolines with an average length of 3.6 nm, 4.3 nm and 5.4 nm for Fe, Co and Ni, respectively, were obtained at RT for a coverage of 0.6 monolayer, which revealed the chemical nature dependency of the atoms on the nanoline length. In contrast, the nanolines of these three elements have the same dimer structure, underlying the Si NR structure effect. Temperature-dependent study confirmed that the in-diffusion process of TM atoms is thermally activated. this process can be partially hindered and thus the length of the nanolines can be increased by realizing depositions at low temperature. In the case of Co, longer nanolines (length ~ 5.7 nm) were obtained for a deposition at 220 K. For high coverages, the Co and Ni growth reproduces the 1D pattern of the Si template with similar dimer structure of the nanolines. We assumed that the length of the first layer nanolines governs the nanoline length of the upper layers.

In chapter 4, we have also attempted to grow ordered 1D Ho nanostructures. Our results showed poorly organized growth of 1D Ho nano-objects and a high tendency of Ho to induce destruction of the Si template upon mild annealing.

Finally, in chapter 5, I have presented the magnetic properties of Co nanolines grown on a 1D Si nanotemplate (described in chapter 4). For this study, XMCD measurements were performed in the temperature range 4 K – 100 K, using different magnetic field orientations. The first two Co layers directly adsorbed onto the Si NRs presented a weak magnetic response while the upper Co layers exhibited an enhanced magnetization. Remarkably, two easy axes of magnetization were evidenced, the direction parallel to the nanolines being slightly more favorable than the perpendicular one. The magnetic moments (spin and orbital) and the magnetic anisotropic energy have been determined quantitatively. The Co nanoline ultrathin film behaves as a superparamagnetic system, with a blocking temperature lying between 20 and 40 K, composed of thermally fluctuating 1D segments (spin blocks) of ~ two layers thick, containing each ~ 74 coupled Co atoms. The length of the spin block is found to be similar to the length of the grown Co nanolines.

In summary, in the aim at growing 1D nanostructures made of magnetic materials to study their structure and magnetic properties, I have conducted several successive studies during my PhD thesis. Firstly, I have performed a study in the purpose to optimize the long-range order of the 1D Si nanotemplate. The optimized Si nanotemplate was thus used to grow high densities of homogeneous 1D nanostructures, referred here as nanolines. Then, I have investigated the growth mechanisms of the TM and lanthanide magnetic elements. Once I have figured out the growth mechanisms, I have optimized the length of the TM nanolines. The structure of these 1D nanolines was also investigated. Finally, I have investigated the magnetic properties of Co nanolines by analysing a full set of XMCD datas. I would like to underline that the PhD work was motivated by two objectives: (i) to grow high densities of homogeneous nanostructures with controlled shape at the atomic scale by the use of nanotemplates, allowing the investigation of their structural and

magnetic properties using local and surface-average probes (ii) to contribute to the fundamental understanding of nanomagnetism related to 1D nanostructures.

I have showed in chapter 5 that Co atoms directly adsorbed on the nanopatterned substrate are weakly magnetic. It is frequently reported that the interaction with the underlying substrate, metallic in most cases, affects the intrinsic properties of the grown nanostructures, with a possible quenching of the local magnetic moment. In my PhD thesis, Co nanolines recover a magnetization while increasing the thickness of the Co film to four monolayers. However, although the Co growth reproduces the 1D pattern of the Si template, the high-control on the atomic structure and geometry providing by the nanotemplate is, in some extent, reduced. To overcome this major fundamental lock of interaction with the substrate, it was recently reported that the growth of an ultrathin MgO(100) film on Ag(110) allows to decouple Ho spin from the underlying metallic substrate by a tunnel barrier.[102] As a result, individual surface-supported Ho atoms exhibit magnetic remanence up to 30 K and a relaxation time of 1500 seconds at 10 kelvin.

In the last decade, several groups have reported, after the pioneering work of Gambardella *et al.*[168] that the growth of 2D metal-organic frameworks allows a decoupling from the substrate and a fine tuning of the magnetic properties of supported magnetic atoms. I will present in the next section “Perspectives” this research activity that our group starts to develop.

Perspectives

In my PhD thesis, as presented in chapters 3 and 4, I have investigated the growth of 1D structures on a long-range ordered nanotemplate. This Si NR template was grown on a silver surface in order to guide the growth of the deposited elements and to insure a homogenous growth of well-defined 1D nanostructures that reproduce the 1D pattern of the substrate. This study was based on inorganic deposited materials (TMs and semiconductors). I have shown in chapter 5 that the Co nanolines grown on the Si template exhibit exalted magnetic properties, as frequently reported for low dimensional TM nanostructures and associated to the reduced atomic coordination of magnetic atoms when passing from the bulk to nanostructures. Nevertheless, in most cases, the nanostructures are superparamagnetic down to the lowest temperature, a feature which prevents any practical application.

In the last decade, a promising alternative route has emerged to manipulate the magnetic properties of supported TM atoms. The approach consists in selectively bonding them to functional ligands in surface-supported metal-organic frameworks (MOFs) to tune the ligand field acting on the atoms. This route has been proven to be an alternative way to control the growth and manipulate the magnetic properties of ligand-transition metal structures, such as the magnetic anisotropy which provides directionality and stability to magnetization and interatomic magnetic coupling which drives the collective behavior of spin centers. Thus, recent pioneering works have shown that (i) supramolecular self-assembly produced 2D magnetic arrays of regularly spaced *3d* metal centers with nanometer spacing, and (ii) magnetic anisotropy and magnetic coupling can be modulated by changing the metal-ligand bonding[169–172]. Interestingly, the observed magnetic coupling is interpreted in terms of a superexchange mechanism mediated by the organic linkers rather than a weaker surface mediated interaction. Nevertheless, the coupling remains weak and new strategies must be considered to strengthen the interplay between the ordered magnetic centers.

In surface-assisted supramolecular self-assembly, the molecular building blocks are linked by weak interactions, such as van der Waals interactions, hydrogen bonds or metal-coordination bonds. The reversibility of such intermolecular bonds during the on-surface growth process can facilitate defect self-healing and can thus promote the formation of highly-ordered 2D architectures. Nevertheless, as many potential applications require high mechanical/thermal stability and high intermolecular charge transport, a novel promising strategy of molecular self-assembly, namely covalent self-assembly, has emerged during the last decade[173–175]. In this approach, molecular building blocks are covalently coupled by on-surface polymerization reactions allowing for the synthesis of 2D covalent organic networks. The main drawback of this procedure is the poor long-range order of such molecular networks, related to the formation of strong irreversible covalent bonds. Interestingly, it has been demonstrated that for supramolecular arrangements, nanopatterned surfaces can efficiently steer the growth process and control the final molecular organization[60].

This new concept of on-surface chemistry to fabricate self-assembled covalent networks, has emerged during the last decade, favored by the combined experience of organic chemists and surface scientists. Since, the seminal work of Grill *et al.* in 2007 demonstrating the covalent coupling of brominated tetraphenyl-porphyrins in UHV environment[173], a wide range of coupling schemes has been proposed, sometimes however with limited success and reproducibility, due the difficulty to efficiently control the reactions mechanisms occurring at surfaces (see for review [172]). In this context, several groups have reported that organometallic complexes can be

synthesized through on-surface metalation processes. A widely developed approach (approach A) consists in the incorporation of metal atoms in macrocycles such as porphyrin- and phthalocyanine-based molecules (see Auwarter *et al.*[176] for a review on porphyrins). Another approach (approach B) has been developed to synthesize organometallic polymers, where metal atoms are not incorporated but linked by ligands such as phthalocyanine[10,11] or quinoid zwitterion molecules through the on-surface formation of covalent metal-ligand coordination bonds. In these studies, metal atoms are regularly incorporated in the polymer lattice.

In this context, our group has launched, in collaboration with organic chemists of CINaM and CEA, investigations of the adsorption of quinones and anthracenyl-porphyrins on different substrates. This study is part of a long-term project that serves the objective of building highly-ordered low dimensional covalent magnetic systems on nanopatterned surfaces to tailor the magnetic properties of nanometer spaced atomic magnetic centers. As for the experiments reported in this manuscript, nanopatterned substrates will be used to steer the assembly of diffusing species deposited on the surface and to achieve long-range order, high degree of structural control and spatial organization of the on-surface synthesized organometallic polymers. The precursors will be designed to strengthen the magnetic coupling between spin centers.

In this section, I present the preliminary results I have obtained on the adsorption of tetra-bromoanthracenyl porphyrins, quinones and dinickel-quinone on Ag(110) which serve in the investigation of on-surface synthesized organic polymers using approaches A and B mentioned above. All the molecules have been synthesized *ex-situ* by chemists.

The deposition of the molecules on Ag(110) was done through their thermal evaporation under UHV. The flat-lying adsorption on the surfaces was expected to be favored by the planar configuration of porphyrins and quinones. It has been widely reported for porphyrins, also after incorporation of metal atoms[176] and also demonstrated with Fe-zwitterionic quinone complexes[177].

Approach A

Figure 62(a) shows the geometry of the tetra-bromoanthracenyl porphyrin (TBrAPorph) molecule. The adsorption of this molecule on Ag(110) was studied for a substrate temperature ranging from RT to 670 K. Figures 62(b) and (c) show the deposition of TBrAPorph on the bare Ag(110) surface at RT and 570 K, respectively. Figure 62(b) reveals the self-assembly of TBrAPorph, forming nanosticks adsorbed one beside each other. The nanosticks are organized in a 2D supramolecular network. At 570 K, the stick structure evolves into self-assembled lines oriented along the $[1\,\bar{1}\,0]$ direction, which could be explained by the thermally activated polymerization of the molecules on the surface. High-resolution XPS measurements should be conducted to confirm this hypothesis.

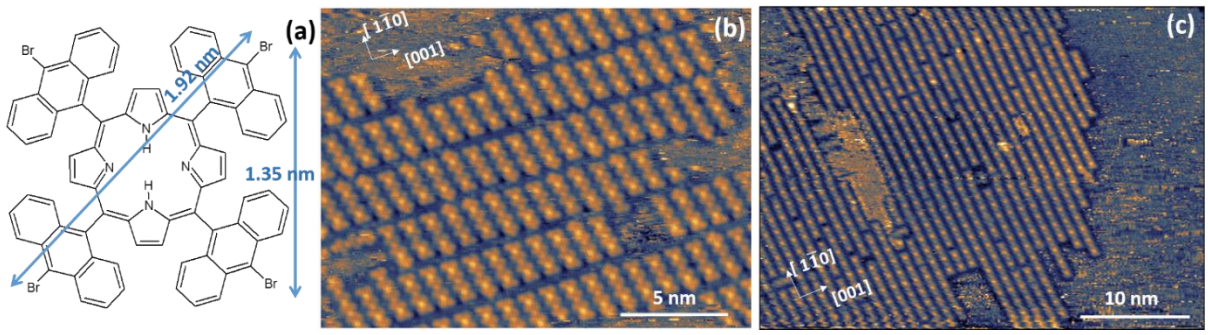

Figure 62: (a) scheme of the TBrAPorph molecule. (b) and (c) STM images showing the deposition of TBrAPorph molecules on Ag(110) at RT and 570 K, respectively.(V_t = 1.2 V ; I_t = 70 pA).

Figure 63 is a close view of Figure 62(b). Interestingly, the species in the white rectangle in Figure 62(a) presents similarities with the TBrAPorph molecule shown in Figure 62(a). The origin of the white dot in the center is not elucidated. The 2D network is composed of nanosticks periodically ordered along and across the [1$\bar{1}$0] direction, forming a 3×21 structure, as presented in Figure 62(b). Thus, our results suggest that TBrAPorph molecules wet the surface in a flat-lying geometry to form a 2D supramolecular networks..

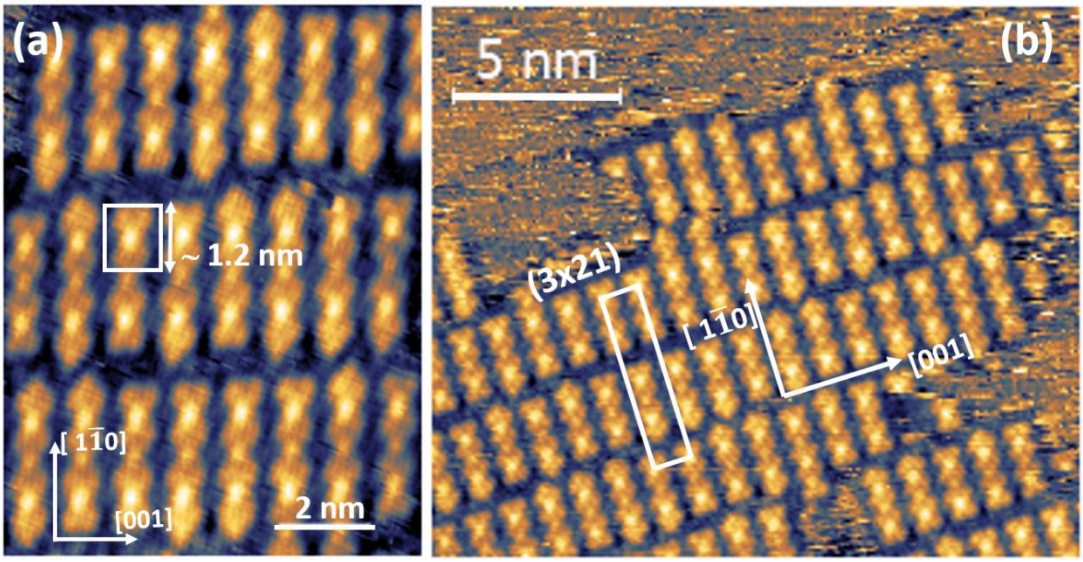

Figure 63: Adsorption of TBrAPorph on Ag(110) at RT. (a) STM image (8×11 nm^2). The white rectangle highlights a species presenting similarities with TBrAPorph. (b) STM image showing the 3×21 structure formed by the self-assembled molecules.

A geometrical description of the self-assembled lines presented in Figure 62(c) is given in Figure 64. Measurements along and across the line axis give profiles with periodic features, as shown in Figures 64 (b) and (c). In the [001] direction, perpendicular to the line axis, the lines are laterally assembled with a periodicity of 1.1 nm i.e. ~3$a_{Ag\perp}$. In the [1$\bar{1}$0] direction, parallel to the line axis, bright spots are periodically located with a period of 1.5 nm, i.e. ~ 5 $a_{Ag//}$. The periodic features mentioned above present the possibility of the formation of a molecular network with a 3×5 structure. This structure, together with the 3×21 structure, have to be confirmed by LEED.

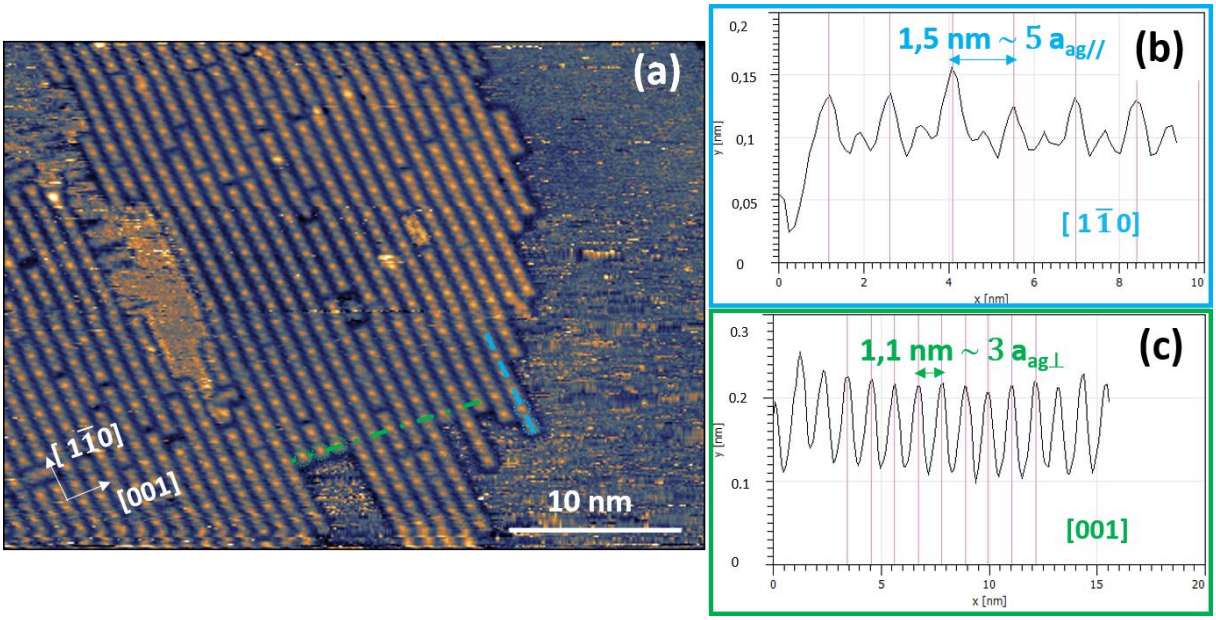

Figure 64: (a) Self-assembled lines of TBrAPorph molecule deposited on Ag(110) at 570 K. (b) and (c) are the height profiles of the dashed-lines traced in (a) along and across the [1$\bar{1}$0] *direction, respectively.*

Approach B

Preliminary results on the deposition of quinones and dinickel-quinones molecules are shown in Figures 65(a) and (b), respectively. Figure 65(a) shows the deposition of quinones on Ag(110) surface held at 170K. Remarkably, the STM image displayed in Figure 65(b) reveal that dinickel-quinones wet the Ag(110) surface to form a 2D supramolecular network. Detailed measurements in the STM image in Figure 65(b) reveal a periodicity of 1.4 nm along the [001] direction. In the next future, experiments on the adsorption of longer nickel-quinone oligomers (tri-, tetra- and pentanuclear complexes[178]), will be conducted on the bare Ag(110) surface and on nanopatterned substrates.

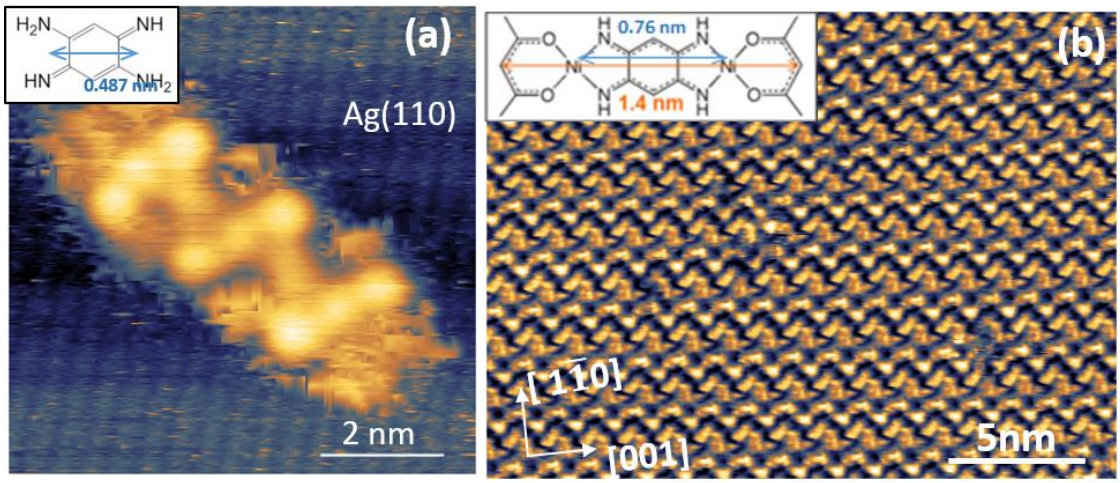

Figure 65: (a) STM image, recorded at 77 K, of quinones deposited on Ag(110) at 170 K. The bumps could be associated to quinones. Scheme of the molecule is presented in the insert. (b) STM image of self-assembled dinickel-quinone oligomers deposited at RT on Ag(110). The scheme of these oligomers is presented in the insert.

The preliminary results shown here, are encouraging since the adsorbed molecules self-assembled to form 2D networks and a process of on-surface polymerization of TBrAPorph, thermally activated, could occurred. Investigations should be pursued to determine the flat-, pi-stacking- or other type of adsorption. Theoretical calculations could be led to predict the adsorption type and thus can accelerate the experimental work. These results are very promising and open new routes to synthesize innovative organometallic networks with potential remarkable magnetic properties.

Figure list

Figure 1: *Illustration of the three growth modes 30*
Figure 2: *Illustration of the atomic processes during the deposition of material on a surface. 31*
Figure 3: *Stable compact island density, n_x, curve as a function of the coverage for different ratio of D/F.[H.Brune et al. ref :14] 33*
Figure 4: *Arrhenius plot: island density at saturation, as a function of the deposition temperature ($F=10^{-3}$ ML/s), for stable dimers regime (i=1). [H.Brune et al. ref: 14] 34*
Figure 5: *(a) and (b) Two STM images (300x300) nm^2. An annealing of 5h33 min has passed between (a) and (b) images, with the substrate held at 343 K. STM images show ripening of an assembly of about 60 Cu adatom islands on Cu(100). [J. B.Hannon et al. Ref: 23] 35*
Figure 6: *Experimental normalized distribution of islands' size before and after the annealing (blue dots). Ostwold ripening (solid line) and nucleation (dashes line, theoretical i=1 scaling curve). [H. Roder et al. ref: 24, Amar et al. ref: 19] 35*
Figure 7: *Mean island size in atoms as a function of annealing temperature derived from STM for Co/Pt(111) (Θ = 0.01ML, t_{ann} = 1h). Red curve shows kinetic Monte Carlo simulations with monomer and dimer diffusion; blue curve represents integration of mean-field rate equations considering in addition trimer diffusion. [H. Brune ref: 8] 36*
Figure 8: *(a) and (b) STM images of the Cu islands on Pd(110) taken at 300 K and 350 K respectively.(c) Arrhenius plot of island density as a function of 1/T revealing energy barriers along and across the $[110]$ direction . [J.P; Bucher et al. ref: 31] 38*
Figure 9: *a) STM $dzdx$ image of the clean vicinal Pt(997) surface. The average terrace width is 20.1±2.9 Å, step down direction is from right to left. (b) Co monatomic chains decorating the Pt step edges. The monatomic chains are obtained by evaporating 0.13 ML of Co onto the substrate held at T= 260 K. The chains are linearly aligned with a periodicity equal to the step width. [P. Gambardella et al. ref: 43] 39*
Figure 10: *(a) STM image displaying regular and straight step array of a single-crystal Au(788) sample. The inset displays a LEED pattern of the specular spot taken at E= 23 eV. (b) STM image showing a close view of Au(788) where the corrugation due to the terrace levels has been subtracted in order to enhance the reconstruction lines (c) STM image of 0.2 ML coverage of Co deposited on Au(788) at 130 K. [V. Repain et al ref:.44-47] 40*
Figure 11: *STM image of the Cu–CuO stripe phase with oxygen coverage Θ_0=0.25 ML. The image was recorded at room temperature using a tip bias voltage V= -1 V and tunneling current I = 5 nA. [L.D. Sun et al. ref : 55] 41*
Figure 12: *(a) High-resolution STM image of the Cu(110)-(2×1)O stripe-phase created by exposure of the Cu(110) surface to O_2 (Θ_o= 0.24 ML). (b) Periodically separated molecular sheets formed on CuO stripes after deposition of 0.55 ML of 4,4 ´ ´-dibromo-meta-terphenyl (DMTP) onto the surface shown in (a) held at 300 K. The inset shows the zoom-in of the white-framed region overlaid with the molecular model; [Q. Fan et al. ref: 61] 42*
Figure 13: *STM images and photoemission spectra on a Ag(110) covered with 0.25 ML of Si. Si NRs before (a), and after (b), annealing at 500 K. Longer NRs were formed by annealing accompanied with the disappearance of the nanodots observed in (a). (c) Si 2p core level spectrum (higher curve) and two asymmetric components (bottom curves) indicating the two non-equivalent Si environments. (d) Valence band spectra for the bare Ag(110) surface (bottom curve) and for the same surface as in (a) and (c) (upper curve) [C. Leandri et al. 2005 ref: 39] 43*
Figure 14: *(a) STM image (17.4 x 8 nm^2) below full Si monolayer coverage of the Ag(110) surface. (b) Height profile along the transverse line in (a). (c) STM image (24 nm)^2 of the surface at completion of the Si layer(d) 5×2 LEED pattern [H. Sahaf et al. 2007 ref: 40] 44*
Figure 15: *Constant current STM images of Si/Ag(110): (a) 6.5×6.5 nm^2 STM image, V = ±1.0 V, I = 2 nA. (b) 15×15 nm2 STM image, V = ±1.0 V, I = 2 nA; (c) 6.5×6.5 nm2 STM image, V = ±0.05 V, I = 200 nA. [F. Roncci et al. 2010 ref: 63] 44*

Figure 16: *(a) STM image revealing honeycomb arrangements with superimposed honeycomb drawings (b) ball model of the corresponding calculated atomic structure (large dark balls (blue)) representing Ag atoms in the first layer; top most Si atoms are represented by small dark balls (red) while others represented by light small balls (green), the whole forming hexagons (highlighted on the silicon NR). (c) ARPES data are displayed for the Si NRs grating. [(a),(b) ref: 66; (c) ref: 67]..... 45*
Figure 17: *LEED patterns measured on 0.8 full Si monolayer coverage on Ag(110) for different deposition temperatures, the red circles evidence the 1×1 spots: (a) 430 K (E = 50 eV), the green dashes indicate the ×3 periodicity along the [001] direction; (b) 490 K (E = 50 eV), the green dashes indicate the ×5 periodicity of the Si NR grating along the [001] direction. The arrows indicate the lines on which the ×5 periodicity is clearly observed [S. Colonna et al. ref: 70]..... 46*
Figure 18: *(a-b) STM images (234×234 nm^2) of the same area showing the evolution of the Ag(110) surface upon Si deposition at RT.. (a) bare silver surface. (b) Θ_{Si} = 0.3 ML. [R. Bernard et al. ref: 71] 47*
Figure 19: *(a) h-scans for k = 0 and l = 0.05 recorded at T_{sub} = 460 K during Si deposition. Dots: bare Ag surface. Empty squares: Θ_{Si} =0.8 ML (completion of the 5×2 Si overlayer). (b) Evolution, during Si deposition at T_{sub} = 460 K, of the integrated intensities associated with the Ag(110) surface at (1,0,0.05) (dots) and with the 5×2 superstructure at (1.4,0,0.05) (empty squares). [R. Bernard et al. ref: 71]..... 47*
Figure 20: *(a) Optical absorption of a silicene layer (black continuous line), of a crystalline Si layer (black dashed line), of an amorphous Si layer (black dotted line) for the same amount of Si atoms. Absorption of a 1 ML of Si NRs on Ag(110) determined from the SDRS measurements performed between 1 and 5 eV, parallel to the NRs (red double line) or normal to the NRs (blue dashed double line) is also shown. [Y. Borensztein et al. ref: 73]..... 48*
Figure 21: *(a,b) top and side view of the SNRs: Si atoms are arranged in pentagonal rings running along the missing rows with alternate orientation. (c) Perspective view of a Si pentagonal strand without the silver surface. The strand is made of alternating buckled pentagons. (d,e) Top and side view of the DNRs; DNRs are generated by placing two SNRs within a c(10×2) cell to form a double-strand Si pentagonal NRs.(f,g) Top and side view of the nanodot structure. [J.I. Cerdà el al. ref: 77] 49*
Figure 22: *(a) Pentamer schematic model of 1.6-nm-wide Si NRs and corresponding simulated STM images (b) STM image (9 × 4.5 nm^2) of Si DNRs below 1 ML. The high resolution allows to visualize both the Ag atoms (left part) of the (110) substrate and the protrusions of the DNRs (right part). Both pentamer and zigzag B models match the STM image. Si adatoms (yellow circles) appear as protrusions in the STM images whereas Si atoms in the missing rows (green circles) are not imaged. The high tunneling current used to resolve the atomic structure of the Ag(110) substrate induced a partial alteration of the Si NRs. The inset in the bottom-left corner shows two unaltered Si DNRs.[G. Prévot et al. ref: 78]..... 50*
Figure 23: *(a,b) STM images at different magnification scales, recorded at 77 K for a Co coverage of ~ 0.6 ML, showing the formation of Co dimer nanolines on the Si NR array grown on Ag(110) after Co deposition at 220 K. [L. Michez et al. ref: 88]..... 51*
Figure 24: *Magnetization curves for the principal axes of a single crystal of Ni. Graph replotted from C. Kittel 1953 ..... 56*
Figure 25: *Anisotropy multiplied by Co layer thickness ($t_{Co}K_u = 2K_{surface}$ Co + K_{volume}) as a function of t_{Co} for a Co/Pt multilayer grown on Si. The data show a crossover to a perpendicular easy axis for t_{Co} less than 1.2 nm. [Zeper et al. ref: 94]..... 57*
Figure 26: *MAE per atom (K) and orbital magnetic moment (m_L) as a function of the number of atoms in the cluster.(blue empty squares for K, red filled dots for m_L) [Barth et al. 2005]..... 58*
Figure 27: *Magnetization of Co monoatomic chains. Filled squares and open circles correspond to measurements along the easy direction and at 80° away from it, respectively: a) M as a function of the magnetic field at T= 45 K. b) hysteresis measured at T= 10K (below the blocking temperature), showing remanence and coercivity. [Gambardella et al. ref 105]..... 59*
Figure 28: *Photo of the experimental set-up mostly used during my thesis at CINaM..... 64*
Figure 29: *Representation of the wavefunction of a particle hitting a rectangular barrier of height U and width L. (L=d for our calculations). Illustration reproduced from 2005 Brooks/Cole – Thomson. 66*
Figure 30: *a) Schematic representation of the functioning of the STM. For each point the voltage needed to the z-piezodrive to maintain the tip at the distance for which $I_t = I_{set}$ is recorded; I_t and I_{set} are respectively the tunneling current and the current requested by the user. b) schematic representation of the tip in Tersoff-Hamman model. Spherical-head tip with a radius of R_0. ..... 68*

Figure 31: *a) set-up of the STM tip fabrication at CINaM. b) Very sharp STM tip inserted on the STM stage and approached to a sample. The diameter of the W rod is 0.3 mm. 69*
Figure 32: *(a) illustration of the two-step model for XMCD, in the first step, spin-polarized photoelectrons are generated. In a second step, they are 'detected' by the spin-split final state. (b) XAS at the Co $L_{2,3}$ for right (μ^+) and left (μ^-) circular polarization together with the difference spectrum: the XMCD. [Van der Laan et al. ref: 143]. 73*
Figure 33: *$L_{2,3}$ edge XAS and XMCD spectra for cobalt: (a)are the XAS absorption spectra; (b) and (c) are the XMCD and summed XAS spectra and their integrations calculated from the spectra shown in (a). p and q shown in (b) and r shown in (c) are the three integrals needed in the sum-rule analysis. [Chen et al. 1995 ref: 137] 74*
Figure 34: *Schematic layout of the experimental XMCD setup at DEIMOS beamline. [Ohresser et al. 2014 ref: 141] 75*
Figure 35: *Representation of the Ag(110) surface. Deep channels along the [1$\bar{1}$0] direction can be seen. Ag(110) lattice parameters are indicated. 81*
Figure 36: *STM images ((70×70) nm2) of Si deposited on Ag(110) at four different substrate temperatures and nearly the same Si coverage $\vartheta_{Si} \sim 0.22$ ML_{Si}, showing the formation of SNRs and DNRs : (a) RT, (b) 350 K, (c) 390 K and (d) 480 K. The four kinds of Si NRs are indicated by colored rectangles: 1D-SNRs (light blue in (a)),1D-DNRs (orange in (c), right side), 2D-SNRs (blue in (c), right middle part) and 2D-DNRs (red in (d)). In (a), the arrows indicate the formation of Si nanodots. 83*
Figure 37: *Transverse linear density (TLD) of Si NRs, perpendicular to the NRs (filled blue and open red triangles) as a function of the substrate temperature for $\theta_{Si} \sim 0.22$ ML_{Si} in (a) and $\theta_{Si} \sim 0.54$ ML_{Si} in (b). 84*
Figure 38: *Percentages of 1D-NRs, 1D-DNRs, 2D-NRs and 2D-DNRs for $\theta_{Si} \sim 0.22$ ML_{Si} and for each substrate temperature. 85*
Figure 39: *(a) Calculated Gibbs free energy of formation of the three reconstructions (IV,V,VI) observed on AlN(0001) for two growth rates (G1 and G2) (b) Corresponding occupation rates calculated using the Boltzmann distributions according to Equation (3-1). [F. Chaumeton et al. ref: 147] 86*
Figure 40: *(a) Arrhenius plot of the transverse linear density (TLD) of Si SNR islands (blue filled dots) and Si DNR islands (red empty dots), in nm^{-1}, and the surface density of Si NRs (black filled square), in nm^{-2}, for $\theta_{Si} \sim 0.22$ ML_{Si} as a function of 1/T. (b) Arrhenius plot of the transverse linear density (TLD) of Si SNR islands (blue filled dots) and Si DNR islands (red open dots), in nm^{-1}, for $\theta_{Si} \sim 0.54$ ML_{Si} as a function of 1/T. 87*
Figure 41: *(a) : transverse linear density (TLD) of Si NRs, expressed in SNRs/nm, as a function of the substrate temperature during Si deposition for $\theta_{Si} \sim 0.22$ ML_{Si} and 0.54 ML_{Si}. (b) : evolution, as a function of the annealing substrate temperature, of the GIXD diffracted intensities associated with the 5×2 DNR superstructure for h=0,6 (blue squares), h=1.2 (blue dots), h=1.4 (blue triangles), k=0 and l=0.05. The intensity of the (1.4,0,0.05) reflection is divided by a factor of 5. (h,k,l) indices are used for indexing a reflection in reciprocal space. 88*
Figure 42: *(a), (b) Top and Side-view of Si nanodot model presented by Cerdà et al. [J.I. Cerdà et al.ref: 77]. (c), (d) Top- and side- view of the Si nanodot model presented by Sheng et al. [S. Sheng et al. ref: 80] 89*
Figure 43: *Side view illustration of the Si structures on the Ag(110) surface: (a) 3×2 structure (b) 5×2 structure and (c) non-observed 2x2 structure expected to be formed; Ag layers (filled dark and light bleu circles), missing Ag atoms (blue open circles), Si atoms of the pentamer chains (filled orange cirles). The missing-row (MR) density is given for each structure. 89*
Figure 44: *(a), (b) and (c) STM images showing the deposition of Fe, Co, Ni on Ag(110) at RT, respectively. Deposition of Fe (d), Co (e), Ni (f) on the 5×2 Si grating, at RT ($\theta_{TM} \sim 0.6$ ML_{TM}). Histograms showing the distribution of Fe (g), Co (h), Ni (i) nanoline lengths L and <L> the mean length of the nanolines. The rectangle and dashed-rectangle in (e) identify the single and coupled nanolines, respectively. 94*
Figure 45: *STM images presenting the growth at RT of Ni nanolines on single Si NRs in a) and double Si NRs in b) for the same coverage of 0.6 ML_{TM} of Ni. 95*
Figure 46: *a) and b) STM images taken after the deposition of Ni on Si SNRs at RT. In b) dimers of Ni nanolines on the Si SNRs and atomic rows of Ag(110) are clearly seen. In c) profile of the blue line traced in b). The distance between two Ni atoms in a dimer is measured. 96*
Figure 47: *High resolution STM images revealing the dimer structures of the Co nanolines grown on Si NRs at RT. [Sahaf et al. 2009 ref: 84] 96*

Figure 48: *(a) STM image of Co nanolines grown at 220 K on the 5×2 Si NR array. Co nanolines of the 1st and 2nd layers are indicated by colored rectangles (b) Height profile along the blue line in (a), showing typical corrugations associated with the different grown nanostructures on Ag(110). 97*
Figure 49: *STM images recorded directly after depostion of Fe on the 5x2 structure, at RT. a) and d) are the same first image recorded, highlighting different parts of of the same area, Consecutive images a), b) and c) focus on the circled area where the formation of a hole with time is observed. Same for the images d), e) and f) but focusing on a second circled area. 98*
Figure 50: *(a) STM image recorded at 77 K, showing the formation of Co nanolines on the Si array template, for Co deposited at 220K and $\theta_{Co} \sim 0.84$ ML_{TM}. (b) Histogram showing the distribution of Co nanoline lengths L and <L> the mean length of the nanolines. 99*
Figure 51: *STM images of an ultrathin film of Ni in (a) and Co in (b) composed of nanolines (coverage < 4 ML_{TM}) after deposition at RT on the 5×2 Si grating. (a) (80 nm x 80 nm). (b) (100 nm x 100 nm). 99*
Figure 52: *Close view (50 nm)^2 of Co deposition on the (5x2) superstructure at RT (coverage < 4 ML_{TM}). Co nanolines of the different layers are indicated by colored rectangles. 100*
Figure 53: *STM images: (a) (50x40 nm^2) Ho deposited at RT on the bare Ag(110) surface. (b) (45x45 nm^2) Ho deposited at RT on Ag(110) partially covered with Si NRs (c) close view of the surface (26x26 nm^2). (d) (24x24 nm^2) After mild annealing of the surface at 310 K for 15 minutes. The circled area shows an etched Si NR. 103*
Figure 54: *(a) and (b) represent XAS and XMCD spectra for 2ML_{Co} and 4ML_{Co}, respectively. The two XMCD spectra reveal the weak vs enhanced magnetic response for the two Co coverages [L. Michez et al. 2015 ref:88] 106*
Figure 55: *a) Magnetization as a function of the applied field of 4 ML_{Co} on Si/Ag(110) measured at 4 K at normal (Θ = 0°) and grazing (Θ = 70°) incidences. (b) Schematic representation of the measurement configuration. (c) Variation of the magnetization at 0.5 T normalized to the saturation magnetization (M_S) as a function of the incidence angle, Θ. The angular dependence of the magnetization evidences the existence of an in-plane easy-axis perpendicular to the nanoline axis. [L. Michez et al. ref:88] 107*
Figure 56: *STM image of an ultrathin film of Co nanolines (average coverage ~4 ML_{Co}) grown at 220 K on the 5×2 Si template in the DEIMOS preparation chamber, prior to XMCD measurements. 108*
Figure 57: *Schematic representation of the $H_{//}$ and $H_{\perp}$ configurations for the XAS and XMCD measurements. For the angle-dependent measurements, the sample was rotated by an angle θ relative to the surface normal, from normal ($\theta = 0^{\circ}$) to grazing incidence ($\theta = \pm 70°$). 109*
Figure 58: *XAS spectra for a Co coverage of 4 ML_{Co}, taken at grazing incidence (ϑ ・・・・・) at 4 K with a magnetic field of 6 T for both light helicities (μ_+ and μ_-) and for $H_{//}$ (upper panel) and $H_{\perp}$ (middle panel). The corresponding XMCD spectra are displayed in the lowest panel for both $H_{//}$ and $H_{\perp}$ configurations. 110*
Figure 59: *Magnetization (M) of 4 ML_{Co} recorded at 4K at the L_3 Co edge. M as a function of the applied field in the (a) $H_{//}$ configuration and (b) $H_{\perp}$ configuration. Magnetization curves are measured at the grazing incidence ($\theta = 70°$, filled red dots and filled blue squares) and at the normal incidence ($\theta = 0°$, open red dots and open blue squares). Inset: angular dependence of the magnetization: variation in both configurations of the magnetization at 0.25 T normalized to the saturation magnetization (M_{sat}) as a function of the incidence angle θ. The solid line are fits according to the function $a|\sin(\theta-\theta_0)|$. 111*
Figure 60: *Variation of the magnetization for an applied magnetic field 0.25 T normalized to the saturation magnetization (M_S) as a function of the temperature, for an applied magnetic field $H_{//}$ (filled red dots) and $H_{\perp}$ (filled blue squares). 112*
Figure 61: *Magnetization (M) of 4 ML_{Co} recorded at 60 K at the L_3 Co edge. (a) M as a function of the applied field measured in the $H_{//}$ configuration with $\theta = 70°$ (filled red dots). The solid line is the fit to the data according to Equation (5-1) with $m_{tot//} = 2.44$ μ_B/at and $K_{//} = 0.11$ meV/at giving $N_{//} = 74$. The dashed line corresponds to the magnetization of an isolated Co atom, given by Equation (5-1) with N =1. (b) the same as (a) in the $H_{\perp}$ configuration with $m_{tot//} = 2.30$ μ_B/at and $K_{//} = 0.10$ meV/at, giving $N_{\perp} = 54$. Experimental magnetization M is represented with filled blue squares. 113*
Figure 62: *(a) scheme of the TBrAPorph molecule. (b) and (c) STM images showing the deposition of TBrAPorph molecules on Ag(110) at RT and 570 K, respectively.($V_t = 1.2$ V ; $I_t = 70$ pA). 121*
Figure 63: *Adsorption of TBrAPorph on Ag(110) at RT. (a) STM image (8×11 nm^2). The white rectangle highlights a species presenting similarities with TBrAPorph. (b) STM image showing the 3×21 structure formed by the self-assembled molecules. 121*

***Figure 64**: (a) Self-assembled lines of TBrAPorph molecule deposited on Ag(110) at 570 K. (b) and (c) are the height profiles of the dashed-lines traced in (a) along and across the [1$\bar{1}$0] direction, respectively. 122*
***Figure 65:** (a) STM image, recorded at 77 K, of quinones deposited on Ag(110) at 170 K. The bumps could be associated to quinones. Scheme of the molecule is presented in the insert. (b) STM image of self-assembled dinickel-quinone oligomers deposited at RT on Ag(110). The scheme of these oligomers is presented in the insert. 122*

References

1. Xu, W., Wong, J., Cheng, C. C., Johnson, R. & Scherer, A. Fabrication of ultrasmall magnets by electroplating. *J. Vac. Sci. Technol. B Microelectron. Nanometer Struct. Process. Meas. Phenom.* **13**, 2372–2375 (1995).

2. Khamsehpour, B., Wilkinson, C. D. W., Chapman, J. N. & Johnston, A. B. High resolution patterning of thin magnetic films to produce ultrasmall magnetic elements. *J. Vac. Sci. Technol. B Microelectron. Nanometer Struct. Process. Meas. Phenom.* **14**, 3361–3366 (1996).

3. Guo, C. X. & Thomson, D. J. Material transfer between metallic tips and surface in the STM. *Ultramicroscopy* **42–44**, 1452–1458 (1992).

4. Becker, R. S., Golovchenko, J. A. & Swartzentruber, B. S. Atomic-scale surface modifications using a tunnelling microscope. *Nature* **325**, 419 (1987).

5. Bauer, E. Phänomenologische Theorie der Kristallabscheidung an Oberflächen. I. *Z. Für Krist. - Cryst. Mater.* **110**, 372–394 (1958).

6. Bauer, E. & Poppa, H. Recent advances in epitaxy. *Thin Solid Films* **12**, 167–185 (1972).

7. Müller, P. & Kern, R. The physical origin of the two-dimensional towards three-dimensional coherent epitaxial Stranski-Krastanov transition. *Proc. Int. Symp. Si Heterostruct. Phys. Devices* **102**, 6–11 (1996).

8. Brune, H. Epitaxial Growth of Thin Films. Surface and Interface Science: Solid-Solid Interfaces and Thin Films, First Edition. Edited by Klaus Wandelt. 2014 Wiley-VCH Verlag GmbH & Co. KGaA. Published 2014 by Wiley-VCH Verlag GmbH & Co. KGaA; 'Physique de la croissance cristalline', collection ALEA Saclay, editing Eyrolles-CEA, 1995, ISBN 2-212-05800-4.

9. Venables, J. A. & Spiller, G. D. T. Nucleation and Growth of Thin Films. in *Surface Mobilities on Solid Materials: Fundamental Concepts and Applications* (ed. Binh, V. T.) 341–404 (Springer US, 1983). doi:10.1007/978-1-4684-4343-1_16

10. Binnig, G. & Rohrer, H. Scanning tunneling microscopy---from birth to adolescence. *Rev. Mod. Phys.* **59**, 615–625 (1987).

11. Binnig, G. & Rohrer, H. Scanning tunneling microscopy. *Surf. Sci.* **126**, 236–244 (1983).

12. Liu, C. L., Cohen, J. M., Adams, J. B. & Voter, A. F. EAM study of surface self-diffusion of single adatoms of fcc metals Ni, Cu, Al, Ag, Au, Pd, and Pt. *Surf. Sci.* **253**, 334–344 (1991).

13. Shiang, K.-D., Wei, C. M. & Tsong, T. T. A molecular dynamics study of self-diffusion on metal surfaces. *Surf. Sci.* **301**, 136–150 (1994).

14. Brune, H., Bales, G. S., Jacobsen, J., Boragno, C. & Kern, K. Measuring surface diffusion from nucleation island densities. *Phys. Rev. B* **60**, 5991–6006 (1999).

15. Venables, J. A. Rate equation approaches to thin film nucleation kinetics. *Philos. Mag. J. Theor. Exp. Appl. Phys.* **27**, 697–738 (1973).

16. Venables, J. A. Nucleation calculations in a pair-binding model. *Phys. Rev. B* **36**, 4153–4162 (1987).

17. Liu, S., Bönig, L. & Metiu, H. Effect of small-cluster mobility and dissociation on the island density in epitaxial growth. *Phys. Rev. B* **52**, 2907–2913 (1995).

18. Bartelt, M. C., Günther, S., Kopatzki, E., Behm, R. J. & Evans, J. W. Island-size distributions in submonolayer epitaxial growth: Influence of the mobility of small clusters. *Phys. Rev. B* **53**, 4099–4104 (1996).

19. Amar, J. G. & Family, F. Critical Cluster Size: Island Morphology and Size Distribution in Submonolayer Epitaxial Growth. *MRS Online Proc. Libr. Arch.* **367**, (1994).

20. Bott, M., Hohage, M., Morgenstern, M., Michely, T. & Comsa, G. New Approach for Determination of Diffusion Parameters of Adatoms. *Phys. Rev. Lett.* **76**, 1304–1307 (1996).

21. Ostwald, W. On the assumed isomerism of red and yellow mercury oxide and the surface-tension of solid bodies. *Z. Für Phys. Chem.* **34U**, 495–503 (1900).

22. Morgenstern, K., Rosenfeld, G. & Comsa, G. Decay of Two-Dimensional Ag Islands on Ag(111). *Phys. Rev. Lett.* **76**, 2113–2116 (1996).

23. Hannon, J. B. *et al.* Surface Self-Diffusion by Vacancy Motion: Island Ripening on Cu(001). *Phys. Rev. Lett.* **79**, 2506–2509 (1997).

24. Röder, H., Hahn, E., Brune, H., Bucher, J.-P. & Kern, K. Building one- and two-dimensional nanostructures by diffusion-controlled aggregation at surfaces. *Nature* **366**, 141 (1993).

25. Fruchart, O. *et al.* Vertical self-organization of epitaxial magnetic nanostructures. *J. Magn. Magn. Mater.* **239**, 224–227 (2002).

26. Omi, H., Bottomley, D. J., Homma, Y. & Ogino, T. Wafer-scale strain engineering on silicon for fabrication of ultimately controlled nanostructures. *Phys. Rev. B* **67**, 115302 (2003).

27. Kammler, M., Hull, R., Reuter, M. C. & Ross, F. M. Lateral control of self-assembled island nucleation by focused-ion-beam micropatterning. *Appl. Phys. Lett.* **82**, 1093–1095 (2003).

28. Repain, V., Baudot, G., Ellmer, H. & Rousset, S. Two-dimensional long-range–ordered growth of uniform cobalt nanostructures on a Au(111) vicinal template. *EPL Europhys. Lett.* **58**, 730 (2002).

29. Brune, H., Giovannini, M., Bromann, K. & Kern, K. Self-organized growth of nanostructure arrays on strain-relief patterns. *Nature* **394**, 451 (1998).

30. Ross, F. M. Growth processes and phase transformations studied in situ transmission electron microscopy. *IBM J. Res. Dev.* **44**, 489–501 (2000).

31. Bucher, J.-P., Hahn, E., Fernandez, P., Massobrio, C. & Kern, K. Transition from One- to Two-Dimensional Growth of Cu on Pd(110) Promoted by Cross-Exchange Migration. *Europhys. Lett. EPL* **27**, 473–478 (1994).

32. Yan, L. *et al.* Fabrication and uniaxial magnetic anisotropy of Co nanowires on a Pd(110) surface. *Appl. Phys. Lett.* **86**, 102503 (2005).

33. Rousset, S., Chiang, S., Fowler, D. E. & Chambliss, D. D. Intermixing and three-dimensional islands in the epitaxial growth of Au on Ag(110). *Phys. Rev. Lett.* **69**, 3200–3203 (1992).

34. Hugenschmidt, M. B., Hitzke, A. & Behm, R. J. Island assisted surface alloying observed after Ni deposition on Au(110)-(1 x 2). *Phys. Rev. Lett.* **76**, 2535–2538 (1996).

35. Pleth Nielsen, L. *et al.* Initial growth of Au on Ni(110): Surface alloying of immiscible metals. *Phys. Rev. Lett.* **71**, 754–757 (1993).

36. Wagner, M. *et al.* Nanostripe Pattern of NaCl Layers on Cu(110). *Phys. Rev. Lett.* **110**, 216101 (2013).

37. Glachant, A., Jaubert, M., Bienfait, M. & Boato, G. Monolayer adsorption of Kr and Xe on metal surfaces: Structures and uniaxial phase transitions on Cu(110). *Surf. Sci.* **115**, 219–235 (1982).

38. Roese, P. *et al.* Structure determination of substrate influenced silicon nano-ribbon growth. *Appl. Surf. Sci.* **467–468**, 580–587 (2019).

39. Leandri, C. *et al.* Self-aligned silicon quantum wires on Ag(110). *Surf. Sci.* **574**, L9–L15 (2005).

40. Sahaf, H. *et al.* Formation of a one-dimensional grating at the molecular scale by self-assembly of straight silicon nanowires. *Appl. Phys. Lett.* **90**, 263110 (2007).

41. Bethge, H. Electron microscopic studies of surface structures and some relations to surface phenomena. *Surf. Sci.* **3**, 33–41 (1965).

42. Bassett, G. A. A new technique for decoration of cleavage and slip steps on ionic crystal surfaces. *Philos. Mag. J. Theor. Exp. Appl. Phys.* **3**, 1042–1045 (1958).

43. Gambardella, P., Blanc, M., Brune, H., Kuhnke, K. & Kern, K. One-dimensional metal chains on Pt vicinal surfaces. *Phys. Rev. B* **61**, 2254–2262 (2000).

44. Rohart, S. *et al.* Atomistic mechanisms for the ordered growth of Co nanodots on Au(788): a comparison between VT-STM experiments and multi-scaled calculations. *Surf. Sci.* **559**, 47–62 (2004).

45. Baudot, G. *et al.* Temperature dependence of ordered cobalt nanodots growth on Au(7 8 8). *11th Int. Conf. Solid Films Surf.* **212–213**, 360–366 (2003).

46. Repain, V., Berroir, J. M., Rousset, S. & Lecoeur, J. Interaction between steps and reconstruction on Au(111). *EPL Europhys. Lett.* **47**, 435 (1999).

47. Repain, V., Baudot, G., Ellmer, H. & Rousset, S. Ordered growth of cobalt nanostructures on a Au(111) vicinal surface: nucleation mechanisms and temperature behavior. *Mater. Sci. Eng. B* **96**, 178–187 (2002).

48. Zhang, L. *et al.* Site- and Configuration-Selective Anchoring of Iron–Phthalocyanine on the Step Edges of Au(111) Surface. *J. Phys. Chem. C* **115**, 10791–10796 (2011).

49. Kröger, J., Jensen, H., Néel, N. & Berndt, R. Self-organization of cobalt-phthalocyanine on a vicinal gold surface revealed by scanning tunnelling microscopy. *ECOSS-24* **601**, 4180–4184 (2007).

50. Kern, *et al.* Long-range spatial self-organization in the adsorbate-induced restructuring of surfaces: Cu{100}-(2 x 1)O. *Phys. Rev. Lett.* **67**, 855–858 (1991).

51. Vanderbilt, D. Phase segregation and work-function variations on metal surfaces: spontaneous formation of periodic domain structures. *Surf. Sci.* **268**, L300–L304 (1992).

52. Coulman, D. J., Wintterlin, J., Behm, R. J. & Ertl, G. Novel mechanism for the formation of chemisorption phases: The (2 x 1)O-Cu(110) ``added row'' reconstruction. *Phys. Rev. Lett.* **64**, 1761–1764 (1990).

53. Jensen, F., Besenbacher, F., Laegsgaard, E. & Stensgaard, I. Surface reconstruction of Cu(110) induced by oxygen chemisorption. *Phys. Rev. B* **41**, 10233–10236 (1990).

54. Zeppenfeld, P., Krzyzowski, M., Romainczyk, C., Comsa, G. & Lagally, M. G. Size relation for surface systems with long-range interactions. *Phys. Rev. Lett.* **72**, 2737–2740 (1994).

55. Sun, L. D., Denk, R., Hohage, M. & Zeppenfeld, P. Scattering of surface electrons from CuO stripes on Cu(110). *Surf. Sci.* **602**, L1–L4 (2008).

56. Zeppenfeld, P., Diercks, V., Tölkes, C., David, R. & Krzyzowski, M. A. Adsorption and growth on nanostructured surfaces. *Appl. Surf. Sci.* **130–132**, 484–490 (1998).

57. Zeppenfeld, P. *et al.* Selective adsorption and structure formation of N2 on the nanostructured Cu-CuO stripe phase. *Phys. Rev. B* **66**, (2002).

58. Boishin, G., Sun, L. D., Hohage, M. & Zeppenfeld, P. Growth of cobalt on the nanostructured Cu–CuO(110) surface. *Surf. Sci.* **512**, 185–193 (2002).

59. Denk, R., Hohage, M. & Zeppenfeld, P. Extremely sharp spin reorientation transition in ultrathin Ni films grown on Cu(110)-(2x1)O. *Phys. Rev. B* **79**, 073407 (2009).

60. Otero, R. *et al.* One-Dimensional Assembly and Selective Orientation of Lander Molecules on an O–Cu Template. *Angew. Chem. Int. Ed.* **43**, 2092–2095 (2004).

61. Fan, Q. *et al.* Confined Synthesis of Organometallic Chains and Macrocycles by Cu–O Surface Templating. *ACS Nano* **10**, 3747–3754 (2016).

62. He, G. Atomic structure of Si nanowires on Ag(110): A density-functional theory study. *Phys. Rev. B* **73**, 035311 (2006).

63. Ronci, F. *et al.* Low temperature STM/STS study of silicon nanowires grown on the Ag(110) surface. *Phys. Status Solidi C* **7**, 2716–2719 (2010).

64. Kara, A. *et al.* Silicon nano-ribbons on Ag(110): a computational investigation. *J. Phys. Condens. Matter* **22**, 045004 (2010).

65. Himpsel, F. J., McFeely, F. R., Taleb-Ibrahimi, A., Yarmoff, J. A. & Hollinger, G. Microscopic structure of the SiO2/Si interface. *Phys. Rev. B* **38**, 6084–6096 (1988).

66. Aufray, B. *et al.* Graphene-like silicon nanoribbons on Ag(110): A possible formation of silicene. *Appl. Phys. Lett.* **96**, 183102 (2010).

67. De Padova, P. *et al.* Evidence of graphene-like electronic signature in silicene nanoribbons. *Appl. Phys. Lett.* **96**, 261905 (2010).

68. Padova, P. D. *et al.* 1D graphene-like silicon systems: silicene nano-ribbons. *J. Phys. Condens. Matter* **24**, 223001 (2012).

69. De Padova, P. *et al.* Multilayer Silicene Nanoribbons. *Nano Lett.* **12**, 5500–5503 (2012).

70. Colonna, S., Serrano, G., Gori, P., Cricenti, A. & Ronci, F. Systematic STM and LEED investigation of the Si/Ag(110) surface. *J. Phys. Condens. Matter* **25**, 315301 (2013).

71. Bernard, R. *et al.* Growth of Si ultrathin films on silver surfaces: Evidence of an Ag(110) reconstruction induced by Si. *Phys. Rev. B* **88**, 121411 (2013).

72. Gori, P., Pulci, O., Ronci, F., Colonna, S. & Bechstedt, F. Origin of Dirac-cone-like features in silicon structures on Ag(111) and Ag(110). *J. Appl. Phys.* **114**, 113710 (2013).

73. Borensztein, Y., Prévot, G. & Masson, L. Large differences in the optical properties of a single layer of Si on Ag(110) compared to silicene. *Phys. Rev. B* **89**, 245410 (2014).

74. Phys. Rev. B 96, 039904 (2017) - Erratum: Large differences in the optical properties of a single layer of Si on Ag(110) compared to silicene [Phys. Rev. B 89, 245410 (2014)]. Available at: https://journals.aps.org/prb/abstract/10.1103/PhysRevB.96.039904. (Accessed: 22nd April 2019)

75. Spencer, M. & Morishita, T. *Silicene: Structure, Properties and Applications*. (Springer, 2016).

76. Hogan, C., Colonna, S., Flammini, R., Cricenti, A. & Ronci, F. Structure and stability of Si/Ag(110) nanoribbons. *Phys. Rev. B* **92**, 115439 (2015).

77. Cerdá, J. I. *et al.* Unveiling the pentagonal nature of perfectly aligned single-and double-strand Si nano-ribbons on Ag(110). *Nat. Commun.* **7**, 13076 (2016).

78. Prévot, G. *et al.* Si Nanoribbons on Ag(110) Studied by Grazing-Incidence X-Ray Diffraction, Scanning Tunneling Microscopy, and Density-Functional Theory: Evidence of a Pentamer Chain Structure. *Phys. Rev. Lett.* **117**, 276102 (2016).

79. Espeter, P. *et al.* Facing the interaction of adsorbed silicon nano-ribbons on silver. *Nanotechnology* **28**, 455701 (2017).

80. Sheng, S. *et al.* The Pentagonal Nature of Self-Assembled Silicon Chains and Magic Clusters on Ag(110). *Nano Lett.* **18**, 2937–2942 (2018).

81. Salomon, E. *et al.* Etching of silicon nanowires on Ag(110) by atomic hydrogen. *Surf. Sci.* **603**, 3350–3354 (2009).

82. Dávila, M. E. *et al.* Comparative structural and electronic studies of hydrogen interaction with isolated versus ordered silicon nanoribbons grown on Ag(110). *Nanotechnology* **23**, 385703 (2012).

83. Padova, P. D., Quaresima, C., Olivieri, B., Perfetti, P. & Lay, G. L. Strong resistance of silicene nanoribbons towards oxidation. *J. Phys. Appl. Phys.* **44**, 312001 (2011).

84. Sahaf, H. *et al.* Growth of Co nanolines on self-assembled Si nanostripes. *EPL Europhys. Lett.* **86**, 28006 (2009).

85. Masson, L. *et al.* Nanoscale Si template for the growth of self-organized one-dimensional nanostructures. *11th Int. Conf. At. Control. Surf. Interfaces Nanostructures* **267**, 192–195 (2013).

86. Salomon, E. & Kahn, A. One-dimensional organic nanostructures: A novel approach based on the selective adsorption of organic molecules on silicon nanowires. *Surf. Sci.* **602**, L79–L83 (2008).

87. Dettoni, F., Sahaf, H., Moyen, E., Masson, L. & Hanbücken, M. Nanoscale template for the growth of one-dimensional nanostructures. *EPL Europhys. Lett.* **94**, 28007 (2011).

88. Michez, L. *et al.* Magnetic properties of self-organized Co dimer nanolines on Si/Ag(110). *Beilstein J. Nanotechnol.* **6**, 777–784 (2015).

89. Padova, P. D. *et al.* Mn-silicide nanostructures aligned on massively parallel silicon nano-ribbons. *J. Phys. Condens. Matter* **25**, 014009 (2012).

90. Brown, W. F. Thermal Fluctuations of a Single-Domain Particle. *Phys. Rev.* **130**, 1677–1686 (1963).

91. Elmers, H. J. *et al.* Submonolayer Magnetism of Fe(110) on W(110): Finite Width Scaling of Stripes and Percolation between Islands. *Phys. Rev. Lett.* **73**, 898–901 (1994).

92. Néel, L. Anisotropie magnétique superficielle et surstructures d'orientation. *J. Phys. Radium* **15**, 225–239 (1954).

93. Bruno, P. Tight-binding approach to the orbital magnetic moment and magnetocrystalline anisotropy of transition-metal monolayers. *Phys. Rev. B* **39**, 865–868 (1989).

94. Zeper, W. B., Greidanus, F. J. a. M., Carcia, P. F. & Fincher, C. R. Perpendicular magnetic anisotropy and magneto-optical Kerr effect of vapor-deposited Co/Pt-layered structures. *J. Appl. Phys.* **65**, 4971–4975 (1989).

95. Gradmann, U. & Müller, J. Flat Ferromagnetic, Epitaxial 48Ni/52Fe(111) Films of few Atomic Layers. *Phys. Status Solidi B* **27**, 313–324 (1968).

96. Weller, D. *et al.* Microscopic Origin of Magnetic Anisotropy in Au/Co/Au Probed with X-Ray Magnetic Circular Dichroism. *Phys. Rev. Lett.* **75**, 3752–3755 (1995).

97. Gambardella, P. *et al.* Giant Magnetic Anisotropy of Single Cobalt Atoms and Nanoparticles. *Science* **300**, 1130 LP – 1133 (2003).

98. Weiss, N. *et al.* Uniform Magnetic Properties for an Ultrahigh-Density Lattice of Noninteracting Co Nanostructures. *Phys. Rev. Lett.* **95**, 157204 (2005).

99. Miyamachi, T. *et al.* Stabilizing the magnetic moment of single holmium atoms by symmetry. *Nature* **503**, 242–246 (2013).

100. Karlewski, C. *et al.* Magnetic adatoms as memory bits: A quantum master equation analysis. *Phys. Rev. B* **91**, 245430 (2015).

101. Donati, F. *et al.* Magnetism of Ho and Er Atoms on Close-Packed Metal Surfaces. *Phys. Rev. Lett.* **113**, 237201 (2014).

102. Donati, F. *et al.* Magnetic remanence in single atoms. *Science* **352**, 318–321 (2016).

103. Ishikawa, N., Sugita, M., Ishikawa, T., Koshihara, S. & Kaizu, Y. Lanthanide Double-Decker Complexes Functioning as Magnets at the Single-Molecular Level. *J. Am. Chem. Soc.* **125**, 8694–8695 (2003).

104. Ishikawa, N., Sugita, M. & Wernsdorfer, W. Nuclear Spin Driven Quantum Tunneling of Magnetization in a New Lanthanide Single-Molecule Magnet: Bis(Phthalocyaninato)holmium Anion. *J. Am. Chem. Soc.* **127**, 3650–3651 (2005).

105. AlDamen, M. A., Clemente-Juan, J. M., Coronado, E., Martí-Gastaldo, C. & Gaita-Ariño, A. Mononuclear Lanthanide Single-Molecule Magnets Based on Polyoxometalates. *J. Am. Chem. Soc.* **130**, 8874–8875 (2008).

106. Gambardella, P. *et al.* Ferromagnetism in one-dimensional monatomic metal chains. *Nature* **416**, 301–304 (2002).

107. Dorantes-Dávila, J. & Pastor, G. M. Magnetic Anisotropy of One-Dimensional Nanostructures of Transition Metals. *Phys. Rev. Lett.* **81**, 208–211 (1998).

108. Félix-Medina, R., Dorantes-Dávila, J. & Pastor, G. M. Spin moments, orbital moments and magnetic anisotropy of finite-length Co wires deposited on Pd(110). *New J. Phys.* **4**, 100–100 (2002).

109. Lazarovits, B., Szunyogh, L., Weinberger, P. & Újfalussy, B. Magnetic properties of finite Fe chains at fcc Cu(001) and Cu(111) surfaces. *Phys. Rev. B* **68**, 024433 (2003).

110. Lazarovits, B., Szunyogh, L. & Weinberger, P. Magnetic properties of finite Co chains on Pt(111). *Phys. Rev. B* **67**, 024415 (2003).

111. de Lima, F. D. C. & Miwa, R. H. Nanolines of transition metals ruled by grain boundaries in graphene: An ab initio study. *Mater. Chem. Phys.* **194**, 118–127 (2017).

112. Honolka, J. *et al.* Complex magnetic phase in submonolayer Fe stripes on Pt(997). *Phys. Rev. B* **79**, 104430 (2009).

113. Dupé, B. *et al.* Giant magnetization canting due to symmetry breaking in zigzag Co chains on Ir(001). *New J. Phys.* **17**, 023014 (2015).

114. Gambardella, P. *et al.* Oscillatory Magnetic Anisotropy in One-Dimensional Atomic Wires. *Phys. Rev. Lett.* **93**, 077203 (2004).

115. Hong, J. & Wu, R. Q. First principles calculations of magnetic anisotropy energy of Co monatomic wires. *Phys. Rev. B* **67**, 020406 (2003).

116. Binnig, G., Rohrer, H., Gerber, Ch. & Weibel, E. Surface Studies by Scanning Tunneling Microscopy. *Phys. Rev. Lett.* **49**, 57–61 (1982).

117. Binnig, G., Rohrer, H., Gerber, Ch. & Weibel, E. Tunneling through a controllable vacuum gap. *Appl. Phys. Lett.* **40**, 178–180 (1982).

118. Nečas, D. & Klapetek, P. Gwyddion: an open-source software for SPM data analysis. *Open Phys.* **10**, 181–188 (2011).

119. Nieuwenhuys, B. E., Van Aardenne, O. G. & Sachtler, W. M. H. Adsorption of xenon on group VIII and ib metals studied by photoelectric work function measurements. *Chem. Phys.* **5**, 418–428 (1974).

120. Simmons, J. G. Generalized Formula for the Electric Tunnel Effect between Similar Electrodes Separated by a Thin Insulating Film. *J. Appl. Phys.* **34**, 1793–1803 (1963).

121. Tersoff, J. & Hamann, D. R. Theory and Application for the Scanning Tunneling Microscope. *Phys. Rev. Lett.* **50**, 1998–2001 (1983).

122. Tersoff, J. & Hamann, D. R. Theory of the scanning tunneling microscope. *Phys. Rev. B* **31**, 805–813 (1985).

123. Lang, N. D. Spectroscopy of single atoms in the scanning tunneling microscope. *Phys. Rev. B* **34**, 5947–5950 (1986).

124. Lucier, A.-S., Mortensen, H., Sun, Y. & Grütter, P. Determination of the atomic structure of scanning probe microscopy tungsten tips by field ion microscopy. *Phys. Rev. B* **72**, 235420 (2005).

125. Wende, H. Recent advances in x-ray absorption spectroscopy. *Rep. Prog. Phys.* **67**, 2105–2181 (2004).

126. de Broglie, M. Sur une nouveau procédé permettant d'obtenir la photographie des spectres de raies des rayons Röntgen. *Com. Ren* (1913).

127. Groot, F. de, Kotani, A. & Kotani, A. *Core Level Spectroscopy of Solids*. (CRC Press, 2008). doi:10.1201/9781420008425

128. Stöhr, J. *NEXAFS Spectroscopy*. (Springer Science & Business Media, 2013).

129. Beaurepaire, E., Bulou, H., Scheurer, F. & Kappler, J.-P. *Magnetism and Synchrotron Radiation*. (2001).

130. Interactions of Polarized Photons with Matter. in *Magnetism: From Fundamentals to Nanoscale Dynamics* (eds. Stöhr, J. & Siegmann, H. C.) 351–429 (Springer Berlin Heidelberg, 2006). doi:10.1007/978-3-540-30283-4_9

131. Erskine, J. L. & Stern, E. A. Calculation of the $M_{2,3}$ magneto-optical absorption spectrum of ferromagnetic nickel. *Phys. Rev. B* **12**, 5016–5024 (1975).

132. Schütz, G. *et al.* Absorption of circularly polarized x rays in iron. *Phys. Rev. Lett.* **58**, 737–740 (1987).

133. van der Laan, G. *et al.* Experimental proof of magnetic x-ray dichroism. *Phys. Rev. B* **34**, 6529–6531 (1986).

134. Thole, B. T., van der Laan, G. & Sawatzky, G. A. Strong Magnetic Dichroism Predicted in the $M_{4,5}$ X-Ray Absorption Spectra of Magnetic Rare-Earth Materials. *Phys. Rev. Lett.* **55**, 2086–2088 (1985).

135. Chen, C. T., Sette, F., Ma, Y. & Modesti, S. Soft-x-ray magnetic circular dichroism at the $L_{2,3}$ edges of nickel. *Phys. Rev. B* **42**, 7262–7265 (1990).

136. Thole, B. T., Carra, P., Sette, F. & van der Laan, G. X-ray circular dichroism as a probe of orbital magnetization. *Phys. Rev. Lett.* **68**, 1943–1946 (1992).

137. Carra, P., Thole, B. T., Altarelli, M. & Wang, X. X-ray circular dichroism and local magnetic fields. *Phys. Rev. Lett.* **70**, 694–697 (1993).

138. Chen, C. T. *et al.* Experimental Confirmation of the X-Ray Magnetic Circular Dichroism Sum Rules for Iron and Cobalt. *Phys. Rev. Lett.* **75**, 152–155 (1995).

139. Guo, G. Y., Ebert, H., Temmerman, W. M. & Durham, P. J. First-principles calculation of magnetic x-ray dichroism in Fe and Co multilayers. *Phys. Rev. B* **50**, 3861–3868 (1994).

140. Wu, R., Wang, D. & Freeman, A. J. First principles investigation of the validity and range of applicability of the x-ray magnetic circular dichroism sum rule. *Phys. Rev. Lett.* **71**, 3581–3584 (1993).

141. Ohresser, P. *et al.* DEIMOS: A beamline dedicated to dichroism measurements in the 350–2500 eV energy range. *Rev. Sci. Instrum.* **85**, 013106 (2014).

142. Chen, C.-T., Sette, F. & Smith, N. V. Double-headed Dragon monochromator for soft x-ray circular dichroism studies. *Appl. Opt.* **29**, 4535–4536 (1990).

143. Sodhi, R. N. S. & Brion, C. E. Reference energies for inner shell electron energy-loss spectroscopy. *J. Electron Spectrosc. Relat. Phenom.* **34**, 363–372 (1984).

144. van der Laan, G. & Figueroa, A. I. X-ray magnetic circular dichroism—A versatile tool to study magnetism. *Chem. Struct. Using Synchrotron Radiat.* **277–278**, 95–129 (2014).

145. Lee, J. *et al.* A direct test of x-ray magnetic circular dichroism sum rules for strained Ni films using polarized neutron reflection. *J. Phys. Condens. Matter* **9**, L137–L143 (1997).

146. Daher Mansour, M., Parret, R. & Masson, L. Nanoscale investigation of Si nanoribbon growth on Ag(110). *J. Vac. Sci. Technol. A* **36**, 061402 (2018).

147. Chaumeton, F. *et al.* Noncontact atomic force microscopy and density functional theory studies of the (2 x 2) reconstructions of the polar AlN(0001) surface. *Phys. Rev. B* **94**, 165305 (2016).

148. Li, Y. *et al.* Transition from one- to two-dimensional island growth on metal (110) surfaces induced by anisotropic corner rounding. *Phys. Rev. B* **56**, 12539–12543 (1997).

149. Degroote, B., Dekoster, J. & Langouche, G. Step decoration and surface alloying: growth of cobalt on Ag(100) as a function of deposition temperature. *Surf. Sci.* **452**, 172–178 (2000).

150. Kumikov, V. K. & Khokonov, Kh. B. On the measurement of surface free energy and surface tension of solid metals. *J. Appl. Phys.* **54**, 1346–1350 (1983).

151. Lachenwitzer, A., Morin, S., Magnussen, O. M. & Behm, R. J. In situ STM study of electrodeposition and anodic dissolution of Ni on Ag(111). *Phys. Chem. Chem. Phys.* **3**, 3351–3363 (2001).

152. Dézsi, I. *et al.* Ultrathin Fe layers on Ag (100) surface. *Surf. Sci.* **601**, 2525–2531 (2007).

153. Dettoni, F., Sahaf, H., Moyen, E., Masson, L. & Hanbücken, M. Nanoscale template for the growth of one-dimensional nanostructures. *EPL Europhys. Lett.* **94**, 28007 (2011).

154. Takano, N., Niwa, D., Yamada, T. & Osaka, T. Nickel deposition behavior on n-type silicon wafer for fabrication of minute nickel dots. *Electrochimica Acta* **45**, 3263–3268 (2000).

155. Tung, R. T., Gibson, J. M. & Poate, J. M. Formation of Ultrathin Single-Crystal Silicide Films on Si: Surface and Interfacial Stabilization of Si-Ni${\mathrm{Si}}_{2}$ Epitaxial Structures. *Phys. Rev. Lett.* **50**, 429–432 (1983).

156. Yoshimura, M., Ono, I. & Ueda, K. STM observation of nickel silicides on Si(001). *Appl. Phys. A* **66**, 1043–1045 (1998).

157. Horsfield, A. P., Kenny, S. D. & Fujitani, H. Density-functional study of adsorption of Co on Si(100). *Phys. Rev. B* **64**, 245332 (2001).

158. Masson, L. & Thibaudau, F. Atomic structures of Si(111) surface during silane UHV-CVD. *Surf. Sci.* **504**, 191–198 (2002).

159. Pong, W. F. *et al.* X-ray-absorption spectroscopy of ${\mathrm{CoSi}}_{2}$. *Phys. Rev. B* **53**, 16510–16515 (1996).

160. Daher Mansour, M., Parret, R., Cheynis, F., Choueikani, F., Michez, L., & Masson, L., Magnetic anisotropy of one-dimensional Co nanonanostructures. in preparation.

161. Thole, B. T., Carra, P., Sette, F. & van der Laan, G. X-ray circular dichroism as a probe of orbital magnetization. *Phys Rev Lett* **68**, 1943–1946 (1992).

162. Carra, P., Thole, B. T., Altarelli, M. & Wang, X. X-ray circular dichroism and local magnetic fields. *Phys Rev Lett* **70**, 694–697 (1993).

163. Chen, C. T. *et al.* Experimental Confirmation of the X-Ray Magnetic Circular Dichroism Sum Rules for Iron and Cobalt. *Phys Rev Lett* **75**, 152–155 (1995).

164. Wu, R., Wang, D. & Freeman, A. J. First principles investigation of the validity and range of applicability of the x-ray magnetic circular dichroism sum rule. *Phys Rev Lett* **71**, 3581–3584 (1993).

165. Guo, G. Y., Ebert, H., Temmerman, W. M. & Durham, P. J. First-principles calculation of magnetic x-ray dichroism in Fe and Co multilayers. *Phys Rev B* **50**, 3861–3868 (1994).

166. Lehnert, A. *et al.* Magnetic anisotropy of Fe and Co ultrathin films deposited on Rh(111) and Pt(111) substrates: An experimental and first-principles investigation. *Phys Rev B* **82**, 94409 (2010).

167. Dorantes-Dávila, J. & Pastor, G. M. Magnetic Anisotropy of One-Dimensional Nanostructures of Transition Metals. *Phys Rev Lett* **81**, 208–211 (1998).

168. Gambardella, P. *et al.* Supramolecular control of the magnetic anisotropy in two-dimensional high-spin Fe arrays at a metal interface. *Nat. Mater.* **8**, 189–193 (2009).

169. Umbach, T. R. *et al.* Ferromagnetic Coupling of Mononuclear Fe Centers in a Self-Assembled Metal-Organic Network on Au(111). *Phys. Rev. Lett.* **109**, 267207 (2012).

170. Abdurakhmanova, N. *et al.* Superexchange-Mediated Ferromagnetic Coupling in Two-Dimensional Ni-TCNQ Networks on Metal Surfaces. *Phys. Rev. Lett.* **110**, 027202 (2013).

171. Giovanelli, L. *et al.* Magnetic Coupling and Single-Ion Anisotropy in Surface-Supported Mn-Based Metal–Organic Networks. *J. Phys. Chem. C* **118**, 11738–11744 (2014).

172. Faraggi, M. N. *et al.* Modeling Ferro- and Antiferromagnetic Interactions in Metal–Organic Coordination Networks. *J. Phys. Chem. C* **119**, 547–555 (2015).

173. Grill, L. *et al.* Nano-architectures by covalent assembly of molecular building blocks. *Nat. Nanotechnol.* **2**, 687–691 (2007).

174. Kalashnyk, N. *et al.* On-surface synthesis of aligned functional nanoribbons monitored by scanning tunnelling microscopy and vibrational spectroscopy. *Nat. Commun.* **8**, 14735 (2017).

175. Clair, S. & de Oteyza, D. G. Controlling a Chemical Coupling Reaction on a Surface: Tools and Strategies for On-Surface Synthesis. *Chem. Rev.* **119**, 4717–4776 (2019).

176. Auwärter, W., Écija, D., Klappenberger, F. & Barth, J. V. Porphyrins at interfaces. *Nat. Chem.* **7**, 105–120 (2015).

177. Koudia, M., Nardi, E., Siri, O. & Abel, M. On-surface synthesis of covalent coordination polymers on micrometer scale. *Nano Res.* **10**, 933–940 (2017).

178. Audi, H. *et al.* Extendable nickel complex tapes that reach NIR absorptions. *Chem. Commun.* **50**, 15140–15143 (2014).